UNIVERSITÀ DEGLI STUDI DI TRIESTE

XXXVI CICLO DEL DOTTORATO DI RICERCA IN

SCIENZE DELLA TERRA, FLUIDODINAMICA E MATEMATICA. INTERAZIONI E METODICHE

SINKHOLES OF THE FRIULI VENEZIA GIULIA REGION: CHARACTERIZATION, DATA COLLECTION AND HAZARD DEFINITION

Settore scientifico-disciplinare: **GEO/05**

DOTTORANDA

ALICE BUSETTI

COORDINATORE

PROF. STEFANO MASET

SUPERVISORE DI TESI

PROF. CHIARA CALLIGARIS

ANNO ACCADEMICO 2022/2023


UNIVERSITÀ
DEGLI STUDI
DI TRIESTE

UNIVERSITÀ DEGLI STUDI DI TRIESTE

TABLE OF CONTENTS

ABSTRACT *1*

THESIS OUTLINE *5*

CHAPTER 1 INTRODUCTION *7*

CHAPTER 2 SINKHOLE GEODATABASE *19*

CHAPTER 3 TEST SITE AREAS *62*

Chapter 3.1 Non-invasive methodological approach applied in Quinis village *65*

Chapter 3.2 A joint geophysical approach applied in Baus village *94*

Chapter 3.3 Gypsum dissolution rate in Quinis village (I part) *111*

Chapter 3.4 Gypsum dissolution rate in Quinis village (II part) *119*

Chapter 3.5 Gypsum dissolution rate - laboratory experiment *125*

CHAPTER 4 SINKHOLE HAZARD *131*

Chapter 4.1 New collapse, old story: Raveo's sinkhole *135*

Chapter 4.2 Analysis of IGM aerial frames in Sauris municipality *147*

Chapter 4.3 Trench excavation in Enemonzo municipality *152*

Chapter 4.4 Different acquisition method for digital preservation of the trench *163*

Chapter 4.5 Methodological approach proposal for the definition of hazard in evaporitic environment *184*

Chapter 4.6 Tool elaboration and application *192*

CHAPTER 5 CONCLUSION *201*

ACKNOWLEDGMENTS

ABSTRACT

The work carried out within the PhD, was focused on the identification, characterization and in-depth study of sinkholes. The goal was to establish setback distances and develop an informatic protocol capable of automatically assigning hazard level to each phenomenon. As test site area, the Friuli Venezia Giulia Region (FVG) was chosen. The FVG and the Classical Karst, with their abundance of sinkholes occurring in different physiographic and geological contexts, represented an ideal training test area.

The PhD activities fits into what in accordance between the Department of Mathematics and Geosciences of the University of Trieste and the Geological Survey of the FVG. The latter in turn, partially transpose the activities proposed by ISPRA (Istituto Superiore per la Protezione e la Ricerca Ambientale) that since 2002, started a project to inventory natural and anthropogenic sinkholes present on the Italian territory into a national geodatabase.

Following national guidelines, the FVG also began collecting information on natural sinkhole, creating a regional geodatabase (*Chapter 2*). From an informatic point of view, the database contains alphanumeric and geometric information for each individual phenomenon.

The initial activity realised within the PhD focused on the geodatabase and involved two distinct actions:

1) Review of the geodatabase structure and information;
2) Geodatabase population update.

The review of the structure has provided the introduction of additional fields and the modification of information within specific fields. Most of the sinkholes were mapped by initially analysing airborne LiDAR data, a process later validated through field surveys. This validation led to a significant revision, reducing the number of "undefined" sinkholes (from 446 in 2020 to 262 in 2023). It also involved the compilation and/or updating of fields such as classification, state of activity and morphometric parameters, contributing to the improvement of the number of cataloged phenomena. Additionally, the review consisted in the reshaping of sinkholes with the recent availability of DTM with a resolution of 0.5m.

The geodatabase initially focused on sinkholes linked to evaporitic bedrocks. Actually, it contains features occurred in different geolithological contexts such as carbonates, evaporites, conglomerates and Quaternary deposits.

During the PhD research, the census particularly emphasized carbonates, starting with the Classical Karst, known as the cradle of karstology. Subsequently, the analysis was spread across the entire regional territory. In this specific environment, characterized by numerous caves, the entrances of sub-horizontal ones can be attributed to bedrock collapse sinkholes. For this reason, the research started with the analysis of available data from the speleological inventory (CSR) of FVG region, examining a total of 8004 caves. A methodological protocol was developed to identify potential sinkholes. Following desk activities, specific caves were selected for field surveys, resulting in the identification of 159 new sinkholes. These were documented and incorporated into the geodatabase.

Simultaneously with the geodatabase review and update, in-depth studies were conducted on different test sites to define the best methodology for characterizing these phenomena in various geolithological contexts.

The application of different methodologies in the Quinis village (Enemonzo municipality), such as the combination of interferometric data analysis and leveling data, geophysical investigations etc., proved to be fundamental not only for the 3D characterization of some subsurface features, but also for understanding their evolution over time (*Chapter 3.1*). In-depth geophysical investigations (ERT, electromagnetometer, refraction seismic etc.) were also carried out in correspondence of Baus (*Chapter 3.2*), a hamlet of Ovaro (UD), where, buildings were monitored using crackmeters. The synergic approach of using different type of investigations highlighted the importance of monitoring these elusive phenomena over time to prevent disasters, as it occurred in 2017 when a collapse blocked part of the regional state road.

In the area of Quinis a detailed investigation was further conducted with the aim of evaluating the dissolution rate (*Chapter 3.3* and *Chapter 3.4*). Gypsum rock samples were placed in piezometer tubes at various depths for a one-year experiment. CTD probes, located in 7 piezometers, continuously monitored the groundwater level, Electrical Conductivity (EC) and Temperature (T). After one year of observations, some samples were nearly completely dissolved, exhibiting a dissolution rate almost eight times higher than expected when compared to available literature data. To better understand this fast dissolution rate, a six-months laboratory experiment was carried out (*Chapter 3.5*). Rock samples were immersed in tap water that was changed respectively once a day, once a week and once a month (the EC was manually measured before every changing of water). The experiment highlighted the significance of the Saturation Index in the dissolution process concerning groundwater recharge. In fact, samples immersed in waters that were changed at different time intervals lost a percentage of weight directly proportional to the

frequency of water change (the more frequent the water change, the greater the weight loss).

All the activities done lead up to the development of a methodological approach to define a setback distance automatically. The protocol, developed for the sinkholes linked to evaporitic bedrock, in a GIS environment, can assign hazard levels to each feature present in the regional geodatabase. Studying these phenomena from a planning perspective is crucial due to their often dramatic interaction with existing infrastructures. This need is further justified by the recent occurrence of the phenomenon, exemplified by the sudden collapse in the Esemon di Sopra hamlet in April 2022 (*Chapter 4.1*). This example is the last of a series of other active sinkholes one of which can be recognised in the Sauris municipality. Since 1940s, the analyses of the IGM aerial frames, already highlighted its presence. Through a detailed investigation, including the analysis of the most recent Google Earth and Bing Maps images and a comparison with previous ones, the evolution and hazard of sinkholes become apparent (*Chapter 4.2*). But aerial images, can only provide information about larger events. If we consider the municipality of Enemonzo, where an active sinkhole is present in a grassy area and houses had to be demolished due to the presence of several others, aerial photos do not allow for their detection. Therefore, additional investigations are required. If you visit the grassy area today, what is visible is a bowl-shaped feature, classified as a cover suffosion sinkhole. Going more into detail and realizing a trench across the active sinkhole, it was possible to clarify its 3D cylindrical shape, characteristic of a cover collapse. The trench, realized in FVG and in Italy for the first time for characterising these type of phenomena, has been for sure essential (*Chapter 4.3*). The correct choice of its length and orientation was possible thanks to previous geophysical investigations in the area. Three different camera-equipped devices (a DJI Air 2S drone, a Nikon D5300 camera, and an iPhone 13 Pro) were used to capture photos of the entire area and the trench. The results and the quality of the data obtained by the 3 different acquisitions were compared, and acquired data were used to publish a paper (*Chapter 4.4*).

Once the precise mapping, classification and definition of the state of activity have been consolidated, the research activities shifted towards creating a methodological approach to define setback distances (*Chapter 4.5*). Currently, there is no specific method in the literature to calculate these values, even within the same study area. In the case of FVG region, a quantitative methodology was chosen, starting from available data collected in the geodatabase. Specific criteria based on the state of activity, the type of sinkhole (classification) and the lithology, led to calculate a buffer zone and attribute a hazard to each identified area. Furthermore, it was decided to comply with the P.A.I. protocol for the

classification of hazards (P1, P2, P3 and P4). The protocol was designed only for the sinkholes linked to the evaporitic environment. This separation between carbonates and evaporites was based on the difference in solution rates between the two rock types and the presence of voids in the subsoil. In carbonates, the dimension and development of sub-horizontal caves are crucial factors in hazard definition. For this reason, defining these aspects required a site-specific approach and couldn't be automated. The method, initially conceptualized, was later implemented using GIS techniques, resulting in a tool capable of assigning hazard levels to individual events (*Chapter 4.6*).

THESIS OUTLINE

The main outcomes of this thesis, with the reference to each paper are outlined as follows:

CHAPTER 1: INTRODUCTION

CHAPTER 2: SINKHOLE GEODATABASE

CHAPTER 3: TEST SITE AREAS

Chapter 3.1: Busetti A., Calligaris C., Forte E., Areggi G., Mocnik A., Zini L., (2020) Non-Invasive Methodological Approach to Detect and Characterize High-Risk Sinkholes in Urban Cover Evaporite Karst: Integrated Reflection Seismics, PS-InSAR, Leveling, 3D-GPR and Ancillary Data. A NE Italian Case Study. Remote Sensing 12, 3814. https://doi.org/10.3390/rs12223814

Chapter 3.2: Calligaris C., Forte E., **Busetti** A., Zini L. (2023) A joint geophysical approach to tune an integrated sinkhole monitoring method in evaporitic environments. Near Surface Geophysics, 1-16. https://doi.org/10.1002/nsg.12261

Chapter 3.3: Busetti A., Calligaris C., Zini L. (2023) Gypsum Dissolution Rate, New Data and Insights. In: Andreo B., Barberá J.A., Durán-Valsero J.J., Gil-Márquez J.M., Mudarra M. (Eds.) EuroKarst 2022, Málaga. Advances in Karst Science. Springer, Cham. https://doi.org/10.1007/978-3-031-16879-6_30

Chapter 3.4: update of the first 4 months of the experiment in village of Quinis

Chapter 3.5: laboratory experiment also involving the gypsum dissolution rate.

CHAPTER 4 SINKHOLE HAZARD

Chapter 4.1 (Abstract): Busetti A., Calligaris C., Fernetti M., Forte E. and Zini L. (2022) New collapse, old story: Raveo's sinkhole occurred on 21th April 2022. Man and Karst 2022; September 12th-17th, Custonaci, Italy

Chapter 4.2: Analysis of IGM aerial frames in Sauris municipality

Chapter 4.3: Trench excavation through an active sinkhole carried out for the first time in Italy (Enemonzo municipality)

Chapter 4.4: Corradetti A., Seers T., Mercuri M., Calligaris C., **Busetti A.,** Zini L. (2022) Benchmarking Different SfM-MVS Photogrammetric and iOS LiDAR Acquisition Methods for the Digital Preservation of a Short-Lived Excavation: A Case Study from an Area of Sinkhole Related Subsidence. Remote Sensing 14, 5187. https://doi.org/10.3390/rs14205187

Chapter 4.5: Methodological approach proposal for the definition of hazard in evaporitic environment
Chapter 4.6: Tool elaboration and application

CHAPTER 5: CONCLUSION

UNIVERSITÀ DEGLI STUDI DI TRIESTE

CHAPTER 1

INTRODUCTION

Sinkholes, also know as dolines, are closed depressions or holes in the ground characterized by internal drainage (Cvijić, 1893). The term "doline", originating from the Slavic word "dolina", was historically predominantly used by geomorphologists in Europe, while "sinkhole" is the more prelevant term in North America and among those dealing with engineering and environmental issues (Sowers, 1996; Sauro, 2003; Williams, 2004; Waltham et al., 2005; Gutiérrez et al., 2014; Gutiérrez, 2016; Parise, 2019 and Parise, 2022).

Sinkholes can vary in size from small depressions (50 cm) to impressive holes (more than 600 m in diameter) with depths typically ranging from a few centimeters to tens of meters. The largest phenomenon in the world is the Xiaozhai Tiankeng sinkhole in the Xinlong fengcong karst, Chongqing Province, China, a bedrock collapse sinkhole 635 meters in length and 511 meters deep from the lowest point of the rim (*Figure 1*).

Figure 1 *Xiaozhai Tiankeng sinkhole in China (https://earthlyemergencies.wordpress.com/2015/04/30/the-xiaozhai-tiankeng-sinkhole/ [accessed 16 Aug, 2023])*

Sinkholes can develop gradually over time or form suddenly, depending on factors such as geological conditions, water flow, and human activities like mining or construction (in this latter case, we refer to anthropogenic sinkholes, related to man-made artificial cavities (Parise et al., 2013)).

Sinkholes exhibit their most prominent formation and preservation within flat terrains, characterized by a gentle topographic gradient that facilitates enhanced water infiltration while impeding surface runoff and mechanical erosion (Gutiérrez & Lizaga, 2016; Öztürk et al., 2018a).

The development of sinkholes is primarily linked to the dissolution of soluble rocks: carbonate and/or evaporite. Notable distinctions exist between carbonate and evaporite karst systems, significantly influencing the formation of sinkholes and associated risks (Martínez et al., 1998; Gutiérrez et al., 2008a; Frumkin, 2013; Cooper & Gutiérrez, 2013). Notably, evaporites dissolve at a considerably faster rate (0.68 – 1.14 mm/y, Klimchouk et al., 1996 and 0.4 – 1.0 mm/y, Cucchi et al., 1998) compared to carbonates (0.117 mm/y, Dreybrodt, 2004 and 0.009 – 0.14 mm/y, Furlani et al., 2009). This difference explains the higher probability of sinkhole occurrences in evaporitic environments, often accompanied by increased subsidence rates (Gutiérrez et al., 2008a). Gypsum and halite have significantly lower mechanical strength and more ductile rheological properties than most carbonate rocks (Gutiérrez, 2016). Additionally, evaporite formations can experience substantial weakening within a human timescale due to rapid dissolution, often along existing discontinuity planes.

Sinkholes represent a severe geo-hazard in many countries, including France (Thierry et al., 2009), Germany (Dahm et al., 2010; Krawczyk et al., 2012), Lithuania (Paukstys et al., 1999), Russia (Koutepov et al., 2008), Spain (Gutiérrez et al., 2008; Sevil et al., 2020), the United Kingdom (Cooper, 1998; Cooper et al., 2011), Albania (Parise et al., 2004), the USA (Kuniansky et al., 2016), South Africa (Buttrick et al., 1998) and Iran (Karimi et al., 2010; Taheri et al., 2015). Italy is also affected by them (Nisio, 2008; Del Prete et al., 2010; De Waele et al., 2017; Calligaris et al., 2017; Busetti et al., 2020 and references therein). Recent investigations have revealed that the Friuli Venezia Giulia (FVG) Region is one of the areas most affected by sinkholes in northern Italy (Zini et al., 2015; Calligaris et al., 2020).

Due to the severe consequences in urban areas, causing physical and socio-economic damages to existing man-made structures, interest in sinkhole problems has greatly increased in recent decades. This has prompted the emergence of numerous genetic classifications within the global scientific literature (Williams, 2005; Waltham et al., 2005; Gutiérrez et al., 2008b, 2014). Historically, variations not only existed in the terminology employed, with terms such as "sinkhole" or "doline", but also in the definition of the processes driving sinkhole formation between American and European scholars. However, recent research efforts have successfully unified these definitions. Notably, the classification introduced by Gutiérrez et al., (2008, 2014) and more recently reproposed by

Parise (2019, 2022) stands out as the most contemporary and comprehensive classification of sinkholes to date.

This classification (*Figure 2*), integrating those proposed by Beck (2004) and Waltham et al., (2005), addresses the subsidence mechanisms occurring in both carbonate and evaporite karst environments. It distinguishes two groups of sinkholes: solution sinkholes and subsidence sinkholes. Solution sinkholes are associated with the gradual differential solutional lowering of the ground where karst rocks are exposed at the surface or covered by soil. These depressions primarily result from chemical denudation processes, rarely leading to ground instability problems (which is why this type of sinkhole has not been considered in the thesis).

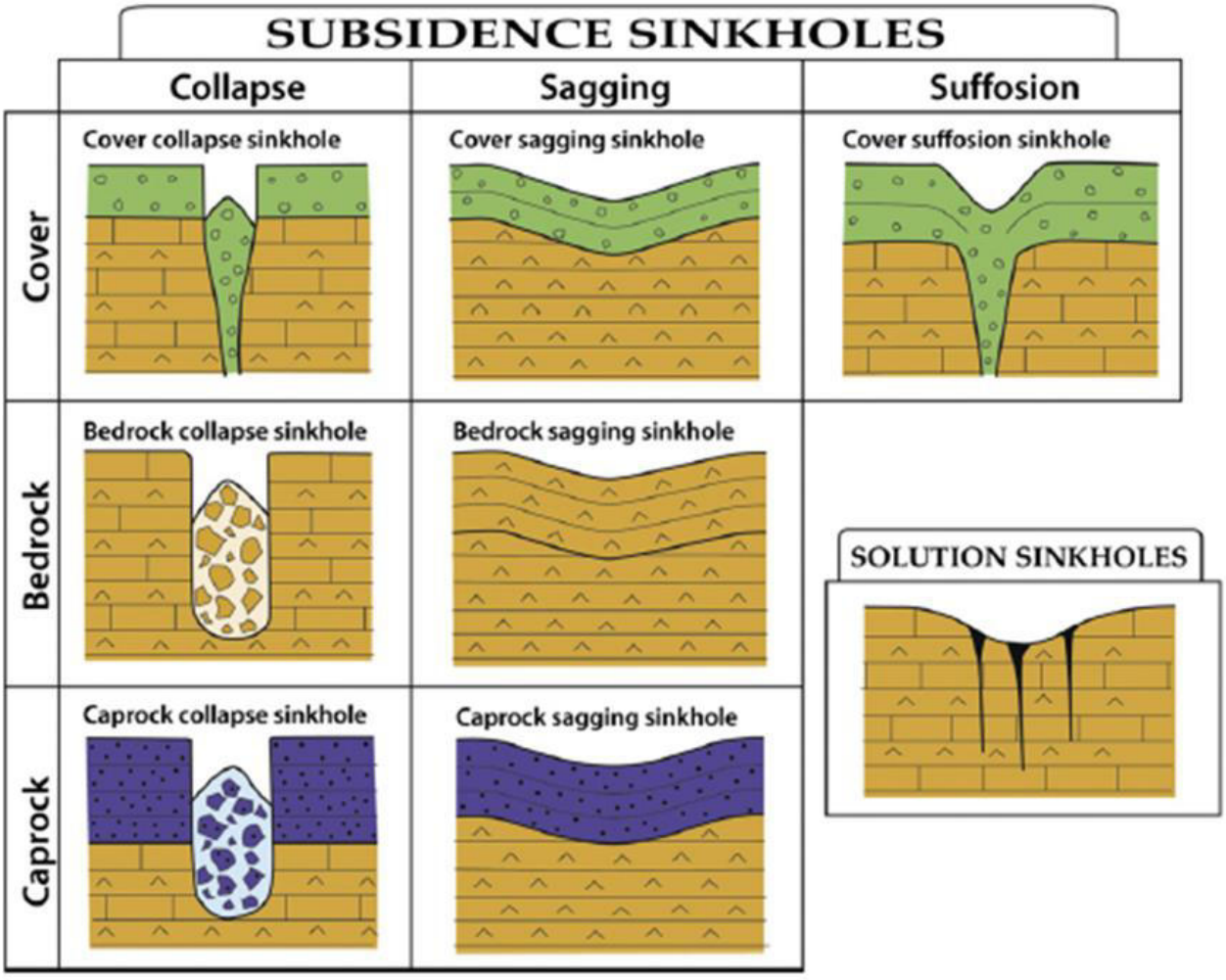

Figure 2 *Classification proposed by Gutiérrez et al., 2014*

Subsidence sinkholes, on the other hand, are linked to the downward ground displacement, regardless of the specific rheology of the altered material and the velocity of the process (Jackson, 1997). These sinkholes are particularly significant from a hazard perspective, as their development involves the settlement of the ground (Parise, 2019, 2022; De Waele & Gutiérrez, 2022).

The classification describes the end-members of subsidence sinkholes using two terms: the first refers to the material affected by internal and/or deformation processes (cover, bedrock, caprock). "Cover" refers to unconsolidated allogenic deposits or residual soil material, "bedrock" to karst rocks, and "caprock" to non-karst rocks.

The second term indicates the main subsidence process involved (collapse, suffosion or sagging). In particular, collapse is the brittle deformation of soil or rock material, either by the development of well-defined failure planes or brecciation; suffosion is the downward migration of cover deposits through voids and their progressive settling, and sagging is the ductile flexing (passive bending) of sediments caused by the lack of basal support.

Frequently, the generation of subsidence sinkholes involves more than one material type and several processes. These complex sinkholes can be described using combinations of the proposed terms with the dominant material and/or process, followed by the secondary one (e.g. cover and bedrock collapse sinkhole).

For the present thesis work, it was decided to adopt the international classification proposed by Gutiérrez et al., (2008b, 2014). The classification introduced by Nisio (2008) (*Figure 3*), currently employed in the Istituto Superiore per la Protezione e la Ricerca Ambientale (ISPRA) sinkhole geodatabase, was intentionally retained. This choice aims to facilitate the subsequent inclusion of sinkholes from the Friuli Venezia Giulia geodatabase into the ISPRA one. The classification proposed by Nisio (2008) is based on three distinct genetic processes: human activity, infiltration waters and rising fluids.

1. The first type is represented by anthropogenic sinkholes linked to the collapse of the ceilings of caves originated by human activity (mines, catacombs etc.);

2. the second type is refered to karst phenomena including solution, subsidence and collapse;

3. the third type is rappresented by deep piping sinkholes.

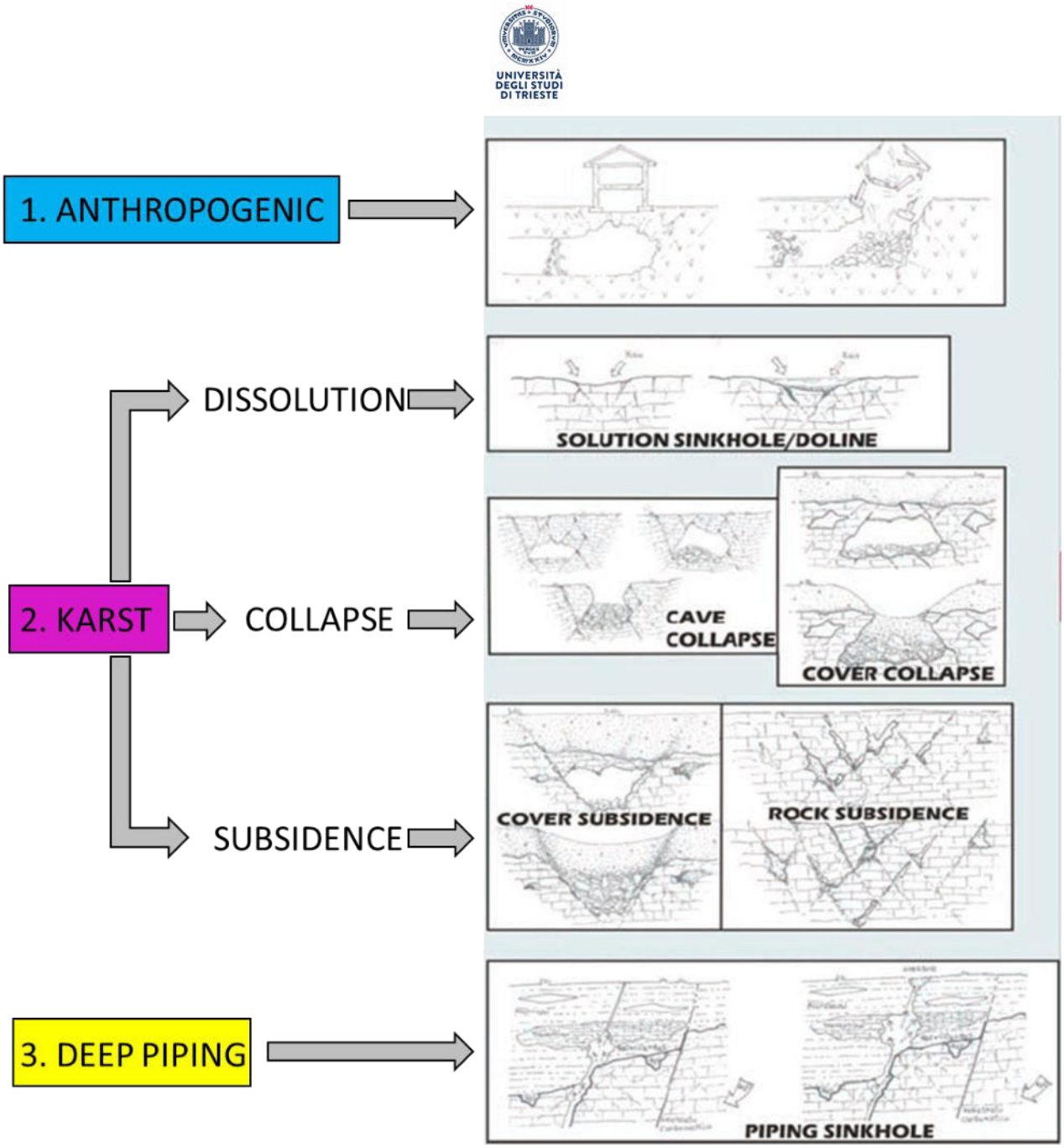

Figure 3 *Classification used in the ISPRA sinkhole geodatabase (proposed by Nisio, 2008)*

Below are some examples of different types of sinkholes identified in the territory of the Friuli Venezia Giulia Region (*Figure 4*, *Figure 5*, *Figure 6* and *Figure 7*).

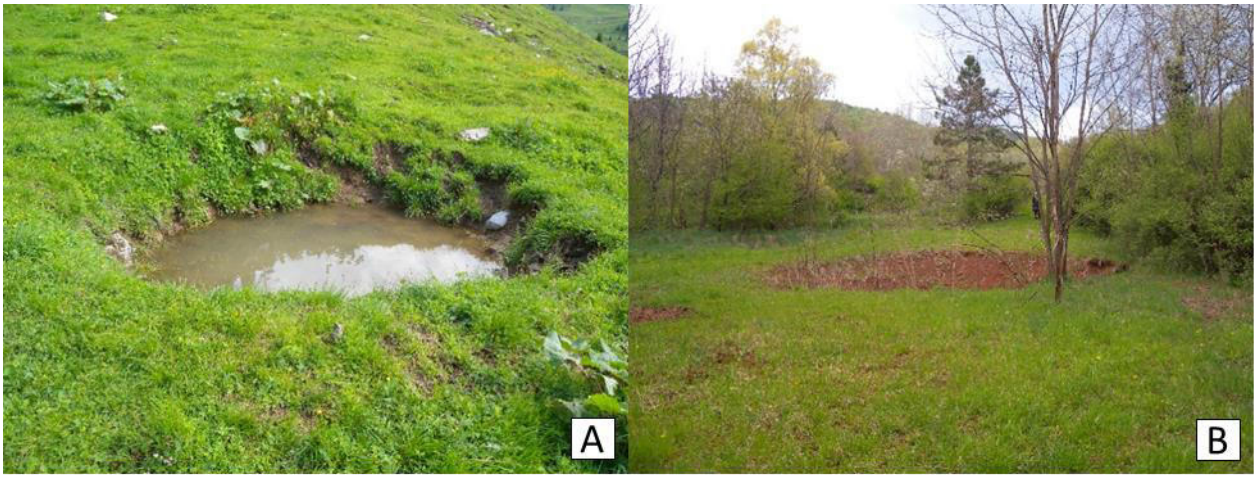

Figure 4 *Active cover collapse sinkholes:* ***A)*** *alluvial deposits (Sauris municipality);* ***B)*** *red soil (Sgonico municipality)*

Figure 5 *Bedrock collapse sinkholes developed in evaporitic environment:* ***A)*** *inactive sinkhole in Ligosullo municipality,* ***B)*** *Active sinkhole in Ampezzo municipality*

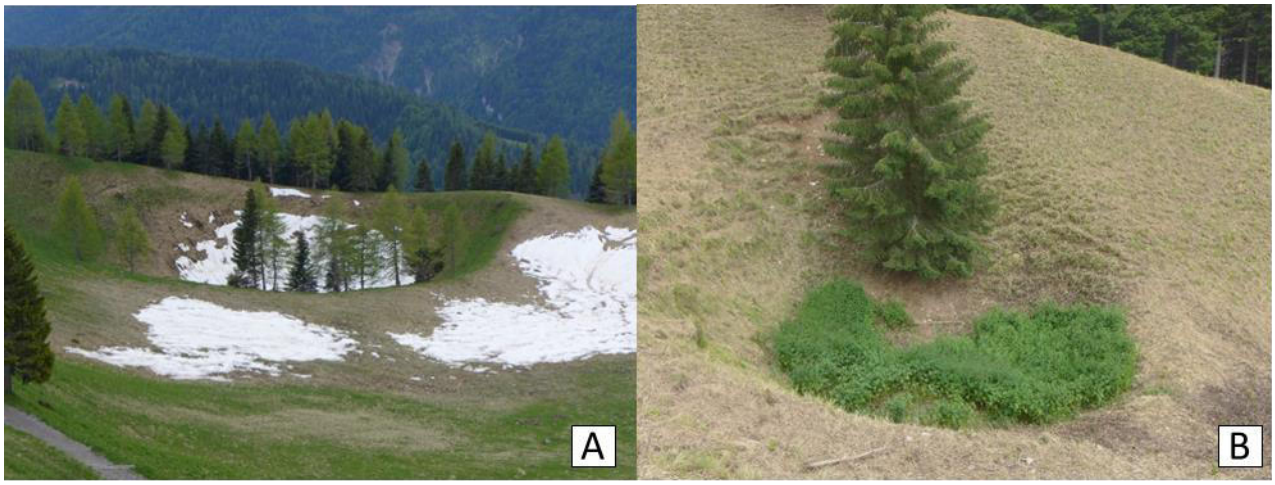

Figure 6 *Caprock collapse sinkhole (caprock material is micaceous quartz siltstones) in Sauris municipality in FVG region.* ***A)*** *Active sinkhole;* ***B)*** *Dormant sinkhole*

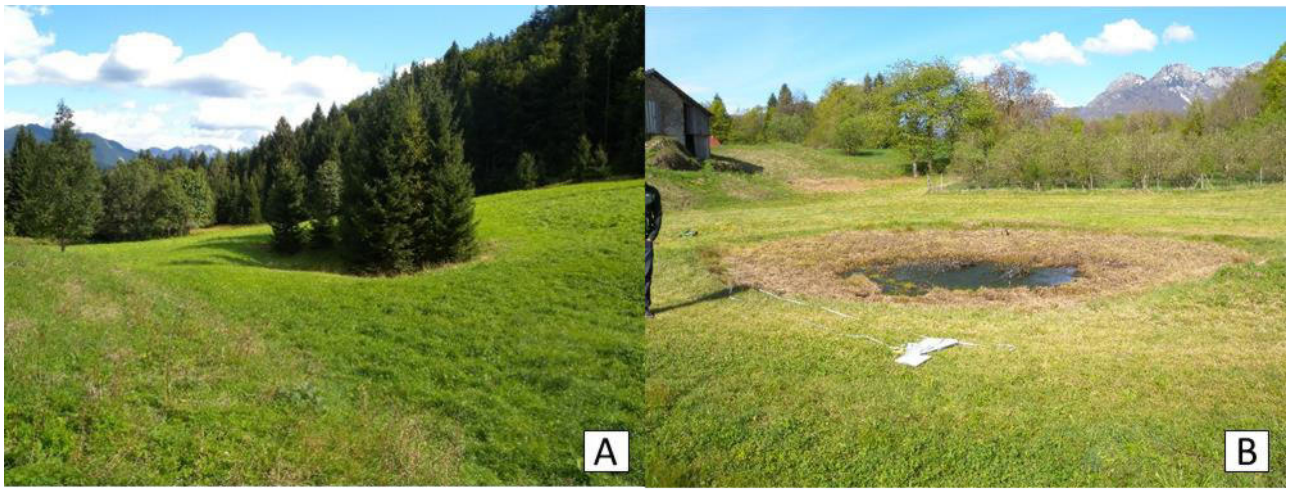

Figure 7 *Cover suffosion sinkholes in FVG region:* ***A)*** *Relict sinkhole with moraine colluvial deposits as cover material (Ligosullo municipality);* ***B)*** *Active sinkhole in colluvial deposits (Socchieve municipality)*

REFERENCES

- Beck B.F. (2004) Soil piping and sinkhole failures. In: White W.B. (Ed.), Encyclopedia of Caves New York: Elsevier. pp. 523-528.
- Buttrick D.B. & van Schalkwyk A. (1998) Hazard and risk assessment for sinkhole formation on dolomite land in South Africa. Environmental Geolology 36, 170–178. https://doi.org/10.1007/s002540050333
- Busetti A., Calligaris C., Forte E., Areggi G., Mocnik A., Zini L. (2020) Non-invasive methodological approach to detect and characterize high-risk sinkholes in urban cover evaporite karst: integrated reflection seismics, PS-InSAR, leveling, 3D-GPR and ancillary data. A NE Italian case study. Remote Sensing 12(22), 3814. https://doi.org/10.3390/rs12223814
- Calligaris C., Devoto S., Zini L., Cucchi F. (2017) An integrated approach for investigations of ground subsidence phenomena in the Ovaro Village (NE Italy). In: Renard P. & Bertrand C. (Eds.) EuroKarst 2016, Neuchâtel. Advances in karst science. Cham: Springer, pp. 71–77. https://doi.org/10.1007/978-3-319-45465-8_8
- Calligaris C., Zini L., Nisio S., Piano C. (2020) Sinkholes in the Friuli Venezia Giulia Region focus on the evaporites. In: Applied geology. Cham: Springer. https://doi.org/10.1007/978-3-030-43953-8_5
- Cooper A.H. (1998) Subsidence hazards caused by the dissolution of Permian gypsum in England: Geology, investigation and remediation. In: Maund J.G. & Eddleston M., (Eds.) Geohazard in Engineering Geology 15. Geological Society Engineering Geology Special Publications, London, UK; pp. 265–275. https://doi.org/10.1144/gsl.eng.1998.015.01.27
- Cooper A.H., Farrant A.R., Price S.J. (2011) The use of karst geomorphology for planning, hazard avoidance and development in Great Britain. Geomorphology 134, 118–131. https://doi.org/10.1016/j.geomorph.2011.06.004
- Cooper A.H. & Gutiérrez F. (2013) Dealing with gypsum karst problems: hazards, environmental issues and planning. In: Frumkin, A. (Ed.), Treatise on Geomorphology Karst. Geomorphology 6. Elsevier, Amsterdam, pp. 451–462.
- Cucchi F., Forti P., Finocchiaro F. (1998) Gypsum degradation in Italy with respect to climatic textural and erosional conditions. Geografia Fisica e Dinamica Quaternaria 3, 41–49
- Cvijić J. (1893) Das Karstphänomen. Versuch einer morphologischen Monographie, Geographische Abhandlungen herausgegeben von A. Penck, Wien, Band V, Heft 3, 1-114.

- Dahm T., Kühn D., Ohrnberger M., Kröger J., Wiederhold H., Reuther C.-D., Dehghani A., Scherbaum F. (2010) Combining geophysical data sets to study the dynamics of shallow evaporites in urban environments: Application to Hamburg, Germany. Geophysical Journal International 181, 154–172. https://doi.org/10.1111/j.1365-246X.2010.04521.x
- Del Prete S., Iovine G., Parise M., Santo A. (2010) Origin and distribution of different types of sinkholes in the plain areas of Southern Italy. Geodinamica Acta 23:1-3, 113-127. https://doi.org/10.3166/ga.23.113-127
- De Waele J., Piccini L., Columbu A., Madonia G., Vattano M., Calligaris C., D'Angeli I., Parise M., Chiesi M., Sivelli M., Vigna B., Zini L., Chiarini V., Sauro F., Drysdale R., Forti P. (2017) Evaporite karst in Italy: a review. International Journal of Speleology 46, 137–168. https://doi.org/10.5038/1827-806X.46.2.2107
- De Waele J. & Gutiérrez F. (2022) Karst Hydrogeology, Geomorfology and Caves. DOI:10.1002/9781119605379
- Dreybrodt W. (2004) Dissolution: Carbonate rocks. Encyclopedia of caves and karst science 295-298.
- Frumkin A. (2013) Salt karst. In: Frumkin, A. (Ed.), Treatise on Geomorphology Karst. Geomorphology 6. Elsevier, Amsterdam, pp. 407–424.
- Furlani S., Cucchi F., Forti F., Rossi A. (2009) Comparison between coastal and inland karst limestone lowering rates in the northeastern Adriatic Region (Italy and Croatia). Geomorphology 104, 73–81. https://doi.org/10.1016/j.geomorph.2008.05.015
- Gutiérrez F., Calaforra J.M., Cardona F., Ortí F., Durán J.J., Garay P. (2008) Geological and environmental implications of the evaporite karst in Spain. Environmental Geology 53, 951–965. https://doi.org/10.1007/s00254-007-0721-y
- Gutiérrez F., Cooper A.H., Johnson K.S. (2008a) Identification, prediction and mitigation of sinkhole hazards in evaporite karst areas. Environmental Geology 53, 1007–1022. 10.1007/s00254-007-0728-4
- Gutiérrez F., Guerrero J., Lucha P. (2008b) A genetic classification of sinkholes illustrated from evaporite paleokarst exposures in Spain. Environmental Geology 53, 993–1006. https://doi.org/10.1007/s00254-007-0727-5
- Gutiérrez F., Parise M., De Waele J., Jourde H. (2014) A review on natural and human-induced geohazards and impacts in karst. Earth-Science Reviews 138, 61–88. https://doi.org/10.1016/j.earscirev.2014.08.002
- Gutiérrez F. (2016) Sinkhole hazards. In: Oxford Research Encyclopedia of Natural Hazard Science. Oxford: Oxford University Press. https://doi.org/10.1093/acrefore/9780199389407.013.40

- Gutiérrez F. & Lizaga I. (2016) Sinkholes, collapse structures and large landslides in an active salt dome submerged by a reservoir: the unique case of the Ambal ridge in the Karun River, Zagros Mountains, Iran. Geomorphology 254, 88–103. https://doi.org/10.1016/j.geomorph.2015.11.020
- Jackson J.A. (1997) Glossary of Geology. Alexandria, Virginia: American Geological Institute.
- Karimi H., Taheri K. (2010) Hazards and mechanism of sinkholes on Kabudar Ahang and Famenin plains of Hamadan, Iran. Natural Hazards 55(2), 481–499. https://doi.org/10.1007/s11069-010-9541-6
- Klimchouk A., Cucchi F., Calaforra J.M., Aksem S., Finocchiaro F., Forti P. (1996) Dissolution of gypsum from field observations. International Journal of Speleology 25, 37–48. https://doi.org/10.5038/1827-806X.25.3.2
- Koutepov V.M., Mironov O.K., Tolmachev V.V. (2008) Assessment of suffosion-related hazards in karst areas using GIS technology. Environmental Geology 54, 957–962. https://doi.org/10.1007/s00254-007-0888-2
- Krawczyk C.M., Polom U., Trabs S., Dahm T. (2012) Sinkholes in the city of Hamburg—New urban shear-wave reflection seismic system enables high-resolution imaging of subrosion structures. Journal of Applied Geophysics 78, 133–143. https://doi.org/10.1016/j.jappgeo.2011.02.003
- Kuniansky E.L., Weary D.L., Kaufmann J.E. (2016) The current status of mapping karst areas and availability of public sinkhole-risk resources in karst terrains of the United States. Hydrogeology Journal 24, 613–624. https://doi.org/10.1007/s10040-015-1333-3
- Martínez J.D., Johnson K.S., Neal J.T. (1998) Sinkholes in evaporite rocks. American Scientist 86, 38–51.
- Nisio S., Salvati R. (2004) Fenomeni di sprofondamento catastrofico. Proposta di classificazione applicate alla casistica italiana. In: Proceeding: state of the art on the study of sinkhole phenomena and role of the national and local government in the territory administration. Rome, 20–21 May 2004, pp. 573–584
- Nisio S. (2008) I sinkholes nelle altre regioni. Memorie Descrittive della Carta Geologica d'Italia 85, 419–426. (In Italian)
- Öztürk M.Z., Şener M.F., Şener M., Şimşek M. (2018) Structural controls on distribution of dolines on Mount Anamas (Taurus Mountains, Turkey). Geomorphology 317, 107–116. https://doi.org/10.1016/j.geomorph.2018.05.023
- Parise M., Qiriazi P., Sala S. (2004) Natural and anthropogenic hazards in karst areas of Albania. Natural Hazards and Earth System Sciences 4, 569–581. https://doi.org/10.5194/nhess-4-569-2004

- Parise M., Galeazzi C., Bixio R., Dixon M., (2013) Classification of artificial cavities: a first contribution by the UIS Commission. In: Filippi M. & Bosak P. (Eds), Proceedings of the 16th International Congress of Speleology, vol. 2, 230-235, Czech Speleological Society, Brno.
- Parise M. (2019) Chapter 110 – sinkholes. In: White W.B., Culver D.C., Pipan T. (Eds.), Encyclopedia of Caves (third ed.), Academic Press, 934-942. https://doi.org/10.1016/B978-0-12-814124-3.00110-2
- Parise M. (2022) Sinkholes, subsidence and related mass movements. In: Shroder J.J.F. (Ed.), Treatise on Geomorphology 5, Academic Press, Elsevier, 200-220. https://doi.org/10.1016/B978-0-12-818234-5.00029-8
- Paukstys B., Cooper A.H., Arustiene J. (1999) Planning for gypsum geohazards in Lithuania and England. Engineering Geolology 52, 93–103. https://doi.org/10.1016/S0013-7952(98)00061-1
- Sauro U. (2003) Dolines and sinkholes: aspects of evolution and problems of classification. Acta Carsologica 32, 41–52.
- Sevil J., Gutiérrez F., Carmicer C., Carbonel D., Desir G., Garcià-Arnay Á., Guerrero J. (2020) Characterizing and monitoring a high-risk sinkhole in an urban area underlain by salt through non-invasive methods: Detailed mapping, high-precision leveling and GPR. Engineering Geolology 272, 105641. https://doi.org/10.1016/j.enggeo.2020.105641
- Sowers G.F. (1996) Building on Sinkholes. New York: ASCE Press.
- Taheri K., Gutiérrez F., Mohseni H., Raeisi E., Taheri M. (2015) Sinkhole susceptibility mapping using the analytical hierarchy process (AHP) and magnitude–frequency relationships: a case study in Hamadan province, Iran. Geomorphology 234, 64–79. https://doi.org/10.1016/j.geomorph.2015.01.005
- Thierry P., Prunier-Leparmentier A.M., Lembezat C., Vanoudheusden E., Vernoux J.F. (2009) 3D geological modelling at urban scale and mapping of ground movement susceptibility from gypsum dissolution: The Paris example (France). Engineering Geology 105, 51–64. https://doi.org/10.1016/j.enggeo.2008.12.010
- Waltham T. (2005) Tiankengs of the world, outside China. Cave and Karst Science 32, 1–12.
- Waltham T., Bell F., Culshaw M. (2005) Sinkholes and Subsidence. Springer, Chichester.
- Williams P. (2004) Dolines. In: Gunn J. (Ed.), Encyclopedia of Caves and Karst Science pp. 628–642. New York: Fitzroy Dearborn.
- Zini L., Calligaris C., Forte E., Petronio L., Zavagno E., Boccali C., Cucchi F. (2015) A multidisciplinary approach in sinkhole analysis: the Quinis village case study (NE-Italy). Engineering Geology 197, 132–144. https://doi.org/10.1016/j.enggeo.2015.07.004

UNIVERSITÀ DEGLI STUDI DI TRIESTE

CHAPTER 2

SINKHOLE GEODATABASE

Sinkholes represent a significant geohazard due to their unpredictability and rapid evolution. They can affect urban areas, infrastructures and agricultural areas, often resulting in the loss of human lives and causing significant damages, thus posing a social problem. In Italy, these phenomena are widespread, prompting ISPRA to initiate a national project in 2002 aimed at inventory sinkholes in a national geodabase (*Figure 8*).

Friuli Venezia Giulia, with its karstifiable outcrops, is one of the most sinkhole prone regions, having recorded over 68 events by 2002. Hence the need to extend ISPRA's sinkhole project to a regional level. In 2014, the Geological Survey of the FVG region, in collaboration with researchers from the Department of Mathematics and Geosciences at the University of Trieste, started specific projects aimed at the identification, characterization and inventory of natural subsidence sinkholes (Calligaris et al., 2020).

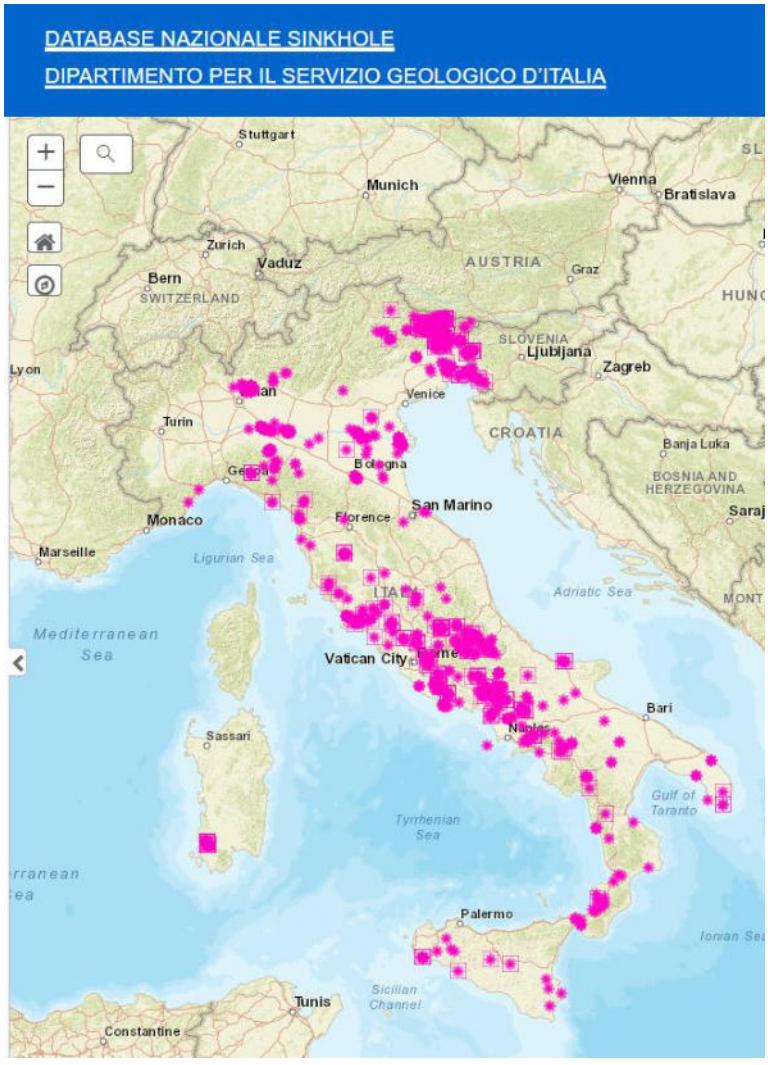

Figure 8 *Sinkholes inventoried in the ISPRA geodatabase (https://sgi.isprambiente.it/sinkholeweb/viewer/index.html, last access: 18 September 2023)*

The Geological Survey of FVG, therefore, started to implement the ISPRA database revising the data already contained in it (deleting or adding information/phenomena only for the FVG region) and giving rise to a regional geodatabase.

The first implementation of the existing regional database involved several phases:

1) historical-bibliographical research;
2) sinkhole data coming from other database sources;
3) analysis of Municipal General Urban Plans (PRGC) and Variants;
4) interviews with technical offices of the 221 municipalities in the FVG.

Historical-bibliographical researches regarded the analysis of historical documents, scientific papers and online maps to gather additional information and upload old pictures of some phenomena (Marinelli 1897, 1902; Gortani, 1904, 1965; Cucchi & Piano, 2002; Cucchi & Piano, 2003; Burelli et al., 2004; Calligaris et al., 2009; Zini et al., 2015) (*Figure 9*).

Data derived from multi-temporal images available on the web, such as those provided by Google Maps® and Bing Maps® (https://www.google.it/maps, https://www.bing.com/maps) and the Regional Numerical Technical Cartography (CTRN) on the scale 1:5.000, were also included in the database.

Data present in the database were also derived from other database sources as the inventory of landslide phenomena in Italy (IFFI) and the reports of instability found within the information system for soil protection (SIDS) of the FVG region.

Furthermore, data were uploaded starting from the geological reports realized within the framework of the Municipal General Urban Plans (PRGC) and the Variants relating to the PRGC and available for each single municipality. The tables associated with the PRGC (*Figure 10*) have provided useful information regarding the presence and spatial distribution of lithologies subject to karst processes, as well as the presence of forms attributable to sinkholes.

Last but not least, data were collected by interviewing the Technical Offices of the 221 Municipalities present in the Friuli Venezia Giulia Region.

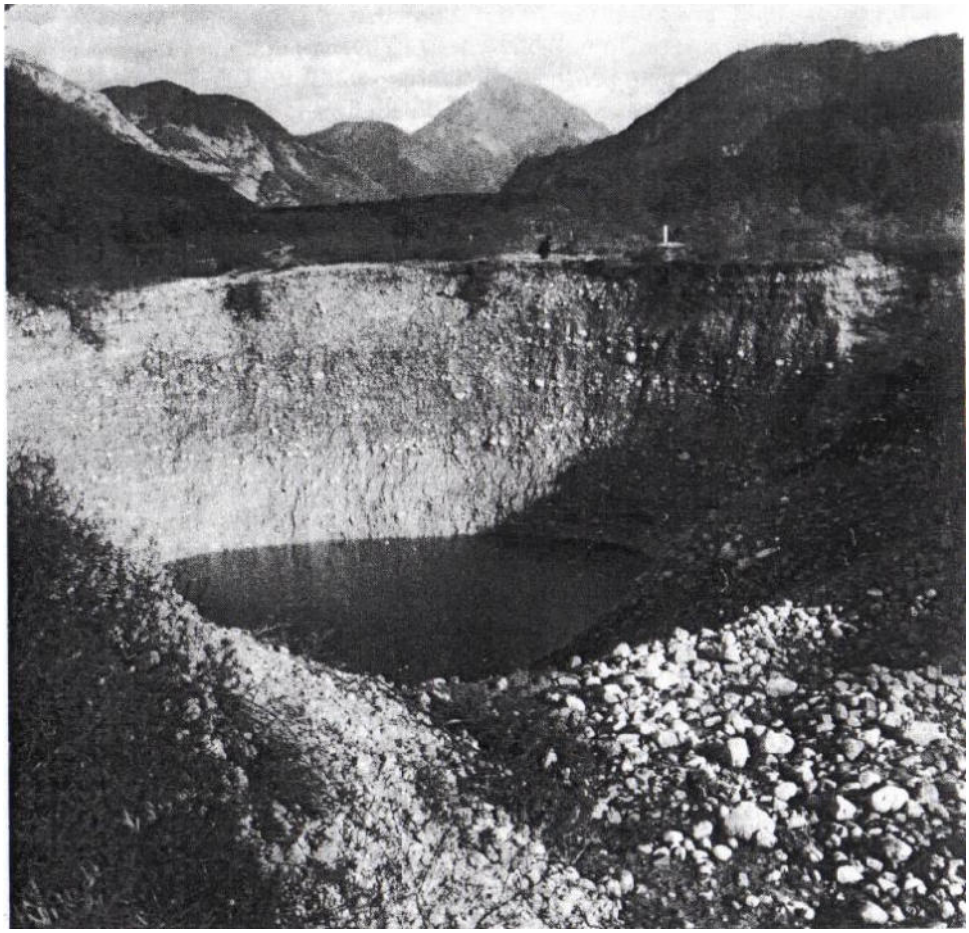

Figure 9 *Cover collapse sinkhole in Quinis village (Enemonzo municipality) from Gortani, 1965*

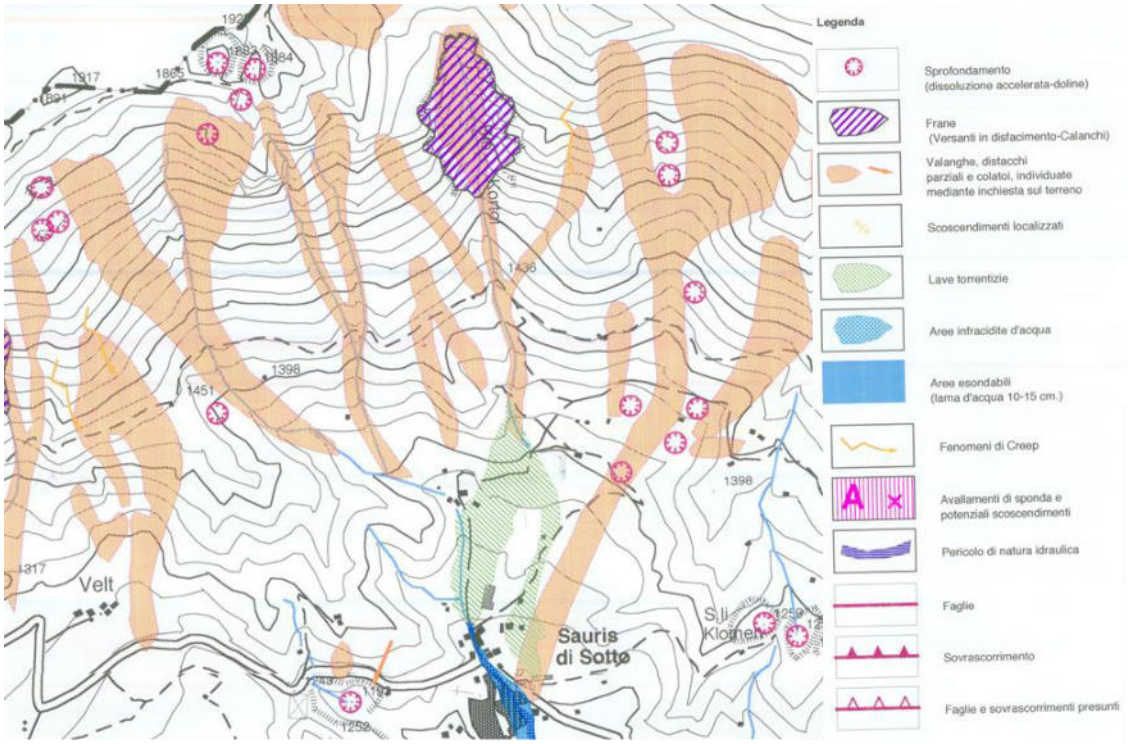

Figure 10 *PRGC of Sauris municipality – Hazard map (Attachment 1 - Table 9 of the PRGC)*

Historical sinkhole data provides valuable information for predicting potential new sinkholes, particularly in regions where they have a concentrated distribution. Sometimes, cases of ground subsidence are associated with the reactivation of pre-existing sinkholes, some of which might have been obliterated due to human intervention. The reliability of sinkhole susceptibility and hazard maps, as well as the efficiency of mitigation strategies, significantly depends on the completeness, precision and quality of sinkhole inventories (Gutiérrez, 2016).

A new updating phase of the catalogue coincided with a part of the PhD project. The latter initially focused on the determination of the best approach for the detection and identification of sinkholes. In the international literature, the identification and comprehensive understanding of sinkholes and potentially unstable terrains often necessitate the use of a variety of surface and subsurface investigative techniques. Gutiérrez et al., 2014, Gutiérrez, 2016 and Calligaris et al., 2023 outline a range of these methods, including but not limited to:

- Aerial and satellite image analysis (Brinkmann et al., 2007; Festa et al., 2012; Panno & Luman, 2013; Dou et al., 2015; Kromhout & Alfieri, 2018);
- Topographic maps analysis (Kasting & Kasting, 2003; Angel et al., 2004; Brinkmann et al., 2008; Gutiérrez et al., 2011; Basso et al., 2013, Zumpano et al. 2019);
- Field surveys (Gutiérrez et al., 2007; Bruno et al., 2008; Margiotta et al., 2012);
- Paleokarst analysis (Gutiérrez et al., 2008);
- Mapping of subsidence-related damage (Gutiérrez & Cooper, 2002; Cooper, 2008);
- Employment of LIDAR (Light Detecting and Ranging) technology (Filin et al., 2011; Miao et al., 2013; Rahimi & Alexander, 2013; Doctor & Young, 2013; Pardo-Igúzquiza et al., 2013; Zhu et al., 2014; Kobal et al., 2015; Bauer, 2015; Wall et al., 2017; Cigna et al., 2017; Panno & Luman, 2018; Shi et al., 2019; Kim et al., 2019; Verbovšek & Gabor, 2019; Zumpano et al., 2019; Zhang et al., 2019; Zhu et al., 2020; De Castro & Rodrigues, 2021);
- Implementation of InSAR (Synthetic Aperture Radar Interferometry) (Baer et al., 2002; Abelson et al., 2003; Closson et al., 2003; Castañeda et al., 2009; Paine et al., 2009; Gutiérrez et al., 2011; Nof et al., 2013; Jones et al., 2014; Intrieri et al., 2015; Galve et al., 2015; Theron et al., 2017; Baer et al., 2018; Malinowska et al., 2019; Oliver-Cabrera et al., 2020; Solari et al., 2020; Jones, 2020; Busetti et al., 2020; Guerrero et al., 2021; Orhan et al., 2021);
- Monitoring of microseismic activity (Dahm et al., 2011; Land, 2013);
- Ground-based observation systems (Kent et al., 2013; Zhende et al., 2013; Kersten et al., 2017; Sevil et al., 2017; Desir et al., 2018; Kobe et al., 2019);

- Hydrochemical modelling (Delkhahi et al., 2020; Taheri et al., 2021);
- Geophysical surveys (Zhou et al., 2002; Batayneh et al., 2002; Ahmed & Carpenter, 2003; Stierman, 2004; Waltham et al., 2005; Thierry et al., 2005; Tallini et al., 2006; Wust-Bloch et al., 2006; Higuera-Diaz et al., 2007; Wightman et al., 2008; Epting et al., 2009, Sargent & Goulty, 2009; Pueyo-Anchuela et al., 2010; Frumkin et al. 2011; Valois et al., 2011; Kühn et al., 2011; García-Moreno et al., 2011; Krawczyk et al., 2012; Margiotta et al., 2012; Carbonel et al., 2013; Samyn et al., 2014; Malehmir et al., 2016; Pazzi et al., 2018; Ronen et al., 2019);
- Use of probing, drilling, and trenching techniques (Milanovic, 2004; Waltham & Fookes, 2003; Carbonel et al., 2014; Carbonel et al., 2015; Sevil et al., 2017; Gutiérrez et al., 2018).

The most advanced techniques are related to the acquisition of remote sensing geodetic data (LiDAR and InSAR). Airborne LiDAR data has a significant potential for automatically mapping sinkholes and extracting of morphometric parameters (Gutiérrez, 2016).

In Friuli Venezia Giulia region, the examination of airborne LiDAR data along with the utilization of DTM derived products like shaded reliefs and slope maps, has been extensively employed for mapping the majority of identified sinkholes. An example of the data quality and usefulness is presented in *Figure 11* and *Figure 12,* comparing an area in the municipality of Sauris (UD) where four sinkholes are present. *Figure 11* illustrates a shaded relief derived from the 1m-DTM, while *Figure 12* represents 0.5m-DTM derived product. Despite the excellent quality of the 1m-DTM hillshade, it lacks the necessary level of detail for providing a comprehensive description of individual phenomena and accurately defining morphometric parameters, as highlighted in the topographic profiles derived from DTMs with different resolutions. The profile constructed using the 0.5m-DTM hillshade reveals impressive details, facilitating a clearer delineation of the bottom and slope of each identified sinkhole.

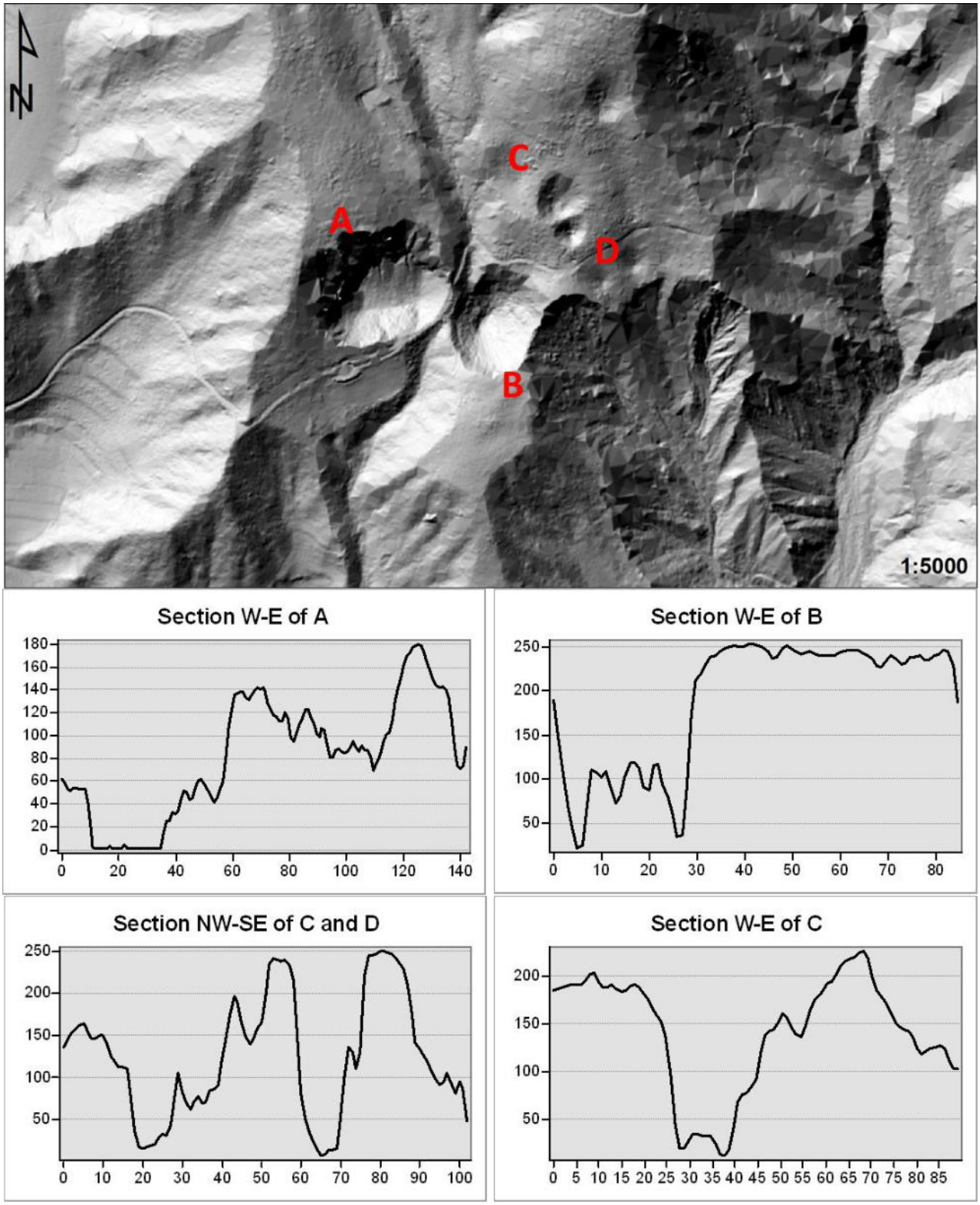

Figure 11 *Shaded relief derived from a Digital Elevation Model (DTM) at 1 m resolution (Sauris municipality). Below the topographic profiles of sinkholes, A, B, C and D*

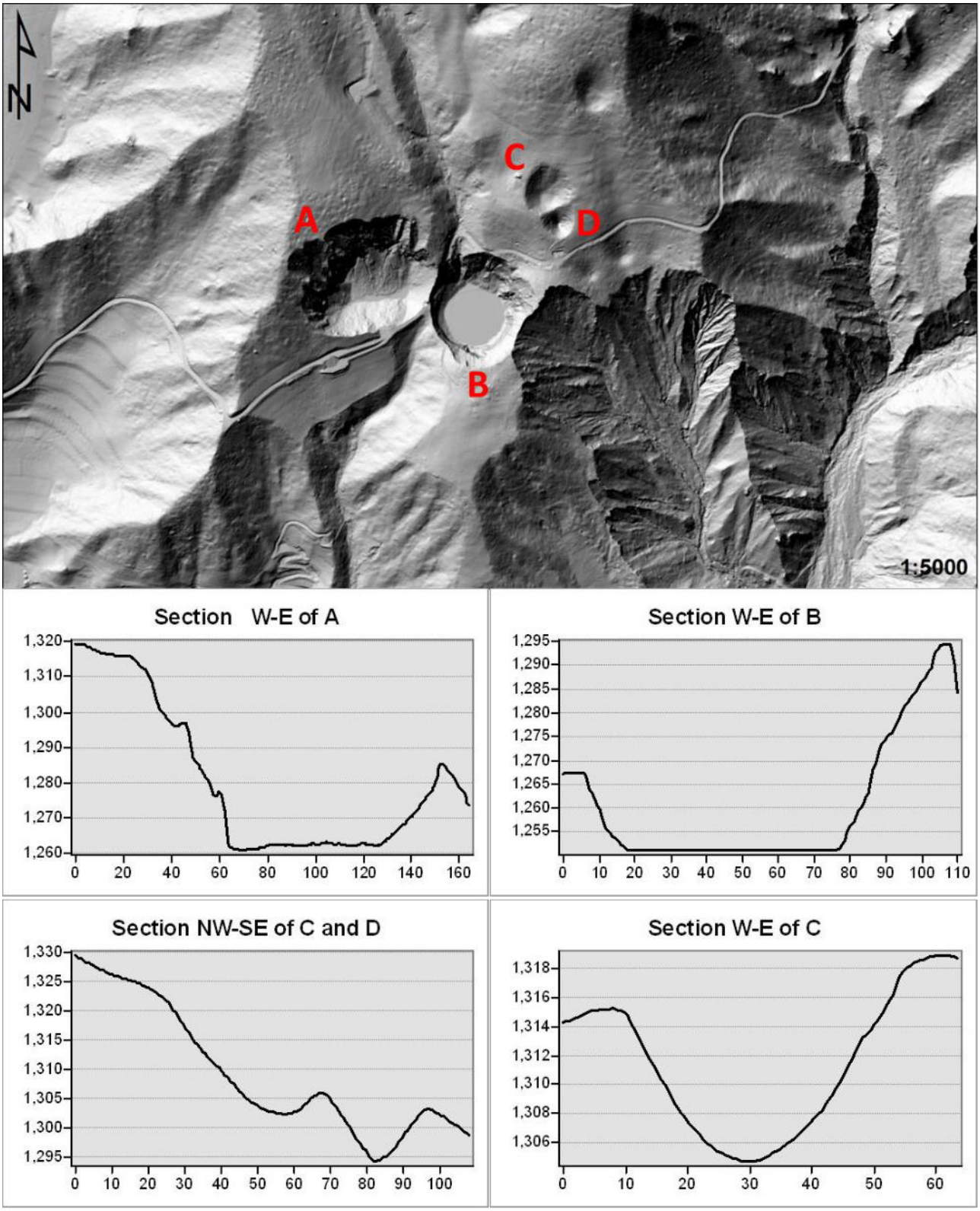

Figure 12 *Shaded relief derived from a Digital Elevation Model (DTM) at 0.5 m resolution (Sauris municipality). Below the topographic profiles of sinkholes, A, B, C and D*

The comparison of data, such as the shaded relief, the slope map (*Figure 13*) and the orthophotos (*Figure 14*) allowed a preliminary identification of potential sinkholes. Once identified, they have been object of field surveys (*Figure 15*). Not all the identified sinkholes during the preliminary desk activities have later been inventoried. Through field surveys, it became evident that some of these features lacked the characteristics necessary for being classified as subsidence sinkholes. This underscores the importance of field surveys as a crucial step to validate the results obtained through desk activities.

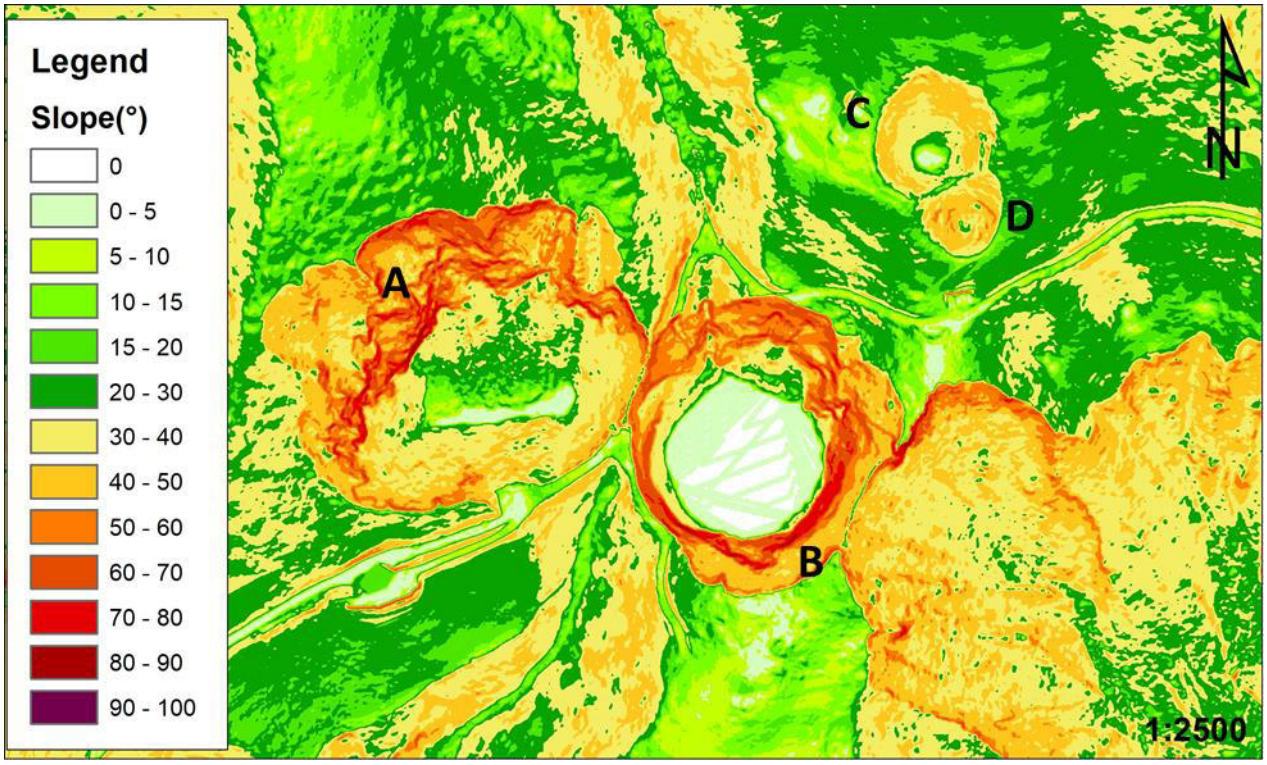

Figure 13 *Slope map of sinkholes A, B, C and D (Sauris municipality)*

Figure 14 *Ortophoto AGEA 2014 (FVG region), resolution 0.2m of the sinkholes A, B, C and D*

Figure 15 *Sinkhole B in Figure 11 pictured on 23/04/2014 (photo by Calligaris C.)*

The geodatabase of the sinkhole in the FVG region from an informatics point of view contains alphanumeric and geometric information regarding each phenomenon and it was created ad hoc on the basis of the national database.

Over the three years of the PhD program, the geodatabase has undergone continuous and significant updates that involved not only a thorough review of the structure incorporating additional fields and modifying information in specific fields, but also the addition of new sinkholes.

STRUCTURAL UPDATE OF THE GEODATABASE

Today, the geodatabase collects information regarding different geolithological (carbonates, evaporites etc.) and geomorphological contexts (plain area, gentle slope etc.).

Hereafter (*Table 1*) is a summary of the fields containing the recorded information.

FIELD NAME	DATA TYPE
ID_SH	Text
MUNICIPALITY	Text
LOCATION	Text
BIBLIO	Text
DATE	Long integer
CLASS	Text
CLASSCODE	Text
CLASS1	Text
SHAPE 2D	Text
SHAPE 3D	Text
DIAM1	Long integer
DIAM2	Long integer
DEPTH	Double
WATER	Text
STAT	Text
STATCODE	Text

FIELD NAME	DATA TYPE
REACT	Long integer
NOTES	Text
RIL1	Text
RILDATE1	Date
RIL2	Text
RILDATE2	Date
IDEN	Text
ACC	Text
BEDROCK	Text
BEDROCK_1	Text
LITHO_SUP	Text
LITHOCODE	Text
GEOMORP	Text
PHOTO	Text

Table 1 *Fields of the geodatabase of FVG region*

- "**ID_SH**" is the most important field, as it is the ID code that uniquely identifies each single sinkhole;

- **"Municipality" and "location"** constitute two primary information to be included in the geodatabase in order to locate where the sinkhole is. In particular, the "**location**" field must include more specific information such as village name, toponym, hamlet, street, etc.;
- "**BIBLIO**": the bibliography field allows for the identification of the sources from which the information primarily derives. For examples, the phenomenon is documented in the PRGC, in scientific papers, in the speleological inventory (CSR), in the ISPRA database, in the IFFI (Inventario dei Fenomeni Franosi Italiani), or it has been identified using Digital Terrain Model (DTM) at both 1m and 0.5m resolutions. Additionally, the information could be sourced from reports submitted by residents or municipal technicians or directly obtained thought field surveys;
- "**DATE**": it is the date of occurrence of the sinkhole;
- **"CLASS"** and "**CLASSCODE"** contain the classification in accordance with Gutiérrez et al., 2014 (*Table 2*);
- "**CLASS1**" contains the classification in accordance with the one proposed for ISPRA geodatabase (*Table 2*);
- **"SHAPE 2D"** describes the 2D shape such as circular, sub-circular, elliptical and irregular as shown in *Figure 16*;
- **"SHAPE 3D"** describes the 3D shape such as bowl-shaped, pan-shaped, cylinder-shaped and funnel-shaped as shown in *Figure 17*;
- **"DIAM1"** and **"DIAM2"** are respectively the minor and major diameter approximately measured during the field survey;
- **"DEPTH"** is approximately measured during field survey;
- **"WATER"**: a field that defines the presence or absence of water at the bottom of the sinkhole at the moment of the field survey.

Gutiérrez et al., 2014 "CLASS" field	ISPRA "CLASS1" field
Anthropogenic sinkhole	Anthropogenic sinkhole
Bedrock collapse sinkhole	Cave collapse sinkhole
Caprock collapse sinkhole	Cave collapse sinkhole
Cover collapse sinkhole	Cover collapse sinkhole
Cover suffosion sinkhole	Suffosion sinkhole
	Cover subsidence sinkhole
	Evorsion sinkhole

Table 2 *Comparison between two different terminologies in the sinkhole classification: Gutiérrez et al., 2014 and ISPRA (Nisio & Salvati, 2004)*

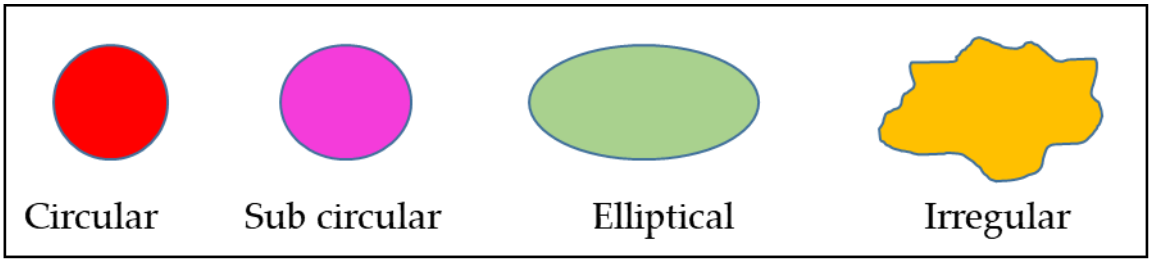

Figure 16 *Type of 2D shape*

Figure 17 *Description proposed by Gutiérrez et al., 2016 for the 3D shape*

- "**STAT**" and "**STATCODE**" describe the state of activity (active, reactivated, dormant, inactive, relict, artificially stabilized and undefined) using definitions modified from WP/WLI (1993a, 1993b), Cruden et al. (2011), Canuti et al. (1995), and ARPA Piemonte (2009);
- "**REACT**" contains the date of the eventual reactivation;
- "**NOTES**": supplementary description or remarks.
- "**RIL1**" and "**RILDATE1**": the name of the surveyor and the date of the survey.
- "**RIL2**" and "**RILDATE2**": the name of the surveyor and the date of any further survey.
- "**IDEN**" contains information regarding the identification of the sinkhole (certain or uncertain);

- "**ACC**": accuracy regarding the position of the sinkhole (such as from GPS, DTM or bibliography);
- "**BEDROCK**" contains information regarding the bedrock (carbonates, evaporites, Quaternary deposits, conglomerates);
- "**BEDROCK_1**" contains information about the prevailing Formation;
- "**LITHO_SUP**" and "**LITHOCODE**" correspond to the outcropping deposits/lithotypes in the area of interest. In particular, "LITHOCODE" distinguishes soil from rock;
- "**GEOMORP**" contains the geomorphological information subdivided as follows:
    i. flat area (sub-flat area with an average slope of less than 10° and dimensions exceeding 1km²),
    ii. gentle slope (side of a hill or mountain relief with a slope ranging between 10° to 25°),
    iii. steep slope (side of a hill or mountain relief with a slope greater than 25°),
    iv. ridge (connecting line between two opposing mountain slopes when their intersection occurs at their roof and their slopes are approximately equal),
    v. river terrace (a flat surface bordered by escarpments representing the result of more or less prolonged episodes of erosion by a stream);
- "**PHOTO**" is the field with a hyperlink that allows access to the directory containing the images related to that sinkhole.

ALPHANUMERIC UPDATES OF THE GEODATASE

Several activities were undertaken to update the geodatabase from the alphanumeric point of view.

In the database, a huge amount of phenomena was identified only through desk activities, involving the analysing of LiDAR data. The term "undefined" present in the "CLASS" field, initially assigned to them, was later modified based on field activities, and the database was accordingly populated.

Subsequently, other fields underwent updates through both desk and field activities, including 2D and 3D shape, bibliography, state of activity, lithology, classification and identification.

The "Photo" field has been completely revised and updated. To each sinkhole was assigned its own folder named following the ID_SH. The entire dataset of images was

renamed including the year, month and day. This system facilitated the comparison of the evolution of the analysed phenomenon in case of pictures acquired in different dates.

GEOMETRIC UPDATES OF THE GEODATASE

The geometric update of the database took place in two phases:

1) some sinkholes, initially identified only through LiDAR data analysis, were later field surveyed. In some cases, the field activities suggested to remove the feature from the geodatabase, as they did not meet the requirements for being classified as sinkhole.
2) With the recent availability of a 0.5m DTM from "Lotto Unico" survey conducted between 2018 and 2020, the entire dataset has been updated, leading to a reshaping of the sinkhole perimeters.

NEW DATA COLLECTION

The initial database of the Friuli Venezia Giulia (FVG) region focused on the evaporitic environment, given its higher solubility and consequent elevated risk. In recent years, the census was expanded to carbonates, starting with the cradle of karst phenomena: The Classical Karst area. In carbonate environment, typically, three types of phenomena can be identified:

- Solution sinkholes (were not considered in this thesis due to their low hazard);
- Bedrock collapse sinkholes (resulting from the collapse of the ceiling of a cave);
- Suffosion sinkholes (resulting from the downwashing of the soil cover through karst fractures and conduits).

As bedrock collapse sinkholes present the highest level of hazard, the research started with the analysis of the available data collected in the speleological inventory (CSR) of FVG region (http://www.catastogrotte.fvg.it). A methodological protocol was developed to identify caves whose entrances were referable to sinkhole features.

The specific study on the Classical Karst concerned the analysis of 3212 records from the CSR inventory, pertaining to explored and catalogued caves. The analysis of these records was conducted by sectors, with the aim of considering areas with homogeneous geological, hydrogeological, and geomorphological characteristics. Descriptions, plans and sections were analysed.

For each identified sector, specific caves were selected to represent the phenomena and these were subsequently subjected to field surveys for further investigation. The criteria that led to the identification of bedrock collapse sinkholes are outlined in *Table 3*.

Indications that the entrance of the cave is a *bedrock collapse sinkhole*	**Indications that the entrance of the cave is not a *bedrock collapse sinkhole***
The entrance of the cave visible from the survey plan is circular or subcircular in shape.	The entrance of the cave visible from the survey plan has an elongated shape, typical of a fracture widened by karst dissolution processes.
The cave has a predominantly horizontal/sub-horizontal development close to the surface, with a well as an entrance. The walls near the entrance are overhanging and may feature concretions.	The cave has a predominantly vertical development, composed of wells or galleries clearly following fractures, widened by dissolution or erosive action of water.
In the description of the cave, a sentence is related to the sudden opening or collapse of the ceiling.	The entrance of the cave consists of a well with a smaller diameter relative to the thickness of the ceiling (the thickness of the stratification and the scarcity of joints do not justify the opening of the entrance due to collapse phenomena).
At the bottom of the cave, visible from the section, there are accumulations of debris with blocks of sufficient sizes to justify their origin from the collapse of the ceiling.	The cave is characterised by horizontal galleries, and the entrance opens in correspondence of depressions that result from the dismantling of the ceiling due to the lowering of the topographic surface. In this case, the cave can be classified as a roofless cave (RC).
During the field survey, remnants of the ancient vault of the cave are visible (natural arches, rock spurs, etc.). In such cases, it is necessary to assess whether it is a bedrock collapse sinkhole (BCS), a roofless cave (RC), or if the forms are remnants of portions of the rock mass that are more resistant to dissolution.	
The entrance of a cave with predominantly vertical development is delimited by fractures that may have isolated a section of the rock mass, resulting in its collapse.	

Table 3 *Proposal of a methodological approach for the identification of sinkholes in a carbonate environment*

Out of the 3212 examined records (each record referring to a single cave), 83 sinkholes have been identified (*Figure 18*), including 69 bedrock collapse sinkholes (example in *Figure 19*), 11 cover collapse sinkholes and 3 cover suffosion sinkholes.

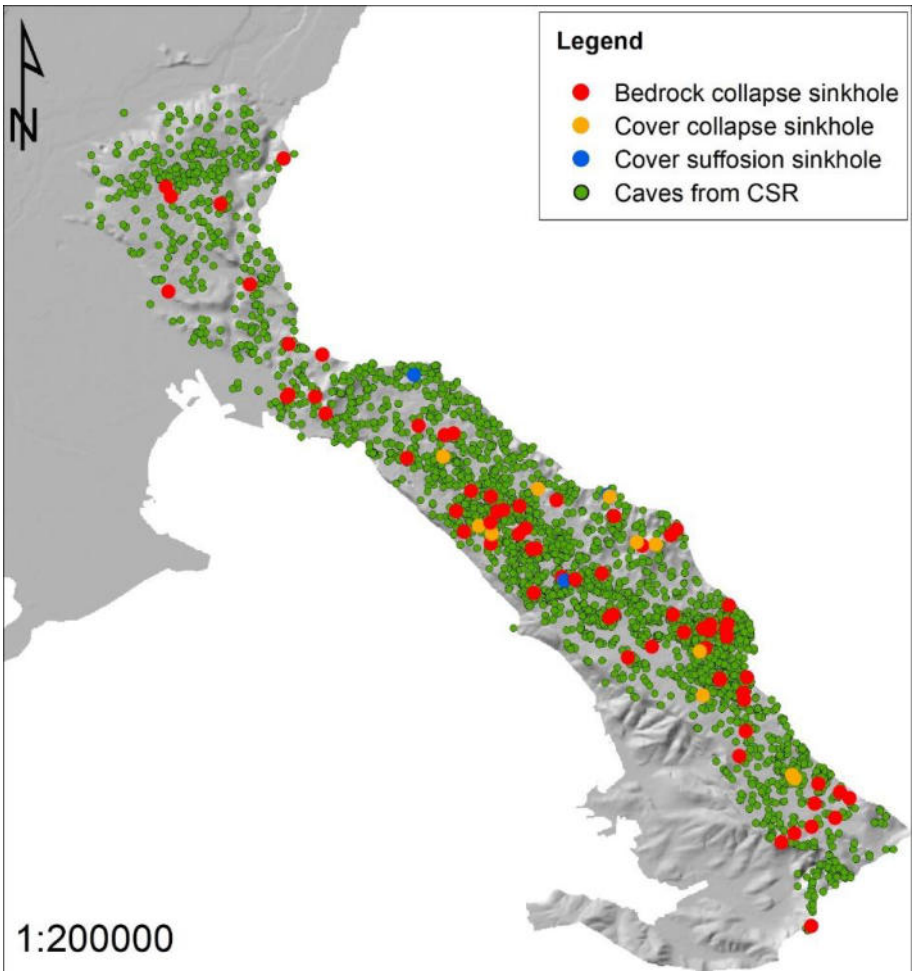

Figure 18 *The distribution of sinkholes identified in the Classical Karst*

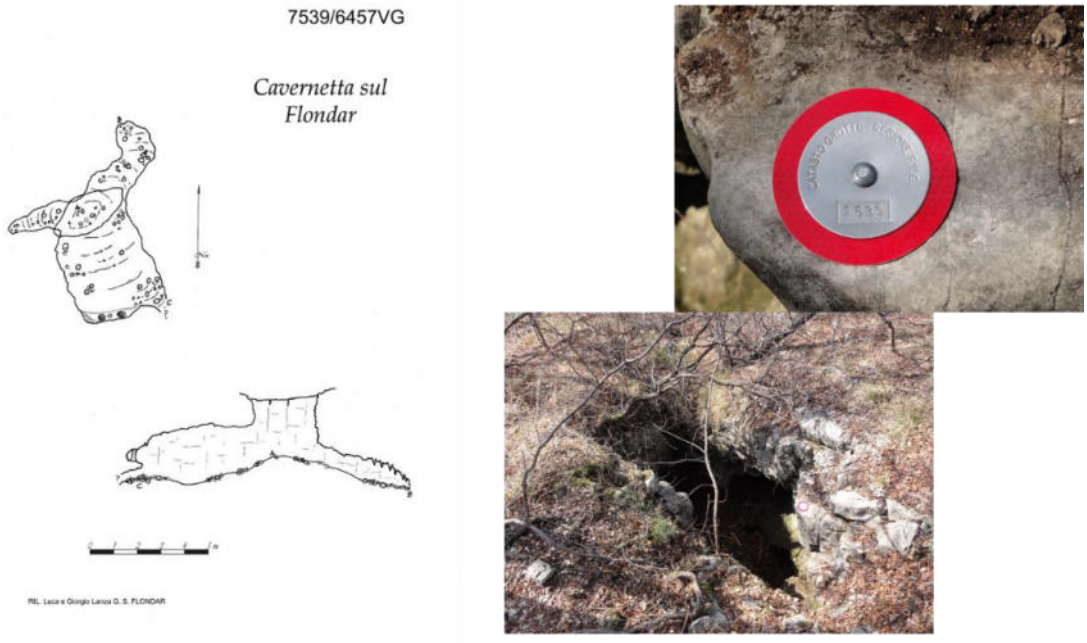

Figure 19 *Example of bedrock collapse sinkhole in the Classical Karst (https://catastogrotte.regione.fvg.it/scheda/7539-Cavernetta_sul_Flondar)*

Once the best methodological approach to identify a sinkhole in a carbonate environment was defined, the remaining 4792 caves of the CSR were analysed (for a total of 8004 caves analysed).

Thanks to this in-depth analysis, other 129 cave entrances were subject to field surveys, of which 103 were identified in the field. 27 phenomena were classified as bedrock collapse sinkholes, while 76 did not meet the criteria for being inventoried *(Figure 20).*

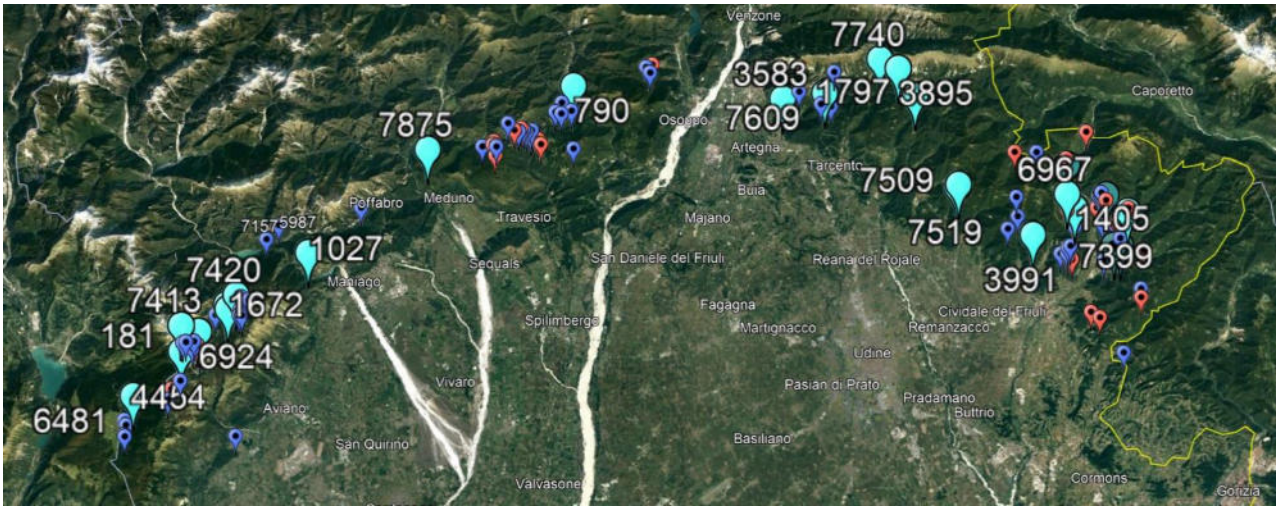

Figure 20 *Location of the 129 cave entrances surveyed from the CSR (in blue the 129 possible sinkholes identified, in light blue the sinkholes classified as bedrock collapses and in red those that were not identified during field activities)*

For each identified sinkhole, all the information was entered in the FVG geodatabase, and a report was filled with all the information: the cave's location, the description from the CSR (where relevant), the section (downloaded from the inventory), a brief geological overview, the morphometric characteristics, new photographs and further descriptions of the entrance and its placement.

In this case as well, some of the phenomena initially identified through desk activities were later excluded from the geodatabase after field surveys, as they did not meet the criteria for classification as sinkholes.

Once the sinkholes were identified, in order to add them to the geodatabase, it was necessary to georeference the cave entrances recognized as sinkhole. The available surveys were scaled and rotated in a CAD environment and subsequently georeferenced using the coordinates found on the CSR. Imported into a GIS environment, as there was no coincidence (*Figure 21*) between the perimeter of the entrances and the shaded relief (from 1m DTM), it was decided to use the latter as a homogeneous database for the entire study area. With the availability of more accurate DTM-derived data (shaded reliefs at 0.5 m resolution), and due to the absence of precise GNSS surveys for all the cave entrances, it was chosen to outline each sinkhole following the slope map (*Figure 21*). In the cases where the sinkhole, due to its dimensions, was not recognizable through the DTM analysis, the perimeter was georeferenced using the coordinates of the CSR and the shape was digitized starting from the plan map (*Figure 22*).

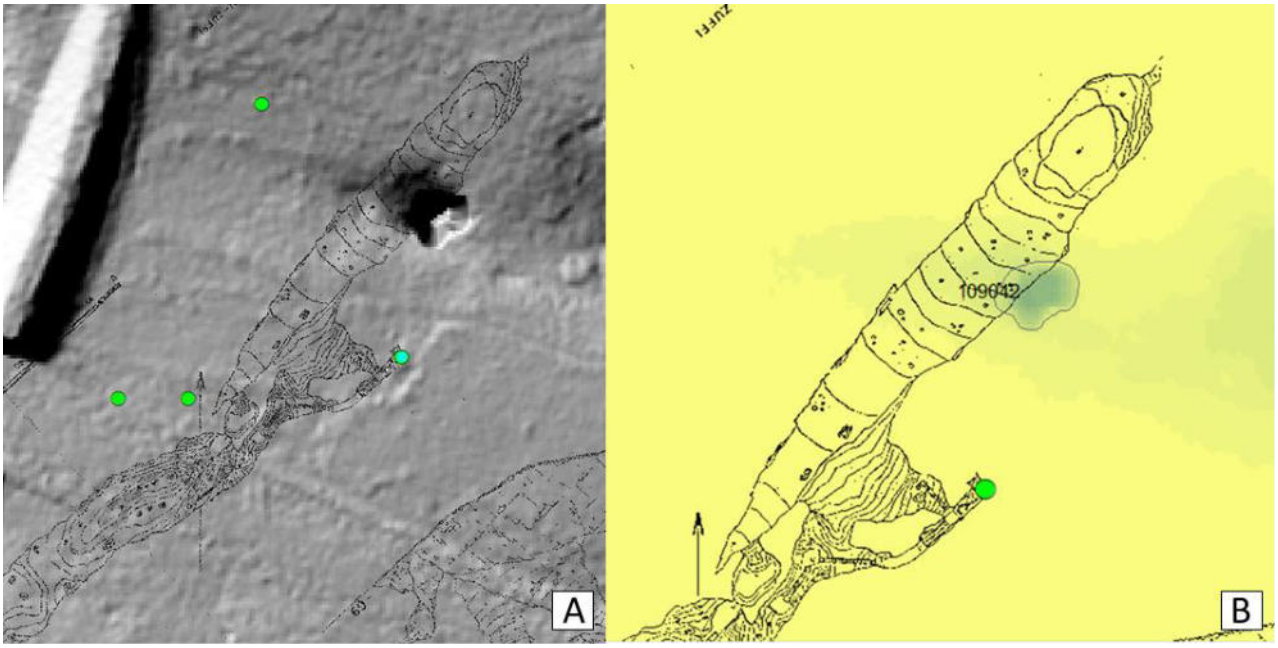

Figure 21 *Overlap of the "Grotta delle Torri di Slivia, CSR 22/39" plan with* ***A)*** *the shaded relief map and* ***B)*** *the slope map. Georeferencing has resulted in a non-coincidence between the cave's position as depicted on the shaded relief map (verified during the field survey) and its position based on CSR coordinates*

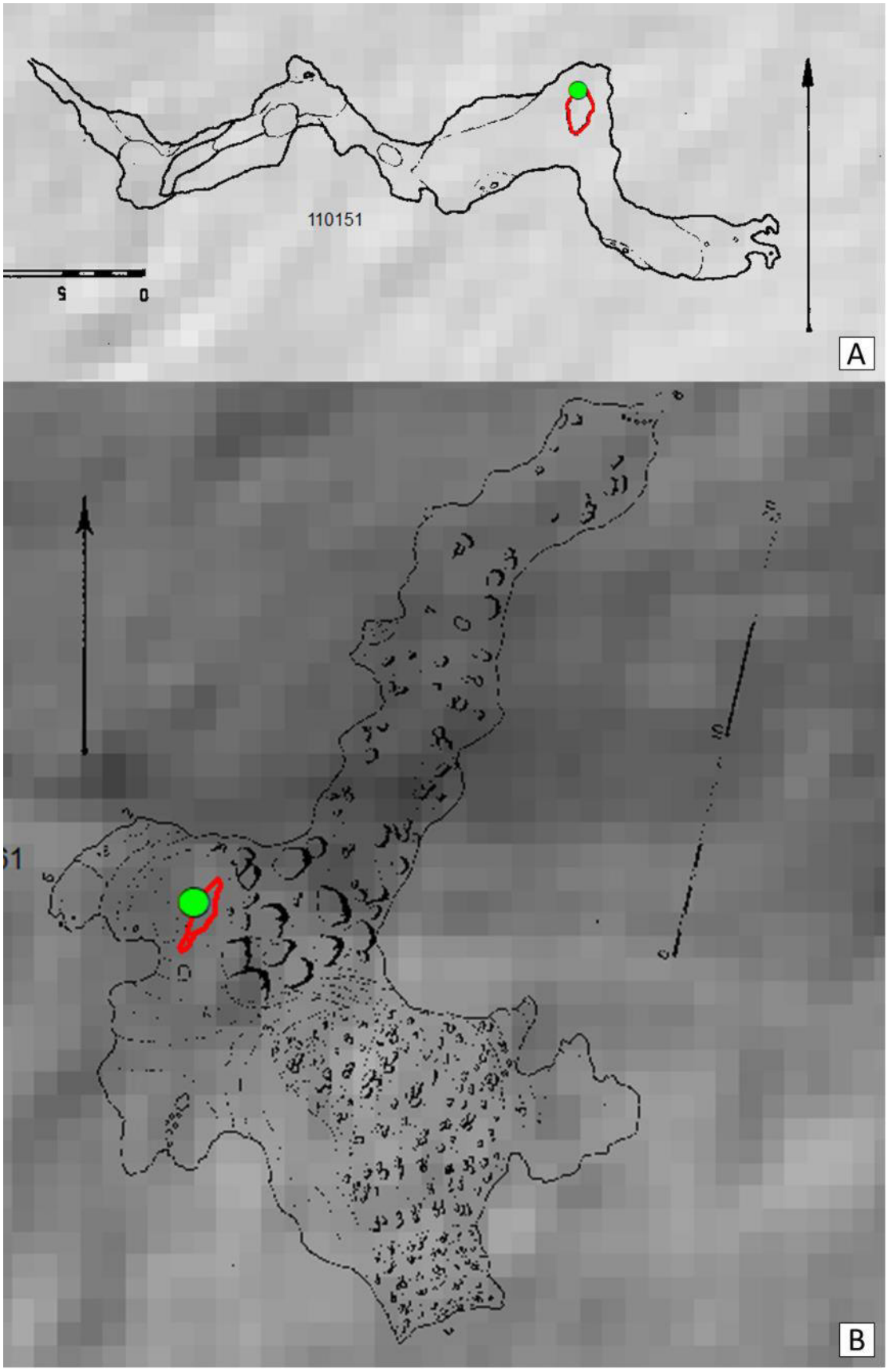

Figure 22 ***A)*** *"Grotta del Monte Cocusso (CSR 67/45)" and* ***B)*** *"Grotta del Monte Lanaro (CSR 186/20)" in which the entrances to the cavities are not visible on the shaded relief*

The LiDAR data with a 1-m resolution, did not always provide the accuracy necessary to easily identified cave entrances. However, with the introduction of new shaded relief with 0.5-m resolution, it become possible to clearly identify the majority of caves and adjust their outlines accordingly (*Figure 23*).

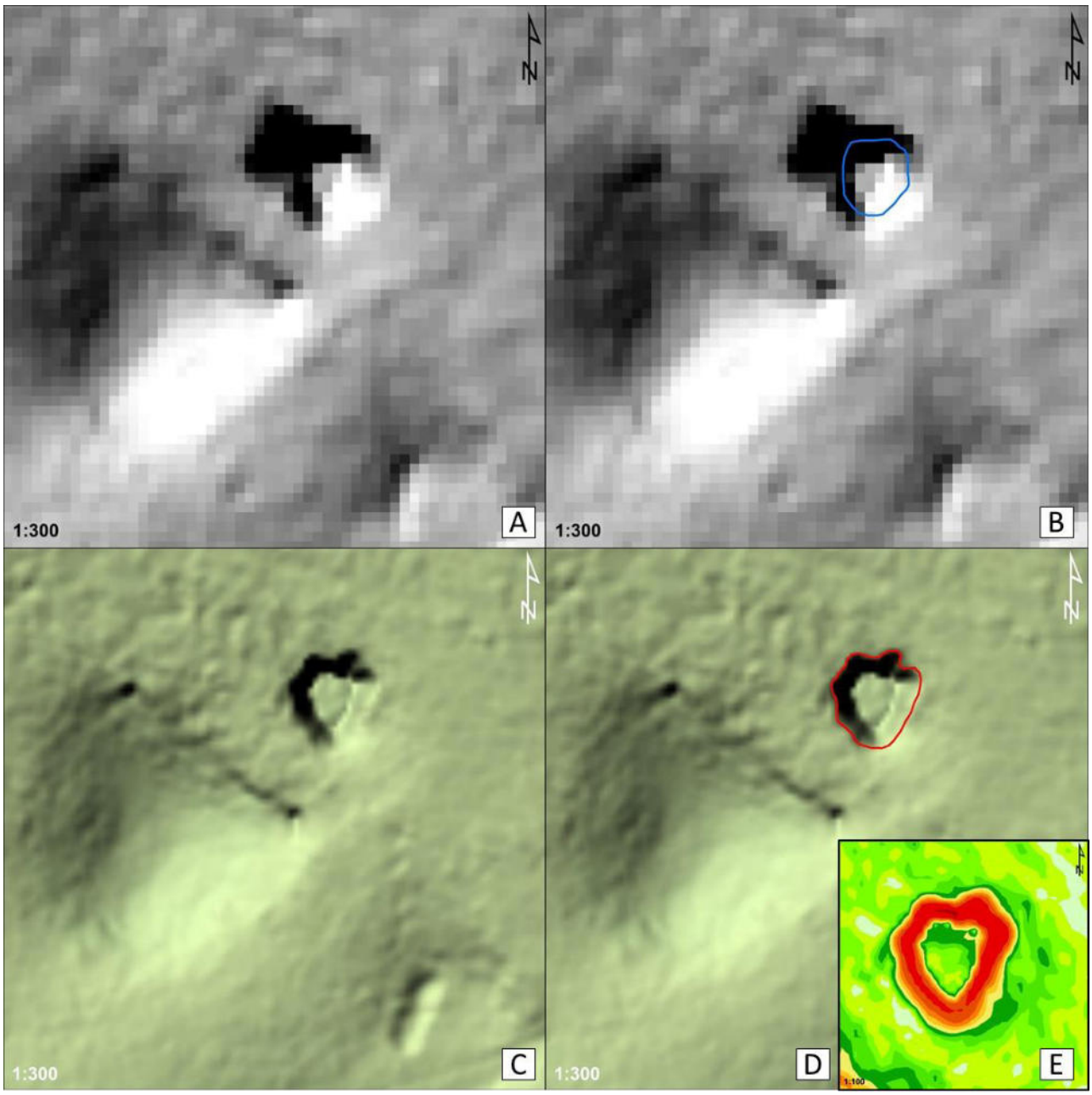

Figure 23 *"Grotta fra Poggioreale e Monrupino" (CSR 1167/4101).* ***A)*** *and* ***B)*** *shaded relief from 1-m resolution DTM, showing the cave entrance outline in blue.* ***C)*** *and* ***D)*** *shaded relief from 0.5-m resolution DT, displaying the revised cave entrance outline in red.* ***E)*** *Slope map derived from the 0.5-m resolution DTM*

In addition to the analysis of the data contained in the CSR, the identification of new subsidence sinkholes in this context was achieved through an in-depth geomorphological investigation of the territory, utilizing the 0.5m resolution DTM, which revealed various interesting areas. Subsequently, these areas were targeted for field surveys that occasionally led to the identification of new sinkholes, which were then documented and included in the geodatabase.

One example is represented in the Meduno municipality, where an area with numerous cover suffosion sinkholes and cover collapse sinkholes was identified and subsequently surveyed *(Figure 24).*

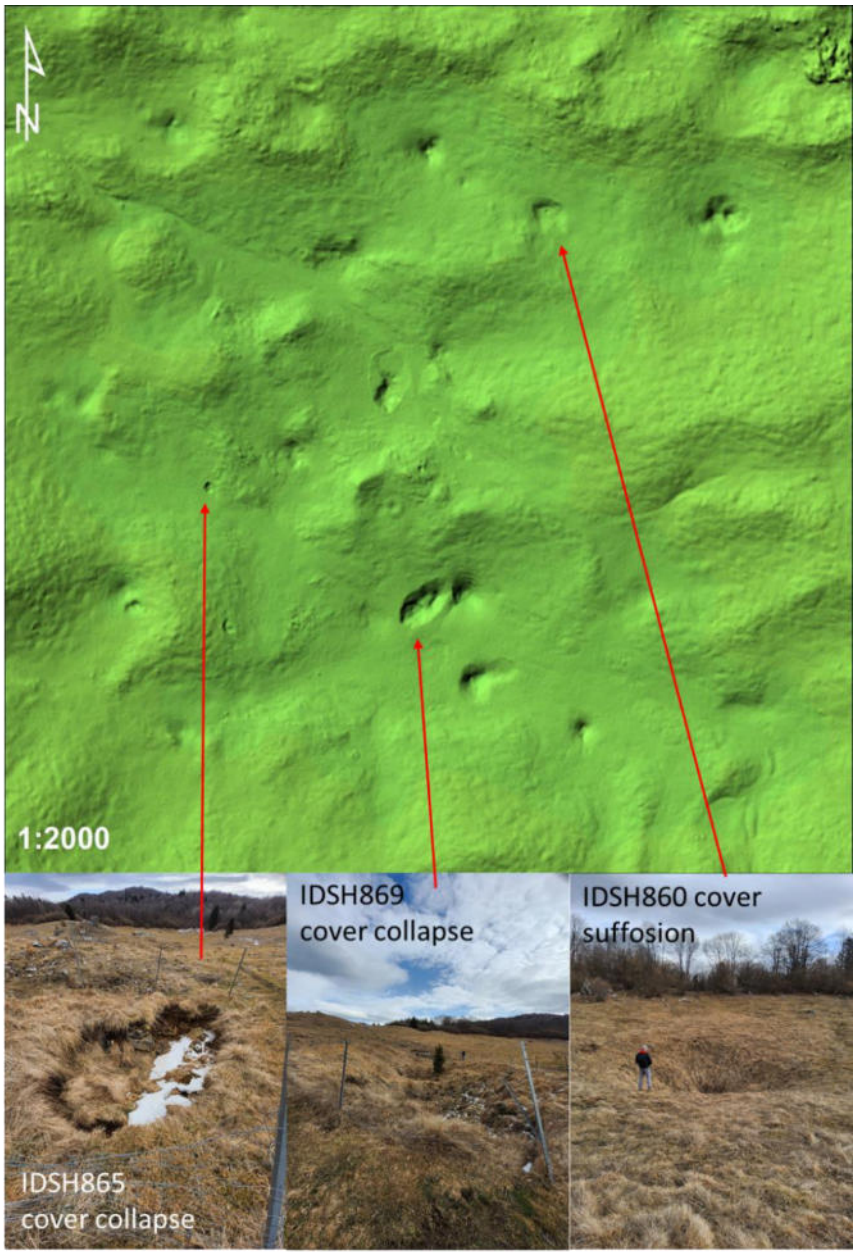

Figure 24 *Sinkholes in Meduno municipality detected using the DTM with 0.5-m resolution*

As of today, 1431 natural sinkholes across the entire regional territory were recorded in the FVG geodatabase and classified as specified in *Table 4*.

Sinkhole type (Gutiérrez et al., 2014)	**Number of sinkholes 2017**	**Number of sinkholes 2018**	**Number of sinkholes 2020**	**Number of sinkholes 2023**
Cover suffosion sinkhole	226	361	362	609
Cover collapse sinkhole	127	178	180	228
Bedrock collapse sinkhole	130	139	207	233
Caprock collapse sinkhole	68	77	77	78
Undefined	485	444	446	262
Fontanazzi				18
Area of widespread sinkholes				3
TOTAL	**1036**	**1199**	**1272**	**1431**

Table 4 *Sinkholes inventory of FVG region over years*

As evident from the table above, a significant revision has been made, notably in reducing the number of "undefined" sinkholes (from 446 in 2020 to 262 in 2023) by assessing them, through on-site surveys, a specific typology according to the Gutierrez et al., 2014 classification. Another noteworthy update is the addition of 159 newly identified sinkholes.

From a statistical standpoint, 63.2% of the sinkholes in FVG region are characterized by an evaporites bedrock, while 31% have a carbonates bedrock. Only 2.6% are characterized by conglomerates and 3.3% by quaternary deposits.

The distribution of sinkhole based on different bedrocks aligns with the lithological pattern across the regional territory. Evaporites are predominant in two E-W aligned sectors in the Tolmezzo Alps and the Carnian Range, while carbonates are present in the Julian Alps, Carnian and Julian Prealps, as well as in the Classical Karst territory (*Figure 25*).

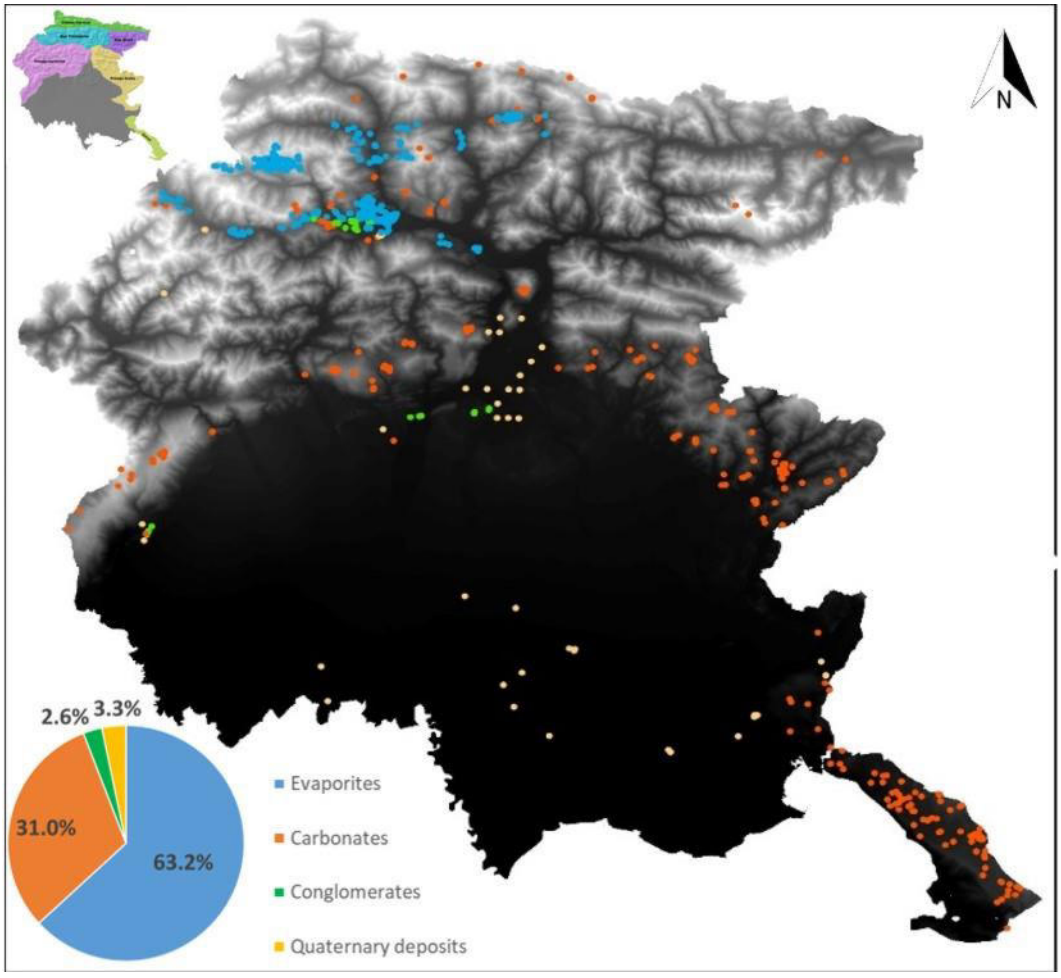

Figure 25 *Percentage of sinkholes related to different bedrocks*

Considering all sinkholes, regardless of the environment of formation, the classification reveals that 42.6% are identified as cover suffusion, while 37.7% are collapse (15.9% as cover collapse, 16.3% as bedrock collapse and 5.5% as caprock collapse). 18.2% is actually classified as "undefined" due to lack of information. The remaining 1.6% comprise 1.3% categorized as "fontanazzi" (indicating a spring formed by water infiltration on the outer side of an embankment during river flood) and 0.3% as a widespread subsidence area (*Figure 26*).

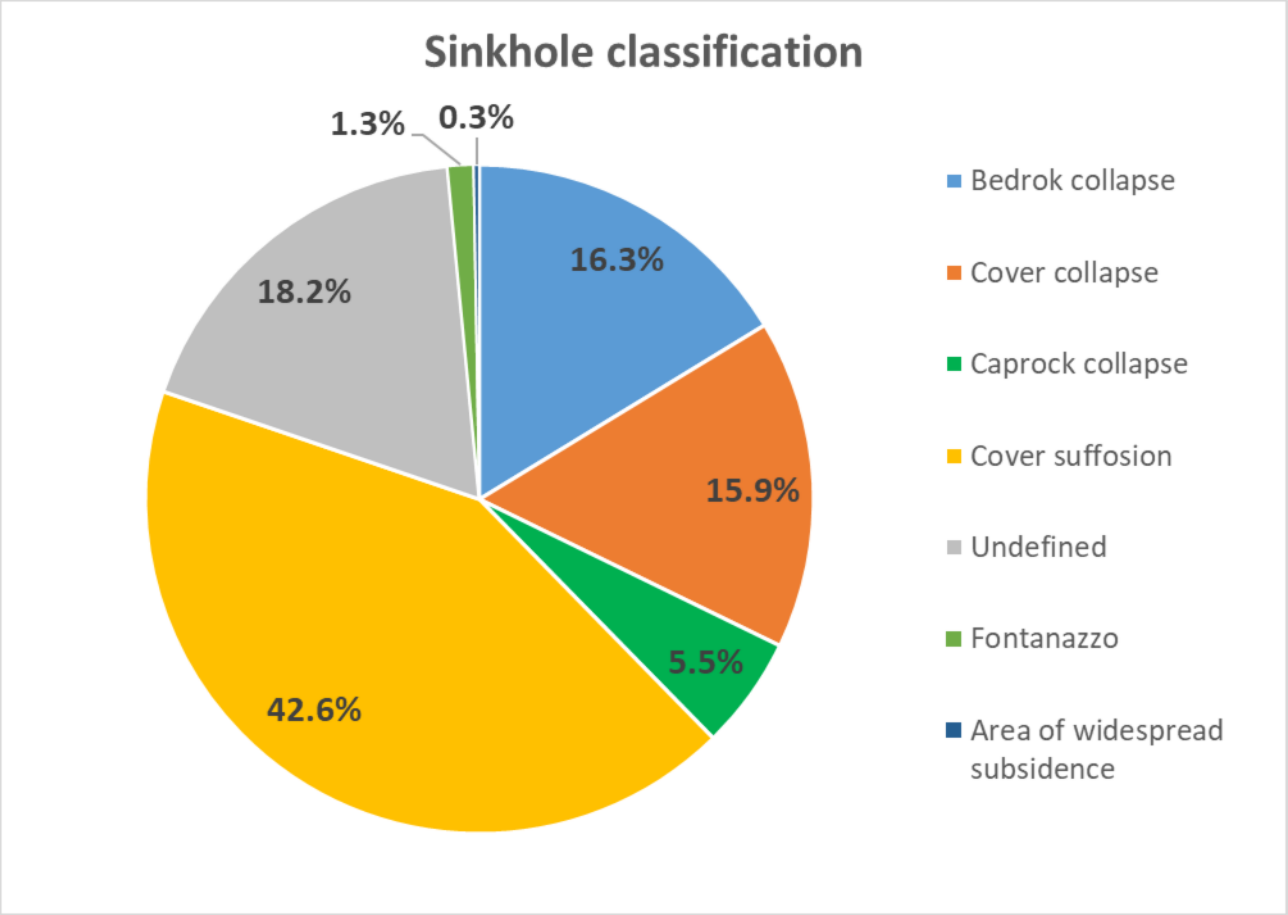

Figure 26 *Sinkhole classification (sensu Gutiérrez et al., 2014)*

If we differentiate the types of bedrock in which sinkholes occurred, both in evaporitic and carbonate environments, the percentage of cover suffosion sinkholes is approximately 40%. The variation lies in the prevalence of bedrock collapses, which are more common in carbonates (32.7% in the carbonates and 9.6% in the evaporites), and the occurrence of cover collapse which are more common in evaporites (18.3% in evaporites and 11.3% in carbonates) (*Figure 27* and *Figure 28*).

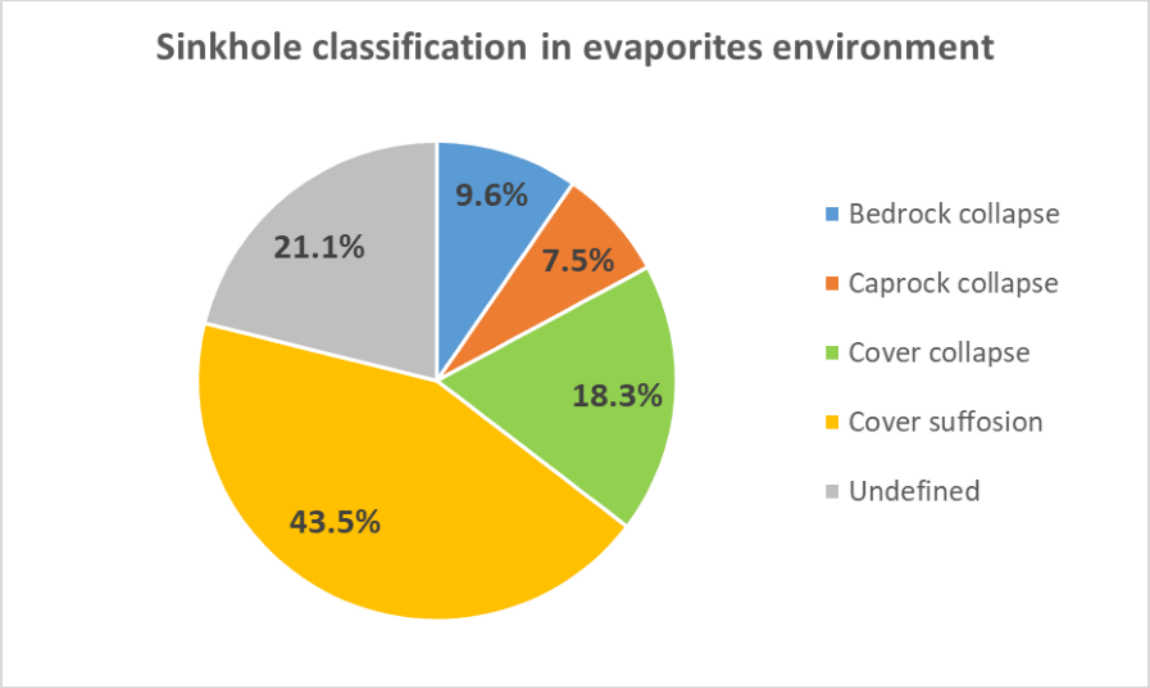

Figure 27 *Sinkhole classification in evaporites environment*

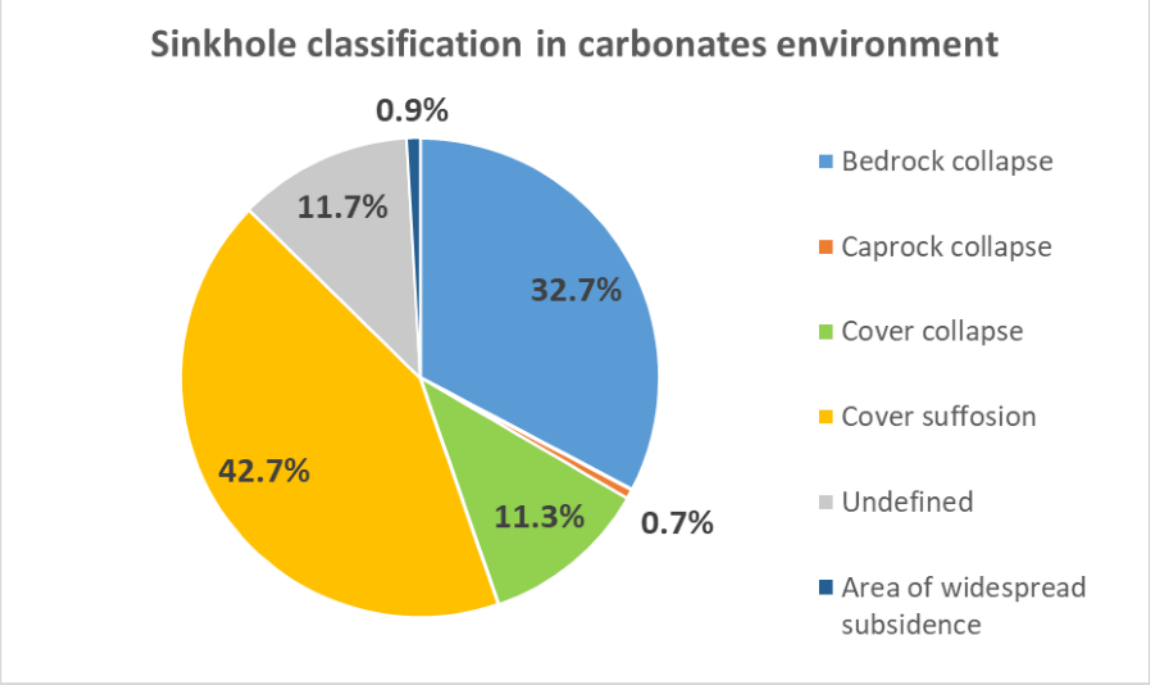

Figure 28 *Sinkhole classification in carbonates environment*

In conglomerate deposits (*Figure 29*) most of the sinkholes are defined as collapse, constituting a total of 48.6%, involving different material (27% cover, 18.9% caprock and 2.7% bedrock collapses). The remaining percentage comprises 37.8% cover suffosion and 13.5% "undefined". In the quaternary deposits environment (*Figure 30*), the predominant forms are cover suffosion sinkholes, "fontanazzi" and undefined each accounting for 31.0%. Other forms present are cover collapse sinkholes (7.1%).

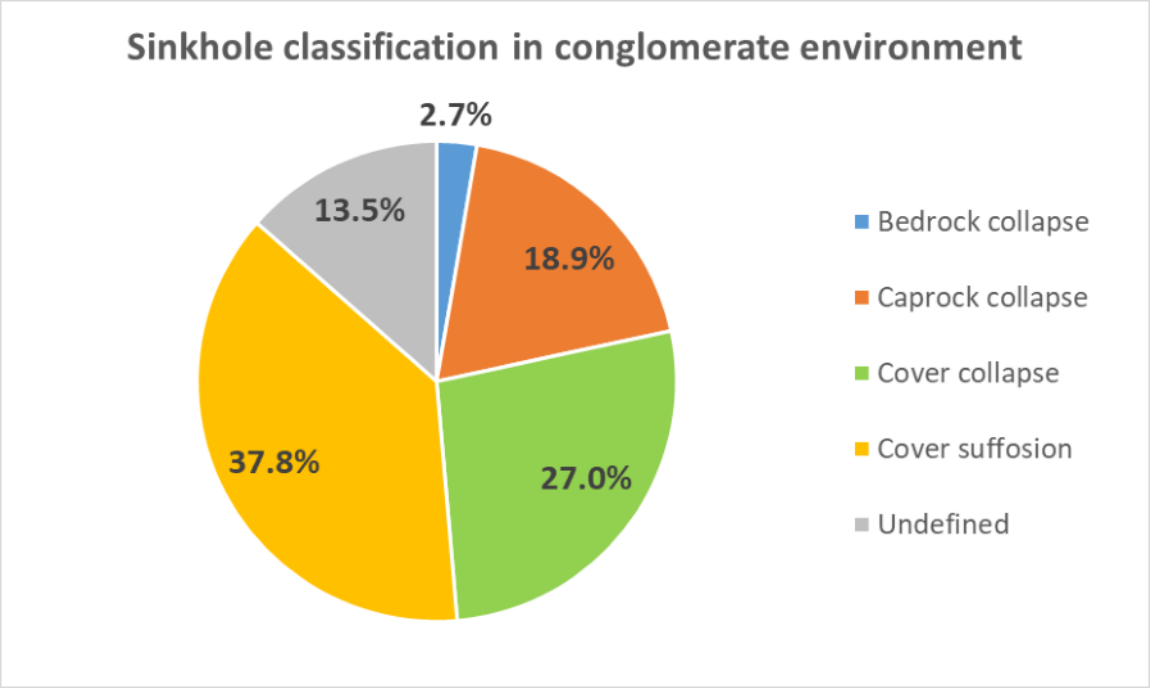

Figure 29 *Sinkhole classification in conglomerate environment*

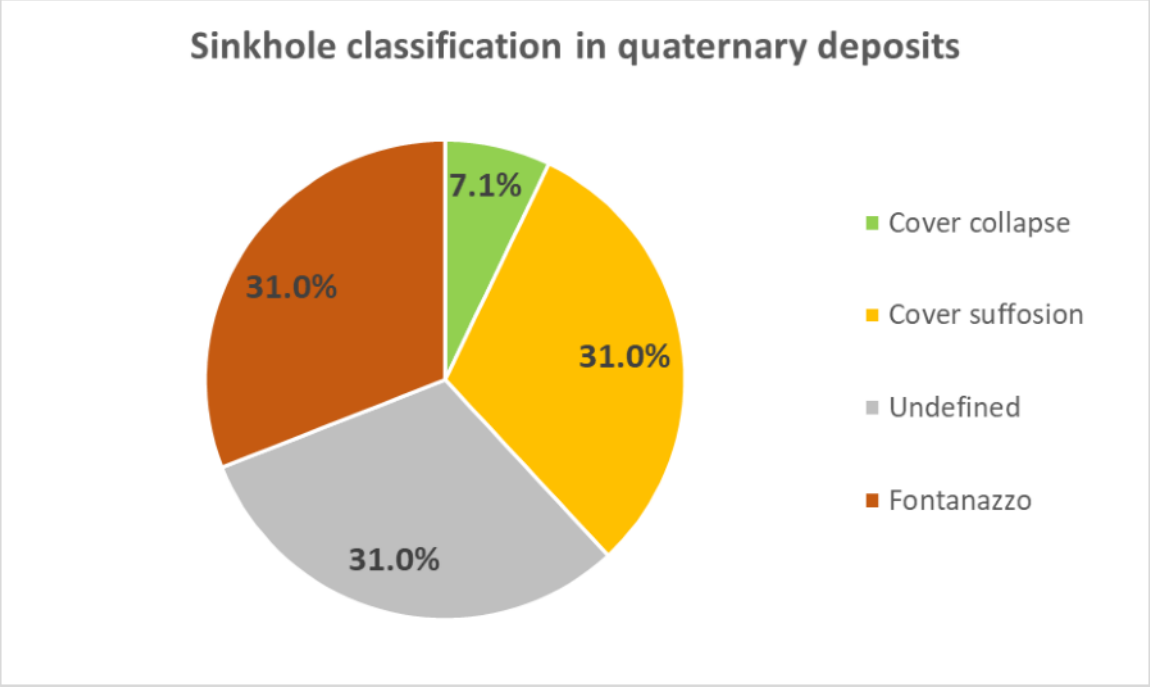

Figure 30 *Sinkhole classification in quaternary deposits*

The state of activity is a crucial parameter in hazard assessment and as such, it is considered fundamental.

In the FVG region, 43.4% of sinkholes are dormant, 21.4% are active and 0.8% are reactivated (*Figure 31*). These data demonstrate that the region, in addition to being highly susceptible to this type of geological hazard, as emerged from the number of identified sinkholes, is also affected by a significant number of active sinkholes.

Only 11.8% are stable (9% inactive, 1.9% artificially stabilized and 0.9% relict), while the remaining 22.6% are classified as "undefined".

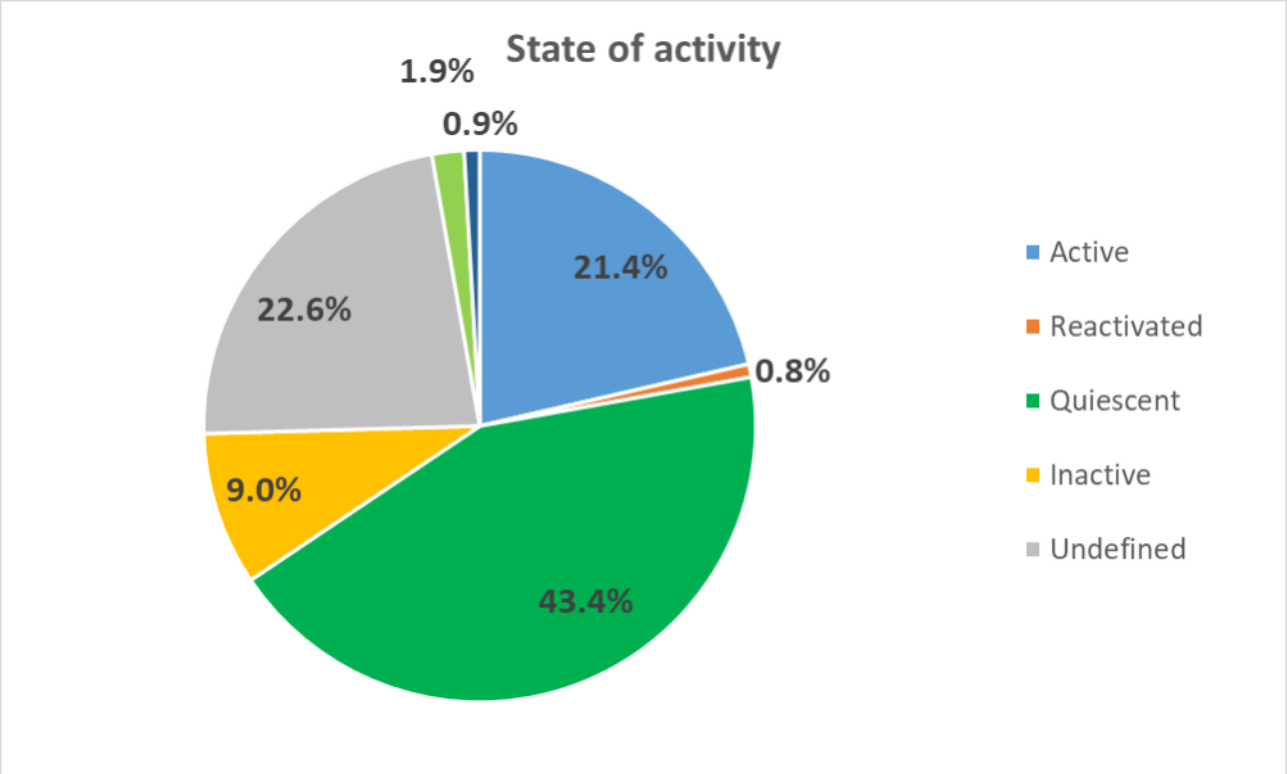

Figure 31 *State of activity of sinkholes in FVG region*

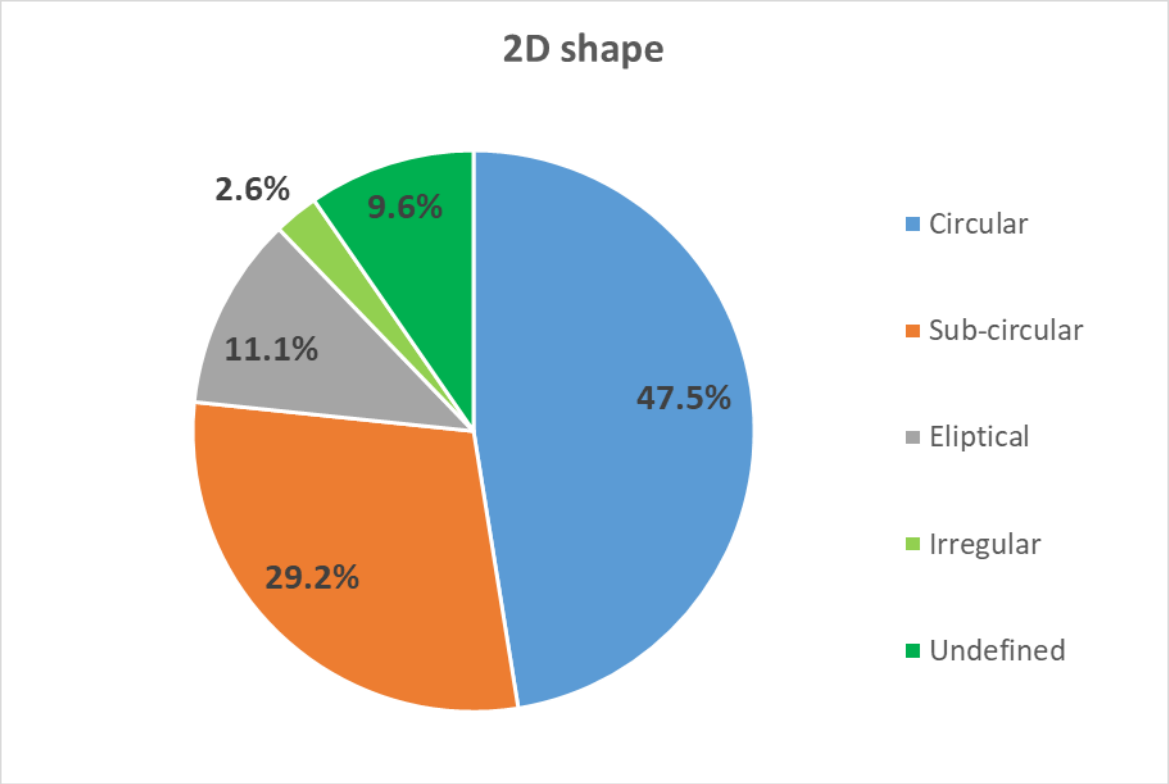

Figure 32 *2D shape of sinkholes present in the geodatabase of FVG region*

According to the definition, 76.7% of the sinkholes have a circular or subcircular shape (47.5% circular and 29.2% subcircular). The remaining forms include elliptical (11.1%), irregular (2.6%) and 9.6% are undefined due to a lack of data.

The identification of sinkhole shape during field surveys is subjective. To enhance data objectivity, an important parameter, the elongation ratio "*Er*", was calculated and incorporated into the geodatabase. This shape index is determined by the relationship between the length and the width. Specifically, the length is the dimension of the straight line between the most distant points of the perimeter (major axis) and the width is the longest axis perpendicular to the major axis (minor axis) (Williams, 1972; Bondesan et al., 1992, Basso et al., 2013; Kobal et al., 2015; De Waele & Gutiérrez, 2022).

According to Basso et al., (2013) and Kobal et al., (2015), sinkholes were categorized into 4 groups (*Table 5*) based on their elongation ratios "*Er*":

Description	*Er* value	Percentage
Circular/sub-circular	$Er \leq 1.21$	58.61%
Elliptical	$1.21 < Er \leq 1.65$	35.26%
Sub-elliptical	$1.65 < Er \leq 1.8$	2.37%
Elongated	$Er > 1.8$	3.76%

Table 5 *Percentage referred to the range of the calculated elongation ratio*

In comparing the calculated and subjective data, it became apparent that during field surveys, there is an overestimation of the circular/sub-circular shape and an underestimation of the elliptical one.

Another parameter that has been incorporated into the geodatabase is the circularity ratio (Cr), calculated using the formula proposed by Brinkmann et al., (2008), Doctor & Young, (2013), Carvalho et al., (2014), Zumpano et al. (2019) and De Waele & Gutiérrez, (2022). This parameter is defined as the ratio between the area of the sinkhole (A) and the area of a circle with a circumference equal to the perimeter (P) of the sinkhole.

$$Cr = \frac{A}{(P^2/4\pi)}$$

The circularity ratio parameter measures the deviation of a polygon from a perfect circle. A circular shape is represented by a value of 1.0, indicating the maximum value. In contrast, elongated shapes are represented by lower values that decrease with the irregularity of the sinkhole perimeter.

In the FVG region, the calculated circularity ratio ranges from a minimum value of 0.419 to a maximum of 0.997, with a mean of 0.933 and a standard deviation of 0.07. From a statistical perspective, only 1.74% have a Cr lower than 0.7, while 14.98% fall within the range of 0.9 to 0.7. The remain 83.28% have a circularity ratio higher than 0.9, confirming that the majority of the sinkholes have a circular shape.

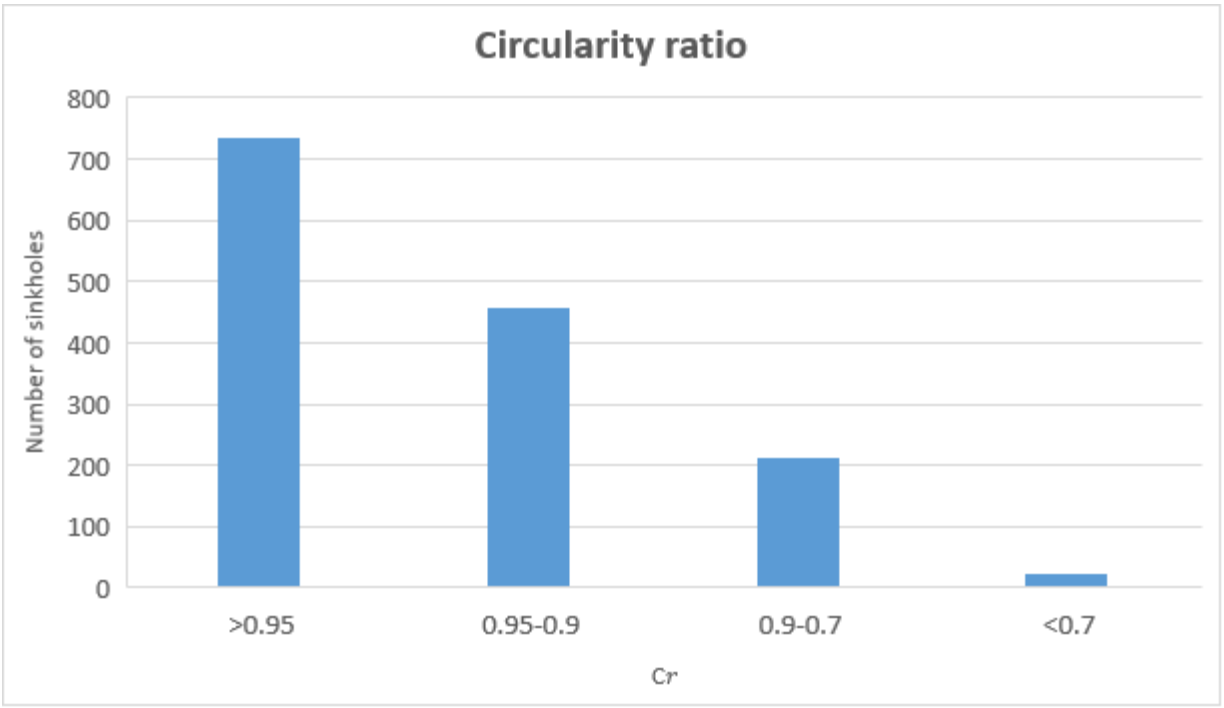

Figure 33 *Circularity ratio vs number of sinkholes*

REFERENCES

- Abelson M., Baer G., Shtivelman V., Wachs D., Raz E., Crouvi O., Kurzon I., Yechieli Y. (2003) Collapse-sinkholes and radar interferometry reveal neotectonics concealed within the Dead Sea basin. Geophysical Research Letters 30, 1545. https://doi.org/10.1029/2003GL017103
- Ahmed S. & Carpenter P.J. (2003) Geophysical response of filled sinkholes, soil pipes and associated bedrock fractures in thinly mantled karst, east-central Illinois. Environmental Geolology 44, 705–716. https://doi.org/10.1007/s00254-003-0812-3
- Angel J. C., Nelson D.O., Panno S.V. (2004) Comparison of a new GIS-based technique and a manual method for determining sinkhole density: An example from Illinois' sinkhole plain. Journal of Cave and Karst Studies 66, 9–17
- ARPA Piemonte (2009) SIFRAP, Sistema Informativo Frane in Piemonte. Guida alla lettura della scheda frane, 44 pp
- Baer G., Schattner U., Wachs D., Sandwell D., Wdonwinski S., Frydman S. (2002) The lowest place on Earth is subsiding; An InSAR Interferometric Synthetic Aperture Radar perspective. Geological Society of America Bulletin 114, 12–23. https://doi.org/10.1130/0016-7606(2002)114<0012:TLPOEI>2.0.CO;2
- Baer G., Magen Y., Nof R.N., Raz E., Lyakhovsky V., Shalev E. (2018) InSAR Measurements and Viscoelastic Modeling of Sinkhole Precursory Subsidence: Implications for Sinkhole Formation, Early Warning, and Sediment Properties. Journal of Geophysical Research: Earth Surface 123 (4):678-693. https://doi.org/10.1002/2017JF004594
- Basso A., Bruno E., Parise M., Pepe M. (2013) Morphometric analysis of sinkholes in a karst coastal area of southern Apulia (Italy). Environmental Earth Sciences 70, 2545–2559. https://doi.org/10.1007/s12665-013-2297-z
- Batayneh A.T., Abueladas A.A., Moumani K.A. (2002) Use of ground-penetrating radar for assessment of potential sinkhole conditions: an example from Ghor al Haditha area, Jordan. Environmental Geology 41, 977–983. https://doi.org/10.1007/s00254-001-0477-8
- Bauer C. (2015) Analysis of dolines using multiple methods applied to airborne laser scanning data. Gomorphology 205: 78-88. https://doi.org/10.1016/j.geomorph.2015.08.015
- Bondesan A., Meneghel M., Sauro U. (1992) Morphometric analysis of dolines. International Journal of Speleology, 21: 1-55. http://dx.doi.org/10.5038/1827-806X.21.1.1
- Brinkmann R., Wilson K., Elko N., Seale L.D., Florea L., Vacher H.L. (2007) Sinkhole distribution based on pre-development mapping in urbanized Pinellas County,

Florida, USA. In: Parise M., & Gunn J. (Eds.), Natural and anthropogenic hazards in karst areas: Recognition, analysis, and mitigation (pp. 5–11). Geological Society of London. https://doi.org/10.1144/sp279.2

- Brinkmann R., Parise M., Dye D. (2008) Sinkhole distribution in a rapidly developing urban environment: Hillsborough County, Tampa Bay area, Florida. Engineering Geology 99, 169–184. https://doi.org/10.1016/j.enggeo.2007.11.020
- Bruno E., Calcaterra D., Parise M. (2008) Development and morphometry of sinkholes in coastal plains of Apulia, southern Italy: Preliminary sinkhole susceptibility assessment. Engineering Geology 99, 198–209. https://doi.org/10.1016/j.enggeo.2007.11.017
- Burelli G., Cleva S., Cucchi F., E. Oberti Di Valnera S. (2004) Stato di evoluzione di sinkholes in alcune aree montane del Friuli Venezia Giulia. Conference proceedings: "Stato dell'arte sullo studio dei fenomeni di sinkholes e ruolo delle amministrazioni statali e locali nel governo del territorio, Roma 20-21 maggio 2004", 159-170.
- Busetti A., Calligaris C., Forte E., Areggi G., Mocnik A., Zini L. (2020) Non-invasive methodological approach to detect and characterize high-risk sinkholes in urban cover evaporite karst: integrated reflection seismics, PS-InSAR, leveling, 3D-GPR and ancillary data. A NE Italian case study. Remote Sensing 12(22), 3814. https://doi.org/10.3390/rs12223814
- Calligaris C., Zini L., Cucchi F., Stefanelli N. (2009) Gypsum's role in the Friuli Venezia Giulia sinkholes. In: Proceedings of the 2° International Workshop: Gli sprofondamenti catastrofici nell'ambiente naturale ed in quello antropizzato, ISPRA, Roma, 213-221.
- Calligaris C., Zini L., Nisio S., Piano C. (2020) Sinkholes in the Friuli Venezia Giulia Region focus on the evaporites. Journal of. Applied Geology, 5 https://doi.org/10.1007/978-3-030-43953-8_5
- Calligaris C., Forte E., Busetti A., Zini L. (2023) A joint geophysical approach to tune an integrated sinkhole monitoring method in evaporitic environments. Near Surface Geophysics, 1-16. https://doi.org/10.1002/nsg.12261
- Canuti P. & Esu F. (1995) Glossario Internazionale per le frane. Rivista Italiana di Geotecnica 2, 143-150
- Carbonel D., Gutiérrez F., Linares R., Roqué C., Zarroca M., McCalpin J.P., Guerrero J., Rodriguez V. (2013) Differentiating between gravitational and tectonic faults by means of geomorphological mapping, trenching and geophysical surveys. The case of the Zenzano Fault (Iberian Chain, N Spain). Geomorphology 189: 93–108. https://doi.org/10.1016/j.geomorph.2013.01.020
- Carbonel D., Rosdríguez V., Gutiérrez F., McCalpin J.P., Linares R., Roqué C., Zarroca M., Guerrero J., Sasowsky I. (2014) Evaluation of trenching, ground penetrating radar

(GPR), and electrical resistivity tomography (ERT) for sinkhole characterization. Earth Surface Processes and Landforms 39, 214–227. https://doi.org/10.1002/esp.3440

- Carbonel D., Rodríguez-Tribaldos V., Gutiérrez F., Galve J.P., Guerrero J., Zarroca M., Roqué C., Linares R., McCalpin J.P., Acosta E. (2015) Investigating a damaging buried sinkhole cluster in an urban area integrating multiple techniques: geomorphological surveys, DInSAR, GPR, ERT, and trenching. Geomorphology 229, 3–16. https://doi.org/10.1016/j.geomorph.2014.02.007
- Carvalho Júnior O.A., Guimarães R.F., Montgomery D.R., Gillespie A.R., Gomes R.A.T., Souza Martins É., Silva N.C. (2014) Karst Depression Detection Using ASTER, ALOS/PRISM and SRTM-Derived Digital Elevation Models in the Bambuí Group, Brazil. Remote Sensing 6, 330-351. DOI: http://dx.doi.org/10.3390/rs6010330
- Castañeda C., Gutiérrez F., Manunta M., Galve J.P. (2009) DInSAR measurements of ground deformation by sinkholes, mining subsidence, and landslides, Ebro River, Spain. Earth Surface Processes and Landforms 34, 1562–1574. https://doi.org/10.1002/esp.1848
- Cigna F., Banks V.J., Donald A.W., Donohue S., Graham C., Hughes D., McKinley J.M., Parker K. (2017) Mapping ground instability in areas of geotechnical infrastructure using satellite InSAR and Small UAV surveying: a case study in Northern Ireland. Geosciences 7:51. https://doi.org/10.3390/geosciences7030051
- Closson D., Karaki N.A., Hussein M.J., Al-Fugha H., Ozer A. (2003) Space-borne radar interferometric mapping of precursory deformations of a dyke collapse, Dead Sea area, Jordan. International Journal of Remote Sensing 24, 843–849. https://doi.org/10.1080/01431160210147388
- Cooper A. H. (2008) The classification, recording, databasing and use of information about building damage caused by subsidence and landslides. Quarterly Journal of Engineering Geology and Hydrogeology 41, 409–424. https://doi.org/10.1144/1470-9236/07-223
- Cruden D.M. & Couture R. (2011) The working classification of landslides: material matters. Proceedings, 64th Canadian Geotechnical Conference, Toronto, 7pp
- Cucchi F. & Piano C. (2002) Ipercarsismo superficiale e sepolto nelle evaporiti del Friuli-Venezia-Giulia. Le voragini catastrofiche, un nuovo problema per la Toscana, Edizioni Regione Toscana, 35–46
- Cucchi F. & Piano C. (2003) Friuli-Venezia Giulia. In: Madonia G., Forti P. Le aree carsiche gessose d'Italia, Memorie dell'Istituto Italiano di Speleologia II, vol. XIV, 149-150, Bologna 2003.
- Dahm T., Heimann S., Bialowons W. (2011) A seismological study of shallow weak micro-earthquakes in the urban area of Hamburg city, Germany, and its possible

relation to salt dissolution. Natural Hazards 58: 1111–1134. https://doi.org/10.1007/s11069-011-9716-9

- De Castro T. & Rodrigues P.C.H. (2021) Assessment of a semi- automatic spatial analysis method to identify and map sinkholes in the Carste Lagoa Santa environmental protection unit, Brazil. Environmental Earth Sciences 80: 1–15. https://doi.org/10.1007/s12665-020-09354-z
- De Waele J. & Gutiérrez F. (2022) Karst hydrogeology, geomorphology and caves. Wiley-Blackwell, Chichester
- Delkhahi B., Nassery H.R., Vilarrasa V., Alijani F., Ayora C. (2020) Impacts of natural CO2 leakage on groundwater chemistry of aquifers from the Hamadan Province, Iran. International Journal of Greenhouse Gas Control 96, 103001. https://doi.org/10.1016/j.ijggc.2020.103001
- Desir G., Gutiérrez F., Merino J., Carbonel D., Benito-Calvo A., Guerrero J., Fabregat I. (2018) Rapid subsidence in damaging sinkholes: measurement by high-precision leveling and the role of salt dissolution. Geomorphology 303, 393–409. https://doi.org/10.1016/j.geomorph.2017.12.004
- Doctor D.H., Young J.A. (2013) An evaluation of automated GIS tools for delineating karst sinkholes and closed depressions from 1-meter LIDAR-derived digital elevation data. In: Land L., Doctor D.H., Stephenson J.B. (Eds.), Sinkholes and the engineering and environmental impacts of karst (pp. 449–458). Carlsbad, NM: National Cave and Karst Research Institute. https://doi.org/10.5038/9780979542275.1156
- Dou J., Li X., Yunus A.P., Paudel U., Chang K-T., Zhu Z., Pourghasemi H.R. (2015) Automatic detection of sinkhole collapses at finer resolutions using a multi-component remote sensing approach. Natural Hazards 78, 1021–1044. https://doi.org/10.1007/s11069-015-1756-0
- Epting J., Huggenberger P., Glur L. (2009) Integrated investigations of karst phenomena in urban environments. Engineering Geology 109, 273–289. https://doi.org/10.1016/j.enggeo.2009.08.013
- Festa V., Fiore A., Parise M., Siniscalchi A. (2012) Sinkhole evolution in the Apulian karst of southern Italy: a case study, with some considerations on sinkhole hazards. Journal of Cave and Karst Studies 74, 137–147. DOI:10.4311/2011JCKS0211
- Filin S., Baruch A., Avni Y., Marco S. (2011) Sinkhole characterization in the Dead Sea area using airborne laser scanning. Natural Hazards 58, 1135–1154. https://doi.org/10.1007/s11069-011-9718-7
- Frumkin A., Ezersky M., Al-Zoubi A., Akkawi E., Abueladas A.-R. (2011) The Dead Sea sinkhole hazard: Geophysical assessment of salt dissolution and collapse. Geomorphology 134, 102–1117. https://doi.org/10.1016/j.geomorph.2011.04.023

- Galve J., Gutiérrez F., Lucha P., Guerrero J., Remondo J., Bonachea J., Remondo J., Cendrero A. (2009) Probabilistic sinkhole modeling for hazard assessment. Earth Surface Processes and Landforms 34, 437–452. https://doi.org/10.1002/esp.1753
- Galve J. P., Castañeda C., Gutiérrez F. (2015) Railway track deformation detected by DInSAR over a dissolution-induced subsidence area of the Ebro Valley evaporite karst, Spain. Natural Hazard and Earth System Science 3, 3967–3981. https://doi.org/10.5194/nhess-15-2439-2015
- García-Moreno I. & Mateos R.M. (2011) Sinkholes related to discontinuous pumping: susceptibility mapping base on geophysical studies. The case of Crestatx (Mallorca, Spain). Environmental Earth Sciences 64, 523–537. https://doi.org/10.1007/s12665-010-0876-9
- Gortani M. (1904) Una dolina di sprofondamento presso Treppo Carnico. Mondo Sotterraneo, 1 (2), 40-41.
- Gortani M. (1965) Le doline alluvionali. Natura e Montagna, 3, 120-128.
- Guerrero J., Sevil J., Desir G., Gutiérrez F., Arnay A.G., Galve J.P. Reyes-Carmona C. (2021) The detection of active sinkholes by airborne differential LiDAR DEMs and InSAR cloud computing tools. Remote Sensing 13, 3261. https://doi.org/10.3390/rs13163261
- Gutiérrez F. & Cooper A. H. (2002) Evaporite dissolution subsidence in the historical city of Calatayud, Spain: Damage appraisal and prevention. Natural Hazards 25, 259–288. https://doi.org/10.1023/A:1014807901461
- Gutiérrez F., Galve J. P., Guerrero J., Lucha P., Cendrero A., Remondo J., Bonachea J., Gutiérrez M., Sànchez J.A. (2007) The origin, typology, spatial distribution, and detrimental effects of the sinkholes developed in the alluvial evaporite karst of the Ebro River valley downstream Zaragoza City (NE Spain). Earth Surface Processes and Landforms 32, 912–928. https://doi.org/10.1002/esp.1456
- Gutiérrez F., Guerrero J., Lucha P. (2008) A genetic classification of sinkholes illustrated from evaporite paleokarst exposures in Spain. Environmental Geology 53, 993–1006. https://doi.org/10.1007/s00254-007-0727-5
- Gutiérrez F., Galve J. P., Lucha P., Castañeda C., Bonachea J., Guerrero J. (2011) Integrating geomorphological mapping, trenching, InSAR and GPR for the identification and characterization of sinkholes in the mantled evaporite karst of the Ebro Valley (NE Spain). Geomorphology 134, 144–156. https://doi.org/10.1016/j.geomorph.2011.01.018
- Gutiérrez F., Parise M., De Waele J., Jourde H. (2014) A review on natural and human-induced geohazards and impacts in karst. Earth- Science Reviews 138, 61–88. https://doi.org/10.1016/j.earscirev.2014.08.002

- Gutiérrez F. (2016) Sinkhole hazards. In: Oxford Research Encyclopedia of Natural Hazard Science. Oxford: Oxford University Press. https://doi.org/10.1093/acrefore/9780199389407.013.40
- Gutiérrez F., Zarroca M., Linares R., Roqué C., Carbonel D., Guerrero J., McCalpin J.P., Comas X., Cooper A.H. (2018) Identifying the boundaries of sinkholes and subsidence areas via trenching and establishing setback distances. Engineering Geology 233, 255–268. https://doi.org/10.1016/j.enggeo.2017.12.015
- Higuera-Diaz I.C., Carpenter P.J., Thompson M.D. (2007) Identification of buried sinkholes using refraction tomography at Ft. Campbell army airfield, Kentucky. Environmental Geology 53, 805–812. https://doi.org/10.1007/s00254-007-0693-y
- Intrieri E., Gigli G., Nocentini M., Lombardi L., Mugnai F., Fidolini F., Casagli N. (2015) Sinkhole monitoring and early warning: An experimental and successful GB-InSAR application. Geomorphology 241, 304–314. https://doi.org/10.1016/j.geomorph.2015.04.018
- Jones C.E. & Blom R.G. (2014) Bayou Corne, Louisiana, sinkhole: Precursory deformation measured by radar interferometry. Geology 42, 111–114. https://doi.org/10.1130/G34972.1
- Jones C.E. (2020) Capabilities, limitations and opportunities for studying sinkholes using synthetic aperture radar interferometry. In: Proceedings of the 16th Multidisciplinary Conference on Sinkholes and the Engineering and Environmental Impacts of Karst (ed. L. Land, C. Kromhout and M.J. Byle), 68–74. Carlsbad: National Cave and Karst Research Institute. https://doi.org/10.5038/9781733375313.1008
- Kasting K.M. & Kasting E.H. (2003) Site characterization of sinkholes based on resolution of mapping. In: Proceeding of the 9th Multidisciplinary Conference on Sinkholes and the Engineering and Environmental Impacts of Karst, Geotechnical Special Publication 122 (ed. B.F. Beck), 72–81. Huntsville, Alabama: ASCE. https://doi.org/10.1061/40698(2003)6
- Kent J.D. & Dunaway L. (2013) Real-time GPS network monitors Bayou Corne sinkhole event. Eos 94, 1–2. https://doi.org/10.1002/2013EO430002
- Kersten T., Kobe M., Gabriel G., Timmen L., Schon S., Vogel D. (2017) Geodetic monitoring of subrosion-induced subsidence processes in urban areas. Journal of Applied Geodesy 11, 21–29. https://doi.org/10.1515/jag-2016-0029
- Kim Y.J., Nam B.H., Youn H. (2019) Sinkhole detection and characterization using LiDAR-derived DEM with logistic regression. Remote Sensing 11, 1592. https://doi.org/10.3390/rs11131592
- Kobal M., Bertoncelj I., Pirotti F., Dakskobler I., Kutnar L. (2015) Using lidar data to analyse sinkhole characteristics relevant for understory vegetation under forest cover -

Case study of a high karst area in the Dinaric Mountains. PLoS One 10 (3): e0122070. https://doi.org/10.1371/journal.pone.0122070

- Kobe M., Gabriel G., Weise A., Vogel D. (2019) Time-lapse gravity and levelling surveys reveal mass loss and ongoing subsidence in the urban subrosion-prone area of Bad Frankenhausen, Germany. Solid Earth 10(3), 599–619. https://doi.org/10.5194/se-10-599-2019
- Krawczyk C.M., Polom U., Trabs S., Dahm T. (2012) Sinkholes in the city of Hamburg—New urban shear-wave reflection seismic system enables high-resolution imaging of subrosion structures. Journal of Applied Geophysics 78, 133–143. https://doi.org/10.1016/j.jappgeo.2011.02.003
- Kromhout C. & Alfieri M.C. (2018) Assesment of historical aerial photography as initial screening tool to identify areas of possible risk to sinkhole development. In: Proceedings of the 15th Multidisciplinary Conference on Sinkholes and the Engineering and Environmental Impacts of Karst and the 3rd Appalachian Symposium (ed. I.D. Sasowsky, M.J. Byle and L. Land), 89–96. Carlsbad: National Cave and Karst Research Institute. https://doi.org/10.5038/9780991000982.1016
- Kühn D., Ohrnberger M., Dahm T. (2011) Imaging a shallow salt diapir using ambient seismic vibrations beneath the densely built-up city area of Hamburg, Northern Germany. Journal of Seismology 15, 507–531. https://doi.org/10.1007/s10950-011-9234-y
- Land L. (2003) Evaporite karst and regional groundwater circulation in the Lower Pecos Valley of Southeastern New Mexico. In: Evaporite Karst and Engineering/Environmental Problems in the United States, vol. 109 (ed. K.S. Johnson and J.T. Neal), 227–232. Oklahoma Geological Survey Circular
- Malehmir A., Socco L.V., Bastani M., Krawczyk C.M., Pfaffhuber A.A., Miller R.D., Maurer H., Frauenfelder R., Suto K., Bazin S., Merz K., Dahlin T. (2016) Near-surface geophysical characterization of areas prone to natural Hazards: a review of the current and perspective on the future. Advances in Geophysics 57, 51–146. https://doi.org/10.1016/bs.agph.2016.08.001
- Malinowska A.A., Witkowski W.T., Hejmanowski R., Chang L., van Leijen F.J., Hanssen R.F. (2019) Sinkhole occurrence monitoring over shallow abandoned coal mines with satellite-based persistent scatterer interferometry. Engineering Geology 262, 105336. https://doi.org/10.1016/j.enggeo.2019.105336Get rights and content
- Margiotta S., Negri S., Parise M., Valloni R. (2012) Mapping the susceptibility to sinkholes in coastal areas, based on stratigraphy, geomorphology and geophysics. Natural Hazards 62, 657–676. https://doi.org/10.1007/s11069-012-0100-1
- Marinelli O. (1897) Fenomeni di tipo carsico nei terrazzi alluvionali della Valle del Tagliamento. Memorie della Società Geografica Italiana, 8 (2), 415-419.

- Marinelli O. (1902) Cavità di sprofondamento nella campagna di Forni di Sotto. In: Studi orografici nelle Alpi Orientali, Serie 1900, Bollettino Società Geografica Italiana, 10, 67-68.
- Miao X., Qiu X., Wu S-S., Luo J., Gouzie D.R., Xie H. (2013) Developing efficient procedures for automated sinkhole extraction from Lidar DEMs. Photogrammetric Engineering & Remote Sensing 79, 545–554. https://doi.org/10.14358/PERS.79.6.545
- Milanovic P.T. (2004) Water resources engineering in karst. Boca Raton: CRC Press. https://doi.org/10.1201/9780203499443
- Nisio S. & Salvati L. (2004) Fenomeni di sprofondamento catastrofico. Proposta di classificazione applicata alla casistica italiana. In Proceedings of the 1st Seminar "Stato dell'arte sullo studio dei fenomeni di sinkholes e ruolo delle amministrazioni statali e locali nel governo del territorio", 20-21 May 2004, Roma, pp. 573-584
- Nisio S. (2008) I sinkholes nelle altre regioni. Memorie Descrittive della Carta Geologica d'Italia 85, 419–426. (In Italian)
- Nof R.N., Baer G., Ziv A., Raz E., Atzori S., Salvi S. (2013) Sinkhole precursors along the Dead Sea, Irsael, revealed by SAR interferometry. Geology 41, 1019–1022. https://doi.org/10.1130/G34505.1
- Oliver-Cabrera T., Wdowinski S., Kruse S., Robinson T. (2020) InSAR detection of localized subsidence induced by sinkhole activity in suburban West-Central Florida. Proceedings of the International Association of Hydrological Sciences 382, 155-159. https://doi.org/10.5194/piahs-382-155-2020
- Orhan O., Oliver-Cabrera T., Wdowinski S., Yalvac S., Yakar M. (2021) Land subsidence and its relations with sinkhole activity in Karapınar region, Turkey: a multi-sensor InSAR time series study. Sensors 21, 774. https://doi.org/10.3390/s21030774
- Paine J.G., Buckley S., Collins E.W., Wilson C.R., Kress W. (2009) Assessing sinkhole potential at Wink and Daisetta, Texas using gravimetry and radar interferometry. In the 22nd Symposium on the Application of Geophysics to Engineering and Environmental Problems, Fort Worth, Texas (pp. 480–488). https://doi.org/10.4133/1.3176733
- Panno S.V., Luman D.E. (2013) Mapping palimpsest karst features on the Illinois sinkhole plain using historical aerial photography. Carbonates and Evaporites 28, 201-214. https://doi.org/10.1007/s13146-012-0107-4
- Panno S.V., Luman D.E. (2018) Characterization of cover- collapse sinkhole morphology on a groundwater basin- wide scale using lidar elevation data: a new conceptual model for sinkhole evolution. Geomorphology 318, 1–17. https://doi.org/10.1016/j.geomorph.2018.05.013

- Pardo-Igúzquiza E., Valsero J.J.D., Dowd P.A. (2013) Automatic detection and delineation of karst terrain depressions and its application in geomorphological mapping and morphometric analysis. Acta Carsologica 42, 17–24. https://doi.org/10.3986/ac.v42i1.637
- Pazzi V., Di Filippo M., Di Nezza M., Carlà T., Bardi F., Marini F., Fontanelli K., Intrieri E., Fanti R. (2018) Integrated geophysical survey in a sinkhole-prone area: microgravity, electrical resistivity tomographies, and seismic noise measurements to delimit its extension. Engineering Geology 243, 282–293. https://doi.org/10.1016/j.enggeo.2018.07.016
- Pueyo-Anchuela O., Casas-Sainz A. M., Soriano M. A., Pocoví-Juan A. (2010) A geophysical survey routine for the detection of doline areas in the surroundings of Zaragoza NE Spain. Engineering Geology 114, 382–396. https://doi.org/10.1016/j.enggeo.2010.05.015
- Rahimi M. & Alexander E.C. (2013) Locating sinkholes in LIDAR coverage of a glaciofluvial karst, Winona County, Minnesota. In L. Land, D.H. Doctor, & J.B. Stephenson (Eds.), Sinkholes and the engineering and environmental impacts of karst (pp. 469–480). Carlsbad, NM: National Cave and Karst Research Institute. https://doi.org/10.5038/9780979542275.1158
- Ronen A., Ezersky M., Beck A., Gatenio B., Simhayov R.B. (2019) Use of GPR method for prediction of sinkholes formation along the Dead Sea Shores, Israel. Geomorphology 328, 28–43. https://doi.org/10.1016/j.geomorph.2018.11.030
- Samyn K., Mathieu F., Bitri A., Nachbaur A., Closset L. (2014) Integrated geophysical approach in assessing karst presence and sinkhole susceptibility along flood protection dykes of the Loire River, Orléans, France. Engineering Geology 183, 170–184. https://doi.org/10.1016/j.enggeo.2014.10.013
- Sargent C. & Goulty N.R. (2009) Seismic reflection survey for the investigation of gypsum dissolution and subsidence at Hell Kettels, Darlington, UK. Quarterly Journal of Engineering Geology and Hydrogeology 42, 31–38. https://doi.org/10.1144/1470-9236/07-071
- Sevil J., Gutiérrez F., Zarroca M., Desir G., Carbonel D., Guerrero J., Linares R., Roqué C., Fabregat I. (2017) Sinkhole investigation in an urban area by trenching in combination with GPR, ERT and high-precision leveling. Mantled evaporite karst of Zaragoza city, NE Spain. Engineering Geology 231, 9–20. https://doi.org/10.1016/j.enggeo.2017.10.009
- Shi Y., Tang Y., Lu Z., Kim J.W., Peng J. (2019) Subsidence of sinkholes in Wink, Texas from 2007 to 2011 detected by time-series InSAR analysis. Geomatics, Natural Hazards and Risk 10, 1125–1138. https://doi.org/10.1080/19475705.2019.1566786

- Solari L., Montalti R., Barra A., Monserrat O., Bianchini S., Crosetto M. (2020) Multi-temporal satellite interferometry for fastmotion detection: an application to salt solution mining. Remote Sensing 12, 3919. https://doi.org/10.3390/rs12233919
- Stierman D.J. (2004) Geophysical detection of caves and Karstic voids. In: Gunn, J. (Ed.) Encyclopedia of caves and karst science. New York: Fitzroy Dearborn, pp. 377–380.
- Taheri K., Missimer T.M., Mohseni H., Fidelibus M.D., Fathollahy M., Taheri M. (2021) Enhancing spatial prediction of sinkhole susceptibility by mixed waters geochemistry evaluation: application of ROC and GIS. Environmental Earth Sciences 80(14), 1–28. https://doi.org/10.1007/s12665-021-09763-8
- Theron A., Engelbrecht J., Kemp J., Kleynhans W., Turnbull T. (2017) Detection of Sinkhole Precursors through SAR Interferometry: Radar and Geological Considerations. IEEE Geoscience and Remote Sensing Letters 14, 871–875. DOI: 10.1109/LGRS.2017.2684905
- Thierry P., Debeblia N., Bitri A. (2005) Geophysical and geological characterization of karst hazards in urban environments: application to Orléans (France). Bulletin of Engineering Geology and the Environment 64, 139–150. https://doi.org/10.1007/s10064-004-0247-4
- Valois R., Camerlynck C., Dhemaied A., Guerin R., Hovhannissian G., Plagnes V., Rejiba F., Robain H. (2011) Assessment of doline geometry using geophysics on the Quercy plateau karst (South France). Earth Surface Processes and Landforms 36, 1183–1192. https://doi.org/10.1002/esp.2144
- Verbovšek T. & Gabor L. (2019) Morphometric properties of dolines in Matarsko podolje, SW Slovenia. Environmental Earth Sciences 78, 1–16. https://doi.org/10.1007/s12665-019-8398-6
- Wall J., Bohnenstiehl D.R., Wegmann K.W., Levine N.S. (2017) Morphometric comparisons between automated and manual karst depression inventories in Apalachicola National Forest, Florida, and Mammoth Cave National Park, Kentucky, USA. Natural Hazards 85, 729–749. https://doi.org/10.1007/s11069-016-2600-x
- Waltham A.C. & Fookes P.G. (2003) Engineering classification of karst ground conditions. Quarterly Journal of Engineering Geology and Hydrogeology 36, 101–118. https://doi.org/10.1144/1470-9236/2002-33
- Waltham T., Bell F., Culshaw M. (2005) Sinkholes and Subsidence. Springer, Chichester. https://doi.org/10.1007/b138363
- Wightman M.J. & Zisman E.D. (2008) The selection and application of geophysical test methods in West Central Florida karst regions. In L.B. Yuhr, E.C. Alexander, & B.F. Beck (Eds.), Proceedings of the Eleventh Multidisciplinary Conference on Sinkholes

and the Engineering and Environmental Impacts of Karst (pp. 81–90). Reston, VA: American Society of Civil Engineers. https://doi.org/10.1061/41003(327)9

- Williams P.W. (1972) Morphometric Analysis of Polygonal Karst in New Guinea. Geological Society of America Bulletin, 83, 761-796. https://doi.org/10.1130/0016-7606(1972)83[761:MAOPKI]2.0.CO;2
- Wust-Bloch G.H. & Joswig M. (2006) Pre-collapse identification of sinkholes in unconsolidated media at Dead Sea area by 'nanoseismic monitoring' (graphical jackknife location of weak sources by few, low-SNR records). Geophysical Journal International 167, 3, 1220–1232, https://doi.org/10.1111/j.1365-246X.2006.03083.x
- Zhang G., Wang Z., Wang L., Chen Y., Wu Y., Ma D., Zhang K. (2019) Mechanism of collapse sinkholes induced by solution mining of salt formations and measures for prediction and prevention. Bulletin of Engineering Geology and the Environment 78, 1401–1415. https://doi.org/10.1007/s10064-017-1173-6
- Zhende G., Xiaozhen J., Ming G. (2013) A calibration test of karst collapse monitoring device by optical time domain reflectomewtry (BOTDR) technique. In L. Land, D.H. Doctor, J.B. Stephenson (Eds.), Sinkholes and the engineering and environmental impacts of karst (pp 71-77). Carlsbad, NM: National Cave and Karst Research Institute
- Zhou W., Beck B. F., Adams A.L. (2002) Effective electrode array in mapping karst hazards with electrical resistivity tomography. Environmental Geology 42, 922–928. https://doi.org/10.1007/s00254-002-0594-z
- Zhu J., Taylor T. P., Currens J.C., Crawford M.M. (2014) Improved karst sinkhole mapping in Kentucky using LIDAR techniques: A pilot study in Floyds Fork watershed. Journal of Cave and Karst Studies 76, 207–216. DOI:10.4311/2013ES0135
- Zhu J., Nolte A.M., Jacobs N., Ye M. (2020) Using machine learning to identify karst sinkholes from LiDAR- derived topographic depressions in the Bluegrass Region of Kentucky. Journal of Hydrology 588, 125049. https://doi.org/10.1016/j.jhydrol.2020.125049
- Zini L., Calligaris C., Forte E., Petronio L., Zavagno E., Boccali C., Cucchi F. (2015) A multidisciplinary approach in sinkhole analysis: The Quinis village case study (NE-Italy). Engineering Geology, 197, 132-144.
- Zumpano V., Pisano L., Parise M. (2019) An integrated framework to identify and analyze karst sinkholes. Geomorphology 332, 213–225. https://doi.org/10.1016/j.geomorph.2019.02.013
- WP/WLI (International Geotechnical Societies' UNESCO Working Party on World Landslide Inventory) (1993a) Multilingual landslide glossary. BiTech Publishers Ltd. ISBN 0-920 505-10-41993; 59 pp

- WP/WLI (International Geotechnical Societies' UNESCO Working Party on World Landslide Inventory) (1993b) A suggested method for describing the activity of a landslide, Bulletin International Association of Engineering Geology 47, 53-57

UNIVERSITÀ DEGLI STUDI DI TRIESTE

CHAPTER 3

TEST SITE AREAS

Mapping the boundaries of sinkholes and the areas affected by subsidences can be a challenging task and may be associated with a high degree of uncertainty (Gutiérrez et al., 2018) due to one or more of the following reasons:

(1) The geomorphic expression of sinkholes is often obliterated or subdued by anthropogenic filling, natural depositional and erosional processes;
(2) some of the sinkholes identified through bibliographic reports may no longer exist in the field, introducing uncertainty regarding the accuracy of their perimeter and position;
(3) some of the sinkholes identified through DTM analysis may be situated in inaccessible areas, leading to the classification of sinkhole type, state of activity and morphometric parameters as "undefined";
(4) the actual area affected by subsidence might be smaller than the topographic depressions suggest, owing to edges recession through erosion and the consequent expansion of the topographic basin;
(5) the area affected by ground settlement might surpass the apparent dimension of the sinkhole mapped on the basis of surface evidence.

In order to properly identify and outline these phenomena, an integrated and multiscale approach is essential, from the analyses of the satellite data down to the site-specific levelling.

During the PhD, a thorough study was conducted on different test sites to define the best methodology for characterizing these phenomena in the geolithological contexts present in the Friuli Venezia Giulia Region.

The first study was conducted in the village of Quinis (*Chapter 3.1*), located in the municipality of Enemonzo, where, thanks to previous study carried out by the researchers of the Department of Mathematics and Geosciences, there is abundance of data.

New geophysical investigations were conducted with the purpose of data comparison, such as 3D GPR (Ground Penetrating Radar). The results were encouraging, highlighting not only the 3D shape of some subsurface features, but also their evolution over time. In-depth geophysical investigations (Electrical resistivity tomography, electomagnetometer, refraction seismic etc.) were carried out also in correspondence of Baus, a hamlet of Ovaro (UD) (*Chapter 3.2*). The synergical approach of using different types of investigations highlighted the importance of monitoring these elusive phenomena over time to avoid disasters, such as the one that occurred in 2017 when a collapse sinkhole blocked part of the regional state road.

The area of Quinis is prone to sinkholes due to significant fluctuations in the groundwater level in an evaporitic environment. So, a detailed investigation was further conducted (*Chapter 3.3*) with the aim of evaluating the dissolution rate by equipping the piezometers with gypsum rock samples. After one year of observations (*Chapter 3.4*), some samples were almost completely dissolved, with a dissolution rate almost eight times higher than expected if compared to the available literature data (0.68 – 1.14 mm/y, Klimchouk et al., 1996 and 0.4 – 1.0 mm/y, Cucchi et al., 1998).

To better understand this fast dissolution rate, a six-month laboratory experiment was carried out (*Chapter 3.5*), which highlighted the importance of the Saturation Index in the dissolution process concerning groundwater recharge.

CHAPTER 3.1

Paper published in Remote Sensing 2020, 12, 3814

doi:10.3390/rs12223814

Non-Invasive Methodological Approach to Detect and Characterize High-Risk Sinkholes in Urban Cover Evaporite Karst: Integrated Reflection Seismics, PS-InSAR, Leveling, 3D-GPR and Ancillary Data. A NE Italian Case Study

Alice Busetti[1], Chiara Calligaris[1], Emanuele Forte[1], Giulia Areggi[1], Arianna Mocnik[2] and Luca Zini[1]

[1] Mathematical and Geosciences Department, University of Trieste, Via Weiss 2, 34128 Trieste, Italy
[2] Esplora Srl, Spin-Off University of Trieste, Via Weiss 1, 34128 Trieste, Italy

remote sensing

MDPI

Article

Non-Invasive Methodological Approach to Detect and Characterize High-Risk Sinkholes in Urban Cover Evaporite Karst: Integrated Reflection Seismics, PS-InSAR, Leveling, 3D-GPR and Ancillary Data. A NE Italian Case Study

Alice Busetti [1], Chiara Calligaris [1,*], Emanuele Forte [1], Giulia Areggi [1], Arianna Mocnik [2] and Luca Zini [1]

[1] Mathematical and Geosciences Department, University of Trieste, Via Weiss 2, 34128 Trieste, Italy; abusetti@units.it (A.B.); eforte@units.it (E.F.); giulia.areggi@phd.units.it (G.A.); zini@units.it (L.Z.)
[2] Esplora Srl, Spin-Off University of Trieste, Via Weiss 1, 34128 Trieste, Italy; arianna@esplorasrl.it
* Correspondence: calligar@units.it

Received: 22 October 2020; Accepted: 18 November 2020; Published: 20 November 2020

Abstract: Sinkholes linked to cover evaporite karst in urban environments still represent a challenge in terms of their clear identification and mapping considering the rehash and man-made structures. In the present research, we have proposed and tested a methodology to identify the subsiding features through an integrated and non-invasive multi-scale approach combining seismic reflection, PS-InSAR (PSI), leveling and full 3D Ground Penetrating Radar (GPR), and thus overpassing the limits of each method. The analysis was conducted in a small village in the Alta Val Tagliamento Valley (Friuli Venezia Giulia region, NE Italy). Here, sinkholes have been reported for a long time as well as the hazards linked to their presence. Within past years, several houses have been demolished and at present many of them are damaged. The PSI investigation allowed the identification of an area with higher vertical velocities; seismic reflection imagined the covered karst bedrock, identifying three depocenters; leveling data presented a downward displacement comparable with PSI results; 3D GPR, applied here for the first time in the study and characterization of sinkholes, defined shallow sinking features. Combining all the obtained results with accurate field observations, we identified and mapped the highest vulnerable zone.

Keywords: sinkhole; PSI; 3D-GPR; reflection seismics; leveling; evaporites; geo-hazard

1. Introduction

Several European regions are affected by ground subsidence phenomena due to the presence of highly soluble evaporite rocks. The dissolution of soluble rocks and deposits at the surface, or in the subsurface, combined with internal erosion and deformational processes can produce depressions named sinkholes or dolines that represent a severe geo-hazard, as has occurred, among others, in France [1], Germany [2], Lithuania [3], Russia [4], Spain [5,6], United Kingdom [7,8], Albania [9], USA [10], South Africa [11] and Italy [12–15].

Sinkholes mainly occur when the bedrock is a soluble rock, mainly carbonates and/or evaporites and in terms of geohazard, there are noteworthy differences between lithologies [16,17]. In fact, gypsum and halite have much lower mechanical strength and more ductile rheology than most carbonate rocks, and their solubility is definitively higher, so in evaporitic terrains, the process is typically much faster and sinkhole frequency is commonly higher ([18] and the references within). These features

can reach depths of tens of meters and diameters of more than hundreds of meters. The largest known collapse sinkhole is Xiaozhai Tiankeng in China, 662 m deep and reaching 119.3 million m^3 in volume [19]. Crveno Jezero in Croatia has a vertical extension of 528 m, including the 280 m deep lake at its bottom [20]. The sinkhole discovered in Malta is a circular to elliptical collapse structure up to 600 m in diameter and with an average area of 56,000 m^2 [21]. Italy is also affected by this type of geohazard [22–27], and the results of recent investigations have shown that Friuli Venezia Giulia region (here after noted as FVG) is one of the most affected areas in northern Italy [18] with 1199 sinkhole phenomena inventoried just considering the evaporate bedrocks [15]. Here, sinkholes are well-known natural phenomena and have been recognized since the end of the 1800s [18,28,29], as they represent a serious threat to man-made structures, such as buildings and roads [14].

Gypsum crops out in almost all Italian regions, over about 1% of the total national territory [13]. Since most of these evaporite outcrops are very small, more or less detailed studies on gypsum karst have been carried out in only a few regions as Piedmont, Friuli Venezia Giulia, Emilia-Romagna, Calabria, and Sicily. In detail, karst areas in FVG are very common [14,30–35], but only 1% of the karstifiable lithologies are represented by evaporites. These crop out along the Alta Val Tagliamento valley and along the northern alignment, encompassing Pesarina, Pontaiba and Lumiei valleys. The Alta Val Tagliamento valley (Figure 1) is the most affected with hundreds of inventoried sinkholes [14]. Here, the combination of an intensively karstified evaporite bedrock, the presence of regional thrust, the high amount of annual rainfall (1600–2000 mm/y) and the large fluctuations of the water table (often greater than 10 m) seem to be responsible for the above-mentioned phenomena. One of the most notable sinkhole areas in the FVG is located in Quinis, a hamlet of the Enemonzo municipality (Figure 1).

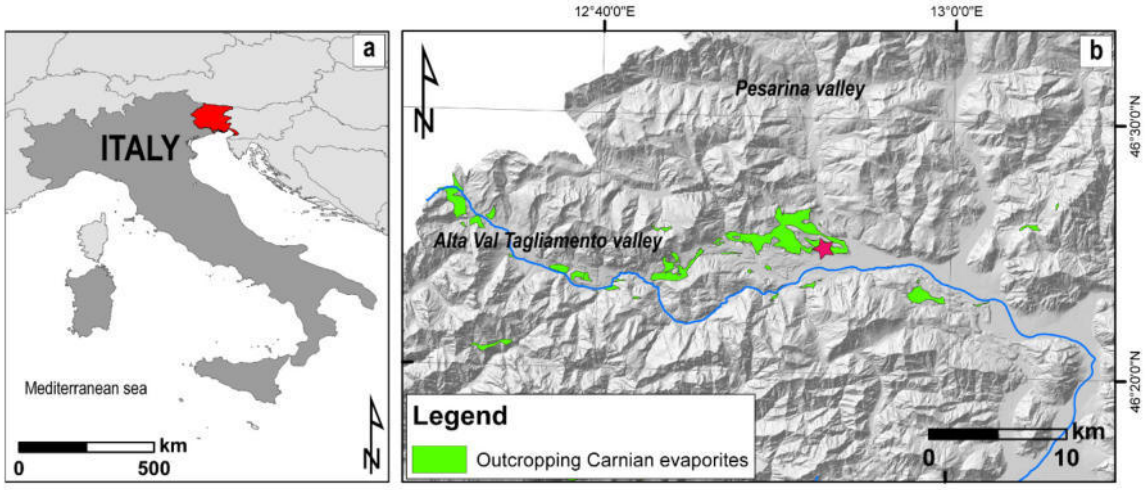

Figure 1. (**a**) Study area location. In red, the Friuli Venezia Giulia region (FVG); (**b**) focus on the Carnian evaporite outcrops (in green) at the NW side of the FVG, mainly within the Alta Val Tagliamento valley. In blue, the Tagliamento River. The red star is placed on Quinis hamlet.

Even in a small place such as Quinis, the identification and precise mapping of sinkholes are difficult tasks. The detection and adequate characterization of sinkholes and potentially unstable ground commonly require the application of multiple surface and subsurface investigation methods. Gutiérrez et al. [36] have described some of them: aerial and satellite images, topographic maps, field surveys, paleokarst analysis, subsidence damage maps, light detecting and ranging (LIDAR), synthetic aperture radar interferometry (InSAR), microseismicity, ground-based monitoring, hydrochemical modeling, speleological explorations, geophysical surveys, probing and drilling and trenching.

The most innovative methodological advances developed in recent years are related to the acquisition of interferometric SAR (InSAR) data that measure the displacement of the ground surface

using the phase difference between different radar acquisitions. In particular, the use of time series InSAR methods such as Persistent Scatterer Interferometry (PSI) provides deformation time series maps including retrospective analyses.

Remote sensing techniques contribute to the field of sinkhole hazard assessment by providing tools to implement sinkhole inventories and lending themselves to the monitoring of precursory deformations prior to sinkhole development [37].

These investigation techniques have been applied in various regions across the world (Figure 2). In general, they are particularly efficient in urban areas where Persistent Scatterers (PSs) can be easily recognized. However, PSs by themselves cannot be considered sufficient to outline subsidence areas, especially at large scales. Moreover, the effects of human activities and the low density of man-made buildings and infrastructures (i.e., vegetated areas) can significantly affect the final results. In these cases, the integration with different techniques such as field surveys, geophysical investigations and topographic monitoring is required to properly identify and monitor the phenomena. Topographic analyses are the most suitable techniques to investigate small building and road movements with time, while Ground Penetrating Radar (GPR) is one of the most efficient and high resolution geophysical techniques to image the subsurface at different depths and with various detail levels [38–41]. In fact, GPR frequencies can be tailored as a function of the expected targets, with high spectral components being able to reach centimetric resolution with a limited depth range while, on the contrary, lower ones can penetrate deeper but the output has a lower overall resolution [38]. In the framework of the research presented in this paper, we collected a full 3D GPR survey (see Section 3.4 within the Materials and Methods section) which, to the best of our knowledge, represents the first example of an application reported in literature for sinkhole characterization, while 2D GPR profiles are quite common e.g., [6,18,42,43].

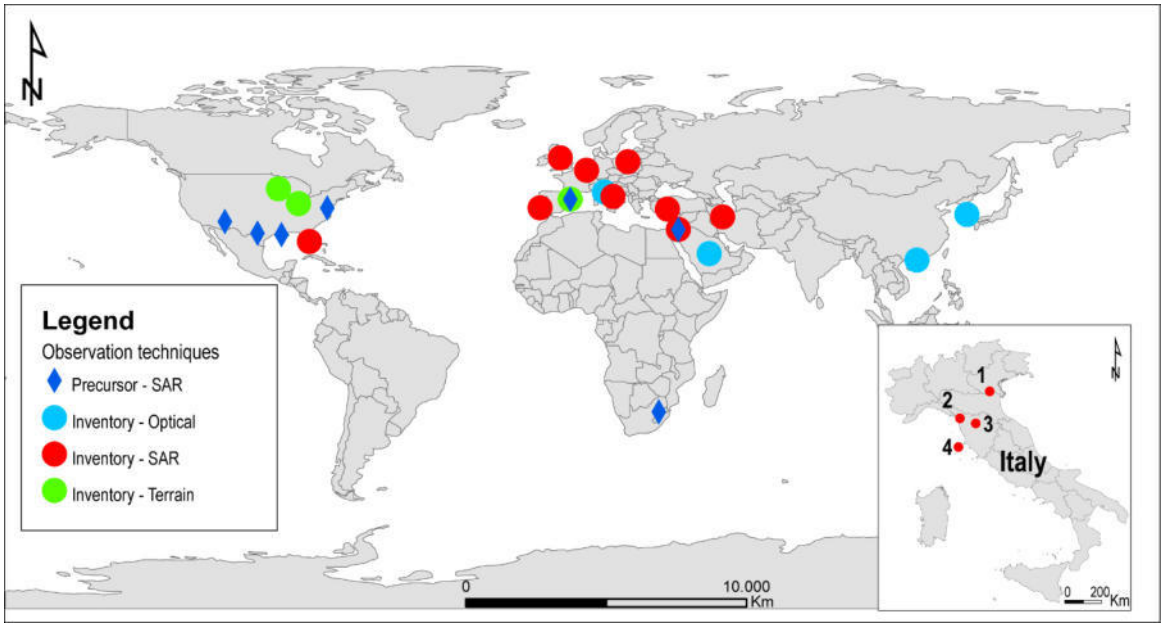

Figure 2. Observation techniques have been used worldwide for sinkhole precursor detection (blue rhombus) and sinkhole inventory using optical remote sensing (blue circles), remotely generated terrain models (green circles) and SAR techniques (red circles) [44–59]. The figure has been updated and modified only concerning the SAR part after Theron et al. 2018 [37]. In the box, SAR technique applied in the Italian territory to detect subsidence phenomena is shown: (1) Rovigo (Veneto region); (2) Camaiore (Tuscany region); (3) Prato (Tuscany region); (4) Elba island (Tuscany region).

In the present paper, the authors analyze the Alta Val Tagliamento Valley, focusing on the Quinis area where sinkholes have been reported since the beginning of the last century [60].

The valley is a good example of the geological context typical of mountain areas where an evaporitic bedrock is mantled by Quaternary deposits with variable thicknesses. This location was chosen as a test site to apply different techniques in order to better outline the most hazardous areas and also integrate PSI, which is applied for the first time to this topic in Italy in the evaporitic context, integrated with topographic leveling and integrated reflection seismic and 3D GPR, which also represents a novelty in such kind of investigations.

2. Study Area

The study area is located in the mountain sector of FVG, NE Italy, in the Alta Val Tagliamento Valley within the Enemonzo municipality, in the hamlet of Quinis. Some findings testify that Enemonzo is certainly one of the most ancient settlements and it has suffered from the presence of sinkholes for a long time. The occurrence of these phenomena is favored by the presence of Triassic evaporites, Carnian in age, in the entire valley floor (Figure 1). The evaporitic bedrock (Figure 3) does not outcrop extensively, it is mainly mantled by Quaternary deposits due to alluvial fan deposits that prograde over the fluvial terraces of the Tagliamento River (Figure 4). The evaporites go under the Raibl Formation and, according to the available literature [61] (Figure 4), are subdivided into three different members, which can be described as follows from the bottom to the top:

- *Red shales member* (RBA1) with a thickness between 80 and 100 m, characterized by red shales and siltstones typical of a fluvial environment close to the coast;
- *Gypsum and grey dolostones member* (RBA2) characterized by a thickness of 350 m; it is primarily composed by grey and white saccharoid gypsum with marl inclusions at the top (Figure 3), yellowish dolomitic marls, and to a lesser extent, blackish or greenish clays and dark limestone in thin layers;
- *Marls and dolostones member* (RBA3) with a thickness of 180 m; it is characterized by grey dolostones often vacuolar and cataclastic, marls and multicolor clays close the depositional sequence.

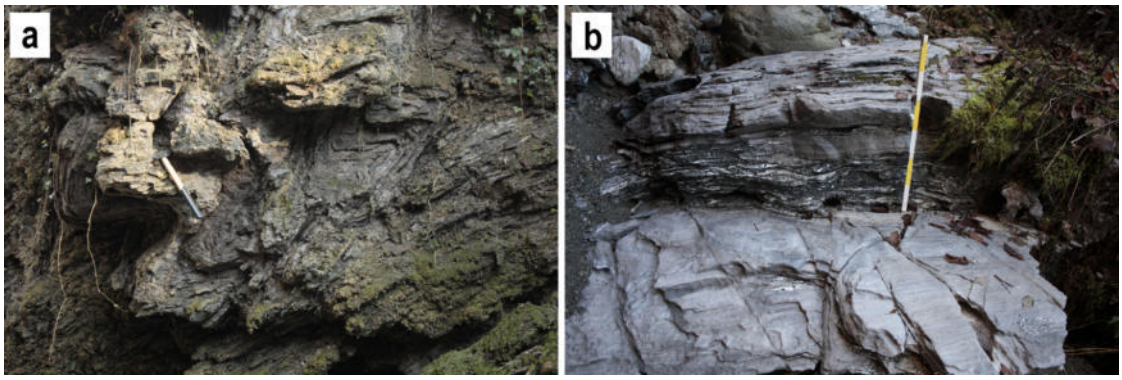

Figure 3. Evaporites outcrop in the hilly areas north of Quinis village. (**a**) Small folds highlighting the plasticity of the lithology; (**b**) intercalations of thin layered gypsum within carbonate clayey silt.

Thanks to the 25 boreholes that were drilled between 2005 and 2013, and to the previously acquired geophysical data, a conceptual model of the area has been already hypothesized [18]. It highlights the presence of Quaternary deposits as glacial till, alluvial and colluvial levels over an evaporitic bedrock. The complexity of the depositional pattern reflects on the heterogeneity. The thickness is variable from north to south of the study area (Figure 4). To the North, it is approximately a few meters and deepens moving towards the South up to more than 60 m in correspondence with the Tagliamento River terraces. The alluvial deposits consist of highly permeable polygenic gravels, which include lenses of less pervious clay and clayey silt. Although the gravels are locally cemented, the geotechnical characteristics of the whole deposit are quite poor, with a high vertical and horizontal variability of the bearing capacity. In the most part of the boreholes, SPT (Standard Penetration Test) investigations have

been realized in correspondence with clay and clayey silt lenses. The SPT results go from a minimum of n SPT equal to 0 up to 18 with some voids up to 2 m wide identified while realizing the tests.

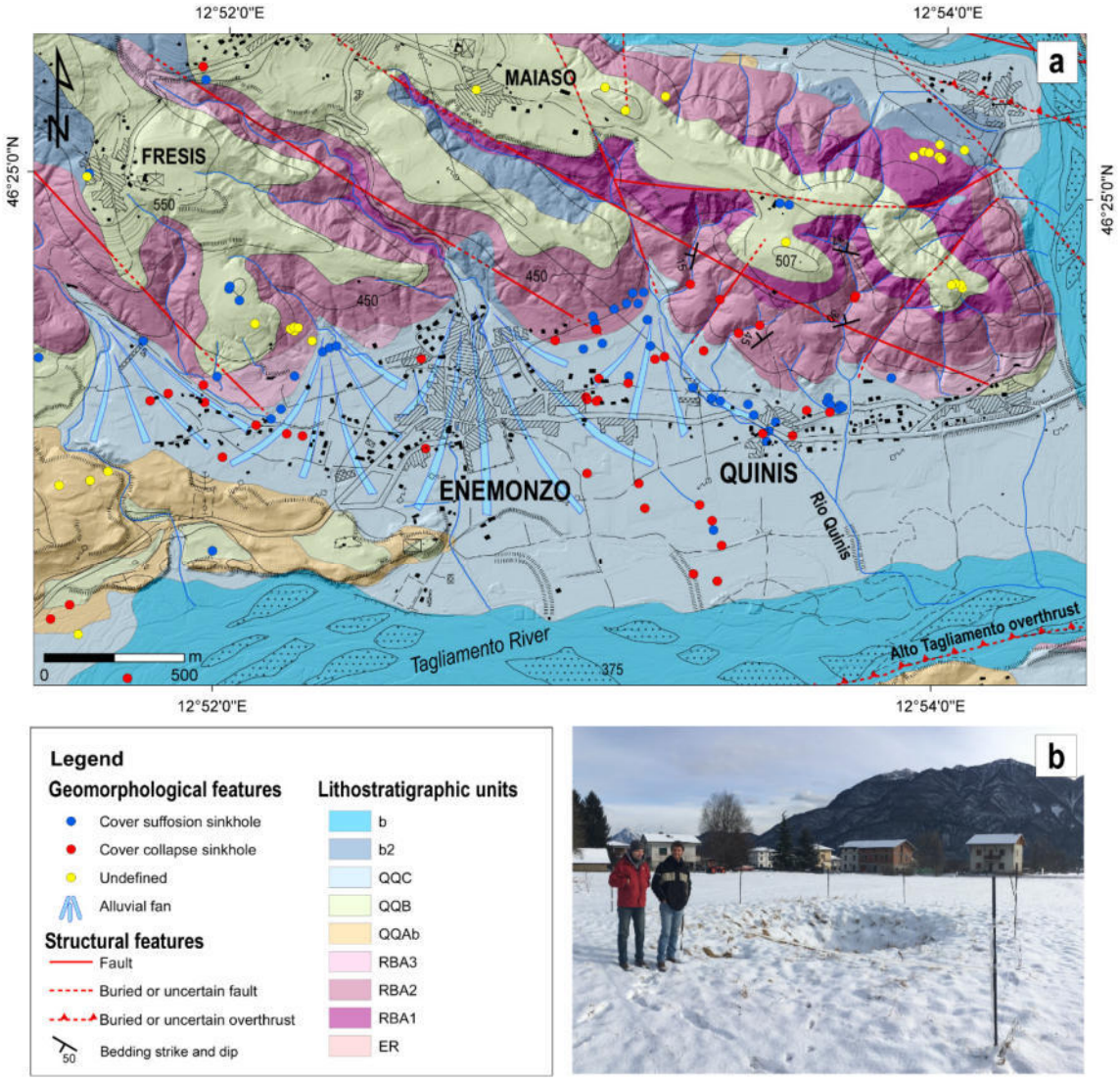

Figure 4. (**a**) Geological and geomorphological map of the study area (modified after [61]). Lithostratigraphic units: (**b**) actual alluvial deposits; (b2) eluvial-colluvial deposits; (QQC) fluvial gravel and sand; (QQB) glacial till; (QQAb) fluvial conglomerates. All these units are Pleistocene–Holocene in age. (RBA3) marls and dolostones member; (RBA2) gypsum and grey dolostones member; (RBA1) red shales member. RBA1, RBA2 and RBA3 belong to the Raibl Formation, Triassic in age. (ER) Siera group (Triassic age), mainly limestones and dolomitic limestones badly stratified, mainly massive. (**b**) One of the cover collapse sinkholes present in the area initially formed in 1977. It reactivated six months after the first collapse and in 2012. In 1985, few meters from where the phenomenon previously occurred, a new sinkhole appeared. Photo in (**b**) was taken in 2013.

From a structural point of view, the study area is characterized by the presence of several faults that are NW–SE oriented [62]. The EW Tagliamento Valley is controlled by the regional Alto Tagliamento line. This overthrust separates the "Alpi Tolmezzine" (northern sector) from the "Prealpi Carniche" (southern sector), resulting in the Raibl Formation in the hanging-wall overthrusting the Monticello Formation (in the S, out of the geological map presented in Figure 4). This structure, buried in the study area and recognizable only to the West, dips approximately 60° to NW [61].

The Quinis village area is characterized by the presence of an extensive phreatic aquifer with relevant water table fluctuations, fed by two contributions: the effective infiltrations from one side and the stream and river leakages from the other side. Stream leakages mainly influence the northern sector, while the Quinis torrent crosses the investigated area in the NE–SW direction. Tagliamento River leakages are instead more important in the southern portion of the area [15,18].

The groundwater flow is conditioned by the structural setting of the evaporitic bedrock and by the extreme heterogeneity of the Quaternary deposits. The aquifer system is very complex, and the water table has a rapid response to rainfall, in particular the water level fluctuations are large, with oscillations between 6 and 32 m. One of the main rainfall events recorded 248 mm of rain in 56 h (24–26 December 2013) with a consequent water table rise of 10 m and a maximum recorded velocity of 40 cm/h [18], witnessing a fast circulation of the groundwaters. This hydrogeological context and especially the wide and fast water table fluctuations have produced high karstification of the gypsum and grey dolostones member (RBA2).

Calligaris et al. [63] described the field experiment of placing rock evaporitic samples into piezometric tubes at different depths, demonstrating a dissolution rate of the evaporites up to 2.8 mm/y, almost three times greater than that expected if compared with the available literature data ([63] and in text references).

In between 1947–1948, Cosano [60], supervised by Professor. A. Desio in his thesis, described the area of Enemonzo-Quinis, observing its geostatical instability due to the presence of chalks in the bedrock.

Gortani, in 1965 [28], described an important cover collapse sinkhole that occurred in 1964 close to the Tagliamento River. After the catastrophic event in 1964, there has been an increment of the phenomena. Actually, six houses have been relocated due to their important damages. On the whole, in the municipality, there are 208 inventoried phenomena, of which 46 are cover suffosion sinkholes, 40 are cover collapse sinkholes and the remaining sinkholes have an undefined typology. They range in size from few tens of cm up to 75 m, reaching depths that are in the range from a few centimeters up to more than 15 m. Focusing just on the Quinis area, 32 phenomena were recognized (Figure 4), some of them are actually quiescent, but some others are active and continue to evolve, causing important damages to the infrastructure (Figure 5).

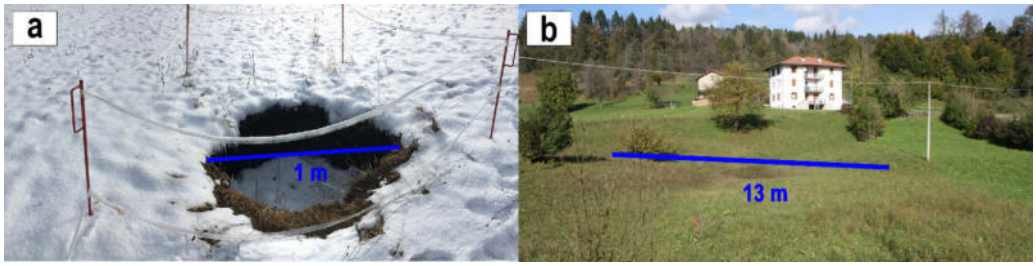

Figure 5. Two sinkholes recognized in the area. (**a**) Cover collapse sinkhole occurred close to the Rio Quinis riverbed. The hole, after the occurrence, has been promptly replenished from the land owner with loose material (about 2 m^3) (photo acquired in 2017); (**b**) historical cover suffusion sinkhole, which transforms to an ephemeral lake when it rains (photo taken in 2015).

3. Materials and Methods

Here, we individually introduce the methods adopted in this study, ideally with increasing resolution level, but we remark that they have to be compared, combined and integrated in order to obtain more constrained and cross-validated results.

3.1. Reflection Seismics

Reflection seismics is a mature geophysical technique applied worldwide both onshore and offshore for many different applications and at various scales. One of the most important objectives is

finding and characterizing hydrocarbon reservoirs [64]. The general principle is based on sending artificially generated seismic waves into the subsurface where the different structures and lithologies reflect back a portion of the transmitted energy as a function of the acoustic impedance contrasts. The reflected energy is then recorded at the surface by dedicated sensors having 2D or 3D geometries. Recorded data have to be properly processed and analyzed, often with sophisticated algorithms [65], obtaining a visual representation of the geological structures down to the depth of kilometers and reaching a resolution of tens of meters. Ultra-high-resolution surveys are also possible for shallower depths and for engineering or shallow geology studies. Here, we remark that reflection seismics is totally different from refraction seismics, as far as their physical bases, the data processing, and the expected results. Reflection seismics have been used for a long time for sinkhole-related issues, usually to give a general overview of the geology of the area prone to subsidence. In particular, there are examples focusing on the failure of anthropic infrastructures [66], on ground deformations induced by mining activities [67] and on sinking in urban areas [68], as well as exploiting shear waves [69].

In this paper, we collected some 2D reflection seismic profiles by using a Geode (Geometrics) seismograph connected to up to 48 channels in order to get information in the first hundred meters below the topographic surface. As a seismic source, we used a 5 kg sledgehammer, which provided enough energy for the objective of the work. After some preliminary tests (walkaway test) to evaluate the best acquisition geometry and parameters, we set the survey parameters as reported in Table 1.

Table 1. Acquisition parameters of the reflection seismics' profiles.

Channel Number	***up to 48***
Channel distance [m]	***2***
Shot interval [m]	***2***
Minimum Offset [m]	***1***
Maximum Offset [m]	***94***
Vertical stacking	***4***
Trace length [s]	***1***
Sampling interval [ms]	***0.25***

Both geophones and shot point positions have been recorded by using an RTK GPS, obtaining centimetric and decimetric accuracy in latitude/longitude, and elevation, respectively. Processing flow is summarized in Table 2. Additional algorithms (coherency filters and deconvolution) have been applied on specific subsets of the data characterized by poor overall continuity and low signal-to-noise ratio. Migration was not applied due to the limited dip of seismic reflectors and because diffractions were used as an additional aid to highlight lateral variations. In order to improve the seismic velocity field reliability, we applied, in addition to the standard velocity analysis, the common reflection surface (CRS) approach. The whole data processing and analysis were performed by using Seispace ProMAX suite (Landmark, Halliburton).

Table 2. Processing flow applied to reflection seismics' profiles.

Data Editing
Geometry assignment and sorting
Static corrections
Coherent noise (ground roll) attenuation
Amplitude analysis and recovery
CMP velocity analysis and NMO correction
Stacking/weighted stack
Depth conversion

3.2. PS-InSAR

Interferometric data (PSI) provide useful information about the surface deformation due to natural and/or anthropogenic phenomena. By exploiting the measure of the signal phase change between two radar images acquired with the same geometry in different time periods, it is possible to obtain maps of the ground displacement over time with respect to the satellite itself in the line-of-sight (LOS) [70–72].

In particular, time series InSAR methods are able to measure and monitor displacement over a given period of time with high accuracy by processing multiple interferograms derived from a stack of radar images. Among the time series InSAR techniques, Persistent Scatterer Interferometry (PSI) focuses on point-like coherent targets dominated by a single scatterer [73]. The scatterers, characterized by high phase stability, can usually be detected in urban areas due to the presence of many stable points such as man-made structures. The PSI approach is based on the processing of many interferometric data pairs derived by a stack of single-complex look (SLC) radar images and a common master image.

In this paper, we used SAR data acquired by the Italian COSMO-SkyMed satellite, characterized by high resolution microwaves in X band (wavelength 3.1 cm) and provided by the geological survey of the FVG in the framework of different research agreements between Trieste University and the survey itself. The used datasets, 3a_A in ascending orbit and 03a_D in descending orbit, span the period 18 February 2012–8 September 2016 and 1 January 2012–8 September 2016, respectively.

Data were initially processed by Planetek Italia S.r.l. for the area of interest of selecting the dataset and the master image (28 April 2014 master chosen for the ascending geometry; 30 July 2013 master chosen for the descending geometry). Then, the Stable Point Interferometry over Un-urbanized Areas (SPINUA algorithm implemented in Rheticus®) algorithm was applied [74]. On the obtained elaborated datasets (co-registered amplitude stack and differential interferograms stack), the algorithm selected the position of pixels with high temporal consistency, known as persistent scatterers (PSs). After the removal of the atmospheric artifacts and the correction of Digital Elevation Model (DEM) errors and terrain motion, the outcomes consisted of PS maps (in shape file format) with their relative information about position and displacement along the line-of-sight (LOS) [74]. In the end, the elaborated data, for every PS, contain the following information:

- An average velocity value (mm/y) referring to the displacement in LOS over the entire period of observation;
- An average velocity value (mm/y) referring to the displacement in LOS over each year;
- An estimated value of the cumulative displacement (mm);
- Standard deviation of the velocity with a mean value of 0.27 mm/y for the ascending dataset and 0.19 mm/y for the descending one.

Since the SAR data provided information about terrain motion with respect to the satellite along its LOS, we computed the vertical and the E-W velocity components by using data acquired in both ascending and descending satellite orbits.

We assumed a zero north contribution because of the lower sensitivity of the satellite to detect motion in the north component due to the near-polar satellite orbit [75].

A grid of 15 × 15 m was initially defined and, for each cell, the average velocity of the PSs was computed in the ascending and descending datasets (Δd_{asc} *and* Δd_{desc}). Then, considering the local incidence angle counted positive from the vertical (θ), and the azimuth of the satellite heading (positive clockwise from north) (φ), we calculated the deformation in E-W and vertical components by using the following formula [75–77]:

$$\begin{pmatrix} \Delta d_{asc} \\ \Delta d_{desc} \end{pmatrix} = \begin{pmatrix} -\cos\varphi_{asc}\sin\theta_{asc} & \sin\varphi_{asc}\sin\theta_{asc} & \cos\theta_{asc} \\ -\cos\varphi_{desc}\sin\theta_{desc} & \sin\varphi_{desc}\sin\theta_{desc} & \cos\theta_{desc} \end{pmatrix} \begin{pmatrix} \Delta_E \\ \Delta_U \end{pmatrix} \quad (1)$$

The values of the φ and θ angles are −12° and 27° for ascending track and −169° and 33° for descending track (as provided by Planetek).

3.3. Precise Geometric Leveling

In between October 2012 and August 2015, 9 leveling monitoring surveys (October 2012, January 2013, May 2013, August 2013, December 2013, April 2014, August 2014, December 2014, August 2015) on selected buildings were performed by a topographical technical study [78] using the DiNi precision level and the total station. Furthermore, 49 points were analyzed by placing 21 optical prisms (TA code) on the upper part of the buildings and 21 vertical landmarks (VB) code) at the base of the same buildings. As reference, 7 benchmarks were placed (initials v and cs in positions considered stable within the village (Figure 6).

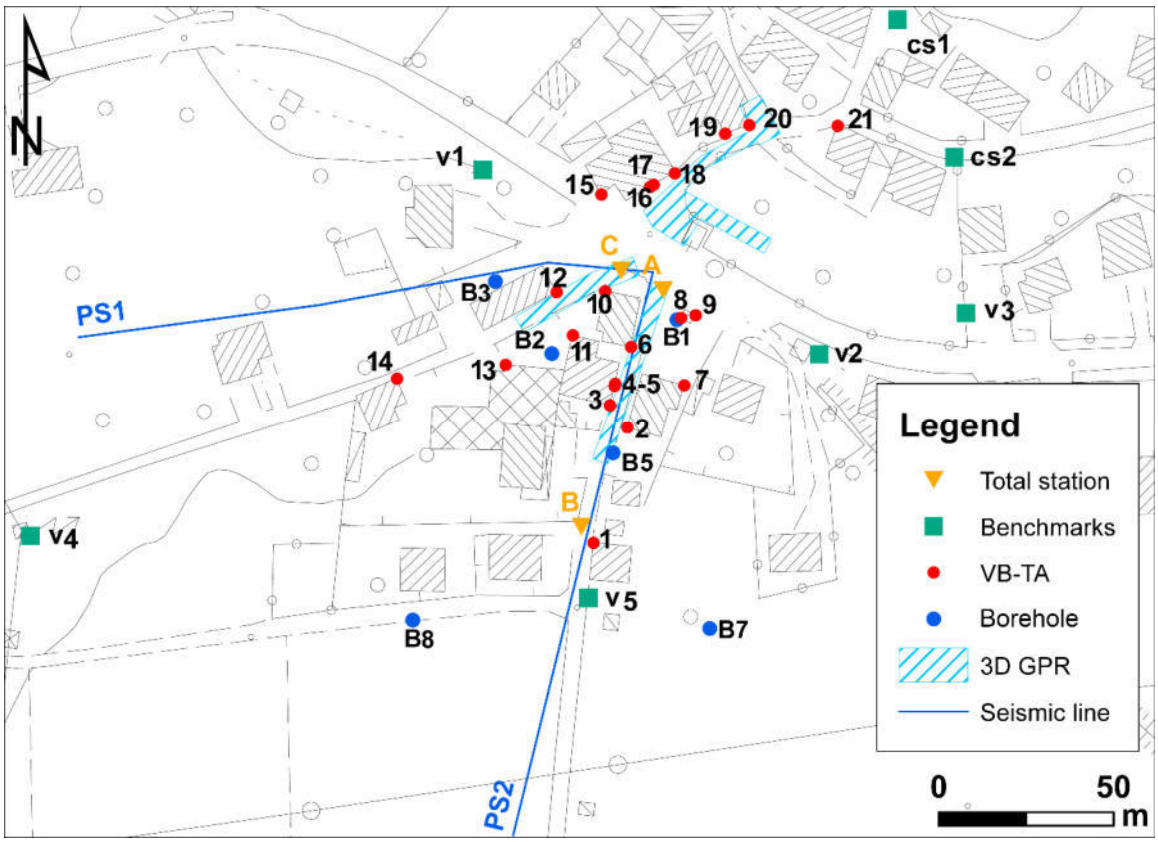

Figure 6. Location of direct and indirect measurements map: seismic lines (PS1 and PS2); benchmarks v1–v5 and cs1–cs2; B1–B8 boreholes; 1–21 leveling monitoring points; A, B, C total station monitored points; in pale blue—the area covered by the full 3D GPR survey.

In detail, precise geometric leveling measurements were carried out using the DiNi precision level with invar barcode stages, reaching an accuracy of 0.3 mm on all the vertical benchmarks (VB). The optical prisms (TA) are detected through total station measurements with TRIMBLE 5601and TRIMBLE S6 robotic total stations, having a precision equal to 2 and 3 mm, respectively.

Leveling data are used to define the vertical movements and are considered reliable to the tenth of a millimeter. The values obtained with the total station are not used for the computation of the quote. With the latter instrument, horizontal movements, along the coordinates E and N, are considered valid if greater than 2 mm.

3.4. 3D GPR

One of the main issues of GPR applications for sinkhole-related studies is the extreme spatial variability, which requires dense surveys. In the last few years, there is an array of GPR equipment on the market, which are able to collect actual 3D GPR data volumes faster e.g., [79,80]. In fact, with single channel (i.e., classical bistatic) GPR equipment, only 2.5D surveys can be collected [81]. Moreover, while until now the new 3D systems were applied mainly for archaeological applications [82,83], for pipe and tree root detections [84] and for pavement assessments [85], geological applications are less common and limited to the detection and imaging of faults and fractures [86,87]. Moreover, the last type of applications are actually very dense 2.5D surveys collected with traditional GPR equipment rather than with antenna arrays due to logistical constraints related to the large dimensions and heaviness of multichannel systems, which in turn make their application on rough surfaces difficult.

In this study, we used the 3D MiniMIRA array GPR (Malå Geoscience) equipped with 5 transmitting and 4 receiving 400 MHz shielded antennas, allowing the collection of 8 parallel profiles with a constant distance equal to 8 cm. In order to optimize the spatial resolution, we set a trace spacing also equal to 8 cm to obtain a constant in-line and crossline coverage. The system is connected with an electromechanical odometer for triggering and with RTK GPS for accurate absolute positioning. All the registered data are then combined in a single project and processed with the dedicated rSlicer software, as well as with an interpretation suite originally developed for reflection seismic data (Petrel, Schlumberger). By using these tools, it was also possible to calculate GPR attributes that further benefit from the full 3D geometry [88]. Details on the application of attributes to GPR data are beyond the purposes of this paper and can be found in [81,89].

4. Results

4.1. Reflection Seismics

The good overall quality of seismic data allowed the investigation down to a depth of at least 60 m, reaching a resolution of a few meters. Figures 7 and 8 report two almost perpendicular profiles, representative of the entire study area (Figure 6). The seismic interpretation was helped and validated by the stratigraphy of some boreholes drilled in the past in the area. In detail, the top of the evaporitic bedrock (TB) is clearly imaged along all profiles. It dips towards S with an irregular trend, locally showing abrupt changes in depth, such as, for instance, in correspondence with the white arrow in Figure 8. In the E-W profile (Figure 7), there are no clear trends but analyzing both the TB horizon and some other reflectors within the evaporites, we can highlight some depocenters characterized by local (about 20 m wide) deepening (white arrows). It is interesting to notice that, despite the intrinsic resolution limits of the method, both profiles show that the sinking is accommodated by the surface sedimentary layers, which are dipping less as they are closer to the topographic surface. By analyzing the P-wave interval velocities inferred from the integrated common midpoint (CMP) and common reflection surface (CRS) analyses (Figures 7b and 8b), the presence of the evaporites is clear due to their high velocity in comparison with the overlying sediments. Even more interesting is a local velocity inversion along the N-S profile (Figure 8), located where the sinking is more evident. This testifies that there are lenses and intercalations of materials with poor geotechnical properties, and thus further increasing the instability of the buildings and the overall risk of the area.

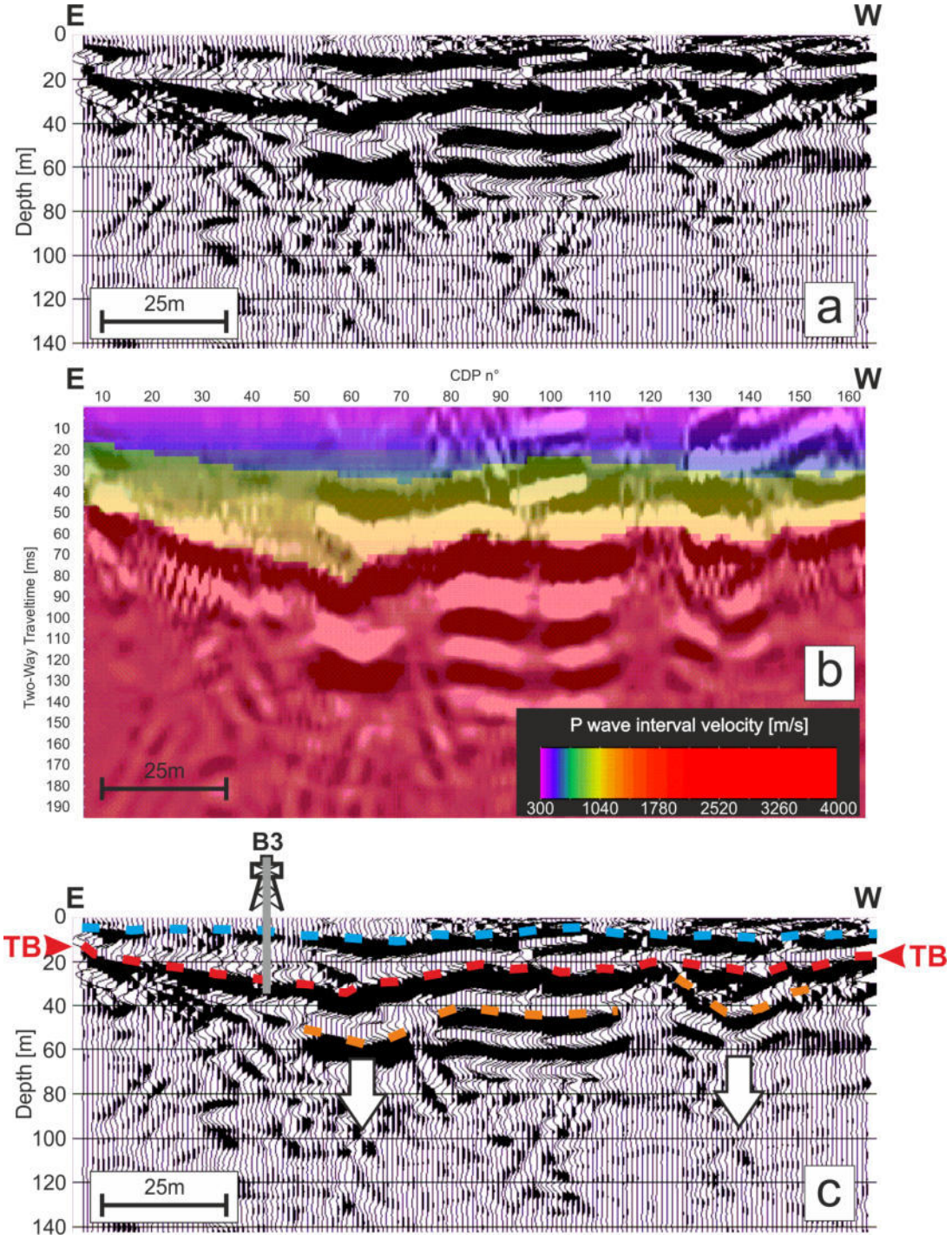

Figure 7. Reflection seismic profile PS1. (**a**) Processed depth converted profile; (**b**) Two-way traveltime (TWT) profile with the interval velocity superimposed; (**c**) interpreted depth converted profile. The red dashed line marks the top of the bedrock (TB), while light blue and orange lines highlight seismic horizons within the sediments and within the evaporites, respectively. The location and depth of borehole B3 used for validation are also provided.

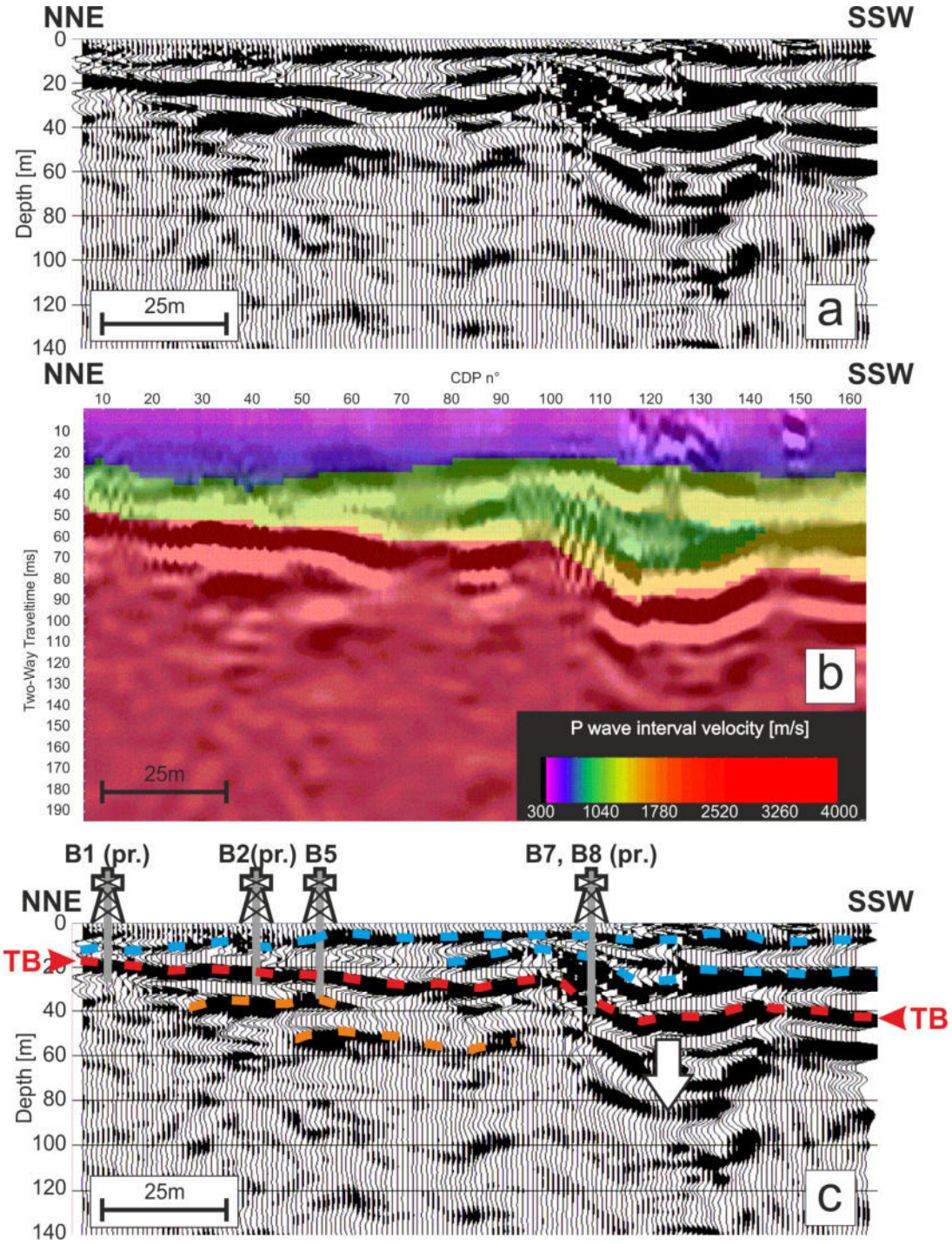

Figure 8. Reflection seismic profile PS1. (**a**) Processed depth converted profile; (**b**) TWT profile with the interval velocity superimposed; (**c**) interpreted depth converted profile. The red dashed line marks the top of the bedrock (TB), while light blue and orange lines highlight seismic horizons within the sediments and within the evaporites, respectively. While the arrow is located where the deformation reaches the maximum. The location and depth of boreholes B1, B2, B5, B7 and B8 used for validation are also provided (Figure 6).

4.2. PS-InSAR and Leveling

The analysis of a territory through a remote sensing approach allows the investigation of an area with a different perspective in addition to just the aerial view. In particular, PSI is considered to be one

of the most effective techniques to investigate subsiding areas based on the characteristics of the SAR instruments on the satellite. The satellite can acquire images during days and nights (active system) and in every meteorological condition thanks to the cloud-penetrating capability of the microwave band. The measure of changes in range distance of the target on the ground with respect to the satellite provides the measurement of centimetric/millimetric surface deformations of the terrain [72].

With this in mind, the interferometric data provided by the geological survey of the FVG region for the area of Enemonzo and Quinis have been analyzed. From both the ascending and descending datasets (Figure 9a,b), emerges an important mean displacement velocity especially in the Quinis hamlet, with values up to −6 mm/y. With the velocity values being negative in both geometries, we notice the presence of a vertical downward displacement, considering that a negative value represents a movement of the surface away from the satellite. This is not a surprise seeing that the area has been considered unstable since the early nineties when Cosano [60], in his master's degree thesis entitled "*Geological Analyses and Investigation of the Enemonzo Area (Carnia)*", highlighted the nature of the territory. Thanks to all the previous studies, it is understandable how the problem of subsidence in Quinis is historical, which goes beyond the construction methods of the buildings, the presence of heavy traffic on the state road and the activation of hydroelectric power plants along the Tagliamento River and its tributaries during the sixties, even if all these phenomena may have exacerbated the instability problems.

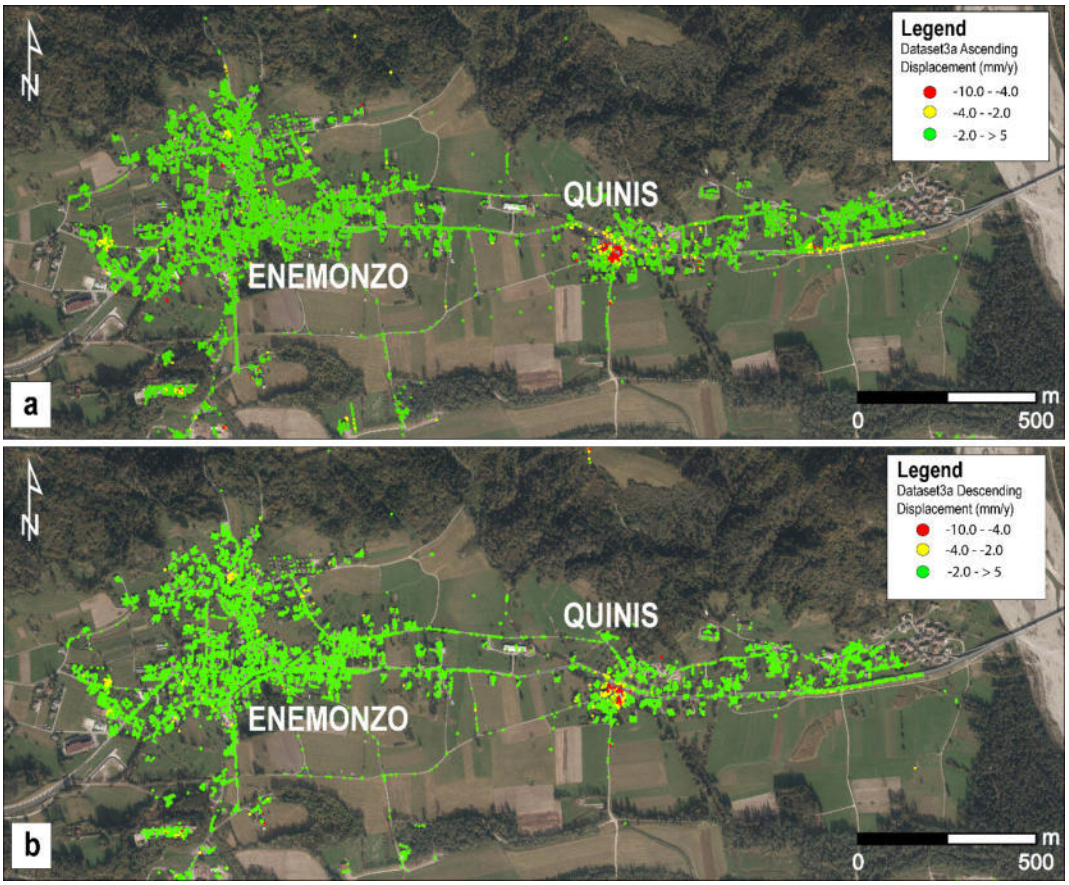

Figure 9. Average velocity of movement of the PS (mm/y) with reference to the entire observation period. The estimated velocity is projected along the line of sight of the satellite. (**a**) Ascending geometry (18 February 2012–08 September 2016); (**b**) descending geometry (01 January 2012–08 September 2016). In red, negative values highlighting high downward deformations; in green, positive values highlighting upward deformations and stable zones.

Despite the important studies funded initially by the civil defense and later by the geological survey of the FVG region, which has been realized in the area since 2009 by the researchers of the mathematics and geosciences department of Trieste University, it is actually difficult to outline the unstable areas. This is mainly due to the intrinsic lithological characteristics of the bedrock, which is heavily karstified and heterogeneous even in very close areas. In addition, even if we are in a mountainous area or in a small hamlet, the anthropic factor is important. Human actions tend to completely mask the geomorphological evidence of sinkhole activity. In sight of this, the interferometric approach, thanks to its coverage and high spatial resolution, represents a useful tool to investigate the study area, not only focusing in the center of Quinis where previous studies have highlighted the main criticisms, but enlarging the analysis to a wide portion of the Tagliamento Valley. To improve our investigation, we subdivided the area with grid size cells of 15 × 15 m. This value is surely larger than the achievable resolution, but it allows us to highlight the most significant and constrained subsidence zones. For each of them, we computed the average velocity in both orbit tracks (ascending and descending) and later, applying Equation (1), we calculated the average vertical and horizontal velocity components. Figure 10a summarizes the areas impacted by the vertical velocities, which are within the range from −6 up to +2 (mm/y).

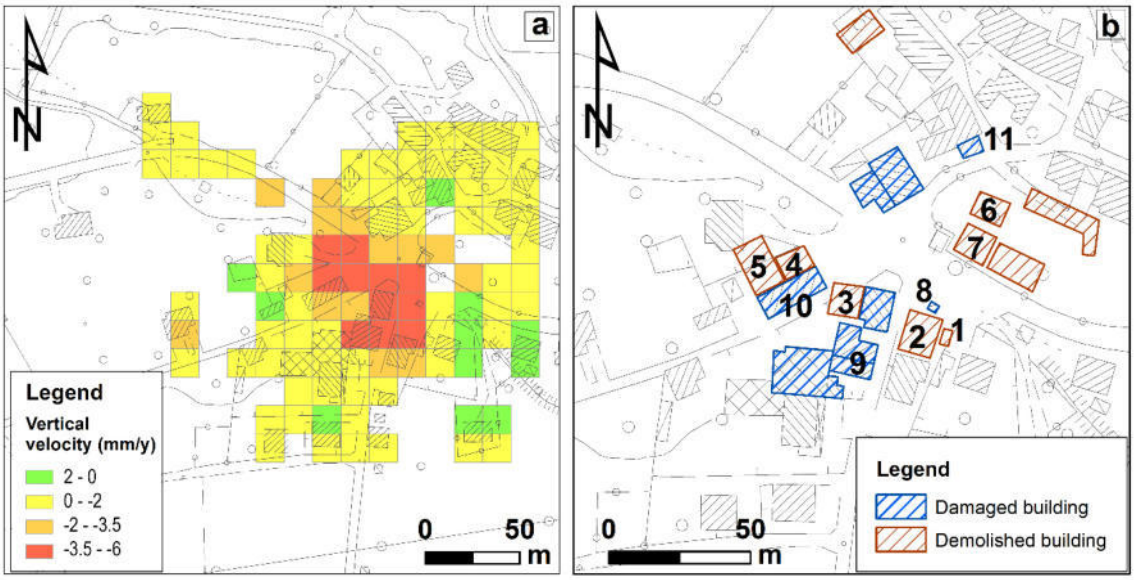

Figure 10. (**a**) Vertical velocities in mm/y computed using Equation (1) on the interferometric available data for the period 2012–2016; (**b**) demolished buildings (brown) and actually damaged houses (blue) in the central part of the study area. Numbers were assigned to the houses described further on in the text and in Figure 11.

Comparing the map with the demolished and damaged buildings highlighted in Figure 10b with the area where the downward vertical velocities are higher in Figure 10a, we can notice a very high correspondence. In fact, it is apparent that the buildings and infrastructures that, within recent years, had instability problems are concentrated in red/orange cells, and thus demonstrating that the present day deformations are mainly concentrated where they occurred in the recent past. Furthermore, we must consider that Quinis now appears different from the past in terms of the number of buildings, mostly as a consequence of the long term effects of subsidence and related damages.

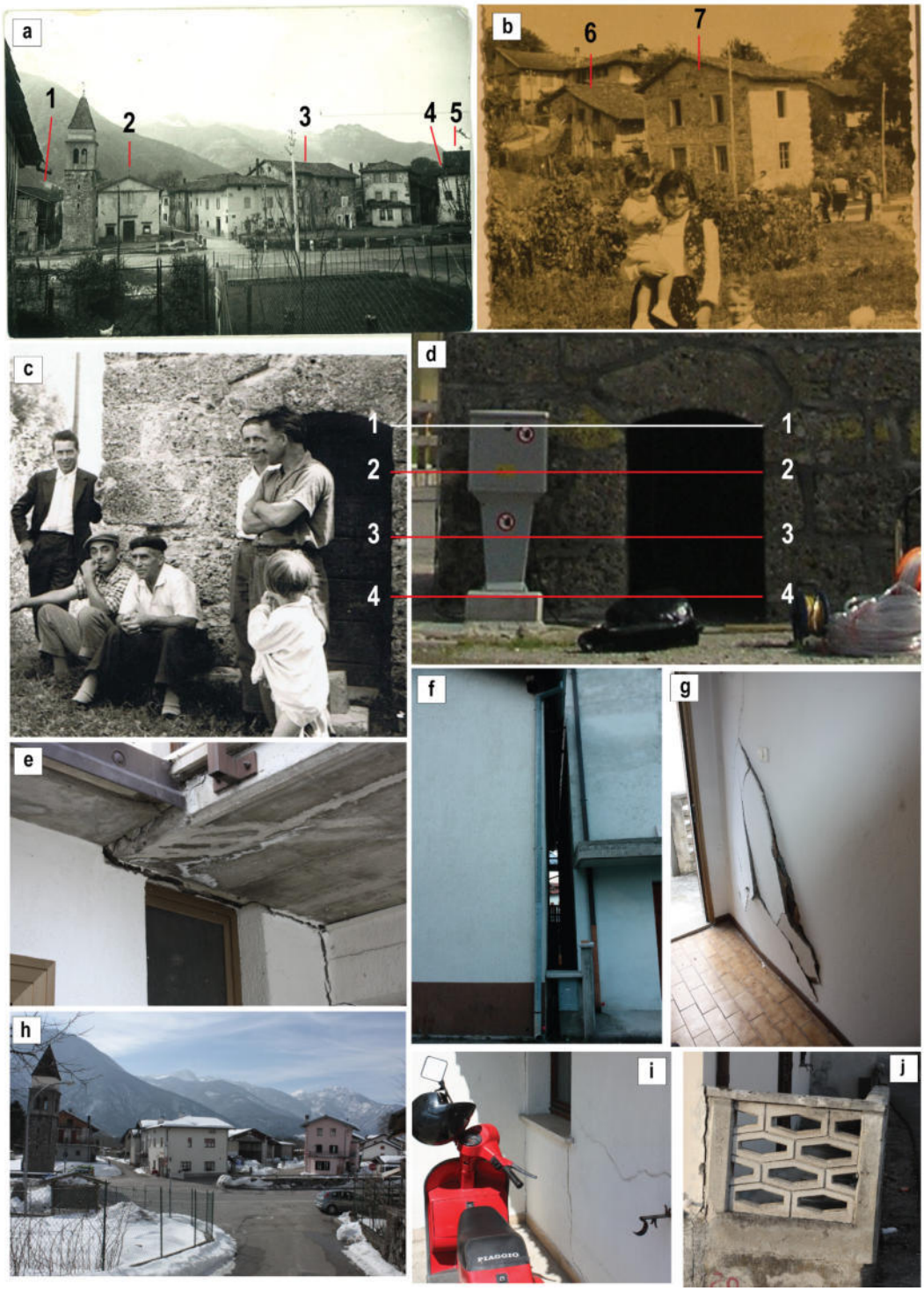

Figure 11. (**a**,**b**) Photos dated back to 1954, witnessing that the subsiding phenomena heavily affected the area in the past and their evolution has led to the demolition of some buildings; (**c**,**d**) the bell tower pictured in the sixties and nowadays, respectively. White lines join the same points on the two pictures, the red line highlights the subsidence of the structure; (**e**,**f**,**i**) report the fractures present on the walls and at the junction with another house noted as number 9 in Figure 10; picture f shows the convergence between two adjacent buildings; (**g**,**j**) damages on the internal wall of the house noted as 11 in Figure 10 and the external concrete fence is shown to be detached from the corner; (**h**) panoramic view where the bending of the bell tower and the white house is evident.

Thanks to the collaboration with the public administration and citizenship, several vintage pictures of the area were collected soon after Second World War, allowing the reconstruction of the housing settlement evolution [90]. Indeed, after the end of the war, several renewed buildings had to be demolished due to instability problems. Among these, the church, close to the bell tower (two in Figure 10b), the hayloft (one in Figure 10b), three buildings S of the main road and four to the N no longer exist (three, four and five and six and seven, respectively in Figure 10b). In the same area, other buildings are actually damaged (in red in Figure 10b). One of the most critical constructions is the bell tower. Comparing the photos of the 1960s with the current photos, it is possible to note the changes in inclination and its evident lowering (Figure 11c,d).

The building marked as nine in Figure 10 not only shows important cracks externally but also internally. When entering the house, the sensation of moving on an inclined plane is very impressive. The building is bending towards its neighbor (Figure 11f) and the inclination is so important that it is difficult to open or close some doors and windows.

The white house (Figure 11h) is bending and its normal use is compromised.

Overlapping the maps of the damaged buildings and the PSI surface displacement, it is possible to find a good correspondence. The only heavily damaged building, which seems to be stable according to the PSI data, is number 11 on Figure 10, but the many internal and external impressive cracks (Figure 11g,j) are irrefutable pieces of evidence of an important on-going movement, which is not apparent on PSI data, possibly because the building is linked with the neighboring building, which limits the overall downward movements. Therefore, the interferometric results were preliminary compared with information provided by the precise leveling campaign completed within the period from October 2012 to August 2015. The campaign was subdivided into nine different surveys performed by the topographical technical study [78]. Benchmarks were placed both at the bottom and at the top of selected buildings, which thus allowed confirmation of noticeable differential movements (Figure 12). In less than three years, data analyses of the bell tower showed a vertical lowering of 2.5 cm and a horizontal NW-displacement of more than 4 cm. The benchmark on building nine (Figure 10), in the same period, highlighted a progressive vertical lowering of about 2 cm and a horizontal E-displacement of 1.5 cm. The pink building (number 10 in Figure 10) showed an NNW horizontal displacement and a vertical lowering of about 2 cm. On the other hand, building number 11 in Figure 10, in three years, had irrelevant vertical and horizontal movements, possibly as a consequence of its connection with the neighboring building, as described above.

Analyzing the 3-year data and comparing the results obtained by combining the precise leveling technique and the interferometric approach, it emerges that the vertical lowering results are in the same order of magnitude and are almost similar, even if the two different techniques are totally independent from the other. In order to make a comparison, the horizontal displacement has been analyzed only in its E-W component (arrows in Figure 12).

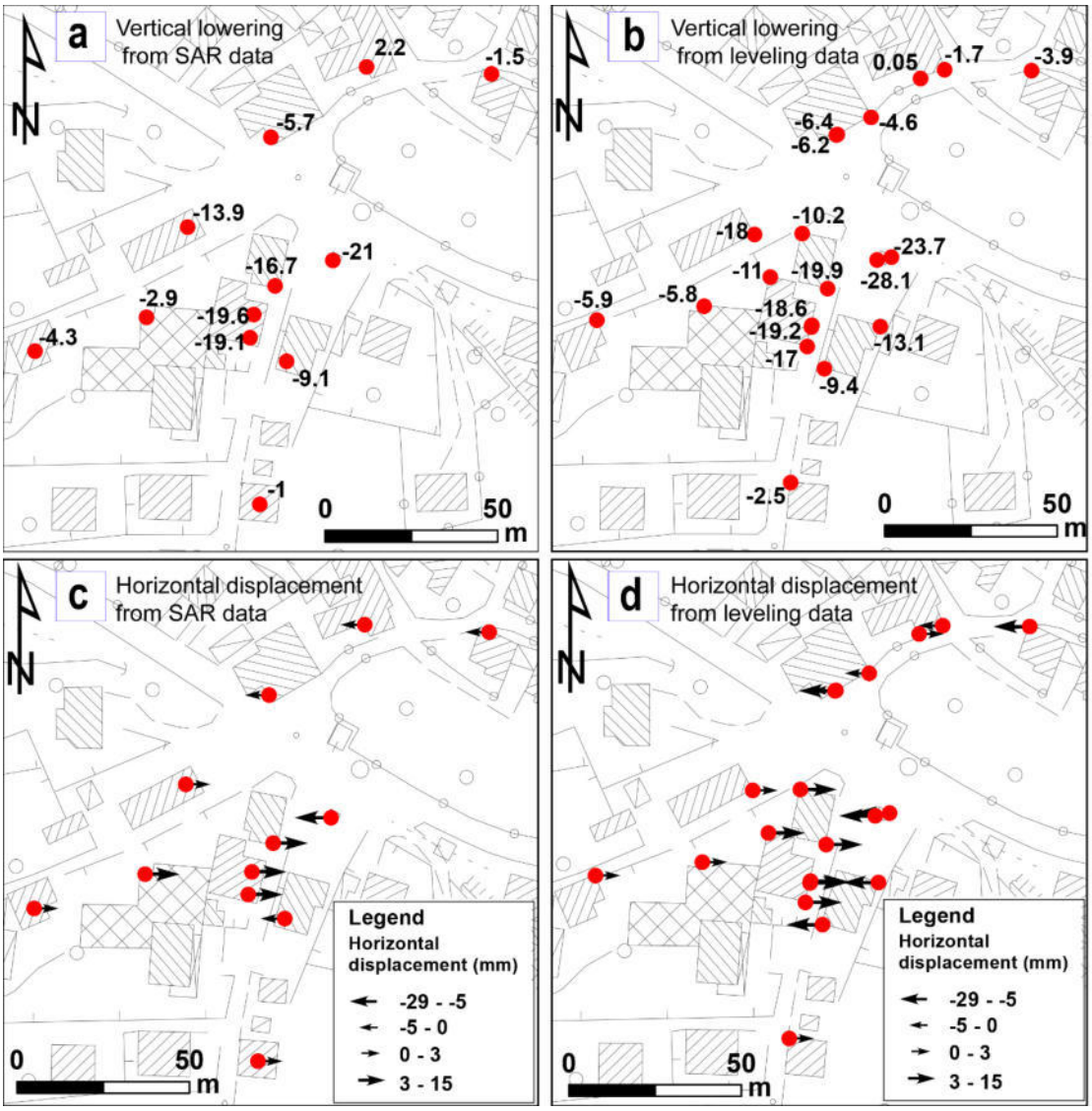

Figure 12. (**a**) Vertical lowering and (**c**) E-W horizontal displacement from interferometric data; (**b**) vertical lowering and (**d**) E-W horizontal displacement from precise leveling. All data are related to the period 2012–2015 and are in mm.

4.3. 3D GPR

In order to characterize the shallow subsurface in all the zones between the most damaged buildings and where the interferometric analysis showed the highest vertical and horizontal deformation rates, we collected a full 3D GPR dataset (Figure 6). At first, we analyzed single 2D profiles to understand if breaks and damages at the surface could be correlated with hidden structures. This correlation was apparent in several cases (e.g., Figure 13a); in fact, below some sub-horizontal reflectors attributable to the road pavements and its base, some sinking structures with different wideness were recognized (Figure 13). In this context, moving just a few meters apart, the shallow subsurface can be totally different with almost stable zones close to each other, characterized by severe sinking. As a consequence, the strong differential subsidence can emphasize the damage of the buildings. Unfortunately, by just considering 2D profiles, it is almost impossible to highlight the lateral limits of the sinkholes. In fact, even when the data are clear, it would be highly subjective to define which is the lateral border and its following areal path.

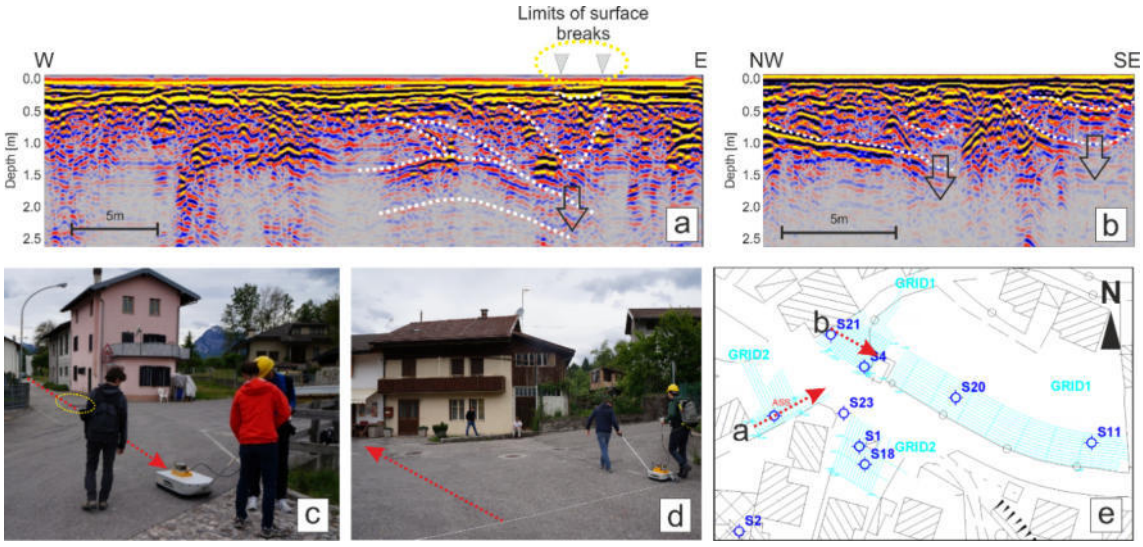

Figure 13. Exemplary 2D processed and interpreted 2D GPR profiles (**a**,**b**). On (**c**,**d**) photographs, the paths of profiles in (**a**,**b**) are highlighted, respectively. (**e**) Location map of the profiles in (**a**,**b**). Dotted white lines mark down-dipping layers related to the presence of sinkhole phenomena; black arrows are located where the deformation reaches the maximum; dotted yellow ellipses on (**a**,**c**) show the area where breaks at the surface are apparent.

We therefore considered the 3D depth volumes integrating 2D (in-line and crossline) visualization with depth slices and with any other arbitrary traced section (Figure 14).

The details of Figure 14b,c show that often the lateral continuity of the reflectors is low due to the pipes (P) and their related excavations or to local diffractions and reverberation effects of manholes. The analysis of amplitude or attribute depth slices can overcome such constraints, allowing the better imaging of the lateral limit of sinking areas, clearly discriminating the pipes and other coherent anthropic structures. Coherency attributes can further help this process as shown in the exemplary case of Figure 14a. In fact, while the original reflection amplitude has a range of values from negative to positive, coherency, as well as other attributes such as instantaneous or RMS amplitude, it can assume only positive values, making data interpretation and feature recognition easier and less subjective.

Furthermore, since the 3D dataset is georeferenced, it is straightforward to plot depth slices on topographic base maps, and/or integrating the geophysical data with any other information, including boreholes, displacement rates, geological data and so on.

Another interesting result is that even when several pipes and technological networks are present, the full 3D GPR dataset allows the highlighting and mapping of the sinking areas. As an example, in Figure 15, 0.50 m and 0.85 m depth slices are plotted on the topographic map of the study area. While at both depths several pipes are recognizable, two subsiding areas (labeled with letter D) are apparent and can be easily delimited. In detail, the northern one is not visible on the shallower slice because the large number of intersecting pipes probably obliterates such a feature, which is instead very clear on the deeper slice lying only 35 cm below the other one. We remark that during the GPR analysis and interpretation process, it is possible to continuously move from one slice to the other, which in the present case are separated by only about 1.5 cm, as a combined function of sampling interval and subsurface EM velocity.

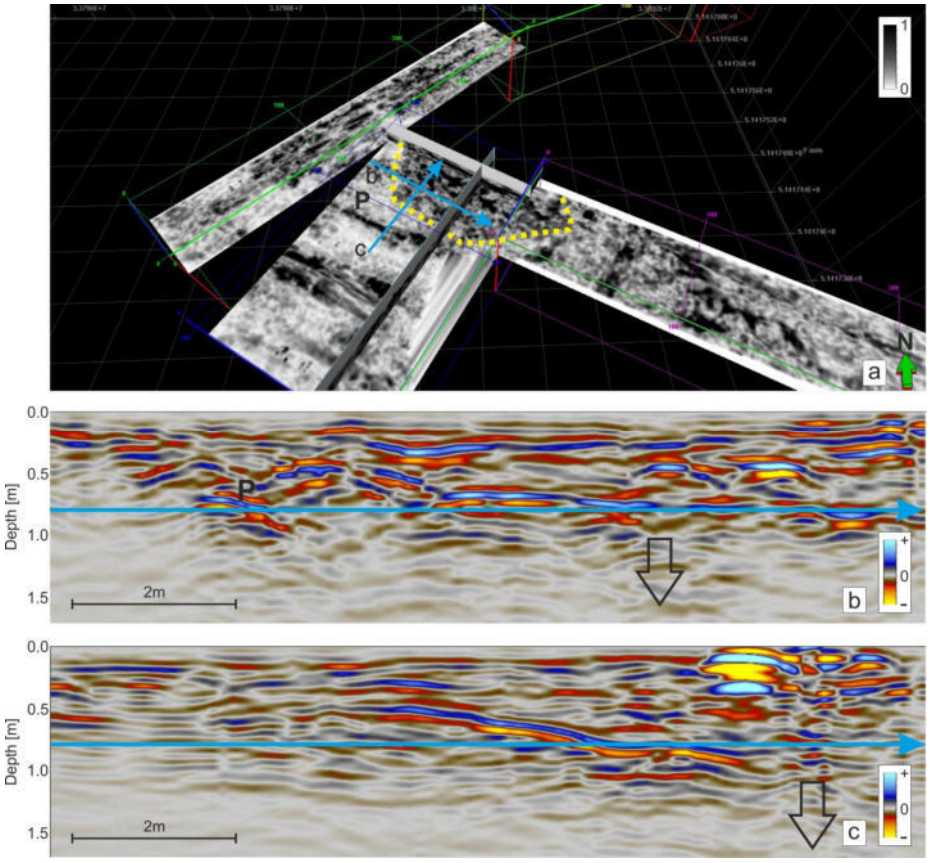

Figure 14. 3D GPR data analysis. (**a**) Perspective view of a portion of the GPR volumes with coherency depth slices at a depth equal to 0.8 m. The dotted yellow line marks the limit of a large depression, which is also imaged by the 2D perpendicular profiles (inline and crossline) in (**b**,**c**). Light blue lines show the location of shown profiles and the depth slice. The P label marks a clear pipe, while black arrows are located where the deformation reaches the maximum.

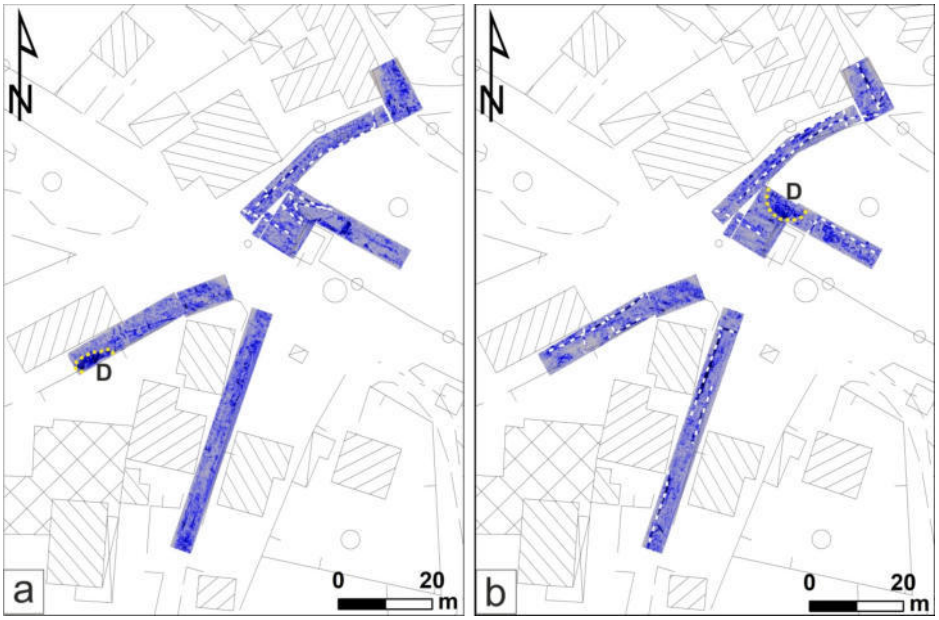

Figure 15. Exemplary 3D GPR depth slices at 0.50 (**a**) and 0.85 m (**b**). Yellow dashed lines mark main depocenters (D), while white lines mark some of the imaged pipes.

5. Discussion

The investigated area, despite being in a wide valley floor, has been known for instability problems since the 1940s. Due to the damage on the infrastructures, already visible in the past, several geological studies have been performed in the area, allowing the reconstruction of a preliminary geological model and to establish the phenomena causing such instabilities. However, being in a mantled karst environment, where roads and buildings cover the existing pieces of geomorphological evidence, the classical approaches or similar approaches, as proposed in the recent paper by Sevil et al. (2020) [6], do not allow very precise outlining and mapping of the single phenomenon, which involves specific infrastructures. The approach used in the area encompassed different multi-scale complementary methods, which allows the investigation of the subsurface of urbanized areas and represents both a novelty and a strength in the research being applied here for the first time. In particular, a multi-scale and multidisciplinary approach is essential to quantitatively evaluate and map the zones that are most vulnerable to sinking phenomena, while also highlighting areas that are still not affected by apparent deformations.

Thanks to reflection seismics, we highlighted the deepening of the evaporitic karstified bedrock towards S, which reaches the study area depths exceeding 60 m. Moreover, we imaged an irregular topography of the bedrock, probably linked to deep karst phenomena and the sinking accommodation by the surface sedimentary layers. This complex situation is not apparent on the surface, mainly due to the anthropic rehash and the presence of the buildings. At a totally different scale and resolution level, 3D GPR provides details about the shallow subsurface morphology showing local depocenters, which are not always linked to seismic reflections, due to the limited penetration depth of GPR technique.

With the PSI approach, we can extend the analyses identifying and mapping the areas where the geostatical criticisms are present to where further investigations should be focused on. From the study of the PSI data in the area of the Enemonzo municipality, emerged the presence of a zone where the velocities of deformation were higher (the Quinis area). Focusing on the latter, the data processing allowed us to be able to calculate the downward and horizontal displacements in the period between 2012 and 2016, identifying a portion of the territory where the sinking phenomenon is active and perceptible on the surface thanks to the damage to several buildings. For the interferometric analyses, we used the above-mentioned period because we had a set of precise leveling data of the damaged houses for the same time range available. Of course, it would be desirable to work with longer datasets, but the aim of this study is to compare results obtained using different sets of data collected with different methods, proposing an integrated multi-scale approach. Therefore, even with the two different analyses obtained with the independent PSI and leveling techniques, the obtained results are impressively coherent, validating the quality and the reliability of both methods. The spatial and temporal resolution of the deformation data acquired by the PSI are frequently not accurate enough for capturing active sinkholes of reduced size and/or characterized by catastrophic collapse. In this case, the characteristics of the movements allow the presented approach to be able to identify just the areas where the velocities are higher. Nonetheless, the use of satellite missions capable of acquiring radar data with much shorter revisit time and higher spatial resolution (such as COSMO-SkyMed) will significantly contribute to reduce these constraints, allowing the better identification of these kinds of phenomena. One of the limits of the leveling approach is that we can precisely define the movement of a single point, but to outline a moving area, it is necessary to test several points, which is a time- and logistically-consuming approach. With the PSI, it is instead possible to delineate the area involved in subsidence phenomena, especially in urban zones where the presence of targets such as buildings, monuments or pylons allows an excellent coverage of the persistent scatterers (PSs). Where PSs are not present, as in cultivated fields and in vegetated areas, the full 3D GPR method can be a helpful alternative. Usually, it is applied for investigations different to sinkhole detection, but this new method provides excellent results especially if used in flat and relatively wide areas, such as on roads or grasslands. The depth of investigation is usually not high (approximately maximum 2 m in

the present case), but the high resolution allowed the clear detection of two mantled subsiding features, which also fall in the area identified by the PSI data as a high sinking zone.

In an anthropized area, we found that local minor damages (such as breaks and fissures of the road pavement, sidewalks and containment walls) can also be directly related to local sinking effects (Figure 16). This is not always clear at a first glance or just by speaking with the citizens, because similar phenomena in other contexts are due to pipe breaks, seasonal freezing or dilatational effects, or are a consequence of roots growth and so on. Therefore, an integrated and multi-scale approach is mandatory in order to cross validate the results obtained by different techniques and observations and to highlight phenomena that cannot be made visible by using just one or a few methodologies.

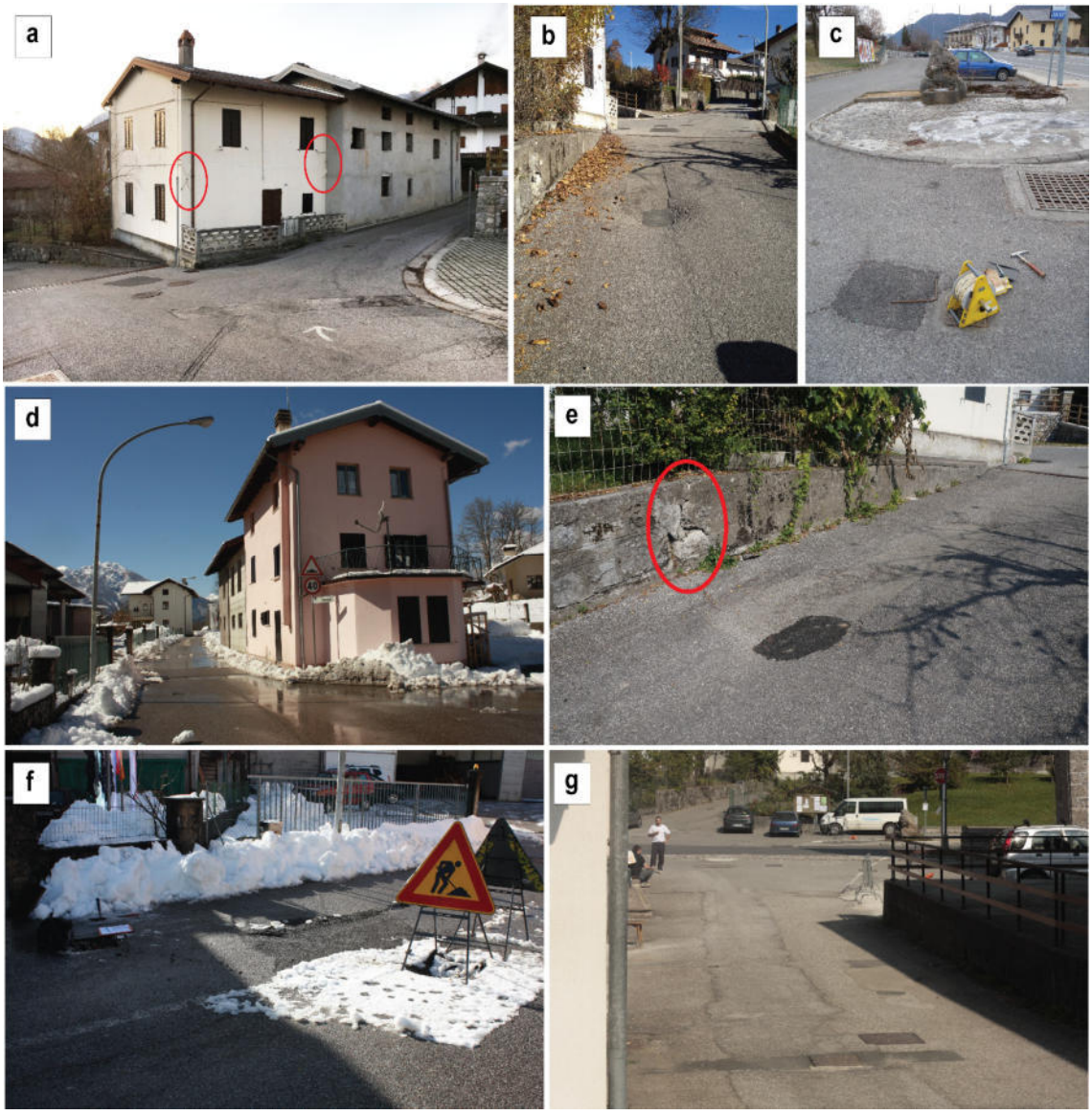

Figure 16. Collage of photos with evidence of breaks and fissures of the road pavement, sidewalks, and containment walls. (**a**–**g**) letters identify the damaged sites and have a corresponding position in Figure 17. (**a**) Red ellipses highlight the presence of strands reinforcing and linking the building; (**e**) cracks on the sidewall correspond to an active sinkhole.

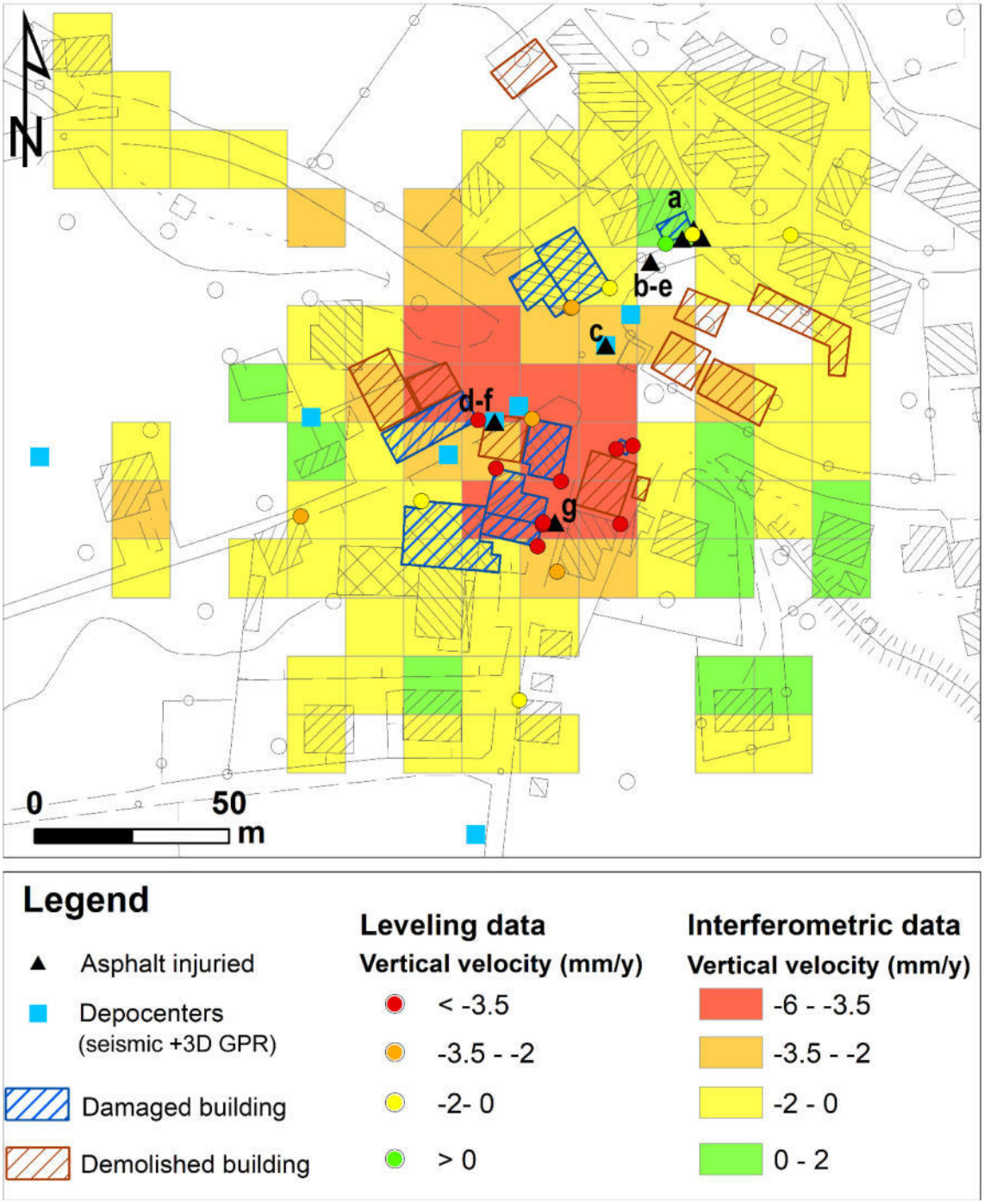

Figure 17. Synthetic map showing the combination of data obtained by the applied methodologies and highlighting the highest vulnerable zone. See text for details. Letters are related to damages presented in Figure 16.

The map shown in Figure 17 provides a synthesis of the obtained results. We combined geophysical, PSI and leveling information, while also locating the damaged buildings and local asphalt pavement breaks or renovation. Furthermore, we drew on the map the buildings that are nowadays demolished, by using vintage photographs and historical maps. The data are consistent, with the most relevant present damages and the demolished buildings within the zones with higher sinking velocity on the basis of both leveling and PSI. Geophysically imaged depocenters are sparser, but most of them lie

within the most critical area and perfectly correlate with the damage to the local pavement. A relevant exception and a still open issue is related to the house identified by number 11 in Figure 10b, which, as already pointed out, clearly presents signs of major damage, but seems to be in a stable area (from both leveling and PSI), where 3D GPR does not image any relevant feature except several shallow pipes (Figure 15). In front of this house, just below the asphalt, a void was present, but it was filled by loose material just before the 3D GPR acquisition, so it possibly masks all the sinking related features. In addition, the strands reinforcing this building and linking it to the house towards the west (see red ellipses in Figure 16a) probably limited the strains and differential settlements.

The lesson learned is that, especially in anthropized environments, it is mandatory to use different integrated techniques, without forgetting the role of the fieldwork of the geologists who can detect the precursors or the already occurred, even elusive, signs of ongoing or incipient sinking. In addition, it is essential when producing large scale maps to consider that local but dangerous and relevant phenomena can be masked by the resolution limits of the adopted methodology and/or by the anthropic rehash and existing infrastructures.

6. Conclusions

In a complex geological and hydrological framework, as in the study area, a multidisciplinary and multi-scale approach is mandatory to identify and map the zone most affected by sinking phenomena. While punctual data such as borehole stratigraphy, local groundwater level variations with time, extensometers measurements and geotechnical parameters are useful to highlight local hazards due to occurring deformation, the proposed integrated methodology addresses a complete and quantitative assessment of the vulnerability of the area.

Even if it is almost impossible to deterministically predict the occurrence of future sinkholes and their precise behavior in terms of both location and evolution with time, with the proposed integrated approach, we were able to:

(1) Image the most relevant subsurface features at a scale of tens of meters thanks to reflection seismics' profiles (checked and validated by borehole stratigraphy);
(2) Identify and map the zones with higher vertical movements thanks to the multi-year interferometric data analysis;
(3) Cross-checking both vertical and horizontal movements by integrating repeated precise leveling measures with interferometry;
(4) Highlight and map the main shallow depocenters thanks to full 3D GPR;
(5) Obtain a summary map showing the highest vulnerable zone as a function of deformation thresholds set on the basis of the observations and peculiarities of the area (Figure 17).

The latter result has not been common in the most recent similar studies. In fact, the current approach to obtain a hazard assessment for sinkholes of an area, even when multidisciplinary, is mainly focused on the visual comparison of aerial photographs and satellite images used to define the limits of one or a few single sinkholes with time, e.g., [6]. It is apparent that such an approach has an intrinsic high subjectivity level and leads to just qualitative results.

Author Contributions: Conceptualization, A.B. and C.C.; data curation, A.B., C.C., E.F., G.A. and A.M.; funding acquisition, C.C. and L.Z.; investigation, C.C., E.F., A.M. and L.Z.; methodology, A.B., C.C., E.F., G.A. and L.Z.; project administration, C.C. and L.Z.; supervision, C.C., E.F. and L.Z.; writing—original draft, A.B., C.C., E.F. and G.A.; writing—review and editing, C.C. and E.F. All authors have read and agreed to the published version of the manuscript.

Funding: This research was partially funded by the Geological Survey of the Friuli Venezia Giulia Region, in the framework of the following projects: (1) Realizzazione del censimento regionale dei sinkhole e relativo GIS con corso formativo e predisposizione delle linee guida di rilevamento ed informatizzazione nonché glossario dei termini utilizzati (prot.no. 801 del 28 October 2013, CUP: J92F16001310002); (2) accordo attuativo di collaborazione per la definizione e quantificazione della pericolosità dei sinkhole nei litotipi evaporitici Carniani dell'alta valle del Tagliamento (prot.no. 877 del 06 October 2016); (3) accordo attuativo di collaborazione per la misurazione delle geometrie e delle deformazioni indotte dalla presenza di sinkhole (prot.no.1254 del 21 November 2018); (4) progetto

di ricerca per la definizione del fenomeno di emissione gassosa in Comune di Enemonzo, località Quinis e delle eventuali correlazioni con i presenti fenomeni di sinkhole finalizzate alla valutazione della pericolosità associata nonché delle soluzioni tecniche di mitigazione o compensazione del dissesto (prot.no.286 del 12 June 2014, CIG: Z4C0C938BE); (5) accordo attuativo di collaborazione per l'aggiornamento censimento e pericolosità dei sinkhole del territorio regionale (prot.no.0035220 del 27 July 2020).

Acknowledgments: The authors would like to acknowledge the functionaries of the Geological Survey of FVG Region: Chiara Piano, Antonio Bratus and Franco Liuzzi as scientific coordinators of the joint different projects with the University of Trieste, Dept. of Mathematics and Geosciences and for providing interferometric data. We acknowledge the Italian Space Agency because the research was carried out using CSK® products © of the Italian Space Agency (ASI), delivered under a license to use by ASI being a product available for the FVG Region. We also acknowledge the service Rheticus® Displacement and Vincenzo Massimi and Sergio Samarelli from Planetek Italia as well as Raffaele Nutricato and Davide Oscar Nitti from Geophysical Applications Processing. We also acknowledge Schlumberger through the Petrel interpretation package and Halliburton through Seispace—ProMAX suite academic grants awarded to University of Trieste. We would like to thank Paolo Gabrielli for his help during seismic data acquisition and processing.

Conflicts of Interest: The authors declare no conflict of interest.

References

1. Thierry, P.; Prunier-Leparmentier, A.M.; Lembezat, C.; Vanoudheusden, E.; Vernoux, J.F. 3D geological modelling at urban scale and mapping of ground movement susceptibility from gypsum dissolution: The Paris example (France). *Eng. Geol.* **2009**, *105*, 51–64. [CrossRef]
2. Dahm, T.; Kühn, D.; Ohrnberger, M.; Kröger, J.; Wiederhold, H.; Reuther, C.-D.; Dehghani, A.; Scherbaum, F. Combining geophysical data sets to study the dynamics of shallow evaporites in urban environments: Application to Hamburg, Germany. *Geophys. J. Int.* **2010**, *181*, 154–172. [CrossRef]
3. Paukstys, B.; Cooper, A.H.; Arustiene, J. Planning for gypsum geohazards in Lithuania and England. *Eng. Geol.* **1999**, *52*, 93–103. [CrossRef]
4. Koutepov, V.M.; Mironov, O.K.; Tolmachev, V.V. Assessment of suffosion-related hazards in karst areas using GIS technology. *Environ. Geol.* **2008**, *54*, 957–962. [CrossRef]
5. Gutiérrez, F.; Calaforra, J.M.; Cardona, F.; Ortí, F.; Durán, J.J.; Garay, P. Geological and environmental implications of the evaporite karst in Spain. *Environ. Geol.* **2008**, *53*, 951–965. [CrossRef]
6. Sevil, J.; Gutiérrez, F.; Carmicer, C.; Carbonel, D.; Desir, G.; Garcià-Arnay, Á.; Guerrero, J. Characterizing and monitoring a high-risk sinkhole in an urban area underlain by salt through non-invasive methods: Detailed mapping, high-precision leveling and GPR. *Eng. Geol.* **2020**, *272*, 105641. [CrossRef]
7. Cooper, A.H. Subsidence hazards caused by the dissolution of Permian gypsum in England: Geology, investigation and remediation. In *Geohazards in Engineering Geology*; Maund, J.G., Eddleston, M., Eds.; Geological Society of London: London, UK, 1998; pp. 265–275.
8. Cooper, A.H.; Farrant, A.R.; Price, S.J. The use of karst geomorphology for planning, hazard avoidance and development in Great Britain. *Geomorphology* **2011**, *134*, 118–131. [CrossRef]
9. Parise, M.; Qiriazi, P.; Sala, S. Natural and anthropogenic hazards in karst areas of Albania. *Nat. Hazards Earth Syst. Sci.* **2004**, *4*, 569–581. [CrossRef]
10. Kuniansky, E.L.; Weary, D.L.; Kaufmann, J.E. The current status of mapping karst areas and availability of public sinkhole-risk resources in karst terrains of the United States. *Hydrogeol. J.* **2016**, *24*, 613–624. [CrossRef]
11. Buttrick, D.B.; van Schalkwyk, A. Hazard and risk assessment for sinkhole formation on dolomite land in South Africa. *Environ. Geol.* **1998**, *36*, 170–178. [CrossRef]
12. Nisio, S. I sinkholes nelle altre regioni. *Mem. Descr. Carta Geol. It.* **2008**, *85*, 419–426. (In Italian)
13. De Waele, J.; Piccini, L.; Columbu, A.; Madonia, G.; Vattano, M.; Calligaris, C.; D'Angeli, I.M.; Parise, M.; Chiesi, M.; Sivelli, M.; et al. Evaporite karst in Italy: A review. *Int. J. Speleol.* **2017**, *46*, 137–168. [CrossRef]
14. Calligaris, C.; Devoto, S.; Zini, L.; Cucchi, F. An integrated approach for investigations of ground subsidence phenomena in the Ovaro village (NE Italy). In *Advance in Karst Science, Proceedings of EuroKarst 2016, Neuchâtel, Switzerland 2017*; Renard, P., Bertrand, C., Eds.; Springer International Publishing: Geneva, Switzerland, 2017; Volume 8, pp. 71–77. [CrossRef]
15. Calligaris, C.; Zini, L.; Nisio, S.; Piano, C. Sinkholes in the Friuli Venezia Giulia Region focus on the evaporites. *J. Appl. Geology* **2020**, *5*. [CrossRef]

16. Cooper, A.H.; Gutiérrez, F. Dealing with gypsum karst problems: Hazards, environmental issues and planning. *Treat. Geomorphol.* **2013**, *6*, 451–462. [CrossRef]
17. Frumkin, A. Salt karst. *Treat. Geomorphol.* **2013**, *6*, 407–424. [CrossRef]
18. Zini, L.; Calligaris, C.; Forte, E.; Petronio, L.; Zavagno, E.; Boccali, C.; Cucchi, F. A multidisciplinary approach in sinkhole analysis: The Quinis village case study (NE-Italy). *Eng. Geol.* **2015**, *197*, 132–144. [CrossRef]
19. Zhu, X.; Chen, W. Tiankengs in the karst of China. *Cave Karst. Sci.* **2005**, *32*, 55–66.
20. Gutiérrez, F. Sinkhole Hazards. *Oxford Res. Encycl. Nat. Hazard Sci.* **2016**. [CrossRef]
21. Soldati, M.; Tonelli, C.; Galve, J.P. Geomorphological evolution of palaeosinkhole features in the Maltese Archipelago (Mediterranean Sea). *Geogr. Fis. Dinam. Quat.* **2013**, *36*, 189–198. [CrossRef]
22. Nisio, S.; Caramanna, G.; Ciotoli, G. Sinkholes in Italy: First results on the inventory and analysis. In *Natural and Anthropogenic Hazards in Karst Areas: Recognition, Analysis and Mitigation*; Parise, M., Gunn, J., Eds.; Geological Society: London, UK, 2007; Volume 279, pp. 23–45. [CrossRef]
23. Caramanna, G.; Ciotoli, G.; Nisio, S. A review of natural sinkhole phenomena in Italian plain areas. *Nat. Hazards* **2008**, *45*, 145–172. [CrossRef]
24. Di Maggio, C.; Di Trapani, F.P.; Madonia, G.; Salvo, D.; Vattano, M. Primo contributo sui sinkhole nelle evaporiti della Sicilia (Italia)/First report on the sinkhole phenomena in the Sicilian evaporites (Italy). In *Proceedings of the I sinkholes. Gli sprofondamenti catastrofici nell'ambiente naturale ed in quello antropizzato, Proceedings of the 2 Workshop Internazionale, Rome, Italy, 3–4 December 2009*; ISPRA, Ed.; ISPRA: Roma, Italy, 2010; pp. 299–313.
25. Iovine, G.; Parise, M.; Trocino, A. Instability phenomena in the evaporite karst of Calabria, Southern Italy. *Zeit. Geomorphol.* **2010**, *54*, 153–178. [CrossRef]
26. Caporale, F.; De Venuto, G.; Leandro, G.; Spilotro, G. Interventi di mitigazione del rischio da sinkholes nell'area di Lesina marina (Provincia di Foggia, Italia). In *Memorie Descrittive della Carta Geologica d'Italia*; ISPRA, Ed.; ISPRA: Roma, Italy, 2013; Volume 93, pp. 121–142. (In Italian)
27. Parise, M.; Vennari, C. A chronological catalogue of sinkholes in Italy: The first step toward a real evaluation of the sinkhole hazard. In Proceedings of the 13th Multidisciplinary Conference on Sinkholes and the Engineering and Environmental Impacts of Karst, Carlsbad, NM, USA, 6–10 May 2013; Land, L., Doctor, D.H., Stephenson, B., Eds.; NCKRI: Carlsbad, NM, USA, 2013; pp. 383–392. [CrossRef]
28. Gortani, M. Le doline alluvionali. *Nat. Mont.* **1965**, *3*, 120–128. (In Italian)
29. Marinelli, O. Fenomeni di tipo carsico nei terrazzi alluvionali della Valle del Tagliamento. *Mem. Soc. Geogr. It.* **1898**, *8*, 415–419. (In Italian)
30. Fabbri, P.; Ortombina, M.; Piccinini, L.; Zampieri, D.; Zini, L. Hydrogeological spring characterization in the Vajont area. *Ital. J. Eng. Geol. Environ.* **2013**, *6*, 541–553. [CrossRef]
31. Zini, L.; Calligaris, C.; Zavagno, E. Classical Karst hydrodynamics: A sheared aquifer within Italy and Slovenia. In *Evolving Water Resources Systems: Understanding, Predicting and Managing Water-Society Interactions*; Castellarin, A., Ceola, S., Toth, E., Montanari, A., Eds.; IAHS Publication: Bologna, Italy, June 2014; Volume 364, pp. 499–504. [CrossRef]
32. Zini, L.; Casagrande, G.; Calligaris, C.; Cucchi, F.; Manca, P.; Treu, F.; Zavagno, E.; Biolchi, S. The Karst hydrostructure of the Mount Canin (Julian Alps, Italy and Slovenia). In *Hydrogeological and Environmental Investigations in Karst Systems. Environmental Earth Sciences*; Andreo, B., Carrasco, F., Durán, J.J., Jiménez, P., LaMoreaux, J., Eds.; Springer: Berlin/Heidelberg, Germany, 2015; Volume 1, pp. 219–226. [CrossRef]
33. Zini, L.; Visintin, L.; Cucchi, F.; Boschin, W. Potential impact of a proposed railway tunnel on the karst environment: The example of Rosandra valley, Classical Karst Region, Italy-Slovenia. *Acta Carsol.* **2011**, *40*, 207–218. [CrossRef]
34. Calligaris, C.; Boschin, W.; Cucchi, F.; Zini, L. The karst hydrostructure of the Verzegnis group (NE Italy). *Carb. Evap.* **2016**, *31*, 407–420. [CrossRef]
35. Cucchi, F.; Finocchiaro, F.; Zini, L. Karst Geosites in NE Italy. *Environ. Earth Sci.* **2010**, 393–398.
36. Gutiérrez, F.; Parise, M.; De Waele, J.; Jourde, H. A review on natural and human-induced geohazards and impacts in karst. *Earth Sci. Rev.* **2014**, *138*, 61–88. [CrossRef]
37. Theron, A.; Engelbrecht, J. The Role of Earth Observation, with a Focus on Sar Interferometry, for Sinkhole Hazard Assessment. *Remote Sens.* **2018**, *10*, 1506. [CrossRef]
38. Jol, H.M. *Ground Penetrating Radar Theory and Application*, 1st ed.; Elsevier Science: Amsterdam, The Netherlands, 2009; p. 524. [CrossRef]

39. Vaughan, D.G.; Corr, H.F.J.; Doake, C.S.M.; Waddington, E.D. Distortion of isochronous layers in ice revealed by ground-penetrating radar. *Nature* **1999**, *398*, 323–326. [CrossRef]
40. Saarenketo, Y.; Scullion, T. Road evaluation with ground penetrating radar. *J. Appl. Geophy* **2000**, *43*, 119–138. [CrossRef]
41. Zhao, E.; Tian, G.; Forte, E.; Pipan, M.; Wang, Y.; Li, X.; Shi, Z.; Liu, H. Advances in GPR data acquisition and analysis for archaeology. *Geophys. J. Int.* **2015**, *202*, 62–71. [CrossRef]
42. Kruse, S.; Grasmueck, M.; Weiss, M.; Viggiano, D. Sinkhole structure imaging in covered Karst terrain. *Geophys. Res. Lett.* **2006**, *33*, L16405. [CrossRef]
43. Ronen, A.; Ezersky, M.; Beck, A.; Gatenio, B.; Simhayov, B.R. Use of GPR method for prediction of sinkholes formation along the Dead Sea Shores, Israel. *Geomorphology* **2019**, *328*, 28–43. [CrossRef]
44. Conway, B.; Cook, J. Monitoring evaporite karst activity and land subsidence in the Holbrook Basin, Arizona using interferometric synthetic aperture radar (InSAR). In Proceedings of the 13th Multidisciplinary Conference on Sinkholes and the Engineering and Environmental Impacts of Karst, Carlsbad, NM, USA, 6–10 May 2013; Land, L., Doctor, D.H., Stephenson, B., Eds.; NCKRI: Carlsbad, NM, USA, 2013; pp. 187–194. [CrossRef]
45. Kim, J.W.; Lu, Z.; Degrandpre, K. Ongoing deformation of sinkholes in Wink, Texas, observed by time-series sentinel-1A SAR interferometry (preliminary results). *Remote Sens.* **2016**, *8*, 313. [CrossRef]
46. Jones, C.E.; Blom, R.G. Bayou Corne, Louisiana, sinkhole: Precursory deformation measured by radar interferometry. *Geology* **2014**, *42*, 111–114. [CrossRef]
47. Castañeda, C.; Gutiérrez, F.; Manunta, M.; Galve, J.P. DInSAR measurements of ground deformation by sinkholes, mining subsidence, and landslides, Ebro River, Spain. *Earth Surf. Process. Landf.* **2009**, *34*, 1562–1574. [CrossRef]
48. Gutiérrez, F.; Galve, J.P.; Lucha, P.; Castañeda, C.; Bonachea, J.; Guerrero, J. Integrating geomorphological mapping, trenching, InSAR and GPR for the identification and characterization of sinkholes: A review and application in the mantled evaporite karst of the Ebro Valley (NE Spain). *Geomorphology* **2011**, *134*, 144–156. [CrossRef]
49. Galve, J.P.; Castañeda, C.; Gutiérrez, F. Railway deformation detected by DInSAR over active sinkholes in the Ebro Valley evaporite karst, Spain. *Nat. Hazards Earth Syst. Sci.* **2015**, *15*, 2439–2448. [CrossRef]
50. Cuenca, M.C.; Hanssen, R.F. Subsidence and uplift at Wassenberg, Germany due to coal mining using persistent scatterer interferometry. In Proceedings of the 13th FIG Symposium on Deformation Measurements and Analysis, Lisbon, Portugal, 12–15 May 2008; Gomez Garcia, V.A., Ed.; LNEC: Lisbon, Portugal, 2008; pp. 1–9.
51. Cuenca, M.C. Improving Radar Interferometry for Monitoring Fault-Related Surface Deformation: Applications for the Roer Valley Graben and Coal Mine Induced Displacements in the Southern Netherlands. Ph.D. Thesis, Delft University of Technology, Delft, The Netherlands, 2 November 2012. [CrossRef]
52. Chang, L.; Hanssen, R.F. Detection of cavity migration and sinkhole risk using radar interferometric time series. *Remote Sens. Environ.* **2014**, *147*, 56–64. [CrossRef]
53. Nof, R.N.; Baer, G.; Ziv, A.; Raz, E.; Atzori, S.; Salvi, S. Sinkhole precursors along the Dead Sea, Israel, revealed by SAR interferometry. *Geology* **2013**, *41*, 1019–1022. [CrossRef]
54. Theron, A.; Engelbrecht, J.; Kemp, J.; Kleynhans, W.; Turnbull, T. Detection of Sinkhole Precursors through SAR Interferometry: Radar and Geological Considerations. *IEEE Geosci. Remote Sens. Lett.* **2017**, *14*, 871–875. [CrossRef]
55. Ferretti, A.; Basilico, M.; Novali, F.; Prati, C. Possibile utilizzo di dati radar satellitari per individuazione e monitoraggio di fenomeni di sinkholes. In Proceedings of the First Seminary on the State of the Art on Sinkhole Study and the role of National and Local Administration on Land Management, Rome, Italy; Nisio, S., Panetta, S., Vita, L., Eds.; APAT: Rome, Italy, 2004; pp. 331–340.
56. Intrieri, E.; Gigli, G.; Nocentini, M.; Lombardi, L.; Mugnai, F.; Fidolini, F.; Casagli, N. Sinkhole monitoring and early warning: An experimental and successful GB-InSAR application. *Geomorphology* **2015**, *241*, 304–314. [CrossRef]
57. Malinowska, A.A.; Witkowski, W.T.; Hejmanowski, R.; Chang, L.; van Leijen, F.J.; Hanssen, R.F. Sinkhole occurrence monitoring over shallow abandoned coal mines with satellite-based persistent scatterer interferometry. *Eng. Geol.* **2019**, *262*, 105336. [CrossRef]

58. Vajedian, S.; Motagh, M. Extracting sinkhole features from time-series of TerraSAR-X/TanDEM-X data. *ISPRS J. Photogramm. Remote Sens.* **2019**, *150*, 274–284. [CrossRef]
59. Novellino, A.; Cigna, F.; Brahmi, M.; Sowter, A.; Bateson, L.; Marsh, S. Assessing the feasibility of a national InSAR ground deformation map of Great Britain with Sentinel-1. *Geosciences* **2017**, *7*, 19. [CrossRef]
60. Cosano, P.A.B. Rilievo Geologico dei Dintorni di Enemonzo (Carnia). Master's Thesis, University of Milan, Milan, Italy, 1948. (In Italian)
61. Venturini, C.; Spalletta, C.; Vai, G.B.; Pondrelli, M.; Delzotto, S.; Fontana, C.; Longo Salvador, G.; Carulli, G.B. *Note Illustrative Carta geologica d'Italia alla scala 1:50.000 Foglio 031 Ampezzo*; ISPRA: Rome, Italy, 2009; pp. 7–222. (In Italian)
62. Carulli, G.B. *Carta geologica del Friuli Venezia Giulia alla scala 1:150.000 e Note Illustrative*; SELCA: Florence, Italy, 2006. (In Italian)
63. Calligaris, C.; Ghezzi, L.; Petrini, R.; Lenaz, D.; Zini, L. Evaporite Dissolution Rate through an on-site Experiment into Piezometric Tubes Applied to the Real Case-Study of Quinis (NE Italy). *Geosciences* **2019**, *9*, 298. [CrossRef]
64. Alsadi, H.N. *Seismic Hydrocarbon Exploration 2D and 3D Techniques*; Springer: Berlin, Germany, 2017; p. 331. ISBN 978-3-319-40325-6.
65. Yilmaz, Ö. *Seismic Data Analysis. Processing, Inversion, and Interpretation of Seismic Data, Society of Exploration Geophysicists*; SEG: Tulsa, OH, USA, 2001; Volume 10, p. 2065. [CrossRef]
66. Steeples, D.; Knapp, R.W.; McElwee, C.D. Seismic reflection investigations of sinkholes beneath Interstate Highway 70 in Kansas. *Geophysics* **1986**, *51*, 295. [CrossRef]
67. Isiaka, A.I.; Durrheim, R.J.; Manzi, M.S.D. High-Resolution Seismic Reflection Investigation of Subsidence and Sinkholes at an Abandoned Coal Mine Site in South Africa. *Pure Appl. Geophys.* **2019**, *176*, 1531–1548. [CrossRef]
68. Krawczyk, C.M.; Polom, U.; Trabs, S.; Dahm, T. Sinkholes in the city of Hamburg—New urban shear-wave reflection seismic system enables high-resolution imaging of subrosion structures. *J. Appl. Geophy.* **2012**, *78*, 133–143. [CrossRef]
69. Wadas, S.H.; Tanner, D.C.; Polom, U.; Krawczyk, C.M. Structural analysis of S-wave seismics around an urban sinkhole: Evidence of enhanced dissolution in a strike-slip fault zone. *Nat. Hazards Earth Syst. Sci.* **2017**, *17*, 2335–2350. [CrossRef]
70. Goldstein, R.M.; Zebker, H.A.; Werner, C.L. Satellite radar interferometry: Two-dimensional phase unwrapping. *Radio Sci.* **1988**, *23*, 713–720. [CrossRef]
71. Bürgmann, R.; Rosen, P.A.; Fielding, E.J. Synthetic aperture radar interferometry to measure Earth's surface topography and its deformation. *Ann. Rev. Earth Planet. Sci.* **2000**, *28*, 169–209. [CrossRef]
72. Bamler, R.; Hartl, P. Synthetic aperture radar interferometry. *InvPr* **1998**, *14*, R1–R54. [CrossRef]
73. Ferretti, A.; Prati, C.; Rocca, F. Permanent scatterers in SAR interferometry. *IEEE Trans. Geosci. Remote Sens.* **2001**, *39*, 8–20. [CrossRef]
74. Bovenga, F.; Refice, A.; Nutricato, R.; Guerriero, L.; Chiaradia, M.T. SPINUA: A flexible processing chain for ERS/ENVISAT long term interferometry. In Proceedings of the ESA-ENVISAT Symposium 2004, Salzburg, Austria, 6–10 September 2004; Lacoste, H., Ouwehand, L., Eds.; Published on CD-Rom, 2004; pp. 1–6, Bibcode: 2005ESASP.572E.76B. Available online: https://www.scopus.com/inward/record.uri?eid=2-s2.0-23844488451&partnerID=40&md5=66fccec6df471bf259e63560d778dd1b (accessed on 19 November 2020).
75. Merryman Boncori, J.P. Measuring Coseismic Deformation with Spaceborne Synthetic Aperture Radar: A Review. *Front. Earth Sci.* **2019**, *7*, 16. [CrossRef]
76. Fialko, Y.; Simons, M.; Agnew, D. The complete (3-D) surface displacement field in the epicentral area of the 1999 M_W7. 1 Hector Mine Earthquake, California, from space geodetic observations. *Geophys. Res. Lett.* **2001**, *28*, 3063–3066. [CrossRef]
77. Mehrabi, H.; Voosoghi, B.; Motagh, M.; Hanssen, R.F. Three-dimensional displacement fields from InSAR through Tikhonov regularization and least-squares variance component estimation. *J. Surv. Eng.* **2019**, *145*, 04019011. [CrossRef]
78. Picco, S. Monitoraggio topografico. Dipartimento di Matematica e Geoscienze, Università degli Studi di Trieste (Italy). Unpublished work, 2014; pp. 1–95. (In Italian)
79. Trinks, I.; Gustafsson, J.; Emilsson, J.; Gustafsson, C.; Johansson, B.; Nissen, J. Efficient, large-scale archaeological prospection using a true 3D GPR array system. *Archeosciences* **2009**, *33*, 367–370. [CrossRef]

80. Novo, A.; Dabas, M.; Morelli, G. The STREAM X Multichannel GPR System: First Test at Vieil-Evreux (France) and Comparison with Other Geophysical Data. *Archaeol. Prospect.* **2012**, *19*, 179–189. [CrossRef]
81. Zhao, W.; Forte, E.; Pipan, M. Texture attribute analysis of GPR data for archaeological prospection. *Pure Appl. Geophys.* **2016**, *173*, 2237–2251. [CrossRef]
82. Trinks, I.; Johansson, B.; Gustafsson, J.; Emilsson, J.; Friborg, J.; Gustafsson, C.; Nissen, J.; Hinterleitner, A. Efficient, large-scale archaeological prospection using a true three-dimensional ground-penetrating radar array system. *Archaeol. Prospect.* **2010**, *17*, 175–186. [CrossRef]
83. Viberg, A.; Gustafsson, C.; Andrén, A. Multi-Channel Ground-Penetrating Radar Array Surveys of the Iron Age and Medieval Ringfort Bårby on the Island of Öland, Sweden. *Remote Sens.* **2020**, *12*, 227. [CrossRef]
84. Grasmueck, M.; Novo, A. 3D GPR imaging of shallow plastic pipes, tree roots, and small objects. In Proceedings of the 16th International Conference on Ground Penetrating Radar (GPR), Hong Kong, China, 13–16 June 2016; pp. 1–6. [CrossRef]
85. Muller, W.B. Semi-automatic determination of layer depth, permittivity and moisture content for unbound granular pavements using multi-offset 3-D GPR. *Int. J. Pavement Eng.* **2018**, *21*, 1281–1296. [CrossRef]
86. Grasmueck, M.; Weger, R.; Horstmeyer, H. Full-resolution 3D GPR imaging. *Geophysics* **2005**, *70*, K12–K19. [CrossRef]
87. McClymont, A.F.; Green, A.G.; Streich, R.; Horstmeyer, H.; Tronicke, J.; Nobes, D.C.; Pettinga, J.; Campbell, J.; Langridge, R. Visualization of active faults using geometric attributes of 3D GPR data: An example from the Alpine Fault Zone, New Zealand. *Geophysics* **2008**, *73*, 1MA-Z29(B11). [CrossRef]
88. Chopra, S.; Marfurt, K.J. *Seismic Attributes for Prospect Identification and Reservoir Characterization, Geophysical developments, n. 11*; Society of Exploration Geophysicists: Tulsa, OH, USA, 2007; p. 481. ISBN 978-1-56080-141-2. [CrossRef]
89. Zhao, W.; Forte, E.; Colucci, R.R.; Pipan, M. High-resolution glacier imaging and characterization by means of GPR attribute analysis. *Geophys. J. Int.* **2016**, *206*, 1366–1374. [CrossRef]
90. Zini, L. Studi, analisi e coordinamento indagini volti alla definizione del fenomeno di emissione gassosa in Comune di Enemonzo, località Quinis, e delle eventuali correlazioni con i presenti fenomeni di sinkhole finalizzate alla valutazione della pericolosità associata nonché delle soluzioni tecniche di mitigazione o compensazione del dissesto. Dipartimento di Matematica e Geoscienze, Università degli Studi di Trieste (Italy), Unpublished work, 2015. (In Italian)

CHAPTER 3.2

Paper published in Near Surface Geophysics 2023, 1-16

https://doi.org/10.1002/nsg.12261

A Joint Geophysical Approach to Tune an Integrated Sinkhole Monitoring Method in Evaporitic Environments

Chiara Calligaris[1], Emanuele Forte[1], Alice Busetti[1], Luca Zini[1]

[1] Department of Mathematics and geosciences, University of Trieste, Trieste, 34128, Italy

Received: 13 February 2023 | Accepted: 24 May 2023

DOI: 10.1002/nsg.12261

Near Surface Geophysics EAGE

ORIGINAL ARTICLE

A joint geophysical approach to tune an integrated sinkhole monitoring method in evaporitic environments

Chiara Calligaris | **Emanuele Forte** | **Alice Busetti** | **Luca Zini**

Department of Mathematics and Geosciences, University of Trieste, Trieste, Italy

Correspondence
Alice Busetti, Department of Mathematics and Geosciences, University of Trieste, Trieste 34128, Italy.
Email: abusetti@units.it

Funding information
Regione Autonoma Friuli Venezia Giulia; Realizzazione del censimentoregionale dei sinkhole e relativo GIS con corso formativo e predisposizionedelle linee guida di rilevamento ed informatizzazione nonché glossario deitermini utilizzati, Grant/Award Number: CUP: J92F16001310002; Accordo attuativo di collaborazione per la definizione e quantificazionedella pericolosità dei sinkhole nei litotipi evaporitici Permiani; Accordo attuativo di collaborazione per lamisurazione delle geometrie e delle deformazioni indotte dalla presenza disinkhole; Accordo attuativo dicollaborazione per l'aggiornamento censimento e pericolosità dei sinkhole delterritorio regionale

Abstract

Several methodologies allow for the detection and mapping of existing sinkholes in order to asses and manage the associated hazards and risks. These phenomena, linked to the presence of soluble rocks, are well known globally as they can cause severe damage to man-made structures. In this paper, we propose an integrated method applied to a test-site area in NE Italy where, on May 11 2017, a failure shaped like a sinkhole, suddenly occurred along a main regional road, which then had to be closed to traffic in part as a result of a landslide developing on the slope just upstream from the surface depression which had already formed. The slope was reprofiled, a paved barrier was placed at the toe of the slope, and the road itself was finally repaired and restored. In the test site, a detailed morphological and geological survey was performed, as well as several integrated multi-scale geophysical investigations, both in correspondence to the sinkhole location and in surrounding areas where other depressions were found. Results confirm the absence of large cavities down to the maximum investigated depth and highlighted a complex geological situation with abrupt lateral variations, a straight correlation between different geomorphological and geological elements, and the role of water paths. Geophysical investigations were found to be a useful tool to monitor the future evolution of the identified phenomena and to prevent further collapses and disasters along roads.

KEYWORDS
electrical resistivity tomography, geohazard, ground-penetrating radar, hydrogeology, sinkhole

INTRODUCTION

Sinkholes, that are natural sub-circular depressions of various dimensions and depths, are caused by the dissolution of soluble rocks or deposits in addition to internal erosion and/or gravitational processes (Gutiérrez, 2016; Parise, 2015; Waltham et al., 2005). These phenomena are globally widespread, for example in France (Thierry et al., 2009), Germany (Dahm et al., 2010; Krawczyk et al., 2012) Lithuania (Paukstys et al., 1999), Russia (Koutepov et al., 2008), Spain (Gutiérrez et al., 2008; Sevil et al., 2020), the United Kingdom (Cooper, 1998; Cooper et al., 2011), Albania (Parise et al., 2004), USA (Kuniansky et al., 2016), South Africa (Buttrick & van Schalkwyk, 1998), Iran (Karimi & Taheri, 2010; Taheri et al., 2015, 2019) and Italy (Busetti et al., 2020; Calligaris et al., 2017a, 2020; De Waele et al., 2017; Nisio, 2008 and all the references therein). They often have serious consequences in urban areas, causing physical and socio-economic damage to existing man-made structures and have a high risk factor due to their rapid occurrence and evolution (Intrieri et al., 2015; Martinotti et al., 2017; Zini et al., 2015 and all the references therein). Unfortunately, it is nearly impossible to precisely predict when and where sinkholes will occur, while monitoring the evolution of those which have already developed is somehow easier (Calligaris et al., 2019; Galve et al., 2011; Parise, 2015). Studying these

geo-hydrological hazards more in-depth would facilitate a better understanding of their prodromal and triggering factors in order to prevent their intrinsic hazard and risk.

The implementation of sinkhole inventories (Calligaris et al., 2017b; Gutiérrez, 2016) is the first essential step in the evaluation of sinkhole hazard and risk assessment and is used as the basis to forecast the spatial and temporal distribution of future phenomena. In other words, the presence of old sinkholes is the best predictor for the potential occurrence of new ones. In addition, once inventoried, it is necessary to find a method to predict new phenomena in order to avoid serious accidents, specifically in urban areas or along the main roads and infrastructures. Different surface and subsurface investigation methods to identify and characterize sinkholes have been applied throughout the world. Among the others, we can report aerial and satellite image analysis (Dou et al., 2015; Festa et al., 2012; Gutiérrez et al., 2011; Panno & Luman, 2013), topographic map analysis (Basso et al., 2013; Brinkmann et al., 2008; Gutiérrez et al., 2011), field surveys (Bruno et al., 2008; Gutiérrez et al., 2007), LiDAR (Kim et al., 2019; Zhu et al., 2014, 2020), InSAR (Baer et al., 2018; Busetti et al., 2020; Galve et al., 2015; Guerrero et al., 2021; Intrieri et al., 2015; Jones & Blom, 2014; Malinowska et al., 2019; Oliver-Cabrera et al., 2020; Orhan et al., 2021; Shi et al., 2019; Solari et al., 2020; Theron et al., 2017), ground-based monitoring (Desir et al., 2018; Kersten et al., 2017; Kobe et al., 2019; Sevil et al., 2017; Zhende et al., 2013), geophysical surveys (De Ritis et al., 2020; García-Moreno & Mateos, 2011; Krawczyk et al., 2012; Kühn et al., 2011; Margiotta et al., 2012; Malehmir et al., 2016; Pazzi et al., 2018; Ronen et al., 2019; Samyn et al., 2014; Stierman, 2004; Waltham et al., 2005; Wust-Bloch & Joswig, 2006), hydrogeochemical studies (Delkhahi et al., 2020; Taheri et al., 2021) and trenching (Carbonel et al., 2015; Gutiérrez et al., 2018; Sevil et al., 2017) have been used in a series of multidisciplinary and multi-technique investigations.

In correspondence of residential zones or along the roads, limited-dimension sinkholes are immediately filled in order to restore infrastructures and reuse the territory. However, filling the sinkhole with coarse material does not eliminate its cause, but at worst can make the situation more dire due to the additional loading. This situation is particularly dangerous when infrastructures are built-up above a sinkhole area, which, due to their construction methods and the materials used (asphalt, reinforced concrete, etc), have a high resistance to breakage and can therefore favour the creation over time of even large voids immediately below the structures themselves, which eventually instantaneously collapse with serious risk to human safety (Pearson, 2013).

In Italy and, in particular, in the Friuli Venezia Giulia region (FVG), NE Italy, some of the mountain municipalities are characterized by the presence of evaporite bedrock and are heavily affected by sinkholes with serious consequences for infrastructures (Calligaris et al., 2017a, 2020). On May 11, 2017, in Baus, a hamlet situated North of the village of Ovaro (Figure 1), a subsidence phenomenon, suddenly occurred affecting regional road n. 355, one of the main N–S connections in the area, which then had to be closed to traffic. No one was crossing the road when the collapse occurred and subsequent vehicles were able to stop in time, thus avoiding a disaster. Due to the importance of the regional road with heavy traffic, the depression which had formed was immediately filled in with incoherent material, creating a concrete foundation and restoring the asphalt.

Several integrated multi-scale geophysical investigations, including electrical resistivity tomography (ERT), refraction seismic (RS), Ground Penetrating Radar (GPR) and electromagnetic induction (frequency domain electromagnetic [FDEM]), were performed on the road at the location of the sinkhole and in surrounding areas where other depressions were found in order to better understand the phenomena which had occurred, the triggering causes, the geological background and to monitor the state of activity and evolution over time. The novelty of the study is not only related to the use of combined electrical, seismic and multi-frequency electromagnetic techniques but also to their link with geological and geomorphological evidence. This integrated multi-scale geophysical approach allows for the non-invasive investigation and characterization of the subsurface as comprehensively as possible.

STUDY AREA

The hamlet of Baus is situated on the left alluvial terrace of the Degano Torrent and, according to Venturini et al. (2009), is built-up on a Permian evaporite and carbonate bedrock of the Bellerophon Fm. (BEL1 and BEL2). The evaporites are predominantly white and saccharoidal gypsum thinly interbedded with grey marls. The carbonates are dolostones and brown and grey limestones often in the form of cohesive granular rock. The Bellerophon Fm., which is in direct stratigraphic overlap with the Werfen Fm. (WER), does not outcrop extensively in the valley floor and it is mainly mantled by quaternary moraine deposits, Pleistocene in age and alluvial deposits, Holocene in age (Figure 1). Among the tectonic features, a regional structural discontinuity called the Sauris Thrust, approximately E–W oriented, crosses the study area to the South. It is included in those deformation structures, characterizing the FVG region, with low dipping angles that determined the

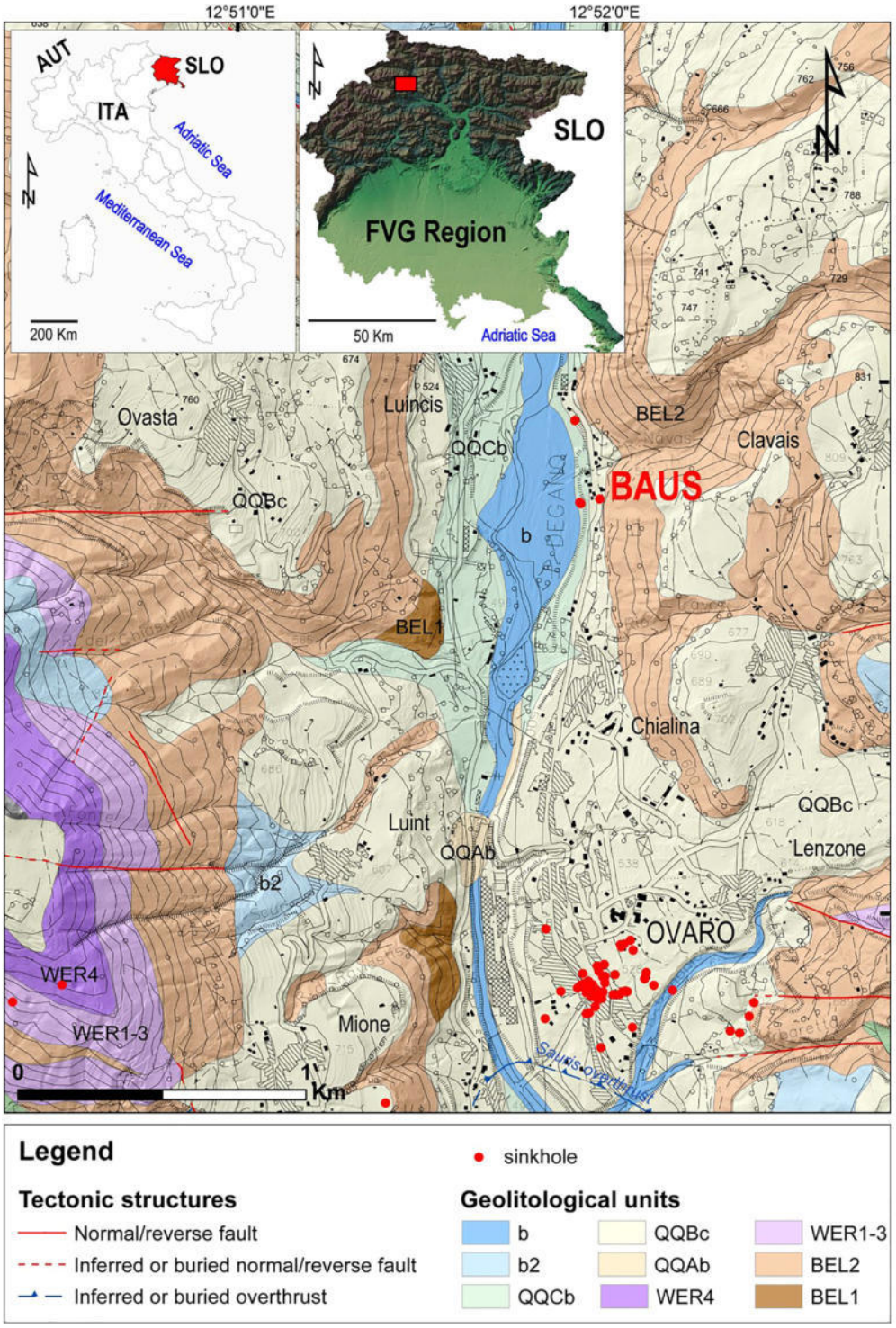

FIGURE 1 Geological map of the study area. Lithological quaternary units: (b) recent alluvial deposits; (b2) eluvial–colluvial deposits; (QQCb) gravels and fluvial sands; (QQBc) diamicton and till; (QQAb) fluvial and delta conglomerates. Permian–Triassic lithological units: Werfen Formation with (WER 4) laminated calcisyltites of the Siusi Member and (WER1-3) oolithic and micritic algal limestone, grey limestone and dolomites and dolomitic limestone; Bellerophon Formation with the dolomites and black limestone Member (BEL2) and gypsum and black dolomites Member (BEL1) (Venturini et al., 2009 – Foglio 31 Ampezzo).

superimposition of the Upper Permian sequences and Lower-Medium Triassic on Carnian units.

From a geomorphological point of view, the municipality of Ovaro is characterized by different elements; reliefs reaching 2075 m a.s.l. (Mt. Col Gentile) are separated by E–W valleys, which join the N–S oriented Degano River Valley. Notable terraces typify the valley floor which experienced different erosional and alluvial phases after the flow reversion of the Degano Torrent, which occurred in the post Last Glacial Maximum as suggested by

Venturini et al. (2009). The alluvial terrace deposits partially mantle the moraines abandoned during the retreat of the glacier tongue. These types of deposits can also be identified on the mountain slopes and highlands.

One of the geomorphological features characterizing the municipality of Ovaro are the sinkholes; phenomena associated with an iperkarst linked to the presence of the evaporites in the subsurface. The 93 sinkholes identified in the area were classified according to Gutiérrez et al. (2014) as follows: 11 bedrock collapses; 9 caprock collapses; 16 cover collapses; and 7 cover suffosion sinkholes. The remaining 50 do not have a precise typological attribution due to a lack of information, most being recognized in 1997 using mainly low-resolution vintage geophysical data (Cucchi & Giorgetti, 1997) and being at present no longer identifiable in the field, thus preventing a typological attribution. The diameters of the inventoried phenomena are very different, bedrock collapse sinkholes are in the range between 2 × 2 m and 49 × 67 m, caprock collapse sinkholes range between 36 × 38 m and 85 × 104 m, cover collapse sinkholes between 1 × 1 m and 30 × 34 m whereas cover suffosion between 1 × 1 m and 2 × 4 m. Considering the depths, in the whole data set they range between 0.5 m and 30 m. Excluding the undefined type, 38.5% are circular, 38.5% sub-circular, 17% elliptical, and 6% have an irregular shape. Overall, 40% are classified as active, 38% as dormant, 20% inactive, and 2% are artificially stabilized. Among the active phenomena, in 2014 and at the end of October 2018, two reactivations of previously known events located in the centre of the village of Ovaro, very close to some houses, bore witness to a quickly evolving situation (Calligaris et al., 2017a; Pearson, 2013).

In the hamlet of Baus, the study area of the present research, three sinkholes which developed on the alluvial terraces of the Degano Torrent have been identified: one is located in a flat zone on the N of Baus (Figure 2a,b); the other two are downstream from regional road 355, at almost the same elevation as the actual torrent bed (Figure 2c,d). The latter two were initially separated, but they are currently almost coalescent into an approximately 6 × 6 m single depression (Figure 2d).

In the proximity to the area where the above-mentioned sinkholes are present, on May 11 2017, along regional road n. 355 in the Degano Valley, a failure shaped like a sinkhole occurred (Caproni, 2017). The road, which is one of the main N–S connections among the mountain valleys in the Carnian Alps, had to be closed to the traffic which prevented people from moving freely and caused notable economic loss.

The event (about 14 m × 5 m) was elliptical in shape with the major axis parallel to the road. The maximum relative deepening was equal to 55 cm (Figure 2e). At the time of the event, the surveys highlighted three different alignments of traction cracks along the slope above the road (Figure 3, in orange). Recently (December 7, 2021), a new traction crack was identified at an altitude of 532 m a.s.l. (i.e., 21 m above the roadway), in the middle of the slope. It has a length of about 20 m and an average opening of about 20 cm with a depth of about 1.5 m (Figure 3, in purple).

After the event, the road was immediately repaired in order to guarantee it was both functional and safe. Important mitigation works were done reprofiling the slope and placing a paved barrier at its toe (Figure 2f).

MATERIALS AND METHODS

After the event occurred, seven crack-metres (CM) were installed on the existing infrastructures and buildings in order to monitor the area and define the state of activity of the movement. To define the depth of the bedrock and to monitor the ongoing situation, geophysical multi-scale integrated investigations were carried out in two different periods, namely on February 13, 2020, N of Baus in correspondence with the sinkhole pictured in Figure 2a, across the depression (Profile 3 – Figure 3) and downstream from the main event (Profile 2 – Figure 3) and on March 26, 2021, along regional road n. 355, in correspondence with the sinking phenomena which occurred in 2017 (Profile 1 – Figure 3).

Table 1 reports some details about the geophysical methods applied and the instruments used, whereas Table 2 lists the software and algorithms applied for data analysis, processing, and inversion for the various techniques exploited and their main parameters.

We decided to use an integrated and multi-scale approach to characterize not only the area along the road in which the sinkhole developed, but also in correspondence with two other zones where other previously unknown sinkhole phenomena were detected during the geomorphological field survey. In particular, we combined ERT with RS to infer the geological setting in the first 20–30 m below the surface, also evaluating possible lateral variations, whereas we integrated GPR with FDEM to characterize the first 4–5 m in the area of the former sinkhole along the road.

All the data sets were at first separately processed and analysed, and then integrated to obtain a more constrained and 'self-validated' interpretation. Such a multi-scale approach was made possible by the accurate positioning of all the collected data and sensors geometry measured with an RTK GPS device having centimetric accuracy.

Before ERT, RS and FDEM data inversion, a careful data quality check was performed in order to highlight and remove outliers or data having low statistical consistence. In particular, we compared ERT data collected with Wenner and Wenner–Schlumberger electrode configurations along the same path considering

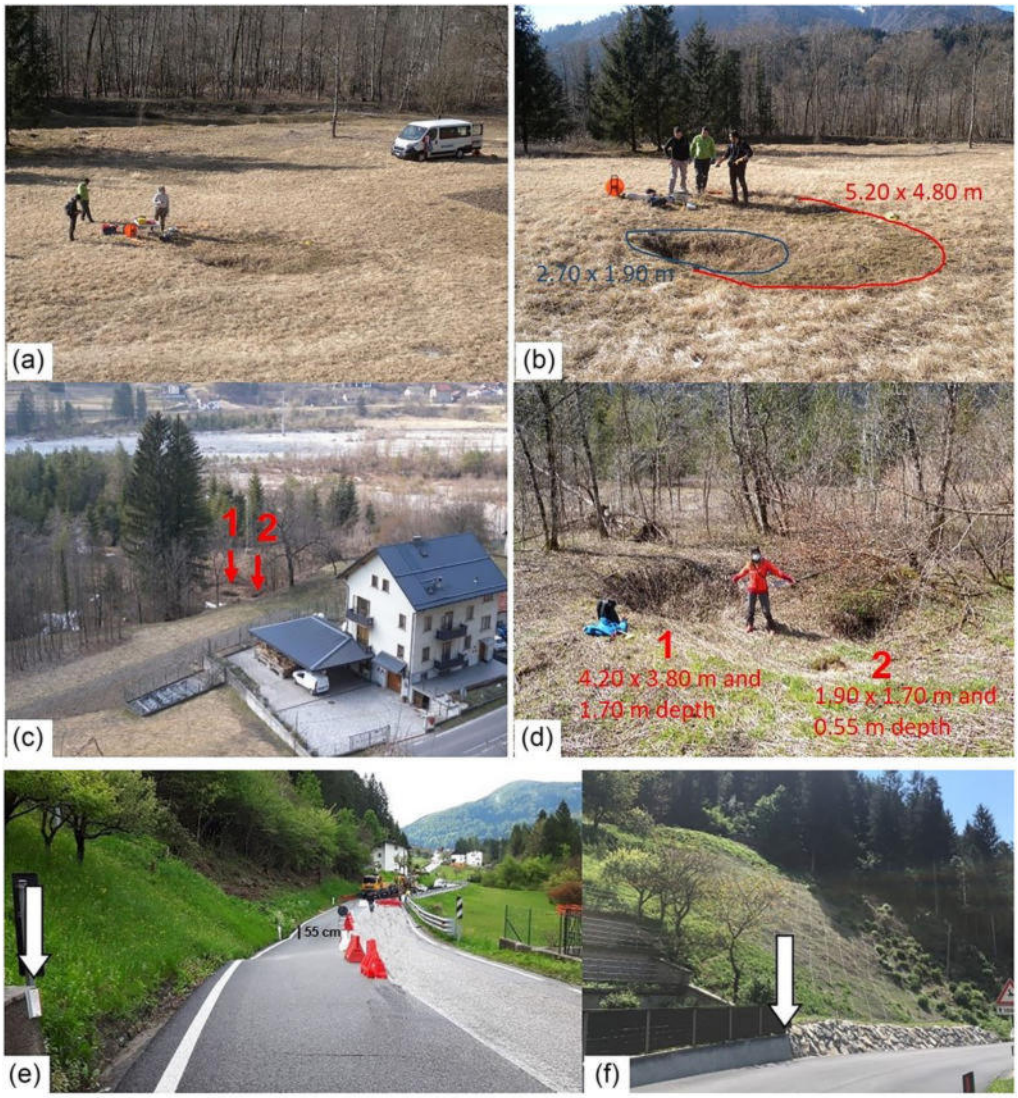

FIGURE 2 Sinkholes in the hamlet of Baus (a–d) with their approximate dimensions. Photo (a) and (b) from February 13, 2020, photo (c) from March 13, 2021 and photo (d) from April 16, 2021. Photographs (e) and (f) (by Dr. Caproni, geologist) documenting the instability phenomenon which occurred on regional road 355 on May 11, 2017 (e) and works done in order to make the road safer (f). Vertical arrows highlight the same location on the two photographs collected in different moments (just after the event (e), and after repairs (f)).

TABLE 1 Geophysical methods used, geometries and acquisition parameters.

Geophysical method	Equipment	Geometry	Main acquisition parameters
ERT Profile 1, 2 and 3	Syscal Pro (Iris) 48 or 72 electrodes	2 profiles 94 m long, 1 profile 142 m long 2 m electrode spacing	Wenner and Wenner–Schlumberger electrode configurations
Refraction seismic Profile 1,2	Geode (Geometrics) 24 channels 5 kg sledgehammer shooting on a metal plate Vertical 14 Hz geophones	2 profiles 102 m long 12 conjugated shots; 24, 4 m spaced vertical geophones	Vertical stacking: 4; 1 s trace length, 0.25 ms sampling interval
GPR Profile 1	ProEx (Malå Geosciences) 250 and 800 MHz shielded antennas	2 profiles along the same path, 96 m long Trace interval: 5 cm	Vertical stacking: 16; trace length: 191.24 ns (250 MHz) and 104.17 ns (800 MHz)
Electromagnetic induction (FDEM) Profile 1	CMD explorer (GF instruments)	2 profiles along the same path, 96 m long	High depth acquisition mode; spatial sampling 1 s

Abbreviations: ERT, electrical resistivity tomography; FDEM, frequency domain electromagnetic; GPR, Ground Penetrating Radar.

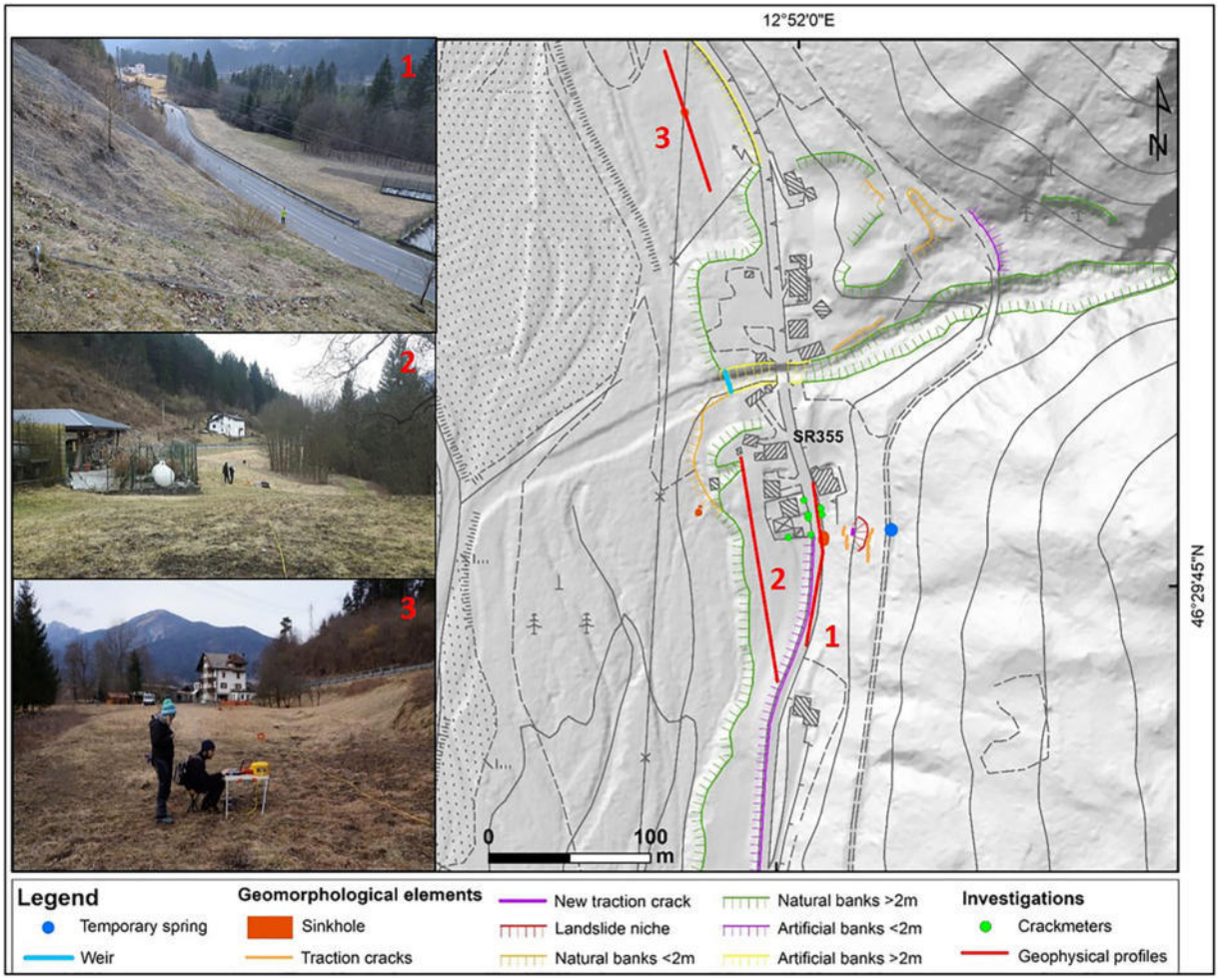

FIGURE 3 Geomorphological map of the hamlet of Baus with the location of the crack-metres and the geophysical profiles. Photos 1, 2 and 3 show the geophysical acquisition of the three profiles and are named accordingly.

the measure obtained with direct and reciprocal electrode combinations, analysing the standard deviation between data repeated with the same quadrupoles, which was always very low. FDEM data were registered first in N–S direction and then in the opposite one in order to guarantee a sufficient statistical repetitiveness. In the RS survey, we set a constant vertical stacking equal to 4 (i.e., four repeated shots for each source location) thus increasing the signal-to-noise ratio by minimizing the random noise level and in turn making the first breaks easier to detect, even for large offsets.

As far as the inversion misfit, it was equal to a maximum of 2 ms for RS after 6 iterations, to 4.3 root mean squared (RMS) mean percentage error for ERT after 5 iterations and to 1.1 RMS mean percentage error for FDEM after 10 iterations. GPR data were collected with 250 MHz and 800 MHz central frequencies shielded antennas to improve both the penetration depth and the attainable resolution. A standard processing is applied considering a constant EM velocity field equal to 0.08 m/ns obtained as a mean value of dedicated diffraction hyperbolas fitting (see, Table 2 to further processing details).

RESULTS

Among all the CM recorded data, only the CM1 showed an initial distensive E–W trend of about 7 mm. The installation was initially done by using only glue and, in February 2018, a particularly intense snowfall detached some of the CM (CM1, CM2 and CM3). The CMs were subsequently reinstalled using screws to fix the devices and since that day only sub-millimetric movements have been recorded.

Regarding geophysical surveys, at first, we considered the RS and ERT profiles crossing the former sinkhole area (Figure 3–Profile 1) in order to highlight subsurface vertical and lateral variations up to a depth of about 30 m. Note that in the sinkhole area, the extensive works done to restore the road encompassed excavations and filling with blocks of rocks and gravel up to

a depth of 3–4 m. In addition, a borehole was drilled approximately at the centre of the sinkhole. Unluckily, a detailed stratigraphy is not available, but eyewitnesses reported that the drilling reached a depth of 10 m from the surface without intercepting cavities or the bedrock, but only sandy and silty gravel sediments.

Using this information as background, it is possible to interpret the highest real resistivity gradient variations highlighted in Figure 4b. The black dotted line marks a laterally quite continuous transition between a shallow low resistivity level and a medium-to-high resistivity level (values between about 300 Ω m and 1000 Ω m). Below such a layer, at about 5–6 m from the surface, there is a sub-horizontal sharp transition towards low resistive materials (values <150 Ω m). At 12–14 m the resistivity increases again (yellow dotted line). By analysing the corresponding RS profile (Figure 4a) we note a good correspondence to the shallowest interface that divides materials having a P-wave velocity below 800 m/s from deeper materials with velocities ranging from 800 m/s to 1200 m/s. The transition marked by the white dotted line is not apparent on the seismic panel, whereas the deepest horizon can be interpreted as the transition to materials with velocities above 2000 m/s.

By combining all the described elements we can interpret the shallower layer as low compaction fine materials also related to road construction; the high resistivity and intermediate seismic velocity layer as coarser sediments (locally with blocks); the layer between white and yellow dotted lines is most probably composed of similar materials as above, but water saturated as evidenced by the low and homogeneous resistivity values and by the absence of an abrupt transition in seismic velocity which has values close to 1500 m/s. The deepest high resistivity and high-velocity layer can be interpreted as the bedrock, which, from the seismic velocity profile has only limited lateral variations (at N and S limits of the sections the lower velocities are most probably just inversion artefacts).

Profile 2 is located 20–40 m to the W from Profile 1 (Figure 3), and both resistivity and P-wave velocity ranges are similar to Profile 1. However, there are some peculiar features (Figure 4c–d) in the distribution of both parameters. The 2D resistivity section (Figure 4d) shows an uppermost relatively low resistive layer just 1–2 m thick (200–400 Ω m) overlaying a layer with resistivity exceeding 1000 Ω m, followed by lower resistive materials (100–400 Ω m). In the northern portion of the profile, the situation is different; in fact, at the surface, there are resistivities higher than 1000 Ω m, which continue in-depth and there is a sharp lateral resistivity variation (marked by the black dashed segment in Figure 4d). If we superimpose the most apparent resistivity change locations on the seismic velocity profile (Figure 4c), whereas there are no relevant variations at the locations of the shallowest two horizons (black and white dotted lines), the deeper horizon (yellow dotted line) and the lateral transition correspond to remarkable increases in seismic velocity. Therefore, we interpreted: the shallower layer as low compaction silty–sandy materials; the high resistivity and intermediate seismic velocity layer as coarser materials similarly to Profile 1; the layer between

TABLE 2 Details about software, algorithms and parameters applied for geophysical data analysis, processing and inversion.

Geophysical method	Software used	Main processing/inversion algorithms	Main processing/inversion parameters
ERT	ProsysII (3.14), Res2Dinv (4.9), ErtLab Studio	Damped least-squares (Marquard) inversion Smoothness constrained least-squared algorithm with Tikhonov model regularization and tetrahedral finite elements inversion (LaBrecque et al., 1999)	Direct and reciprocal data check. No resistivity model constraints. Convergence limit 5% of absolute variation
Refraction seismic	SeisImager (3.14)	Automated first beak picking (with manual check) Combined inversion methods (reciprocal and travel time tomography approaches)	12 shot gathers No vertical smoothing, no minimum and maximum velocity constraints Difference between observed and calculated travel times always below 2 ms
GPR	Prism2 (2.70.03) Matlab scripts	Zero-time correction, Background removal, bandpass filtering, Velocity analysis by hyperbola fitting, exponential amplitude recovery, dominant frequency analysis, hyperbolic summation migration and depth conversion	Bandpass corner frequencies: 50–80–450–550 MHz (250 MHz antenna); 200–300–1200–1400 MHz (800 MHz antenna) Velocity used for migration, and depth conversion: 8 cm/ns
Electromagnetic induction (FDEM)	EM4soil (3.05)	1D laterally constrained inversion. No resistivity range constraints	

Abbreviations: ERT, electrical resistivity tomography; FDEM, frequency domain electromagnetic; GPR, Ground Penetrating Radar.

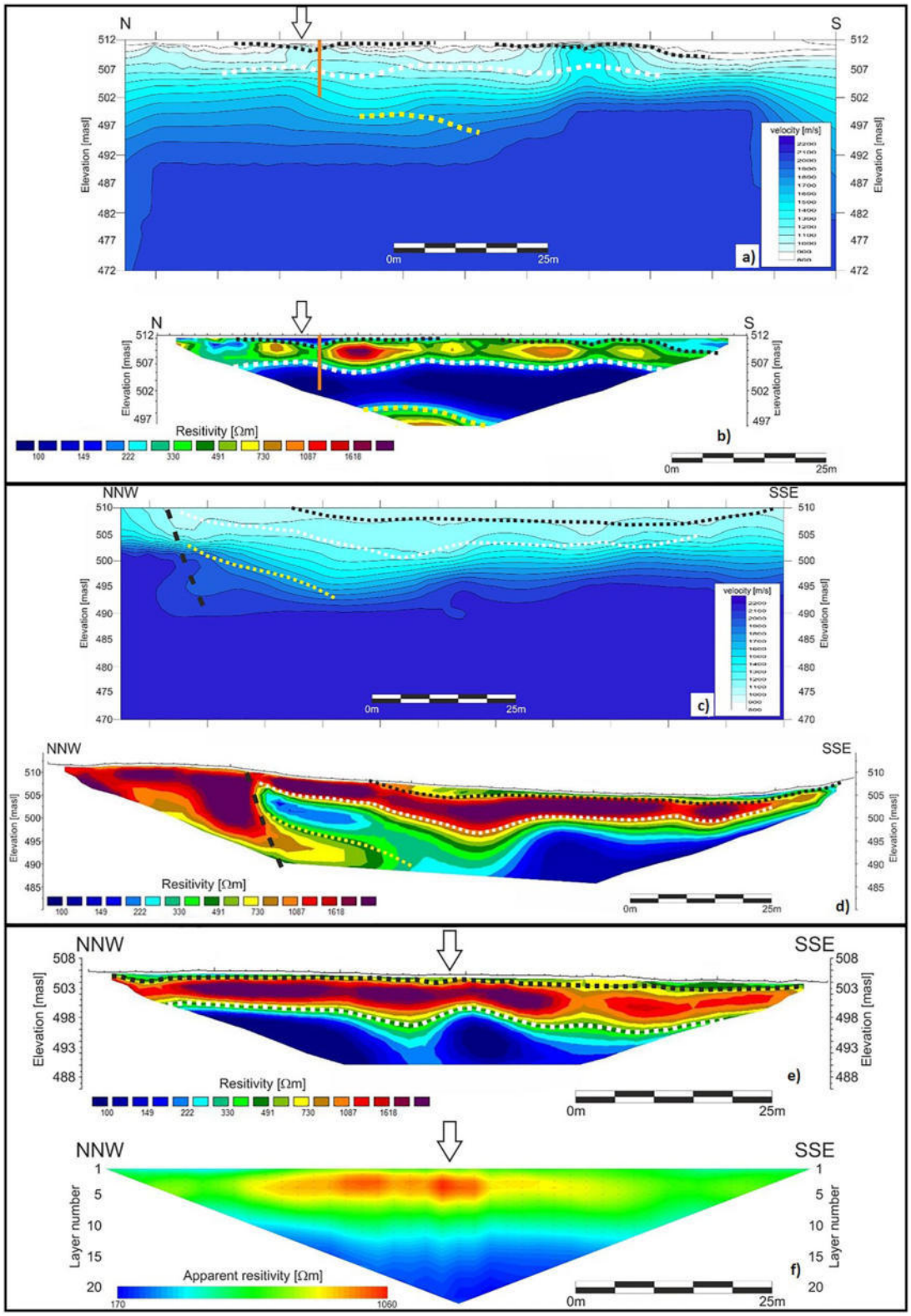

FIGURE 4 (a) RS P wave velocity along Profile 1; (b) ERT inverted resistivity along Profile 1. Vertical white arrows mark the approximate centre of the former sinkhole; black, white and yellow dotted lines highlight the larger resistivity gradients and have also been superimposed on the RS profile. The orange vertical segment depicts the location and depth of a borehole drilled soon after the sinkhole occurrence. All profiles have the same vertical and horizontal scales. (c) RS velocity along Profile 2; (d) ERT inverted resistivity along Profile 2. Black, white and yellow dotted lines highlight the larger resistivity gradients, while the black dashed segment marks the location of an abrupt lateral change. All lines have also been superimposed on the RS profile. All profiles have the same vertical and horizontal scales. (e) ERT inverted resistivity along Profile 3. Black and white dotted lines highlight the larger resistivity gradients. (f) apparent resistivity profile. Vertical arrows indicate the location of the newly developed sinkhole. Please see text for further details. For the location of Profile 1, 2 and 3 see Figure 3.

the white and yellow dotted lines as water-saturated materials. The yellow dotted line is most probably the top of the bedrock. It is interesting to note that the lateral resistivity and seismic velocity variations are located in correspondence to the former sinkhole (about 30 m to the E) and are related to a main geological element. Moreover, we can note a morphological change from almost constant elevations further north from this point to a lower elevation to the south (Figure 4d). We cannot exclude that this lateral variation is due to a tectonic element responsible for the shallowing of the bedrock to the N, but it could also be a filled erosional channel. The localized low resistivity zone to the E of the sharp lateral transition can be attributed to a water flow from the mountain to the river, possibly acting as a triggering or pushing cause for the sinkhole occurrence.

In order to better understand the geological and hydrological backgrounds in the area of the former sinkhole, we extended our analyses to Profile 3 collected about 150 m to the N and crossing a newly developed depression (Figure 3–Profile 3). The resistivity profile does not show relevant lateral variations, whereas the vertical resistivity distribution is very similar to that already described for the southern part of Profile 2, as well as the resistivity range. The lowest resistivity zone can also be interpreted in this case as related to water-saturated sediments which can be linked to the river bed having a mean elevation of 502 m a.s.l. in this area. At the location where the profile crosses the newly developed sinkhole (cover suffosion sinkhole), no relevant resistivity variations can be found on the inverted model (Figure 4e), whereas on the apparent resistivity data (Figure 4f), the highest values of the whole profile are recorded, but no clear 'anomalies' can be detected.

Considering high-resolution and shallow geophysical data (i.e. GPR and FDEM) collected along the road (Figure 5, see Figure 3 for location), some interesting additional features can be noted. From both low and high-frequency GPR data, several horizons are imaged: while to the S of the former sinkhole they are subhorizontal or regularly gently dipping to the S, in the depressed zone (the centre of which is marked by the vertical white arrow in Figure 5a–c) many horizons are concave up, thus depicting local depocentres (marked by red arrows) with general higher dipping for increasing depths. In addition, below the zone in which the sinkhole developed, the electromagnetic attenuation is higher, especially on the 250 MHz profile (light blue texture). Please note that extensive restoration works were done after the sinkhole occurrence in 2017 with excavations and refilling; however, the GPR horizons concavity could suggest movements occurred after the restoration, whereas the high attenuation zone can be interpreted as higher water saturation than the other portions of the profile. Such information can be very helpful, especially when repeated surveys are available because by comparing data collected at different times it is possible to highlight and monitor possible deformations and movements which occurred between the subsequent surveys. For instance, high-frequency GPR data are able to detect horizons and structures even very close to the surface at a decimetric resolution level. In order to follow this approach, positioning at centimetric accuracy is mandatory in order to make it possible to repeat surveys along the same profiles.

FDEM data (Figure 5c) show a quite homogeneous decreasing vertical resistivity trend, except for the northern portion of the profile where medium to low resistivities are detected. The range of resistivities is similar to the one obtained in the corresponding ERT profile (Figure 4c), as well as the resistivity distribution, excluding the shallower portion for which the FDEM method registers high resistivities, whereas ERT images low values. This discrepancy is limited to the shallower layer and can be related to both the intrinsic physical differences between the two techniques and the field operations (see, e.g., Borgatti et al., 2017). In fact, while for the induction method (i.e., FDEM) we moved the coils at a constant elevation equal to one metre above the road, for ERT we drilled 2–3 decimetre deep holes to fix electrodes bypassing the high resistive asphalt cover. In any case, the locations of transitions between high-to-medium and medium-to-low resistivities obtained by FDEM are similar to the ones resulting from the ERT survey, as well as the overall correspondence between FDEM and GPR results, even at a different resolution level (Figure 5).

DISCUSSION

Sinkholes can generally be considered elusive structures due to the intrinsic difficulty in detecting the precursor signs which come before their occurrence. An emblematic case is the one just happened (May 21, 2022) in a small village in NE Italy (Rosso, 2022). A cover collapse sinkhole of about 18 m in diameter and 15 m in-depth suddenly occurred on a terrace where only a few hours before the landowner had crossed without noticing any evidence of a further sudden collapse. This event is just one of the several examples that we could cite but points to how little knowledge there is regarding the predictability of these phenomena. In Italy, scientists are currently mainly focused on cataloguing (Vennari & Parise, 2022), and no monitoring is taking place as well as on the identification of possible future occurrences in terms of evolution and susceptibility (Calligaris et al., 2017b; Ciotoli et al., 2015). The methodological approach presented here is preliminary to an investigation protocol aimed at identifying,

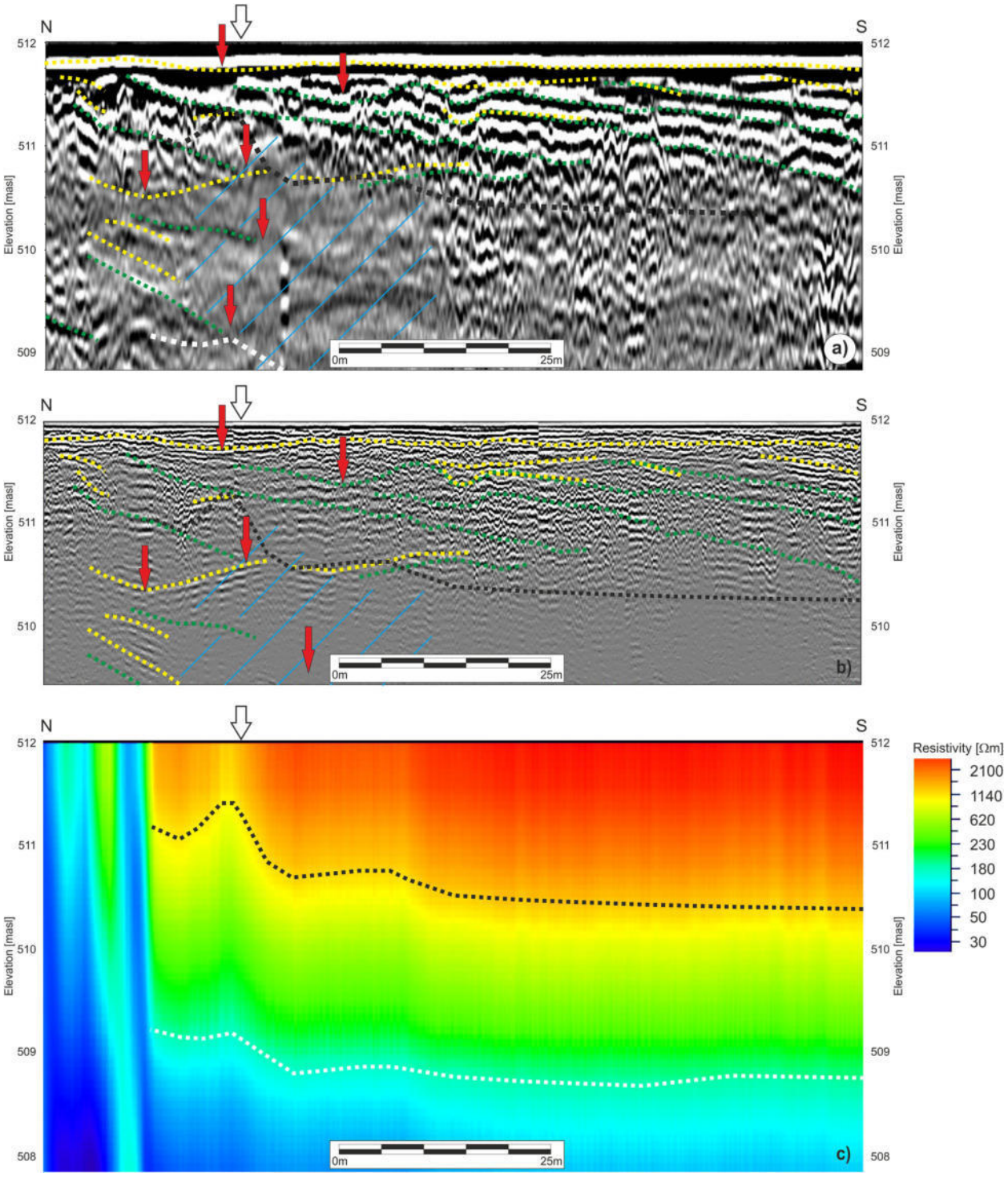

FIGURE 5 (a) 250 MHz Ground Penetrating Radar (GPR) profile; (b) 800 MHz GPR profile; (c) frequency domain electromagnetic (FDEM) profile. White arrows point to the centre of the sinkhole; red arrows highlight depocentres; red and yellow dotted lines follow the main GPR horizons interpreted respectively on 250 and 800 MHz profiles and are superimposed on both for a better visual comparison; light blue texture marks a higher attenuation zone on GPR sections. Black and white dotted lines follow the maximum resistivity gradients as in Figure 4 and are also superimposed on GPR profiles for a better visual comparison. All profiles have the same vertical and horizontal scales. See Figure 3 for profiles location.

TABLE 3 Summary of some of the most recent papers related to sinkhole investigations in carbonate and evaporite environments.

Type of sinkhole	Involved material	Used approach	Location	Reference
Collapse	Limestone	ERT, seismic tomography, MASW	Thailand	Yordkayhun et al. (2022)
Undefined	Roadway substructure	Seismic tomography	Florida	Wang et al. (2022)
Collapse	Limestone/sandstone	GPR	Brazil	Lago et al. (2022)
Collapse	Carbonate deposits	InSAR and spatial clustering analysis (DBSCAN)	West-central Florida	Talib et al. (2022)
Cover collapse	Mudstone, muddy limestone	MERM	Hunan province, China	Pan et al. (2022)
Collapse	Limestone	ERT	Thailand	Arjwech et al. (2021)
Collapse	Travertine	Altimetry, magnetic, microgravity, seismic refraction, electrical resistivity and soli gas surveys	Italy	Argentieri et al. (2015)
Cover collapse	Limestone/quaternary	GPR and electrical resistivity tomography	Algeria	Nouioua et al. (2013)
Undefined	Triassic brecciated dolomitic limestone and Cretaceous slate/alluvial deposits	2D- and 3D-electrical resistivity tomography, microgravity and single-station seismic noise measures	Italy	Pazzi et al. (2018)
Sagging vs. collapse	Evaporites	GPR	Spain	Rodriguez et al. (2014)
Collapse	Evaporites in urban area	Trenching, GPR, ERT and high precision levelling	Spain	Sevil et al. (2017)
All types	Evaporite karst	Trenching, geophysical investigations	Spain	Gutierréz et al. (2018)

Abbreviations: ERT, electrical resistivity tomography; GPR, Ground Penetrating Radar; MERM, multi-electrode resistivity method.

characterizing and monitoring such phenomena in heavily infrastructured environments. From this perspective, 'the use' of small well-known areas as test sites could also be extremely useful to implement, check and validate a multi-technique non-invasive approach, with short acquisition periods and moderate acquisition costs, not negligible when scheduling long-term monitoring.

At the international level, in those parts of the world where these phenomena are present, in the recent years ever more detailed investigations have been done in order to detect and outline these sometimes catastrophic events (Table 3).

The geophysical approaches used have been applied mainly on non-evaporitic lithologies and gave results of excellent quality with regards to sinkhole sagging and collapsing. There are few examples of evaporites and even fewer of evaporites mantled by quaternary deposits. This is the case of the sinkholes found in the FVG integrating ERT, RS, GPR and FDEM, where large voids were not imaged by the applied geophysical techniques.

As also reported in other similar studies (e.g., Busetti et al., 2020; Gutiérrez et al., 2011; Zini et al., 2015) this is an interesting indication for sinkhole origin, classification and evolution. In fact, although there are many examples of caves detected at different scales by geophysical surveys (e.g., Carbonel et al., 2015; Giampaolo et al., 2016; Youssef et al., 2012), cover collapse and cover suffosion sinkholes are more elusive structures having a less peculiar geophysical signature. However, repeated ERT and/or FDEM surveys could be very useful in the detection of the formation of relatively large voids and, more importantly, to highlight local water filling time variations that can be serious triggering causes to activate or reactivate sinkholes. On the other hand, repeated GPR surveys may be able to detect even small changes and movements by comparing the same horizon locations at different temporal steps. The latter can be done at first by just a visual comparison, but improved results can be achieved exploiting the various attributes of GPR in particular related to phase and frequency or texture attributes (Zhao et al., 2016). GPR has shown high potential in the early imaging of failures, voids and defects of road pavements (e.g., Saarenketo & Scullion,2000; Thitimakorn et al., 2016). Similarly, GPR could be used in this context to highlight centimetric–decimetric voids formed just below the binder/foundation/subgrade thanks to its very high resolution.

In the present case, the integration of geomorphological analysis, crack monitoring, and combined

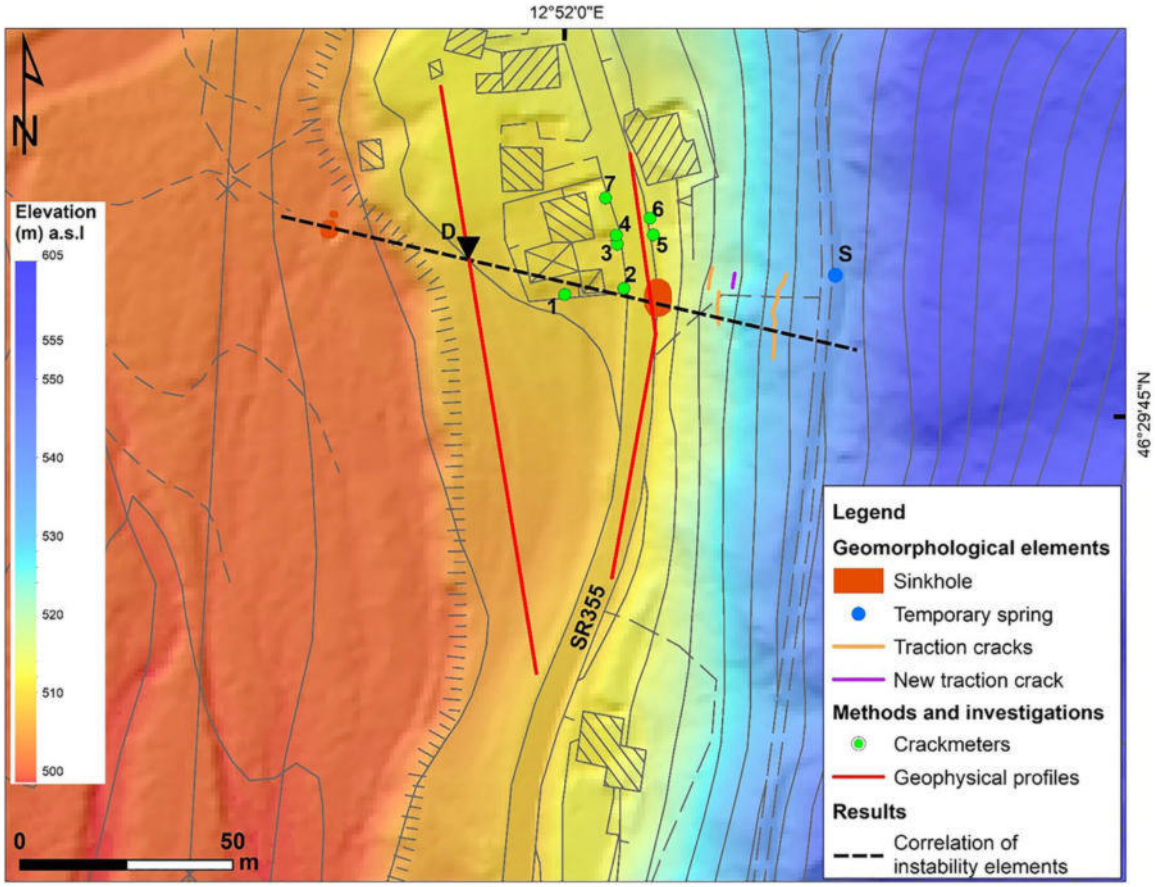

FIGURE 6 Spatial correlation of sinkholes, ground and infrastructure cracks and hydrological elements in the study area. Green points represent the crack-metres (on walls and pavements); orange and purple lines depict main ground fractures; D refers to the location of the abrupt lateral discontinuity as highlighted by a geophysics analysis (Figure 4); S label marks a temporary spring. The black dotted segment spatially links the previous elements. See text for further details and discussion.

multi-resolution geophysical techniques, allowed for a broader examination of the sinkhole in a wider context (Figure 6). However, for analysis at the scale of several square kilometres, other techniques and acquisition protocols can be essential such as, for instance, airborne geophysics combined with dedicated LiDAR and InSAR analyses.

We found that there is a straight ESE–WNW correlation between the main and the other two sinkholes, as well as with the abrupt lateral discontinuity imaged by ERT and RS data (letter 'D' in Figure 6). Traction cracks developed along the same line-up and there is a spring located only a few metres to the North. This ESE–WNW trend can be correlated with a main groundwater path acting as a cause or concurrent cause of the sinkhole development. This demonstrates that it is not sufficient to focus on the zone where a specific event occurred, but it is mandatory to broaden the area of analysis taking into consideration a multi-scale, multi-technique, and integrated approach.

None of the analyses showed evidence of relatively large caves and agree that in this area sinkholes are not linked to the bedrock depth: a deeper bedrock does not mean a safer area. The presence of a groundwater path represents a triggering factor by increasing local karstification and favouring sinkhole processes. The sinkhole could start as cover suffosion coupled with downward migration of the cover material into pipes present in the bedrock enlarged by solution (Gutiérrez et al., 2008) (Figure 7a). The presence of more competent layers on the shallower portion of the stratigraphic profile that, in the case of the damaged road is represented by the road pavement and by a layer of more cohesive cover, allows for the formation of a void beneath (Figure 7b) without any visible evidence of what is occurring below the surface. With the evolution of the suffosion sinkhole, the void under the anthropogenic cover enlarges up to the occurrence of a collapse (Figure 7c).

A situation like the one just described is a definitive risk in an urban environment, especially due to the lack of precursor signs on the surface. Following the evolution of the phenomena by the use of a geophysical integrated approach would not prevent collapses but may prevent

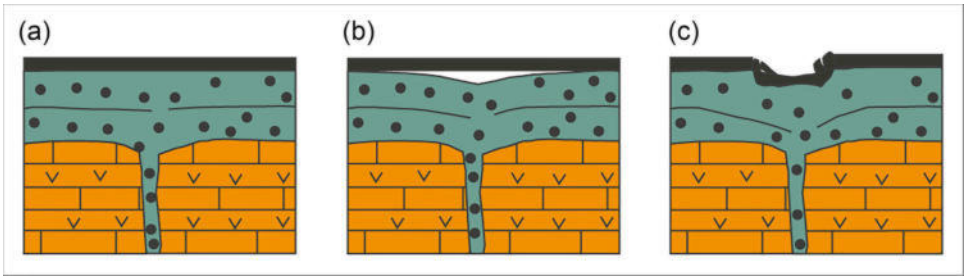

FIGURE 7 Subsidence mechanism generating the occurred sinkhole. The thick black line corresponds to the man-made cover, the green colour represents the granular sediments and the evaporitic bedrock is represented in orange. (a) Migration of particles through dissolution conduits in an early stage; (b) migration of particles through dissolution conduits and void formation beneath the man-made cover; (c) collapse of the man-made cover.

possible future road disasters. Moreover, if the problem is correctly identified, a monitoring programme can be design in order to detect possible precursors of large failures.

CONCLUSIONS

The presence of evaporitic bedrock is certainly the main predisposing factor for sinkhole occurrence in infrastructured areas and it has to be monitored over time given its fast dissolution (Calligaris et al., 2020) in order to avoid the occurrence of sudden collapses which could represent a serious risk for people and man-made structures. On a test site area located in the extreme NE corner of the Italian peninsula, a joint geophysical approach was applied in order to tune an integrated monitoring method in a site where a sinkhole formed in 2017 causing an interruption to traffic on a major roadway. From this study emerged the importance of applying and integrating different methods at a time to clarify the imaged geological model and to explain the sinkhole occurrence. Electrical and seismic tomographies allow for the image of the subsurface down to a depth exceeding 15–20 m, whereas GPR and EM techniques imaged the shallowest portion down to about 4–5 m from the surface. Repeated ERT and/or FDEM surveys could be very useful to detect the formation of relatively large voids and, even more important, to highlight local water filling time variations that can be significant triggering causes to activate or reactivate sinkholes. Repeated use of GPR could image superficial void of decimetric dimension, and this could help monitor the road over time not in terms of preventing a collapse, but to avoid possible future disasters on roads. In the present case, the formed sinkhole occurred due to the presence of the evaporitic bedrock which had been heavily karstified by the circulation of the ground and spring waters. The phenomenon likely has a complex genesis and the presence of a more competent layer at the surface, that is the road, did not allow for researchers to follow the ongoing natural process of sinkhole formation due to the asphalt cover.

ACKNOWLEDGEMENTS

The authors would like to acknowledge the functionaries of the Geological Survey of the Friuli Venezia Giulia (FVG) Region: Chiara Piano, Franco Liuzzi and Fabrizio Kranitz, the scientific coordinators from the various joint projects with the University of Trieste, Dept. of Mathematics and Geosciences. The Authors wish to thank the functionaries from FVG Strade, Alessandra Biondin and Alessio Vidoni, who facilitated the road closures necessary to conduct our investigations. We thank Dario Saponaro and Alessandra Lanzoni for data collection in the field. The associate editor Sebastian Uhlemann and two anonymous reviewers are acknowledged for their advisable comments and suggestions.

DATA AVAILABILITY STATEMENT

The data sets generated and analysed during the current study are available from the corresponding author on reasonable request or from Geological Survey of the Friuli Venezia Giulia Region (Italy).

REFERENCES

Argentieri, A., Carluccio, R., Cecchini, F., Chiappini, M., Ciotoli, G., De Ritis, R. et al. (2015) Early stage sinkhole formation in the Acque Albule basin of central Italy from geophysical and geochemical observations. *Engineering Geology*, 191, 36–47. https://doi.org/10.1016/j.enggeo.2015.03.010

Arjwech, R., Ruansorn, T., Schulmeister, M., Everett, M.E., Thitimakorn, T., Pondthai, P. et al. (2021) Protection of electricity transmission infrastructure from sinkhole hazard based on electrical resistivity tomography. *Engineering Geology*, 293, 106318. https://doi.org/10.1016/j.enggeo.2021.106318

Baer, G., Magen, Y., Nof, R., Raz, E., Lyakhovsky, V. & Shalev, E. (2018) InSAR measurements and viscoelastic modelling of sinkhole precursory subsidence: implications for sinkhole formation, early warning, and sediment properties. *Journal of Geophysical Research-Earth Surface*, 123, 678–693. https://doi.org/10.1002/2017JF004594

Basso, A., Bruno, E., Parise, M. & Pepe, M. (2013) Morphometric analysis of sinkholes in a karst coastal area of southern Apulia (Italy). *Environmental Earth Sciences*, 70, 2545–2559. https://doi.org/10.1007/s12665-013-2297-z

Borgatti, L., Forte, E., Mocnik, A., Zambrini, R., Cervi, F., Martinucci, D. et al. (2017) Detection and characterization of animal burrows within river embankments by means of coupled remote sensing and

geophysical techniques: lessons from River Panaro (northern Italy). *Engineering Geology*, 226, 30, 277–289. https://doi.org/10.1016/j.enggeo.2017.06.017.

Brinkmann, R., Parise, M. & Dye, D. (2008) Sinkhole distribution in a rapidly developing urban environment: Hillsborough County, Tampa Bay area, Florida. *Engineering Geology*, 99, 169–184. https://doi.org/10.1016/j.enggeo.2007.11.020

Bruno, E., Calcaterra, D. & Parise, M. (2008) Development and morphometry of sinkholes in coastal plains of Apulia, southern Italy: preliminary sinkhole susceptibility assessment. *Engineering Geology*, 99, 198–209. https://doi.org/10.1016/j.enggeo.2007.11.017

Busetti, A., Calligaris, C., Forte, E., Areggi, G., Mocnik, A. & Zini, L. (2020) Non-invasive methodological approach to detect and characterize high-risk sinkholes in urban cover evaporite karst: integrated reflection seismics, PS-InSAR, leveling, 3D-GPR and ancillary data. A NE Italian case study. *Remote Sensing*, 12(22), 3814. https://doi.org/10.3390/rs12223814

Buttrick, D.B. & van Schalkwyk, A. (1998) Hazard and risk assessment for sinkhole formation on dolomite land in South Africa. *Environmental Geology*, 36, 170–178. https://doi.org/10.1007/s002540050333

Calligaris, C., Devoto, S., Zini, L. & Cucchi, F. (2017a) An integrated approach for investigations of ground subsidence phenomena in the Ovaro Village (NE Italy). In: Renard, P. & Bertrand, C. (Eds.) *EuroKarst 2016, Neuchâtel. Advances in karst science*. Cham: Springer, pp. 71–77. https://doi.org/10.1007/978-3-319-45465-8_8

Calligaris, C., Devoto, S. & Zini, L. (2017b) Evaporite sinkholes of the Friuli Venezia Giulia region (NE Italy). *Journal of Maps*, 13(2), 406–414. https://doi.org/10.1080/17445647.2017.1316321

Calligaris, C., Ghezzi, L., Petrini, R., Lenaz, D. & Zini, L. (2019) Evaporite dissolution rate through an on-site experiment into piezometric tubes applied to the real case-study of Quinis (NE Italy). *Geosciences*, 9, 298. https://doi.org/10.3390/geosciences9070298

Calligaris, C., Zini, L., Nisio, S. & Piano, C. (2020) Sinkholes in the Friuli Venezia Giulia Region focus on the evaporites. In: *Applied geology*. Cham: Springer. https://doi.org/10.1007/978-3-030-43953-8_5

Caproni, F. (2017) *Intervento urgente per la sistemazione del dissesto geologico avvenuto al km 11+182 della SR n° 355 "della Val Degano"*. Technical report, p. 16.

Carbonel, D., Rodríguez-Tribaldos, V., Gutiérrez, F., Galve, J.P., Guerrero, J., Zarroca, M. et al. (2015) Investigating a damaging buried sinkhole cluster in an urban area integrating multiple techniques: geomorphological surveys, DInSAR, GPR, ERT, and trenching. *Geomorphology*, 229, 3–16. https://doi.org/10.1016/j.geomorph.2014.02.007

Ciotoli, G., Finoia, M.G., Liperi, L., Meloni, F., Nisio, S., Tonelli, V. et al. (2015) Sinkhole susceptibility map of the Lazio Region, Central Italy. *Journal of Maps*, 12, 287–294. https://doi.org/10.1080/17445647.2015.1014939

Cooper, A.H. (1998) In: Maund, J.G. & Eddleston, M. (Eds.) *Subsidence hazards caused by the dissolution of Permian gypsum in England: geology, investigation and remediation*. London, UK: Geohazards in Engineering Geology, Geological Society of London, pp. 265–275. https://www.lyellcollection.org/doi/10.1144/gsl.eng.1998.015.01.27

Cooper, A.H., Farrant, A.R. & Price, S.J. (2011) The use of karst geomorphology for planning, hazard avoidance and development in Great Britain. *Geomorphology*, 134, 118–131. https://doi.org/10.1016/j.geomorph.2011.06.004

Cucchi, F. & Giorgetti, F. (1997) *Relazione sulle risultanze delle campagne geofisiche e dei rilevamenti geologici eseguiti sul terreno*. Final report. Department of Geological, Environmental and Marine Sciences, University of Trieste, p. 23.

Dahm, T., Kühn, D., Ohrnberger, M., Kröger, J., Wiederhold, H., Reuther, C.-D. et al. (2010) Combining geophysical data sets to study the dynamics of shallow evaporites in urban environments: application to Hamburg, Germany. *Geophysical Journal International*, 181, 154–172. https://doi.org/10.1111/j.1365-246X.2010.04521.x

De Ritis, R., Nardi, A., Materni, V., Venuti, A., Stefanelli, P., Rotella, G. et al. (2020) Multidisciplinary study of subsidence and sinkhole occurrences in the Acque Albule Basin (Roma, Italy). *Earth and Space Science*, 7, e2019EA000870. https://doi.org/10.1029/2019EA000870

De Waele, J., Piccini, L., Columbu, A., Madonia, G., Vattano, M., Calligaris, C. et al. (2017) Evaporite karst in Italy: a review. *International Journal of Speleology*, 46, 137–168. https://doi.org/10.5038/1827-806X.46.2.2107

Delkhahi, B., Nassery, H.R., Vilarrasa, V., Alijani, F. & Ayora, C. (2020) Impacts of natural CO_2 leakage on groundwater chemistry of aquifers from the Hamadan Province, Iran. *International Journal of Greenhouse Gas Control*, 96, 103001. https://doi.org/10.1016/j.ijggc.2020.103001

Desir, G., Gutiérrez, F., Merino, J., Carbonel, D., Benito-Calvo, A., Guerrero, J. et al. (2018) Rapid subsidence in damaging sinkholes: measurement by high-precision leveling and the role of salt dissolution. *Geomorphology*, 303, 393–409. https://doi.org/10.1016/j.geomorph.2017.12.004

Dou, J., Li, X., Yunus, A.P., Paudel, U., Chang, K.-T., Zhu, Z. et al. (2015) Automatic detection of sinkhole collapses at finer resolutions using a multi-component remote sensing approach. *Natural Hazards*, 78, 1021–1044. https://doi.org/10.1007/s11069-015-1756-0

Festa, V., Fiore, A., Parise, M. & Siniscalchi, A. (2012) Sinkhole evolution in the Apulian karst of southern Italy: a case study, with some considerations on sinkhole hazards. *Journal of Cave and Karst Studies*, 74, 137–147. https://doi.org/10.4311/2011JCKS0211

Galve, J.P., Remondo, J. & Gutiérrez, F. (2011) Improving sinkhole hazard models incorporating magnitude-frequency relationships and nearest neighbor analysis. *Geomorphology*, 134, 157–170. https://doi.org/10.1016/j.geomorph.2011.05.020

Galve, J.P., Castañeda, C. & Gutiérrez, F. (2015) Railway track deformation detected by DInSAR over a dissolution-induced subsidence area of the Ebro Valley evaporite karst, Spain. *Natural Hazards and Earth System Sciences*, 3, 3967–3981. https://doi.org/10.5194/nhessd-3-3967-2015

García-Moreno, I. & Mateos, R.M. (2011) Sinkholes related to discontinuous pumping: susceptibility mapping base on geophysical studies. The case of Crestatx (Mallorca, Spain). *Environmental Earth Sciences*, 64, 523–537. https://doi.org/10.1007/s12665-010-0876-9

Giampaolo, V., Capozzoli, L., Grimaldi, S. & Rizzo, E. (2016) Sinkhole risk assessment by ERT: the case study of Sirino Lake (Basilicata, Italy). *Geomorphology*, 253, 1–9. https://doi.org/10.1016/j.geomorph.2015.09.028

Guerrero, J., Sevil, J., Desir, G., Gutiérrez, F., Arnay, A.G., Galve, J.P. et al. (2021) The detection of active sinkholes by airborne differential LiDAR DEMs and InSAR cloud computing tools. *Remote Sensing*, 13, 3261. https://doi.org/10.3390/rs13163261

Gutiérrez, F., Galve, J.P., Guerrero, J., Lucha, P., Cendrero, A., Remondo, J. et al. (2007) The origin, typology, spatial distribution, and detrimental effects of the sinkholes developed in the alluvial evaporite karst of the Ebro River valley downstream Zaragoza City (NE Spain). *Earth Surface Processes Landforms*, 32, 912–928. https://doi.org/10.1002/esp.1456

Gutiérrez, F., Guerrero, J. & Lucha, P. (2008) A genetic classification of sinkholes illustrated from evaporite paleokarst exposures in Spain. *Environmental Geology*, 53, 993–1006. https://doi.org/10.1007/s00254-007-0727-5

Gutiérrez, F., Galve, J.P., Lucha, P., Castañeda, C., Bonachea, J. & Guerrero, J. (2011) Integrating geomorphological mapping, trenching, InSAR and GPR for the identification and characterization of sinkholes in the mantled evaporite karst of the Ebro Valley (NE Spain). *Geomorphology*, 134, 144–156. https://doi.org/10.1016/j.geomorph.2011.01.018

Gutiérrez, F., Parise, M., DeWaele, J. & Jourde, H. (2014) A review on natural and human-induced geohazards and impacts in karst. *Earth*

Science Reviews, 138, 61–88. https://doi.org/10.1016/j.earscirev.2014.08.002

Gutiérrez, F. (2016) *Sinkhole hazards*. Oxford Research Encyclopedia of Natural Hazard Science. https://doi.org/10.1093/acrefore/9780199389407.013.40

Gutiérrez, F., Zarroca, M., Linares, R., Roqué, C., Carbonel, D., Guerrero, J. et al. (2018) Identifying the boundaries of sinkholes and subsidence areas via trenching and establishing setback distances. *Engineering Geology*, 233, 255–268. https://doi.org/10.1016/j.enggeo.2017.12.015

Intrieri, E., Gigli, G., Nocentini, M., Lombardi, L., Mugnai, F., Fidolini, F. et al. (2015) Sinkhole monitoring and early warning: an experimental and successful GB-InSAR application. *Geomorphology*, 241, 304–314. https://doi.org/10.1016/j.geomorph.2015.04.018

Jones, C.E. & Blom, R.G. (2014) Bayou Corne, Louisiana, sinkhole: precursory deformation measured by radar interferometry. *Geology*, 42, 111–114. https://doi.org/10.1130/G34972.1

Karimi, H. & Taheri, K. (2010) Hazards and mechanism of sinkholes on Kabudar Ahang and Famenin plains of Hamadan, Iran. *Natural Hazards*, 55(2), 481–499. https://doi.org/10.1007/s11069-010-9541-6

Kersten, T., Kobe, M., Gabriel, G., Timmen, L., Schon, S. & Vogel, D. (2017) Geodetic monitoring of subrosion-induced subsidence processes in urban areas. *Journal of Applied Geodesy*, 11, 21–29. https://doi.org/10.1515/jag-2016-0029

Kim, Y.J., Nam, B.H. & Youn, H. (2019) Sinkhole detection and characterization using LiDAR-derived DEM with logistic regression. *Remote Sensing*, 11, 1592. https://doi.org/10.3390/rs11131592

Kobe, M., Gabriel, G., Weise, A. & Vogel, D. (2019) Time-lapse gravity and levelling surveys reveal mass loss and ongoing subsidence in the urban subrosion-prone area of Bad Frankenhausen, Germany. *Solid Earth*, 10(3), 599–619. https://doi.org/10.5194/se-10-599-2019

Koutepov, V.M., Mironov, O.K. & Tolmachev, V.V. (2008) Assessment of suffosion-related hazards in karst areas using GIS technology. *Environmental Geology*, 54, 957–962. https://doi.org/10.1007/s00254-007-0888-2

Krawczyk, C.M., Polom, U., Trabs, S. & Dahm, T. (2012) Sinkholes in the city of Hamburg-New urban shear-wave reflection seismic system enables high-resolution imaging of subrosion structures. *Journal of Applied Geophysics*, 78, 133–143. https://doi.org/10.1016/j.jappgeo.2011.02.003

Kühn, D., Ohrnberger, M. & Dahm, T. (2011) Imaging a shallow salt diapir using ambient seismic vibrations beneath the densely built-up city area of Hamburg, Northern Germany. *Journal of Seismology*, 15, 507–531, https://doi.org/10.1007/s10950-011-9234-y

Kuniansky, E.L., Weary, D.L. & Kaufmann, J.E. (2016) The current status of mapping karst areas and availability of public sinkhole-risk resources in karst terrains of the United States. *Hydrogeology Journal*, 24, 613–624. https://doi.org/10.1007/s10040-015-1333-3

LaBrecque, D., Morelli, G., Daily, W., Ramirez, A. & Lundegard, P. (1999) Occam's inversion of 3D electrical resistivity tomography. In: Oristaglio, M., Spies, B. & Cooper, M.R. (Eds.) *Three dimensional electromagnetics*. Tulsa, Oklahoma: Society of Exploration Geophysicists, pp. 575–590.

Lago, A.L., Borges, W.R., Barros, J.S. & de Sousa Amaral, E. (2022) GPR application for the characterization of sinkholes in Teresina, Brazil. *Environmental Earth Sciences*, 81, 132. https://doi.org/10.1007/s12665-022-10265-4

Malehmir, A., Socco, L.V., Bastani, M., Krawczyk, C.M., Pfaffhuber, A.A., Miller, R.D. et al. (2016). Near-surface geophysical characterization of areas prone to natural Hazards: a review of the current and perspective on the future. *Advances in Geophysics*, 57, 51–146. https://doi.org/10.1016/bs.agph.2016.08.001

Malinowska, A.A., Witkowski, W.T., Hejmanowski, R., Chang, L., van Leijen, F.J. & Hanssen, R.F. (2019) Sinkhole occurrence monitoring over shallow abandoned coal mines with satellite-based persistent scatterer interferometry. *Engineering Geology*, 262, 105336. https://doi.org/10.1016/j.enggeo.2019.105336

Margiotta, S., Negri, S., Parise, M. & Valloni, R. (2012) Mapping the susceptibility to sinkholes in coastal areas, based on stratigraphy, geomorphology and geophysics. *Natural Hazards*, 62, 657–676. https://doi.org/10.1007/s11069-012-0100-1

Martinotti, M.E., Pisano, L., Marchesini, I., Rossi, M., Peruccacci, S., Brunetti, M.T. et al. (2017) Landslides, floods and sinkholes in a karst environment: the 1–6 September 2014 Gargano event, southern Italy. *Natural Hazards and Earth System Sciences*, 17, 467–480. https://doi.org/10.5194/nhess-17-467-2017

Nisio, S. (2008) I sinkholes nelle altre regioni. *Memorie Descrittive della Carta Geologica d'Italia*, 85, 419–426. (In Italian)

Nouioua, I., Rouabhia, A., Fehdi, C., Boukelloul, M.L., Gadri, L., Chabou, D. et al. (2013) The application of GPR and electrical resistivity tomography as useful tools in detection of sinkholes in the Cheria Basin (northeast of Algeria). *Environmental Earth Sciences*, 68, 1661–1672. https://doi.org/10.1007/s12665-012-1859-9

Oliver-Cabrera, T., Wdowinski, S., Kruse, S. & Robinson, T. (2020) InSAR detection of localized subsidence induced by sinkhole activity in suburban West-Central Florida. *Proceeding of the International Association of Hydrological Sciences*, 382, 155–159. https://doi.org/10.5194/piahs-382-155-2020

Orhan, O., Oliver-Cabrera, T., Wdowinski, S., Yalvac, S. & Yakar, M. (2021) Land subsidence and its relations with sinkhole activity in Karapınar region, Turkey: a multi-sensor InSAR time series study. *Sensors*, 21, 774. https://doi.org/10.3390/s21030774

Pan, Z., Chen, X., Yang, X., Song, Y., Ban, R. & Zhang, M. (2022) Formation mechanism analysis of cover collapse sinkholes in Wugaishan Town, Chenzhou City, Hunan province, China. *Environmental Earth Sciences*, 81, 48. https://doi.org/10.1007/s12665-022-10171-9

Panno, S.V. & Luman, D.E. (2013) Mapping palimpsest karst features on the Illinois sinkhole plain using historical aerial photography. *Carbonates and Evaporites*, 28, 201–214. https://doi.org/10.1007/s13146-012-0107-4

Parise, M., Qiriazi, P. & Sala, S. (2004) Natural and anthropogenic hazards in karst areas of Albania. *Natural Hazards and Earth System Sciences*, 4, 569–581. https://doi.org/10.5194/nhess-4-569-2004

Parise, M. (2015) A procedure for evaluating the susceptibility to natural and anthropogenic sinkholes. *Georisk*, 9, 272–285. https://doi.org/10.1080/17499518.2015.1045002

Paukstys, B., Cooper, A.H. & Arustiene, J. (1999) Planning for gypsum geohazards in Lithuania and England. *Engineering Geology*, 52, 93–103. https://doi.org/10.1016/S0013-7952(98)00061-1

Pazzi, V., Di Filippo, M., Di Nezzac, M., Carlàa, T., Bardia, F., Marinia, F. et al. (2018) Integrated geophysical survey in a sinkhole-prone area: microgravity, electrical resistivity tomographies, and seismic noise measurements to delimit its extension. *Engineering Geology*, 243, 282–293 https://doi.org/10.1016/j.enggeo.2018.07.016

Pearson, M. (2013) *Sinkholes: common, costly and sometimes deadly*. CNN. Retrieved March 7, 2022, from https://edition.cnn.com/2013/03/01/us/florida-sinkhole-explainer/index.html.

Rodriguez, V., Gutiérrez, F., Green, A.G., Carbonel, D., Horstmeyer, H. & Schmelzbach, C. (2014) Characterizing sagging and collapse sinkholes in a mantled karst by means of Ground Penetrating Radar (GPR). *Environmental and Engineering Geosciences*, 20(2), 109–132. https://doi.org/10.2113/gseegeosci.20.2.109

Ronen, A., Ezersky, M., Beck, A., Gatenio, B. & Simhayov, R.B. (2019) Use of GPR method for prediction of sinkholes formation along the Dead Sea Shores, Israel. *Geomorphology*, 328, 28–43. https://doi.org/10.1016/j.geomorph.2018.11.030

Rosso, A. (2022). Si apre una voragine di 20 metri in un terreno a Raveo: inghiottito un frutteto. *Il Piccolo*. Retrieved October 24, 2022, from https://ilpiccolo.gelocal.it/trieste/cronaca/2022/04/22/news/si-apre-una-voragine-di-20-metri-in-un-terreno-a-raveo-inghiottito-un-frutteto-1.41391831

Saarenketo, T. & Scullion, T. (2000) Road evaluation with ground penetrating radar. *Journal of Applied Geophysics*, 43(2–4), 119–138. https://doi.org/10.1016/S0926-9851(99)00052-X

Samyn, K., Mathieu, F., Bitri, A., Nachbaur, A. & Closset, L. (2014) Integrated geophysical approach in assessing karst presence and sinkhole susceptibility along flood protection dykes of the Loire River, Orléans, France. *Engineering Geology*, 183, 170–184. https://doi.org/10.1016/j.enggeo.2014.10.013

Sevil, J., Gutiérrez, F., Zarroca, M., Desir, G., Carbonel, D., Guerrero, J. et al. (2017) Sinkhole investigation in an urban area by trenching in combination with GPR, ERT and high-precision leveling. Mantled evaporite karst of Zaragoza city, NE Spain. *Engineering Geology*, 231, 9–20. https://doi.org/10.1016/j.enggeo.2017.10.009

Sevil, J., Gutiérrez, F., Carmicer, C., Carbonel, D., Desir, G., Garcià-Arnay, Á. et al. (2020) Characterizing and monitoring a high-risk sinkhole in an urban area underlain by salt through non-invasive methods: detailed mapping, high-precision leveling and GPR. *Engineering Geology*, 272, 105641. https://doi.org/10.1016/j.enggeo.2020.105641

Shi, Y., Tang, Y., Lu, Z., Kim, J.W. & Peng, J. (2019) Subsidence of sinkholes in Wink, Texas from 2007 to 2011 detected by time-series InSAR analysis. *Geomatics, Natural Hazards and Risk*, 10, 1125–1138. https://doi.org/10.1080/19475705.2019.1566786

Solari, L., Montalti, R., Barra, A., Monserrat, O., Bianchini, S. & Crosetto, M. (2020) Multi-temporal satellite interferometry for fast-motion detection: an application to salt solution mining. *Remote Sensing*, 12, 3919. https://doi.org/10.3390/rs12233919

Stierman, D.J. (2004). Geophysical detection of caves and Karstic voids. In: Gunn, J. (Ed.) *Encyclopedia of caves and karst science*. New York: Fitzroy Dearborn, pp. 377–380.

Taheri, K., Gutiérrez, F., Mohseni, H., Raeisi, E. & Taheri, M. (2015) Sinkhole susceptibility mapping using the analytical hierarchy process (AHP) and magnitude–frequency relationships: a case study in Hamadan province, Iran. *Geomorphology*, 234, 64–79. https://doi.org/10.1016/j.geomorph.2015.01.005

Taheri, K., Shahabi, H., Chapi, K., Shirzadi, A., Gutiérrez, F. & Khosravi, K. (2019) Sinkhole susceptibility mapping: a comparison between Bayes-based machine learning algorithms. *Land Degradation and Development*, 30(7), 730–745. https://doi.org/10.1002/ldr.3255

Taheri, K., Missimer, T.M., Mohseni, H., Fidelibus, M.D., Fathollahy, M. & Taheri, M. (2021) Enhancing spatial prediction of sinkhole susceptibility by mixed waters geochemistry evaluation: application of ROC and GIS. *Environmental Earth Sciences*, 80(14), 1–28. https://doi.org/10.1007/s12665-021-09763-8

Talib, O.C., Shimon, W., Sarah, K. & Tonian, R. (2022) Detection of sinkhole activity in West-Central Florida using InSAR time series observations. *Remote Sensing of Environment*, 269, 112793. https://doi.org/10.1016/j.rse.2021.112793

Theron, A., Engelbrecht, J., Kemp, J., Kleynhans, W. & Turnbull, T. (2017) Detection of sinkhole precursors through SAR interferometry: radar and geological considerations. *IEEE Geoscience and Remote Sensing Letters*, 14(6), 871–875. https://doi.org/10.1109/LGRS.2017.2684905

Thierry, P., Prunier-Leparmentier, A.M., Lembezat, C., Vanoudheusden, E. & Vernoux, J.F. (2009) 3D geological modelling at urban scale and mapping of ground movement susceptibility from gypsum dissolution: the Paris example (France). *Engineering Geology*, 105, 51–64. https://doi.org/10.1016/j.enggeo.2008.12.010

Thitimakorn, T., Kampananon, N., Jongjaiwanichkit, N. & Kupongsak, S. (2016) Subsurface void detection under the road surface using ground penetrating radar (GPR), a case study in the Bangkok metropolitan area, Thailand. *International Journal of Geo-Engineering*, 7(2). https://doi.org/10.1186/s40703-016-0017-8

Vennari, C. & Parise, M. (2022) A chronological database about natural and anthropogenic Sinkholes in Italy. *Geosciences*, 12, 200. https://doi.org/10.3390/geosciences12050200

Venturini, C., Spalletta, C., Vai, G.B., Pondrelli, M., Delzotto, S., Fontana, C. et al. (2009) *Note Illustrative Carta geologica d'Italia alla scala 1:50.000 Foglio 031 Ampezzo*. Rome, Italy: ISPRA, pp. 7–222.

Waltham, T., Bell, F. & Culshaw, M. (2005) *Sinkholes and subsidence: karst and cavernous rocks in engineering and construction*. Chichester, UK: Springer. https://doi.org/10.1007/b138363

Wang, Y., Tran, K.T. & Horhota, D. (2022) *Road sinkhole imaging with ambient noise tomography*. Charlotte, North Carolina: Geo-Congress: Geophysical and Earthquake Engineering and Soil Dynamics. https://doi.org/10.1061/9780784484043.004

Wust-Bloch, G.H. & Joswig, M. (2006) Pre-collapse identification of sinkholes in unconsolidated media at Dead Sea area by 'nano-seismic monitoring' (graphical jackknife location of weak sources by few, low-SNR records). *Geophysical Journal International*, 167, 3, 1220–1232, https://doi.org/10.1111/j.1365-246X.2006.03083.x

Yordkayhun, S., Wattanasen, K. & Thungpru, N. (2022) Geophysical investigation of the karst geosites in Satun UNESCO Global Geopark, Thailand: implication for sinkhole hazard assessment. *Geosciences Journal*, 26(2), 249–266. https://doi.org/10.1007/s12303-021-0025-3

Youssef, A.M., El-Kaliouby, H. & Zabramawi, Y.A. (2012) Sinkhole detection using electrical resistivity tomography in Saudi Arabia. *Journal of Geophysics and Engineering*, 9, 655–663. https://doi.org/10.1088/1742-2132/9/6/655

Zhao, W., Forte, E. & Pipan, M. (2016) Texture attribute analysis of GPR data for archaeological prospection. *Pure and Applied Geophysics*, 173, 2237–2251. https://doi.org/10.1007/s00024-016-1355-3

Zhu, J., Taylor, T.P., Currens, J.C. & Crawford, M.M. (2014) Improved karst sinkhole mapping in Kentucky using LiDAR techniques: a pilot study in Floyds Fork watershed. *Journal of Cave and Karst Studies*, 76, 207–216. https://doi.org/10.4311/2013ES0135

Zhu, J., Nolte, A.M., Jacobs, N. & Ye, M. (2020) Using machine learning to identify karst sinkholes from LiDAR-derived topographic depressions in the Bluegrass Region of Kentucky. *Journal of Hydrology*, 588, 125049. https://doi.org/10.1016/j.jhydrol.2020.125049

Zhende, G., Xiaozhen, J., Ming, G. (2013) A calibration test of karst collapse monitor-ing device by optical time domain reflectomewtry (BOTDR) technique. In L. Land, D.H. Doctor, J.B. Stephenson (Eds.), Sinkholes and the engineering and environmental impacts of karst (pp 71.77). Carlsbad, NM: National Cave and Karst Research Institute.

Zini, L., Calligaris, C., Forte, E., Petronio, L., Zavagno, E., Boccali, C. et al. (2015) A multidisciplinary approach in sinkhole analysis: the Quinis village case study (NE-Italy). *Engineering Geology*, 197, 132–144. https://doi.org/10.1016/j.enggeo.2015.07.004

How to cite this article: Calligaris, C., Forte, E., Busetti, A. & Zini, L. (2023) A joint geophysical approach to tune an integrated sinkhole monitoring method in evaporitic environments. *Near Surface Geophysics*, 1–16. https://doi.org/10.1002/nsg.12261

CHAPTER 3.3

Published in: Andreo, B., Barberá, J.A., Durán-Valsero, J.J., Gil-Márquez, J.M., Mudarra, M. (eds) EuroKarst 2022, Málaga. Advances in Karst Science. Springer, Cham.

https://dx.doi.org/10.1007/978-3-031-16879-6_30

Gypsum Dissolution Rate, New Data and Insights

Alice Busetti[1]*, Chiara Calligaris[1], Luca Zini[1]

[1] Mathematical and Geosciences Department, University of Trieste, Via Weiss 2, 34128 Trieste, Italy

Gypsum Dissolution Rate, New Data and Insights

A. Busetti, C. Calligaris, and L. Zini

Abstract

Sinkholes linked to covered evaporite karst in urban environments still represent a challenge in hazard and risk assessment. The Quinis hamlet, located in Friuli Venezia Giulia region (NE Italy), is heavily affected by sinkhole phenomena (linked to an evaporitic bedrock), which deeply interested infrastructures and houses. In order to understand the evolution of the sinking phenomena, a field experiment started on the dissolution rate of the gypsum. In 17 existing piezometers, at different depths, 51 evaporitic rock samples were exposed to the naturally occurring variation of relative humidity, air flow and hydrodynamics. The rock samples were placed respectively in the aeration, in the fluctuation and in the phreatic section of the piezometric tubes. Data related to groundwater level fluctuations, temperature and electrical conductivity were collected. After four months, rock samples were removed, weighted and the volume loss evaluated. The obtained results indicate that rock sample reduction is not only dependent on the groundwater level fluctuations and on the number of days during which the samples are immersed in the groundwaters but also on the mineralization of the latter. Some of the rock samples have been almost completely dissolved, with dissolution rate values almost eight times bigger than expected if compared to the available literature data. The proposed approach had as aim to evaluate the quickness of the dissolution process, which is dependant on several causes (groundwater level fluctuations, type of rocks, chemical characteristics of the groundwaters, etc.) and represents a novel contribution to the overall knowledge of karst processes with noticeable impacts on human-built construction.

Keywords

Sinkhole • Evaporite karst • Dissolution rate • Risk assessment

1 Introduction

Sinkhole phenomena, linked to the presence of an evaporitic bedrock, developed in urban areas are very dangerous if considering the damage that they can cause on man-made structures. The results of recent investigations (Calligaris et al. 2020) have shown that Friuli Venezia Giulia region (here after noted as FVG) is one of the most affected areas in northern Italy with 1199 sinkholes inventoried.

In FVG, only 1% of the karstifiable lithologies are represented by evaporites (Calligaris et al. 2017), which can be identified mainly along two E–W alignments: one in correspondence with the Tagliamento valley to the south, and the other along Pesarina and Pontaiba valleys (Fig. 1) to the north.

The main problem with these phenomena is the occurrence speed with which they take place and develop over time due to the extremely high karstifiability and solution rate of the evaporites (0.68–1.14 mm/y, Klimchouk et al. 1996 and 0.4–1.0 mm/y, Cucchi et al. 1998). The latter is very high if compared for example to limestone one (0.009–0.14 mm/y, Furlani et al. 2009) allowing thus to understand the extreme vulnerability linked to territories where these lithologies are present.

The hazard assessment jointly with the presence of element at risk took Calligaris et al. (2019) to try to quantify, thanks to an on field experiment, the solution rate of the evaporite bedrock in the test site area of Quinis (Enemonzo—UD). The field experiment, carried out for the first time, consisted of installing core rock evaporitic samples, drawn from the drilled boreholes, in 7 piezometers at different depths for a period of one year. The aim was to recreate for

A. Busetti (✉) · C. Calligaris · L. Zini
Mathematics and Geosciences Department (DMG), University of Trieste, Via Weiss 2, 34128 Trieste, Italy
e-mail: abusetti@units.it

B. Andreo et al. (eds.), *EuroKarst 2022, Málaga*, Advances in Karst Science,
https://doi.org/10.1007/978-3-031-16879-6_30

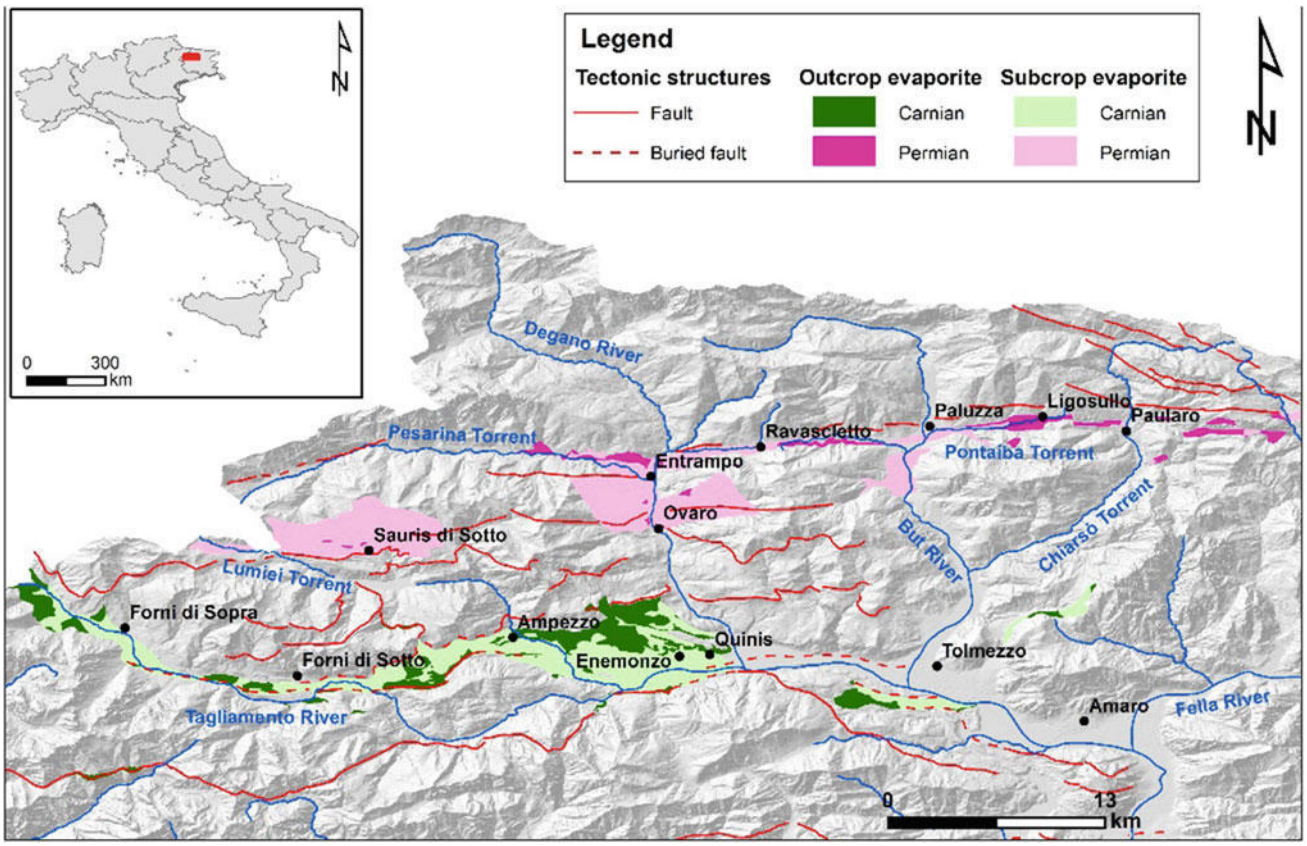

Fig. 1 Sketch of the evaporite outcrops (dark green and dark pink) and of the mantled or overlaid by a non-karst rock evaporites (light green and light pink) in the NW sector of the Friuli Venezia Giulia region

the rock samples the original conditions in order to assess their loss of weight and volume. The obtained results witnessed a range of solubility in between 0 and 8.1 mm/y with an average value of 2.1 mm/y, double the known maximum one. The high dissolution rate demonstrated and its spatial variability encouraged to investigate more in detail the particular situation in the inhabited area of Quinis.

In the present paper, we propose a new field experiment by placing rock samples in piezometric tubes at different depths to better understand the causes of the fast dissolution rate.

2 Study Area

The sinkhole evolution at Quinis is related to the presence of the Raibl Formation (RBA—Carnian in age) in the bedrock, which is subdivided into three different members (Venturini et al. 2009): red shales member (RBA1), gypsum and gray dolostones member (RBA2) and marls and dolostones member (RBA3). The RBA2 is the one present in the study area, and according to Venturini et al. (2009) is composed mainly by gray and white saccharoid gypsum with marl inclusions at the top, yellowish dolomitic marls, and to a lesser extent, blackish or greenish clays and dark limestone in thin layers.

The evaporitic bedrock is mantled by loose quaternary deposits such as glacial till, alluvial and colluvial deposits having a variable thickness, increasing from north to south, from a few meters up to more than 50 in correspondence of the Tagliamento riverbed. These materials are extremely heterogeneous due to complex and articulated depositional patterns conditioned by the tectonical setting, the alternation of glacial and interglacial periods, the recent depositional events due to the Tagliamento River and the overlapping alluvial fan present northern of Quinis.

In this framework, the high solubility of the gypsum and gray dolomites, scarcely outcropping in the investigated area, together with important oscillations of the groundwater level (Zini et al. 2015), has led over time to the formation of important sinkhole phenomena (Gutiérrez et al. 2008), which in turn caused extensive damages to local infrastructures and houses.

In the Enemonzo municipality, since the end of the nineteenth century, 208 sinkholes were inventoried, of which

46 are cover suffosion, 40 are cover collapse, and the remaining have an undefined typology. The latter was detected by desk activities and were not surveyed or not anymore identifiable in the field. In the Quinis village, actually 32 are the recognized sinkholes and most of them are active. Since the first time that these phenomena have been identified in the area (Marinelli 1898), some buildings have been demolished (Fig. 2) and others are actually damaged.

3 Materials and Methods

In the Quinis village, over time, 24 boreholes were drilled and later equipped with different instruments: 2 assestimeters, 2 Casagrande piezometers, 1 borehole drilled for geophysical proposes, and 19 piezometric tubes. 17 of the 19 piezometers (Fig. 2) have been used in the ongoing field experiment. The piezometers are well spread, covering the whole study area.

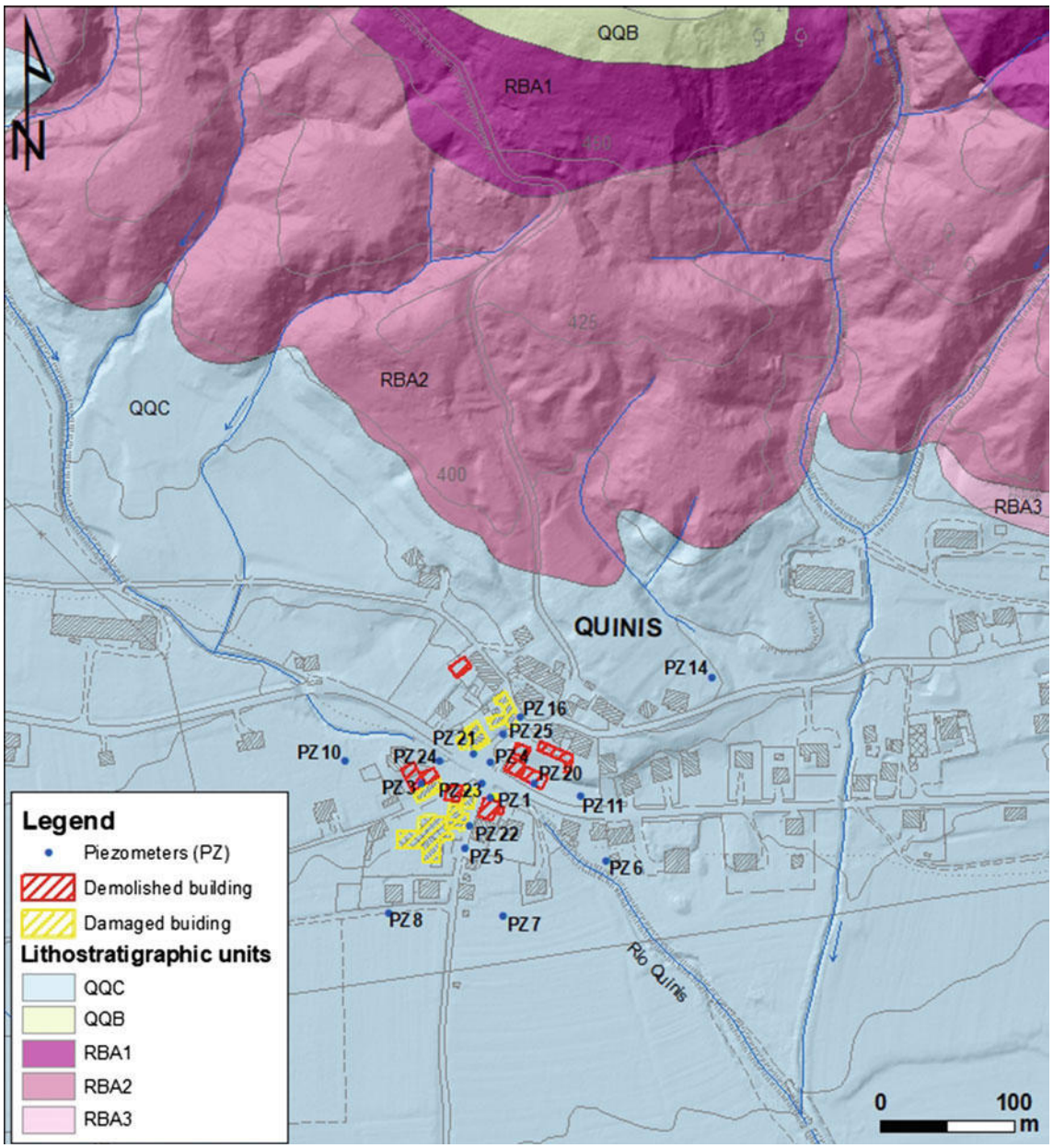

Fig. 2 Geological map of the study area with the evidence of the demolished and damaged building from 1800s to nowadays. Piezometers are identified as PZ. Lithostratigraphic units: (QQC) fluvial gravel and sand and (QQB) glacial till, Pleistocene-Holocene in age; (RBA1) red shales member, (RBA2) gypsum and gray dolostones member and (RBA3) marls and dolostone member belong to the Raibl Formation, Triassic in age (modified after Venturini et al. 2009)

In each piezometer, 3 rock samples have been installed placed at different depths:

- the shallower one at about 2 m below the ground level (in the vadose zone never reached by the groundwater);
- the middle one in the epiphreatic zone, where the groundwater level fluctuates;
- the third one in the phreatic zone (always immersed in the groundwater).

The positioning depth has been decided according to the level of the groundwater and the position of the screens.

Before the installation, a preparatory phase took place. In order to prepare rock samples as uniform as possible not only from a dimensional point of view, but also from a mineralogical one. 12 boulders were collected in the Entrampo (Ovaro) quarry and later shaped as 115 parallelepiped having 8 cm of height and a square base of 4 cm with an area (A) of 160 cm^2.

All samples were weighed and 78 of these were selected choosing the most similar in weight (range from 273.4 to 300 g) and dimension. Once over-dried in the oven at 50 °C for 48 h, a second weight (W_1) was done.

Before the installation, volume and density (ρ) were also measured. The first as volume difference by using a graduated cylinder containing water. Density was calculated as the quotient between dry weight and volume. The whole process is summarized in Fig. 3.

The 51 rock samples chosen were then installed in the piezometers wrapping each single parallelepiped in a plastic net and later fixed to a rope.

After the first 4 months (June 18, 2021–October 1, 2021), the samples were collected, over-dried for 48 h at 50 °C, weighted (W_2) and weight loss calculated (W_1-W_2).

The weight loss is functional to the dissolution rate evaluation according to the formula proposed by Plan (2005):

$$R = \left[\frac{(W_1 - W_2)}{A\rho}\right] * 10(\text{mm/4 month})$$

Data-logger devices, able to record in continuous groundwater level, temperature and electrical conductivity variations, were installed in 7 piezometers.

Two data-loggers WLT-Diver Eijekelkamp (pressure range 10 m, accuracy ± 0.5 cm, resolution 0.2 cm; temperature range −20 °C to +80 °C, accuracy ± 0.1 °C, resolution 0.01 °C) were installed in PZ10 and PZ11; five CTD-Diver Eijekelkamp (pressure range 10 m, accuracy ± 0.5 cm, resolution 0.2 cm; temperature range −20 °C to +80 °C, accuracy ± 0.1 °C, resolution 0.01 °C, Electrical Conductivity range 0–120 mS/cm, accuracy ± 1%, resolution ± 0.1%) were installed in PZ7, PZ22, PZ23, PZ24 and PZ25. The compensation of the atmospheric pressure variability was ensured by a Baro-Diver from Eijekelkamp (pressure range 150 cm, accuracy ± 0.5 cm, resolution 0.2 cm) installed in the PZ1, in the core of the study area. All instruments were synchronized and had a recording range interval of 30 min.

Rainfall data were downloaded from the OSMER FVG network (https://www.osmer.fvg.it/archivio.php?ln=&p=dati) for the Enemonzo rainfall station.

4 Results

Within the 1-year project, during the first check, after four months after the installation, data-logger devices were downloaded, and rock samples were collected. The monitored period coincided with a summer season characterized by a maximum daily precipitation of 60.5 mm (June 18, 2021–October 1, 2021). Six are the main rainfall events that had a meaningful response on the groundwater levels recorded by the data-logger devices (Fig. 4).

In accordance with the bedrock deepening from north of Quinis where it is seldom exposed to the south where it is mantled by even more than 50 m of deposits, the groundwater level fluctuation is lower in the northern part (PZ11 and PZ25, a few centimeters) and higher (PZ7 and PZ8, 13 m) in the southern of the study area.

During the four-month experiment, 27 rock samples always remained always above the groundwater level. Twenty-three of them recorded a weight loss of up to 6%; three (PZ1, PZ10 and PZ23) showed a weight loss of about 20%. The remaining PZ11 had a higher weight loss of about 42%.

The complete dissolution of the sample in PZ3 requires a separate explanation. In fact, a later inflow is present (at about 6.5 m b.g.l.) within the piezometer due to a local perched aquifer above the rock sample placed at 9.7 m b.g.l. The sample is thus always wet due to the water leaching from above.

Only 4 rock samples (PZ6, PZ7, PZ8, PZ23) in the epiphreatic zone got wet by the fluctuating groundwaters. They recorded a loss of weight between 15 and 25%.

Eighteen rock samples remained always immersed. PZ14, PZ16, PZ20, PZ21, and PZ25 recorded a loss of weight of less than 1%. PZ6, PZ8, PZ11, PZ23 and PZ24 are between 4 and 9%. PZ3, PZ4, PZ5, PZ7, PZ10 and PZ22 are between 30 and 50%. PZ1 had a loss of 96%.

In general, all the samples in the vadose zone never reached by the groundwater show a very low loss of weight. Instead, when the rock samples are occasionally or always immersed in the groundwater, the dissolution is higher. The dissolution rate strongly depends on the mineralization of the groundwaters and so on their saturation index. It comes out (Table 1) that when the groundwaters are characterized by low electrical conductivity values up to 2 mS/cm (PZ1, PZ3,

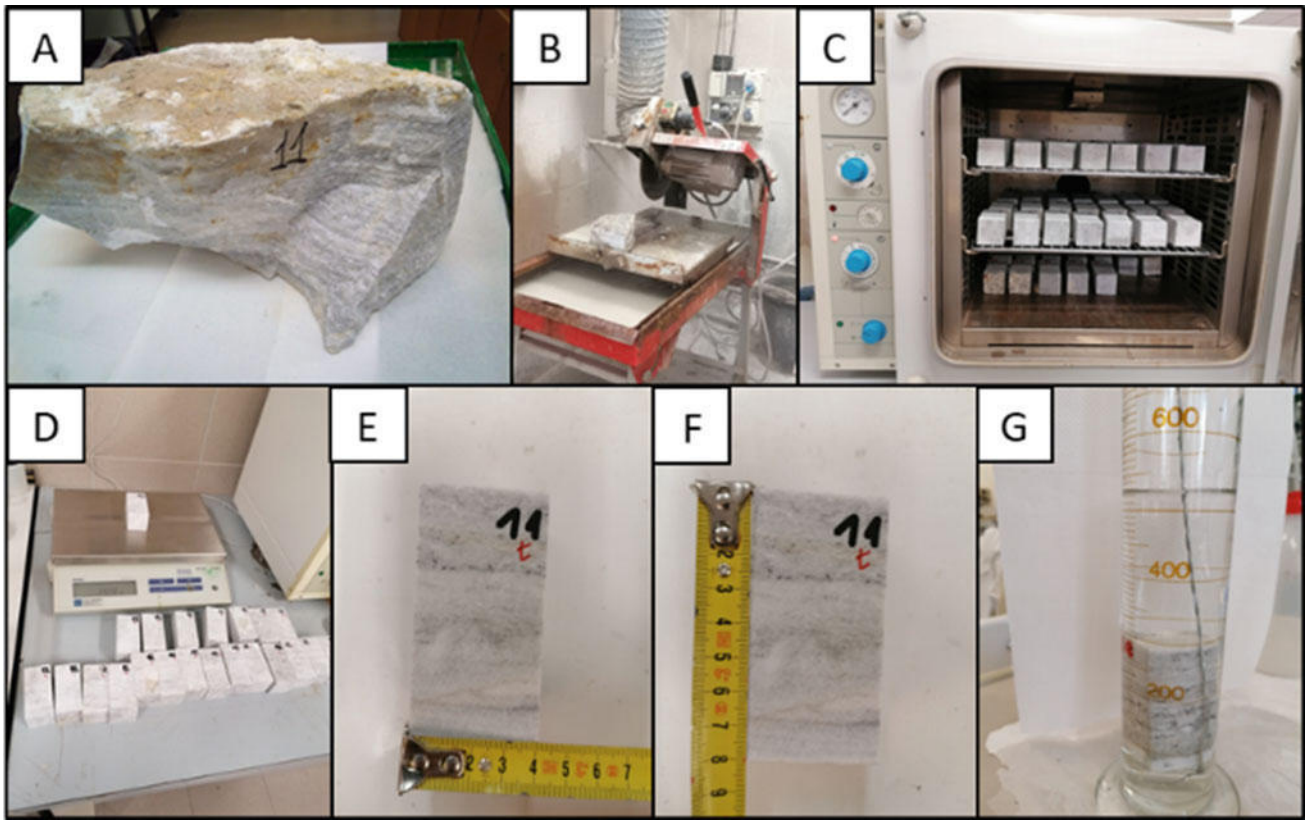

Fig. 3 Rock samples preparation process: **a** a boulder selected at the Entrampo quarry, **b** cutting and shaping phase, **c** over dried samples in the oven at 50 °C for 48 h, **d** weight procedure, **e–f** measurement of the dimensions **g** volume calculation

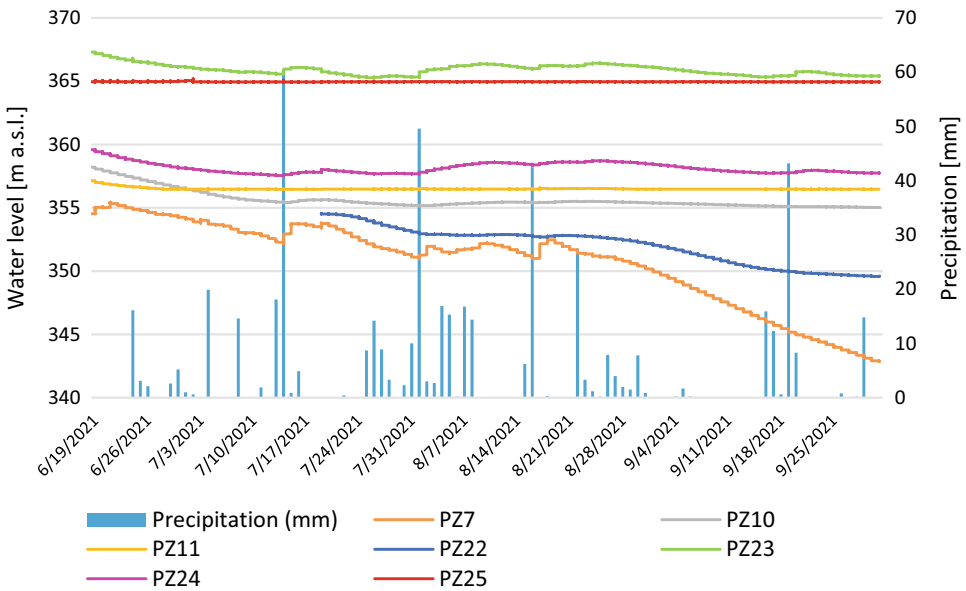

Fig. 4 Groundwater level fluctuations recorded in the piezometers of the Quinis village in the period June 18, 2021–October 1, 2021. Daily rainfall registered in Enemonzo station (OSMER FVG)

Table 1 Weight loss, dissolution rate (R) and electrical conductivity (EC) calculated for the rock samples used in the field experiment.

PZ	Depth (m b.g.l.)	Weight loss (%)	R (mm/4 months)	EC (mS/cm)	PZ	Depth (m b.g.l.)	Weight loss (%)	R (mm/4 months)	EC (mS/cm)
PZ1	−1.5	1.7	0.13	0.51	PZ14	−2	0.1	0.01	2.87
	−8	19.5	1.65			−12.7	0.1	0.01	
	−15*	95.9	7.68			−19.4*	0.2	0.02	
PZ3	−2	2.2	0.18	1.41	PZ16	−2	0.1	0.01	3.10
	−9.7**	100.0	> 8.125			−16.3*	0.2	0.01	
	−21.2*	49.4	3.77		PZ20	−2	1.3	0.10	10.70
PZ4	−2	2.1	0.16	1.75		−8.15	3.1	0.25	
	−7.7	0.9	0.07			−15.15*	0.3	0.02	
	−15.6*	49.7	3.85		PZ21	−2	0.5	0.03	3.28
PZ5	−0.5	0.9	0.07	1.40		−7.7	0.5	0.03	
	−13.7	6.1	0.50			−16.8*	0.7	0.05	
	−24.7*	40.1	3.21		PZ22	−2	0.2	0.02	2.18
PZ6	−2	0.2	0.01	1.80		−13	0.3	0.02	
	−15.6**	25.1	2.01			−28.1*	46.6	3.73	
	−36.7*	6.9	0.55		PZ23	−2	22.5	1.83	2.40
PZ7	−2	0.4	0.04			−10**	20.4	1.63	
	−19.6**	15.0	1.17	1.36		−30*	4.9	0.39	
	−37*	55.3	4.32	1.99	PZ24	−2	0.1	0.01	4.40
PZ8	−2	0.6	0.05			−11.6	0.2	0.01	
	−20**	20.6	1.65	1.60		−29*	4.2	0.34	
	−37.5*	4.5	0.35	2.50	PZ25	−2	0.4	0.03	
PZ10	−2	0.0	0.00	1.65		−12.6*	0.6	0.05	7.06
	−15	20.6	1.57			−17.4*	1.0	0.07	8.73
	−29*	32.0	2.50						
PZ11	−2	0.1	0.01	2.50					
	−11.6	42.0	3.20						
	−18.9*	8.8	0.69						

Depth (b.g.l.): rock samples depths
*when always inmmersed
**if inmersed only occasionally

PZ4, PZ5, PZ7, PZ8, PZ10, and PZ22), the rock samples dissolve more (in the range between 30 and 50%).

In the piezometers, PZ14, PZ16, PZ20, PZ21, and PZ25 instead, it have been observed stability of the groundwater levels, which indicates a low water replacement and a consequent high mineralization (EC > 2.5 mS/cm). In this situation, the weight loss is quite low, less than 1%. The remaining (PZ6, PZ11, PZ23 ,and PZ24) showed a weight loss between 2 and 9%.

5 Conclusion

Quinis is one of the most prone areas to sinkhole phenomena in the FVG (NE Italy). Known since the 1800s, they are still active and involve built-up structures. Despite the intense activity developed over the years, researchers are still working in the area, trying to understand the evolution rate in order to assess the jointed risk.

During the summer of 2021, 51 evaporite rock samples were placed in 17 piezometers at different depths in order to evaluate the loss of weight and the relative dissolution rate. From data analysis emerged that the samples always above groundwater level have a minimum weight loss. The ones always immersed in the groundwaters have a weight loss related to the mineralization and the water replacement. The result is a non-homogenous dissolution within the area and depth mainly linked to the permeability and the groundwater circulation.

Regarding the dissolution rate, in the four months investigated, some values can reach rates of 8 mm, which if compared with literature (Cucchi et al. 1998; Klimchouk

et al. 1996), yearly value is already much higher (at least eight times).

The experiment is still ongoing and future months will be used to evaluate the dissolution of rock samples according to seasonal variations.

References

Calligaris C, Devoto S, Zini L (2017) Evaporite sinkholes of the Friuli Venezia Giulia region (NE Italy). J Maps 13:406–414. https://doi.org/10.1080/17445647.2017.1316321

Calligaris C, Ghezzi L, Petrini R, Lenaz D, Zini L (2019) Evaporite dissolution rate through an on-site experiment into piezometric tubes applied to the real case-study of Quinis (NE Italy). Geosciences 9:298. https://doi.org/10.3390/geosciences9070298

Calligaris C, Zini L, Nisio S, Piano C (2020) Sinkholes in the Friuli Venezia Giulia Region focus on the evaporites. J Appl Geol 5. https://doi.org/10.1007/978-3-030-43953-8_5

Cucchi F, Forti P, Finocchiaro F (1998) Gypsum degradation in Italy with respect to climatic textural and erosional conditions. Geogr Fis Din Quat 3:41–49

Furlani S, Cucchi F, Forti F, Rossi A (2009) Comparison between coastal and inland karst limestone lowering rates in the northeastern Adriatic Region (Italy and Croatia). Geomorphology 104:73–81. https://doi.org/10.1016/j.geomorph.2008.05.015

Gutiérrez F, Cooper AH, Johnson KS (2008) Identification, prediction and mitigation of sinkhole hazards in evaporite karst areas. Environ Geol 53:1007–1022. https://doi.org/10.1007/s00254-007-0728-4

Klimchouk A, Cucchi F, Calaforra JM, Aksem S, Finocchiaro F, Forti P (1996) Dissolution of gypsum from field observations. Int J Speleol 25:37–48. https://doi.org/10.5038/1827-806X.25.3.2

Marinelli O (1898) Fenomeni di tipo carsico nei terrazzi alluvionali della Valle del Tagliamento. Studi orografici nelle Alpi orientali. Mem Soc Geol Ital 8(2):415–419

Plan L (2005) Factors controlling carbonate dissolution rates quantified in a field test in the Austrian alps. Geomorphology 68:201–212. https://doi.org/10.1016/j.geomorph.2004.11.014

Venturini C, Spalletta C, Vai GB, Pondrelli M, Delzotto S, Fontana C, Longo Salvador G, Carulli GB (2009) Note illustrative carta geologica d'Italia alla scala 1:50.000 foglio 031 ampezzo. ISPRA: Rome, Italy, pp 7–222 (In Italian)

Zini L, Calligaris C, Forte E, Petronio L, Zavagno E, Boccali C, Cucchi F (2015) A multidisciplinary approach in sinkhole analysis: the Quinis village case study (NE-Italy). Eng Geol 197:132–144. https://doi.org/10.1016/j.enggeo.2015.07.004

CHAPTER 3.4

GYPSUM DISSOLUTION RATE IN QUINIS VILLAGE (II PART)

In the paper previously presented are outlined the results coming out after the first 4 months of the experiment which, on the whole, lasted 1 year, up to June 2022.

Samples were recovered and photographed (*Figure 34* and *Figure 35*) every 3-4 months. For each rock sample collection, a manual measurement of EC, T and water level was conducted to validate CTD data.

Each row in *Figure 34* and *Figure 35* represents one sample collection and each column correspond to a different piezometer. Moving from the top to the bottom of the figures it is possible to appreciate the progressive dissolution of the gypsum rock samples.

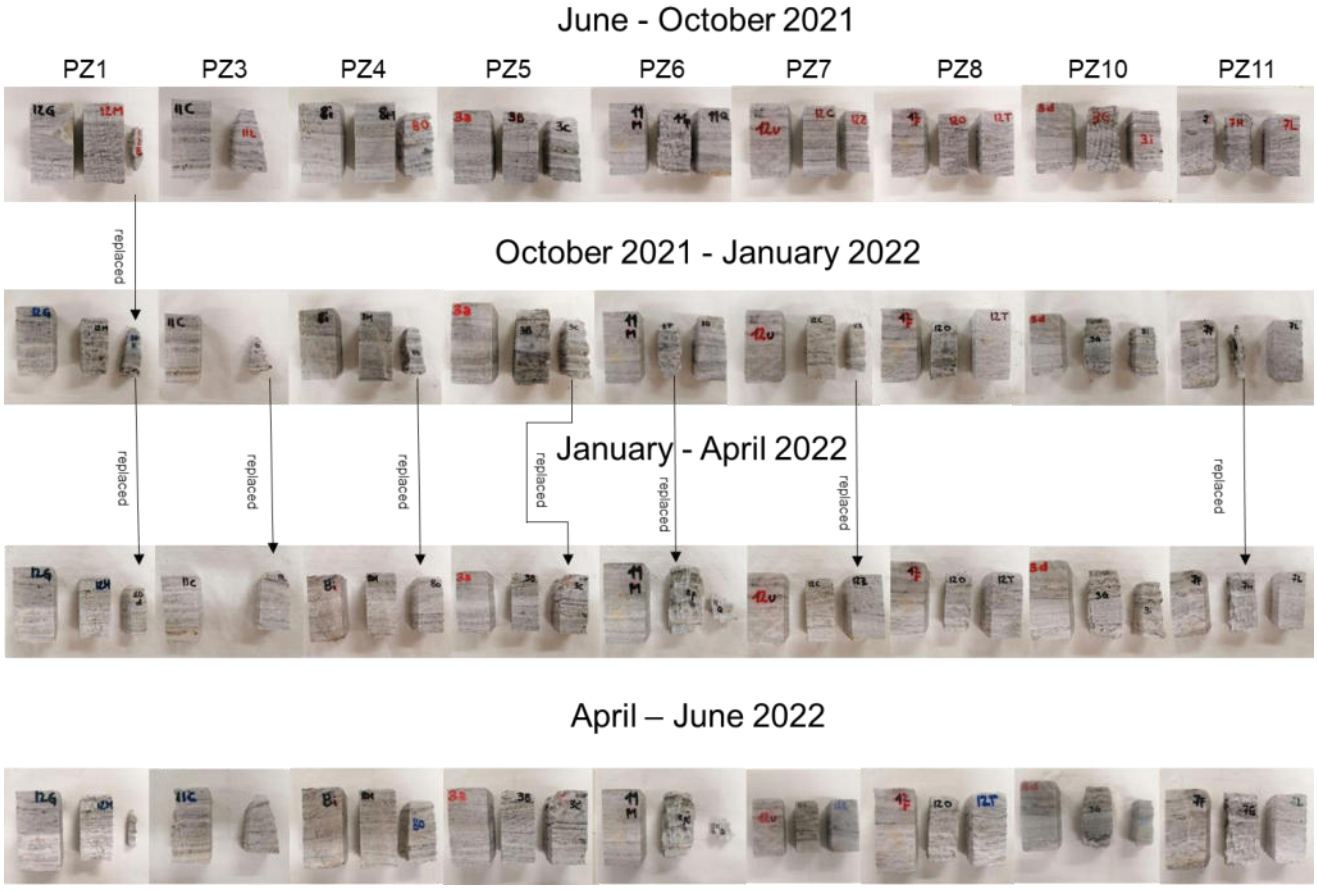

Figure 34 *Gypsum rock samples (PZ1, PZ3, PZ4, PZ5, PZ6, PZ7, PZ8, PZ10, PZ11)*

Figure 35 *Gypsum rock samples (PZ14, PZ16, PZ20, PZ21, PZ22, PZ23, PZ24, PZ25)*

Weight loss and dissolution rate were calculated for each sample and summarized in *Table 6* and *Table 7*. In each piezometer, two or three samples were placed according to the depth of the piezometer itself and the water level:

- GROUP I: the shallower sample was placed at about 2 m below the ground level (in the vadose zone never reached by the groundwater) (no colour in *Table 6* and Table 7*);*
- GROUP II: the middle sample was placed in the epiphreatic zone, where the groundwater level fluctuates (light blue in *Table 6* and *Table 7*);
- GROUP III: the third sample was placed in the phreatic zone (always immersed in groundwater) (dark blue in *Table 6* and *Table 7*).

In some piezometers (PZ1, PZ3, PZ4, PZ5, PZ6, PZ7, PZ11), where the percentage of weight loss exceeded 70% in the first months of monitoring, certain samples were replaced with new ones, highlighted in red in *Table 6*. The samples always submerged in PZ1 were replaced twice. All replaced samples are marked with an asterisk (*) in *Table 6*.

All samples placed in the subsurface (2 m b.g.l.) (GROUP I) showed a similar trend, with a dissolution rate below 1 mm/y. However, the sample PZ23_A, belonging to this group, showed a deviating dissolution rate of 3.63 mm/y after one year. In the case of PZ23, the question regarding the process responsible for the dissolution of the shallower rock sample, which was never submerged, remains open. The measured change in weight cannot be only attributed to air drying; its behaviour might reflect the role of H_2S gas released by water.

Analyzing submerged and occasionally submerged samples requires information on the groundwater level. Not all piezometers were equipped with CTD probes recording in continuous. Divers were installed in the piezometers PZ7, PZ10, PZ11, PZ22, PZ23, PZ24 and PZ25. From the data analyses, it is possible to derive a trend also for those piezometers not having the recordings available.

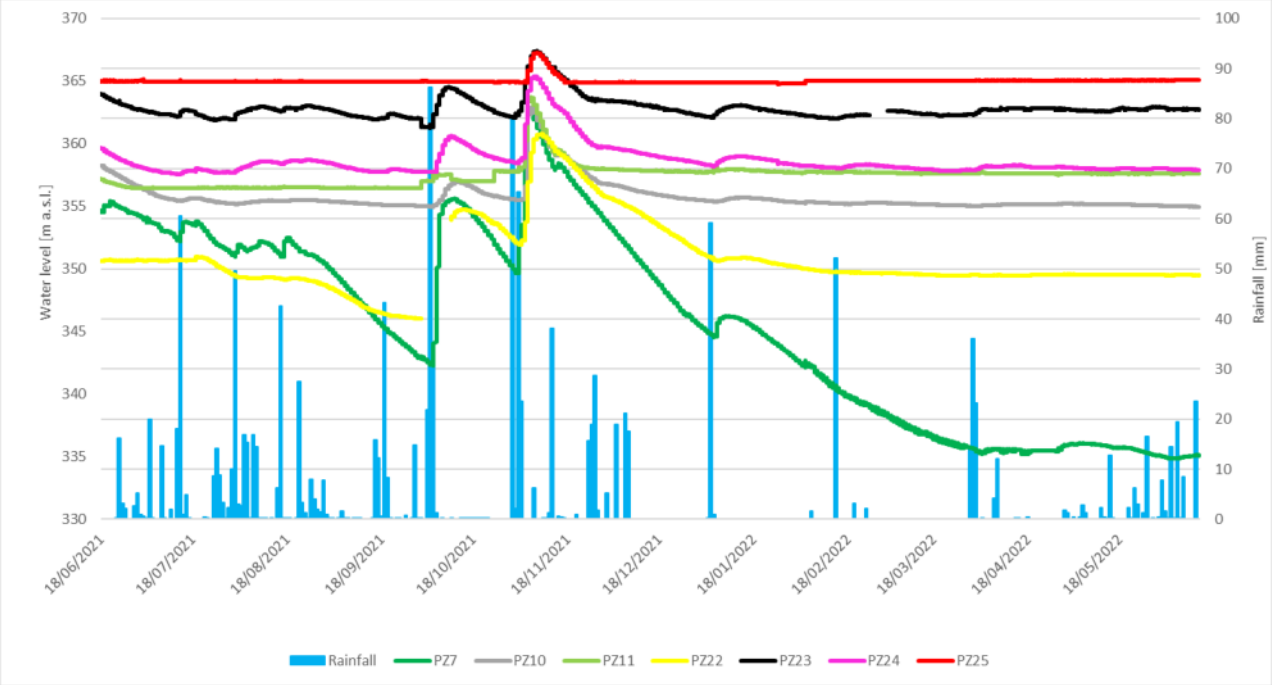

Figure 36 *Rainfall and water level data recorded during the one-year experiment*

The samples in GROUP II recorded a dissolution rate ranging from a minimum value of 0.04 mm/y to a maximum of 6.86 mm/y. However, the dissolution rate was not homogeneous throughout the entire period. The CTD monitoring data, in particular, highlighted two increases in groundwater levels, one in October 2022 and another in November 2022. This aligns with the higher weight loss observed in the first 7 months compared to the last 5 months when the groundwater level was lower, and the samples were no longer submerged.

The higher dissolution rates have been registered in samples PZ3_B, PZ6_B, and PZ11_B, prompting their replacement after the first 7 months. The complete dissolution of the sample PZ3_B requires a separate explanation. A shallow lateral inflow is present in the piezometer at about 6.5 m b.g.l., originating from a local perched aquifer. The latter is above the rock sample placed at 9.7 m b.g.l., resulting in the sample always being wet due to water leaching from above. Therefore, it was decided not to replace it after the first 4 months.

The third group of samples (GROUP III), placed in the phreatic zone, showed a dissolution rate ranging from a minimum of 0.02 mm/y to a maximum of 7.85 mm/y. Several samples belonging to this group (PZ1_C, PZ3_C, PZ4_C, PZ5_C and PZ7_C) were replaced after 7 months, with weight loss recorded from 72.92% to 90.51%. In particular, the PZ1_C sample was also replaced after the first 4 months due to its high dissolution rate.

Cross-analyses between EC (*Table 6* and *Table 7*) and weight loss indicated a strong dependence on the groundwater mineralization and, consequently, on the relative saturation index. In piezometers with low EC values (up to 2.5 mS/cm), high fluctuations in the water table and rapid groundwater replacement, the rock samples dissolved more, with weight loss ranging between 20% and 98%).

In piezometers with high mineralization (EC>2.5 mS/cm) and a stable groundwater levels with low water replacement, weight loss was relatively quite low, less than 1%.

PZ	Depth (m b.g.l)	Weight loss after 4 months (%)	R after 4 months	Weight loss after 7 months (%)	R after 7 months	Weight loss last 5 months (%)	R in the last 5 months	Weight loss after 1 year (%)	R TOT (mm/y)	EC (mS/cm) min-max
PZ1_A	-1.5	1.7	0.13	3.7	0.29			3.79	0.3	
PZ1_B	-8	19.5	1.65	44.7	3.54			46.19	3.58	
PZ1_C	-15	95.92*	7.67	85.54*	6.8	97.62	7.54			0.34-0.51
PZ3_A	-2	2.2	0.18	2.2	0.18			9.58	0.77	
PZ3_B	-9.7	100	8.13							
PZ3_C	-21.2	49.4	3.77	90.51*	6.9	49.91	3.79			1.06-1.95
PZ4_A	-2	2.1	0.16	2.1	0.16			2.2	0.17	
PZ4_B	-7.7	0.9	0.07	7.3	0.59			7.88	0.64	
PZ4_C	-15.6	49.7	3.85	80.10*	6.21	49.91	3.78			1.64-1.81
PZ5_A	-0.5	0.9	0.07	1.1	0.09			1.77	0.14	
PZ5_B	-13.7	6.1	0.50	25	2.02			25.97	2.09	
PZ5_C	-24.7	40.1	3.21	72.92*	5.83	6.54	0.5			2.16-2.20
PZ6_A	-2	0.17	0.01	0.2	0.02			0.17	0.01	
PZ6_B	-15.6	25.1	2.01	73.05*	5.84	35.08	2.64			
PZ6_C	-36.7	6.9	0.55	40.3	3.25			97.36	7.85	1.8
PZ7_A	-2	0.4	0.03	0.4	0.03			0.54	0.04	
PZ7_B	-19.6	15	1.17	32.3	2.52			32.99	2.58	1.36
PZ7_C	-37	55.3	4.42	82.02*	6.41	10.21	0.75			1.92-2.37
PZ8_A	-2	0.58	0.05	0.6	0.05			0.58	0.05	
PZ8_B	-20	20.6	1.65	47.7	3.82			47.72	3.82	1.6
PZ8_C	-37.5	4.5	0.35	4.9	0.38			20.16	1.55	2.05-2.3
PZ10_A	-2	0.0	0.00	0.1	0.01			0.03	0.00	
PZ10_B	-15	20.6	1.57	27.1	2.07			32.71	2.50	
PZ10_C	-29	32	2.50	53.8	4.2			77.75	6.07	0.91-1.84
PZ11_A	-2	0.1	0.01	0.3	0.02			0.27	0.02	
PZ11_B	-11.6	42	3.20	89.99*	6.86	22.27	1.67			
PZ11_C	-18.9	8.8	0.69	21.3	1.66			26.16	2.04	2.48-2.52

Table 6 *Weight loss and dissolution rate of samples in PZ1, PZ3, PZ4, PZ5, PZ6, PZ7, PZ8, PZ10, PZ11 (in white the sample in the vadose zone - GROUP I, in light blue the samples in the ephiphreatic zone – GROUP II and in dark blue the samples in the phreatic zone – GROUP III). In red the samples that have been replace once or twice due to the high weight loss (>70%). All the replaced samples are marked with a *. EC in the last column shows value registered in term of minimum and maximum*

PZ	Depth (m b.g.l)	Weight loss after 4 months (%)	R after 4 months	Weight loss after 7 months (%)	R after 7 months	Weight loss after 1 year (%)	R TOT (mm/y)	EC (mS/cm) Min-max
PZ14_A	-2	0.1	0.01	0.1	0.01	0.07	0.01	
PZ14_B	-12.7	0.1	0.01	0.2	0.02	0.52	0.04	
PZ14_C	-19.4	0.2	0.02	0.3	0.03	0.38	0.03	2.87-4.05
PZ16_A	-2	0.1	0.01	0.1	0.01	0.1	0.01	
PZ16_B	-16.3	0.2	0.01	0.2	0.01	0.2	0.02	2.98-3.83
PZ20_A	-2	1.3	0.1	1.2	0.09	1.5	0.11	
PZ20_B	-8.15	3.1	0.25	3.3	0.26	3.85	0.31	
PZ20_C	-15.15	0.3	0.02	0.2	0.02	0.31	0.02	9.09-10.7
PZ21_A	-2	0.5	0.03	0.6	0.05	0.39	0.03	
PZ21_B	-7.7	0.5	0.03	1.8	0.14	1.74	0.13	
PZ21_C	-16.8	0.7	0.05	1.1	0.09	1.3	0.1	3.28-3.32
PZ22_A	-2	0.2	0.02	0.2	0.02	0.2	0.02	
PZ22_B	-13	0.3	0.02	0.3	0.02	0.55	0.04	
PZ22_C	-28.1	46.6	3.73	60	4.8	64.29	5.14	2.18-2.35
PZ23_A	-2	22.5	1.83			44.65	3.63	
PZ23_B	-10	20.4	1.63			56.92	4.55	0.14-1.60
PZ23_C	-30	4.9	0.39			16.11	1.3	0.20-3.06
PZ24_A	-2	0.1	0.01	0.1	0.01	0.07	0.01	
PZ24_B	-11.6	0.2	0.01	10.8	0.83	10.83	0.83	3.29-3.32
PZ24_C	-29	4.2	0.34	5	0.4	5.78	0.47	3.47-4.4
PZ25_A	-2	0.4	0.03	0.3	0.02	0.07	0.01	
PZ25_B	-12.6	0.6	0.05	1	0.07	0.92	0.07	5.63-7.06
PZ25_C	-17.4	1	0.07	1.3	0.1	1.52	0.11	8.52-8.85

Table 7 *Weight loss and dissolution rate of samples in PZ14, PZ16, PZ20, PZ21, PZ22, PZ23, PZ24, PZ25 (in white the sample in the vadose zone - GROUP I, in light blue the samples in the ephiphreatic zone – GROUP II and in dark blue the samples in the phreatic zone – GROUP III). EC in the last column shows value registered in term of minimum and maximum*

CHAPTER 3.5

GYPSUM DISSOLUTION RATE - LABORATORY EXPERIMENT

To better understand the fast dissolution rate in the Quinis hamlet, a six-months laboratory experiment (from September 2022 to March 2023) was carried out. Six evaporitic rock samples, with the same dimensions and characteristics of those used in the field experiment, were placed in six different hermetic glass vessels (*Figure 37*A).

In the first glass vessel, tap water was changed daily and the electrical conductivity (EC) was measured manually each day (samples 7i). In the second glass vessel, tap water was changed once a week and the EC was measured manually on a weekly basis (sample 8d). In the third glass vessel, tap water was changed and the EC was measured manually once a month (sample 7a). In the remaining 3 hermetic glass vessels, three additional evaporitic rock samples were immersed in 3 different types of water (tap water, distilled water and Rio Quinis water) and were never changed throughout the entire experimental period. In each of these latter a CTD probe measured in continuous, hourly, EC and T.

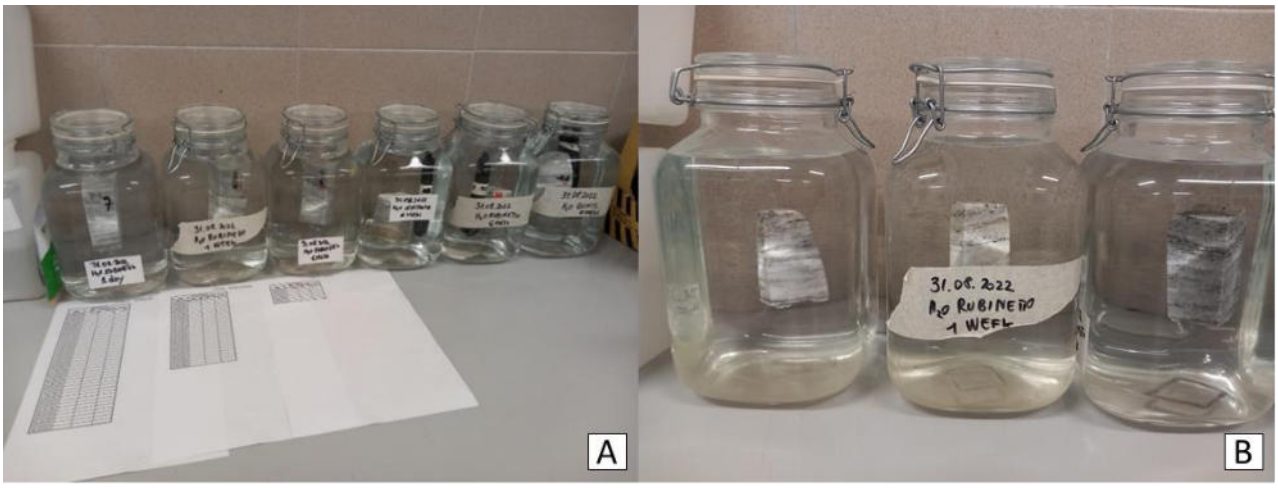

Figure 37 *Laboratory experiment:* ***A)*** *6 evaporitic rock samples in 6 hermetic glass vessels;* ***B)*** *the 3 hermetic glass vessels in which the water were changed respectively every day, once a week and once a month*

The aim of the experiment was to better understand the role of fresh water in the dissolution process (simulating the water recharge).

Samples 7i and 8d, with water changes respectively every day and once a week, were dried in the oven for 48 hours every weekend. They were then weighed and returned to new fresh waters. The sample 7a, with water changes every month, was dried in the oven for 48 hours every 4 weeks, weighed, and subsequently returned to new fresh water.

After just one month, the difference in weight loss among the 3 samples with different water change periods became evident (*Figure 38*).

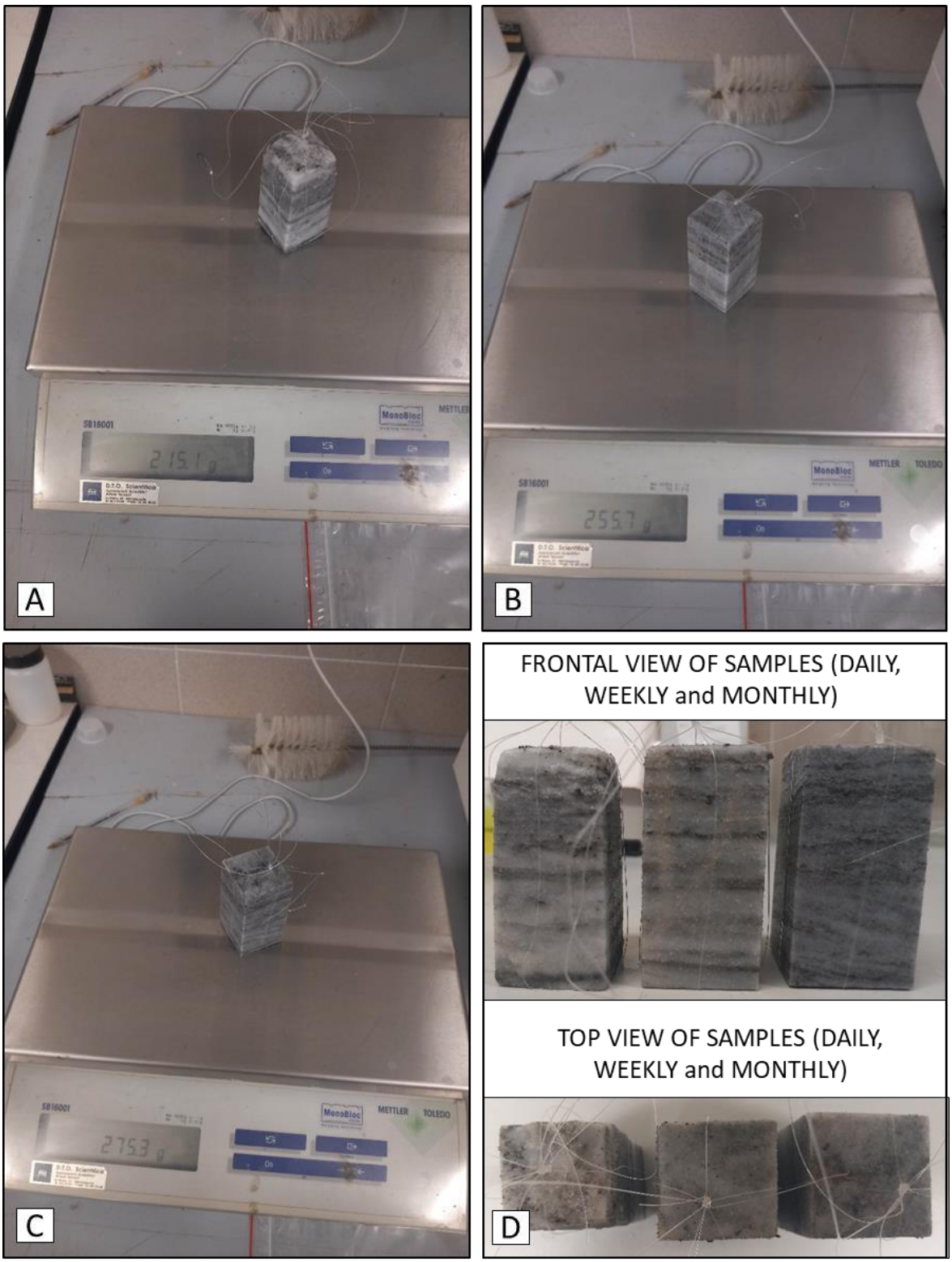

Figure 38 *Weight loss after 1 month (30/09/2022):* ***A)*** *weight of sample with daily water change,* ***B)*** *weight of sample with weekly water change,* ***C)*** *weight of sample with monthly water change,* ***D)*** *frontal and top view photos of the 3 samples*

After six months of the experiment, it emerged that the three samples immersed in the tap water exhibited different behaviors. The sample with daily water changes lost 78.60% of its weight; the sample with weekly water changes lost 45.64% of its weight; and the sample with monthly water changes lost 14.82% of its weight *(Figure 38*). Samples immersed in waters changed at different intervals lost a percentage of weight directly proportional to the frequency of water change, indicating that more frequent the water changes resulted in greater weight loss.

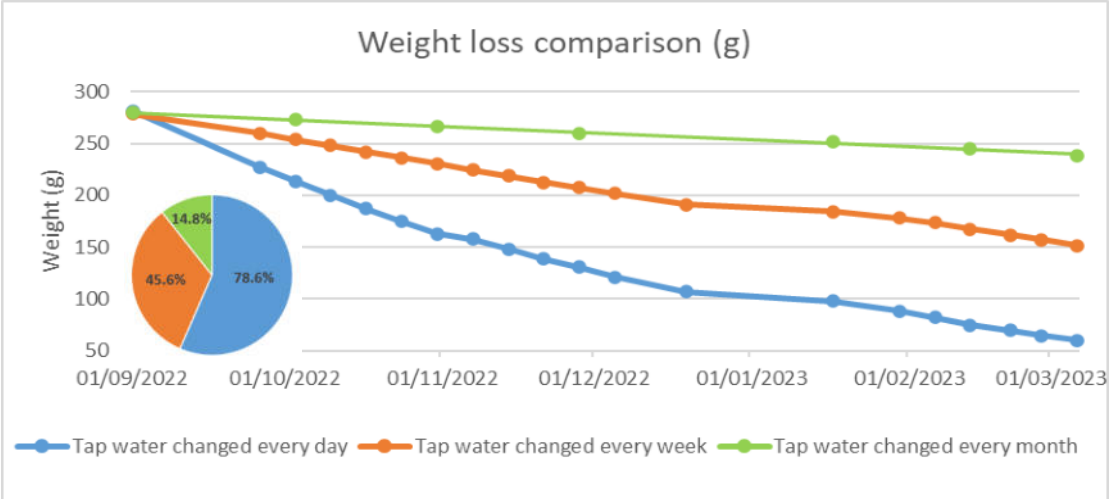

Figure 39 *Comparison of weight loss among samples in tap waters with different water change time-periods*

The samples immersed in the waters that were never changed lost from 1.38% to 2.55% of their weight, which are extremely low values compared to the other considered samples (*Figure 40).* This behavior can be explained when compared with what happens at the EC level.

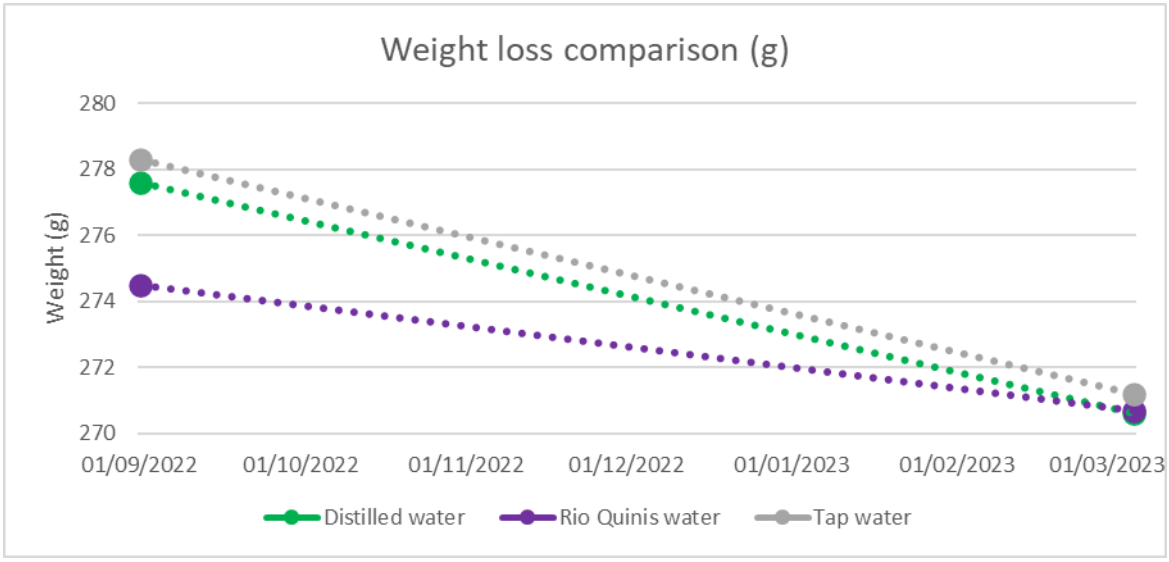

Figure 40 *Comparison of weight loss among samples in different waters (distilled water, Rio Quinis water and tap water) that were never changed*

Figure 41 shows the comparison between rock samples immersed in tap water changed respectively every day (A) and every week (B) (November 2022 - February 2023).

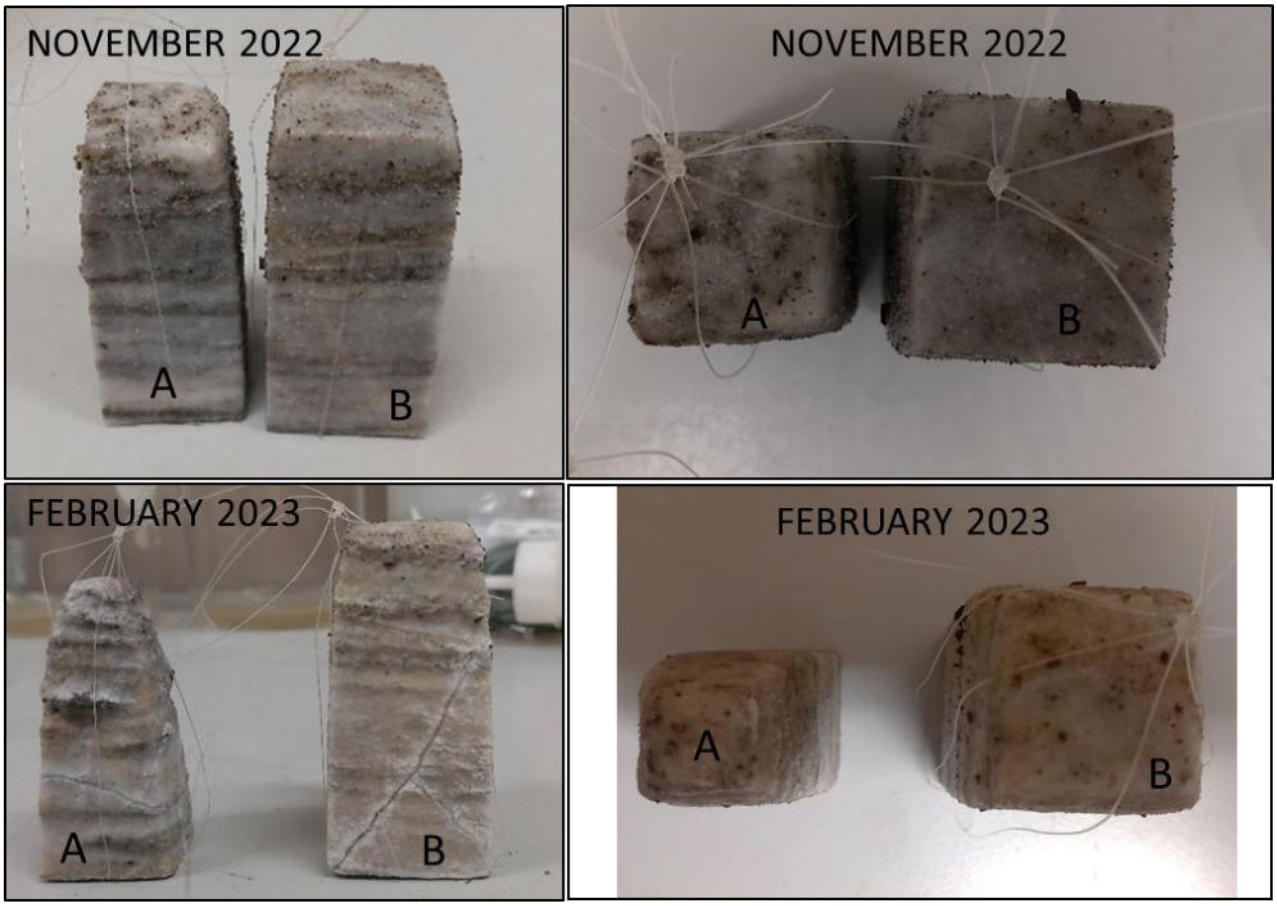

Figure 41 *Comparison of rock samples between November 2022 and February 2023. Sample with daily changing water is marked with letter A, and sample with weekly changing water marked is with letter B*

The tap water in which the samples were immersed had an initial conductivity within a range that varies from 409 to 428 μS/cm. Every day, the EC was measured at 3 different depths in the glass vessel (surface, middle and bottom) and later on, the water was replaced. On average, the shallower layer of water had an EC value of 670 μS/cm, the middle layer of water a value of 1640 μS/cm, and the lower one (values acquired at the bottom of the glass vessel) a value of 1790 μS/cm, showing a stratification already after one day of immersion.

In the glass vessel where EC was measured once a week, the shallow layer of water had an average value of 1990 μS/cm, the middle layer of water a value of 2270 μS/cm, and the lower one a value of 2300 μS/cm.

In the glass vessel where EC was measured once a month, the shallower layer of water had an average value of 2340 μS/cm, the middle layer of water a value of 2395 μS/cm, and the lower one, a value of 2400 μS/cm.

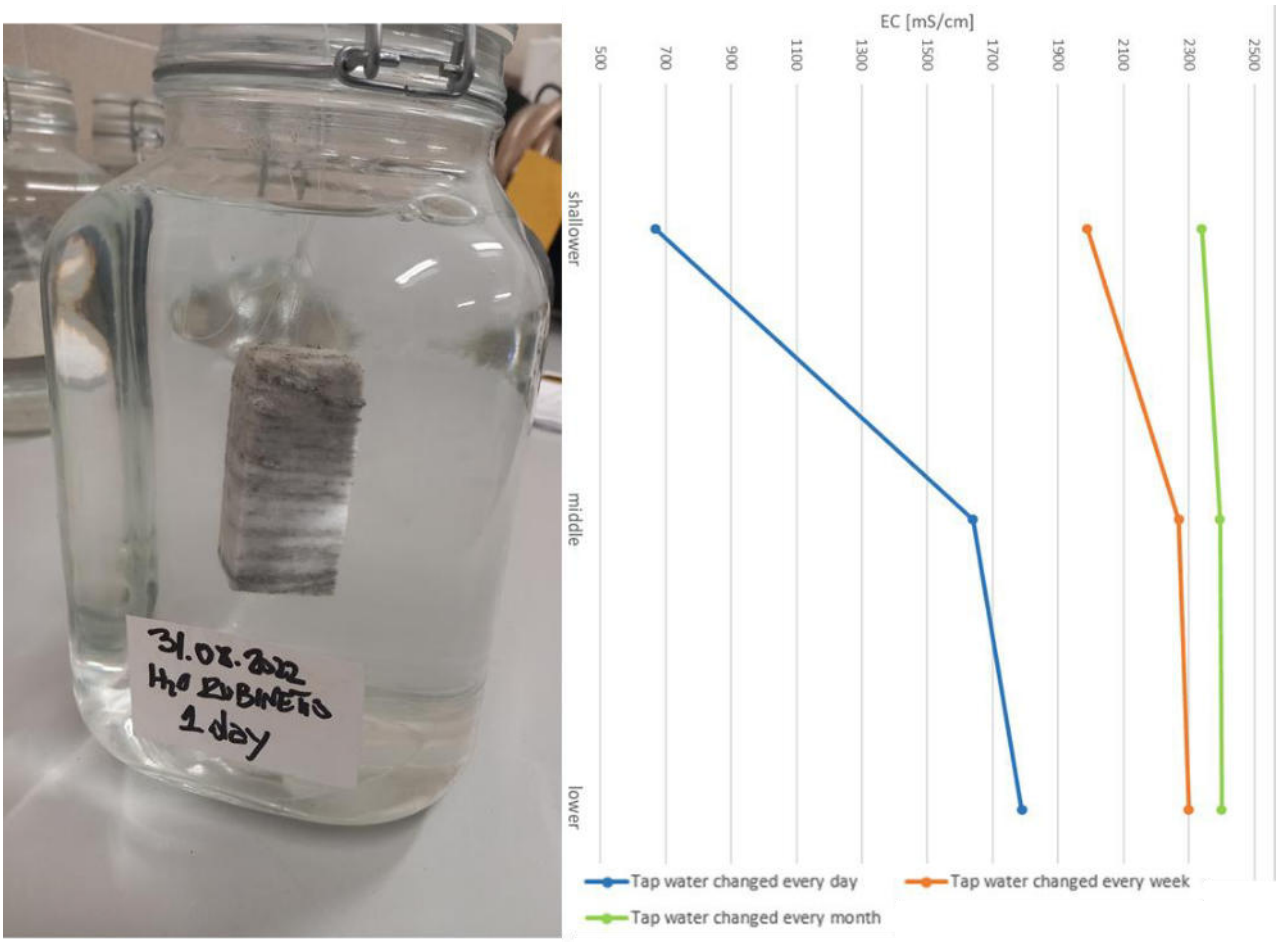

Figure 42 *Summary of the EC measured in different glass vessels with varying water change frequencies (daily in blue, weekly in orange and monthly in green). Measurements were taken at three different depths within the glass vessel (shallower, middle and lower)*

Regarding the samples immersed in different waters (Rio Quinis, distilled and tap), the initial EC values were different: tap water had a value of 412 μS/cm, Rio Quinis had 1200 μS/cm and distilled water had a value of 1 μS/cm. During the 6 months of the experiment, waters were never changed, and EC reached extremely fast the 2000 μS/cm (5 days for all the considered samples) stabilizing approximately around values of 2374 μS/cm, 2466 μS/cm and 2398 μS/cm respectively (*Figure 43*). This implies that in approximately a week the waters are saturated and no more dissolution can occur.

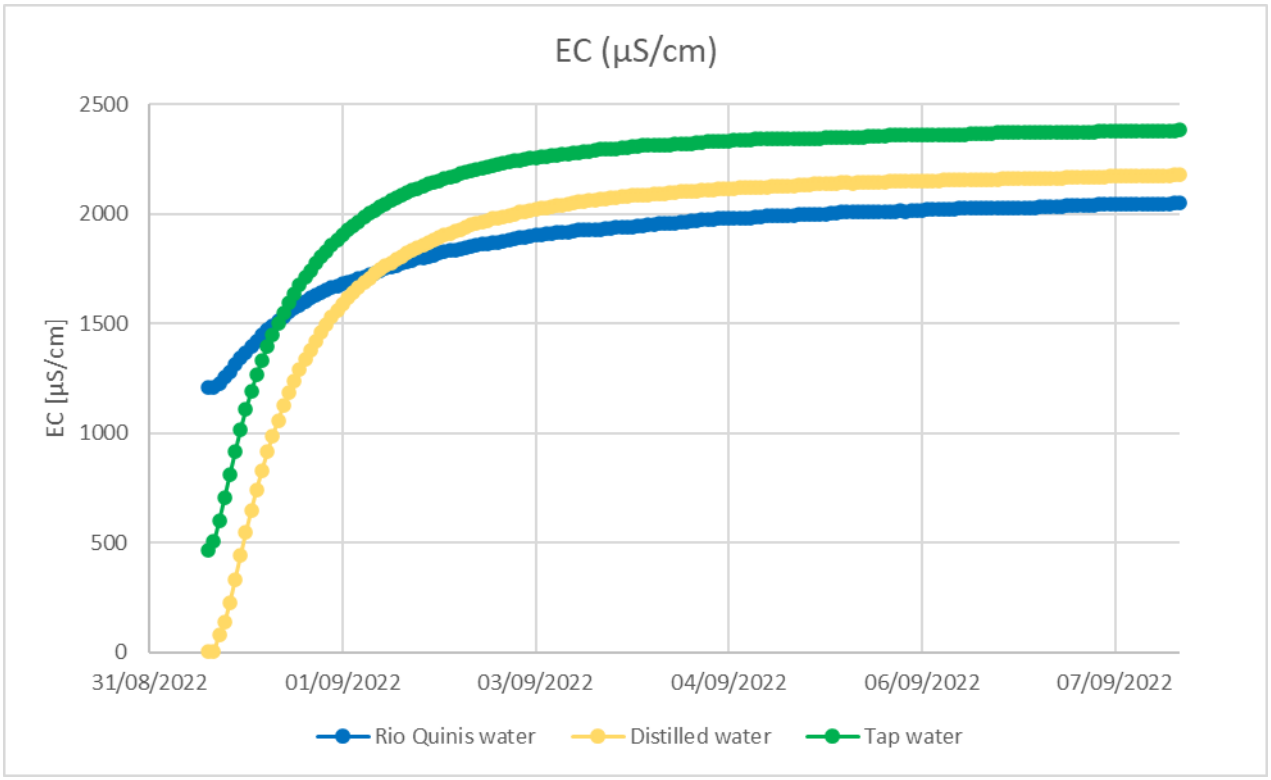

Figure 43 *Comparison of EC measurement in three different waters (Rio Quinis, distilled and tap waters)*

UNIVERSITÀ DEGLI STUDI DI TRIESTE

CHAPTER 4

SINKHOLE HAZARD

Sinkholes are complex phenomena that, depending on their origin, can have various evolutions and may interact with existing infrastructure in different and sometimes dramatic ways. In the case of collapse sinkholes, the paroxysmal phase is extremely rapid and often lacks precursor signs (as observed in the event at Esemon di Sopra in April 2022, described further on *Chapter 4.1*). This makes these phenomena generally unpredictable and highly dangerous. In the area of occurrence, a preliminary study was done to characterise it (*Chapter 4.1*). In the case of suffosion sinkholes, the process itself involves a gradual surface adjustment that persists over time and can evolve to achieve a state of equilibrium, often corresponding to a characteristic angle of repose for the affected debris material. While they are less critical than collapse sinkholes, they can still cause permanent damages to structures within a specific area, as demonstrated by the active cases in Quinis village (Enemonzo Municipality).

The "regional-scale" approach, conducted at municipal level, for instance, through interferometric analyses (InSAR), is preliminary and informative. It provides an indication of areas that warrant more detailed investigation at a later "local-scale" phase.

The "local-scale" approach necessitates a detailed examination of the territory, focusing on individual phenomena, defining their spatial characteristics, typology, and potential evolution. Investigations such as the installation and monitoring of crackmeters (sometimes with continuous reading capabilities), precision geometric levelling for topographic monitoring, planimetric-altimetric tracking of displacements are required, but for what concern the hazard also the analysis of the aerial photo can be useful to understand the evolution of the sinkhole (*Chapter 4.2* - Analysis of the IGM frames in the Sauris municipality). For deeper insights, inclinometric/assestimetric measurements are crucial in understanding the development of a phenomenon that may not have immediate surface repercussions. Another significant investigation involves the excavation of an exploratory trench through the sinkhole(s). Whenever feasible, such trenches allow for characterizing the morphology of the phenomenon, defining its contours and superficial geometries. This was precisely the case in Enemonzo, where in the spring of 2022, thanks to the collaboration of municipal technicians and landowners, an exploratory trench was excavated through an active sinkhole (*Chapter 4.3*).

Once the precise mapping, classification and definition of the state of activity have been consolidated, where possible, the establishment of adequate setback distances is the next step in the definition of the hazard.

The setback distances concept has been applied for managing a number of geo-environmental problems defining zones that may be affected by hazardous processes

spatially associated with mappable geological or geomorphological features (Gutierrez et al., 2018). The existing research regarding setback distances from sinkhole is limited also because very often, sinkhole data is not available for the area of interest. Different authors proposed different value of setback distances such as Kemmerly (1993), who in his hazard planning model for sinkholes, suggested a setback of 152 meters from the edges of sinkholes to restrict development. Different approaches are taken in parts of the USA (Fleury, 2009) with various setback distances ranging up to 150 m, depending on the municipality.

In Monroe County of Indiana, Zhou and Beck (2008), define a setback of 7.6 m from the residential and commercial buildings for sinkhole no more than 0.1ha and a setback of 15 meters from the post development sinkhole flooding area for those exceeding 0.1ha. In Knox County, in the town of Farragut, the same authors recommended a uniform 15 m setback for all sinkholes.

The Karst Management Plan of Virginia, specified a minimum buffer of 30 meters for karst assessments around the boundaries of inventoried dolines (Virginia Cave Board, 2017).

For the Atlantic Coast Pipeline project, which crosses 52 kilometres of karst terrain in West Virginia and North Carolina, a recommended setback of 91 meters was advised (GeoConcepts Engineering, 2015).

Setbacks are established case by case in Zaragoza municipality where damages to infrastructures caused by sinkhole are very common. Nonetheless, in the city land-use planning a buffer zone of 15 m around every sinkhole is proposed in order to take into account the errors in the definition of the sinkhole edges and the potential occurrence of minor collapses.

The concepts discussed regarding the definition of correct setback distances reveal that there is no specific method to calculate their value, even within the same study area. Here, there need to propose a methodological and automatic protocol to define the buffer area and assign the hazard to each sinkhole for the entire regional territory.

To achieve the goal, there are two ways to go:

1) The use of qualitative methods that involve the inventory of phenomena;

2) The use of quantitative methods that involve the use of statistical and/or deterministic models for the evaluation of the spatial component.

The application of quantitative methods involves the acquisition of a series of information not yet available on the entire analyzed regional territory. Therefore, it was chosen to

apply a qualitative methodology based on the available data collected in the geodatabase. Furthermore, given that sinkholes still lack a proper Hazard Plan, it was decided to comply with the P.A.I. (Piano di Assetto Idrogeologico/Hydrogeological Plan) protocol for their hazard classification (P1, P2, P3 and P4).

REFERENCES

- Board Virginia Cave, (2017) In: Virginia Department of Environmental Quality (Ed.), Karst Assessment Standard Practice, 9 pp. https://www.dcr.virginia.gov/natural-heritage/document/karst-assessment-guidelines.pdf
- Fleury S., (2009) Land Use Policy and Practice on Karst Terrains. Springer 187pp.
- GeoConcepts Engineering, (2015) Karst terrain assessment, construction, monitoring and mitigation plan. In: Atlantic Coat Pipeline and Dominion Transmission, 17 pp. http://deq.state.va.us/Portals/0/DEQ/Water/Pipelines/ACP_DomResponse401WQCResponse.pdf.
- Gutiérrez F., Zarroca M., Linares R., Roqué C., Carbonel D., Guerrero J., McCalpin J.P., Comas X., Cooper A.H. (2018) Identifying the boundaries of sinkholes and subsidence areas via trenching and establishing setback distances. Engineering Geology 233, 255-268. https://doi.org/10.1016/j.enggeo.2017.12.015
- Kemmerly P.R., (1993) Sinkhole hazards and risk assessment in a planning context. Journal of American Planning Association 59, 221–229. https://doi.org/10.1080/01944369308975871
- Zhou W. & Beck B.F., (2008) Management and mitigation of sinkholes on karst lands: an overview of practical applications. Environmental Geology 55, 837–851. https://doi.org/10.1007/s00254-007-1035-9

CHAPTER 4.1

Man and Karst 2022

New collapse, old story: Raveo's sinkhole occurred on 21th April 2022

A. Busetti[1], C. Calligaris[1], M. Fernetti[1], E. Forte[1] and L. Zini[1]

1. Mathematics and Geosciences Department (DMG), University of Trieste, Via Weiss 2, 34128 Trieste (Italy)

REGIONE SICILIANA
Assessorato dei Beni Culturali e dell'Identità Siciliana
Dipartimento dei Beni Culturali e dell'Identità Siciliana

ARS

Città di Custonaci

PARROCCHIA SANTUARIO VARIA SS. DI CUSTONACI

United Nations Educational Scientific and Cultural Organization

UNESCO Chair on Karst Education
University of Nova Gorica in cooperation with ZRC SAZU Karst Research Institute

Hyblean Center of Speleo-Hydrogeological Research

UNIVERSITÀ DI CATANIA

UNIVERSITY OF BENGHAZI

DiSTeM
Dipartimento di Scienze della Terra e del Mare
UNIVERSITÀ DI PALERMO

Università degli Studi di TRIESTE

dipartimento di matematica e geoscienze

UNIVERSITÀ DEGLI STUDI DI MESSINA - MIFT

UNIVERSITÀ DEGLI STUDI DI BARI ALDO MORO

ISPRA
Istituto Superiore per la Protezione e la Ricerca Ambientale

Sistema Nazionale per la Protezione dell'Ambiente

Karst Commission

TETIDE APS

Ordine Regionale Geologi Sicilia

ManandKarst2022

in Sicily

INTERNATIONAL SCIENTIFIC CONFERENCE

September 12th - 17th Custonaci, Italy

CAI CLUB ALPINO ITALIANO

SSI SOCIETÀ SPELEOLOGICA ITALIANA
Esplorare, conoscere e proteggere

UIS

EuroSpeleo Projects

Federazione Speleologica Regionale Siciliana

ZRC SAZU

PELA GeoEnvironmental

CKH

Department of Geography
University of Zadar
Universitas Studiorum Jadertina | 1396 | 2002

Zingaro

Parco archeologico Segesta

CoSci
Commission Scientifique
Fédération Française de Spéléologie

Man and Karst 2022
in Sicily
INTERNATIONAL SCIENTIFIC CONFERENCE
September 12th - 17th Custonaci, Italy

IMPORTANCE OF DARNAH FORMATION FOR KARSTIFICATION IN AL JABAL AL AKHDAR, NORTHEAST LIBYA: ITS DIAGENETIC PROCESS AND BURIAL HISTORY

Moftah H. El Shawaihdi
Department of Earth Sciences, Faculty of Science, University of Benghazi, P. O. Box 1984-1308, Benghazi, Libya

Lithologic texture and diagenetic history of Darnah Formation is considered as important factors led to developing karstic features in Al Jabal Al Akhdar, Northeast Libya. These karst phenomena are much occurred in great variety of distinctive features, such as dolines, caves and underground caves, etc. The main diagenetic processes that affected this formation are dissolution, early cementation, pyrite formation, fracturing, dolomitization, and neomorphism. Dissolution seems to take place in early stage of the diagenetic process and affecting the unstable carbonate grains, which represented by fossils that originally composed of aragonite and (or) high magnesium calcite. Cementation, on the other hand, was acting against dissolution by filling the pore space left by dissolution. However, this process is very limited and sparsely noticed as syntaxial overgrowth early cement within most samples. Pyrite is formed as aggregate of spherical microconcretions (framboids) that usually replace skeletal fragments. Microscopic fractures are predominant along the fossil grains and micrite. Aggrading neomorphism was also affecting the micrite by changed it into microspar? Dolomite is formed as replacement of the micrite at few samples. The dissolution of unstable fossil grains and fracturing are the major processes that left microscopic voids which in turn increased the porosity within the samples. These microscopic opening were probably acted as the initial trigger of forming the karstification phenomena by enlargement of such dolines, surface and subsurface caves that widely spread in Darnah Formation, Al Jabal Al Akhdar, NE, Libya.

NEW COLLAPSE, OLD STORY: RAVEO'S SINKHOLE OCCURRED ON 21ST APRIL 2022

Alice Busetti[1], Chiara Calligaris[1], Michele Fernetti[1], Emanuele Forte[1] & Luca Zini[1]
Mathematics and Geosciences Department (DMG),
University of Trieste, Via Weiss 2, 34128 Trieste (Italy)

In the Friuli Venezia Giulia region (NE Italy), numerous are the sinkholes linked to the presence of an evaporitic bedrock also in highly infrastructured areas. These subsidence phenomena are known since a long time and documented since the early sixties when a cover collapse sinkhole occured in the Alta Val Tagliamento valley in correspondence of the terraces of the Tagliamento riverbed, southern of Quinis hamlet. The sinkhole, shaped as a cylinder, had a diameter of 45 m and was 15 m deep. After that occurrence no other phenomena similar in dimension took place, since April 21st, 2022 when a collapse of approximately 18 m of diameter and 15 m of depht opened in the Raveo municipality (almost 2 km as the crow flies from Quinis). Even if the area was not interested by previous sinkholes, it was known to be potentially affected by this type of phenomena due to the presence of Carnian evaporities in the subsurface. Since 2000 unevenly, and with more continuity since 2014, the Geological Survey of the FVG region jointly with the Department of Mathematics and Geosciences of the University of Trieste, started to inventory all the regional sinkholes and recently there are several studies aimed at the identification of the related hazard. The occurrence of this last phenomenon aroused a specific interest, so that the day after the researchers went to the place and organized geophysical (integrated Electrical Resistivity Tomography) and Refraction Seismic) and unmanned aerial vehicle (UAV), commonly known as a drone, surveys. Not far (less than 200 m) from the occurred collapse, several are the infrastructures (bridge, roads..) and buildings that could be subjected to other similar phenomena. Furthermore, at less than 50 m, there is an important pipeline. The geometry and volume of the sinkhole was reconstructed and preliminary results evidenced a probable important role of subsurface water, while the bedrock was not detected down to at least 30 m. Further researches focused to the causes of the sinkhole occurrence are still ongoing.

Keywords: Sinkhole • evaporites • hazard • karst hydrogeology

The Friuli Venezia Giulia region is characterized by the presence of more than thousand sinkholes. As seen in previous chapters, in the Quinis village (Enemonzo municipality), near the study area (Esemon di Sopra), collapses have been occurring since the 1960s, with dimension ranging from 15-45 m in diameter and 10-15 m in depth (*Figure 46*C and D). The recent and sudden collapse, occurred on 21st April 2022 in Esemon di Sopra village (Raveo municipality), testifies the ongoing nature of these phenomena (*Figure 44* and *Figure 46*).

Figure 44 *The collapse sinkhole of Esemon di Sopra (22 April 2022)*

From a lithological, geomorphological and hydrogeological point of view, the area of Esemon di Sopra is similar to that of Quinis village. Both areas are characterized by an evaporitic bedrock (Raibl Formation) and are situated in a river terrace area. In particular, Esemon di Sopra is located near the riverbed of the Degano Torrent, immediately downstream of reliefs where evaporites outcrop *(Figure 45).*

Figure 45 *Gypsum outcrop along the road few meters from the collapse*

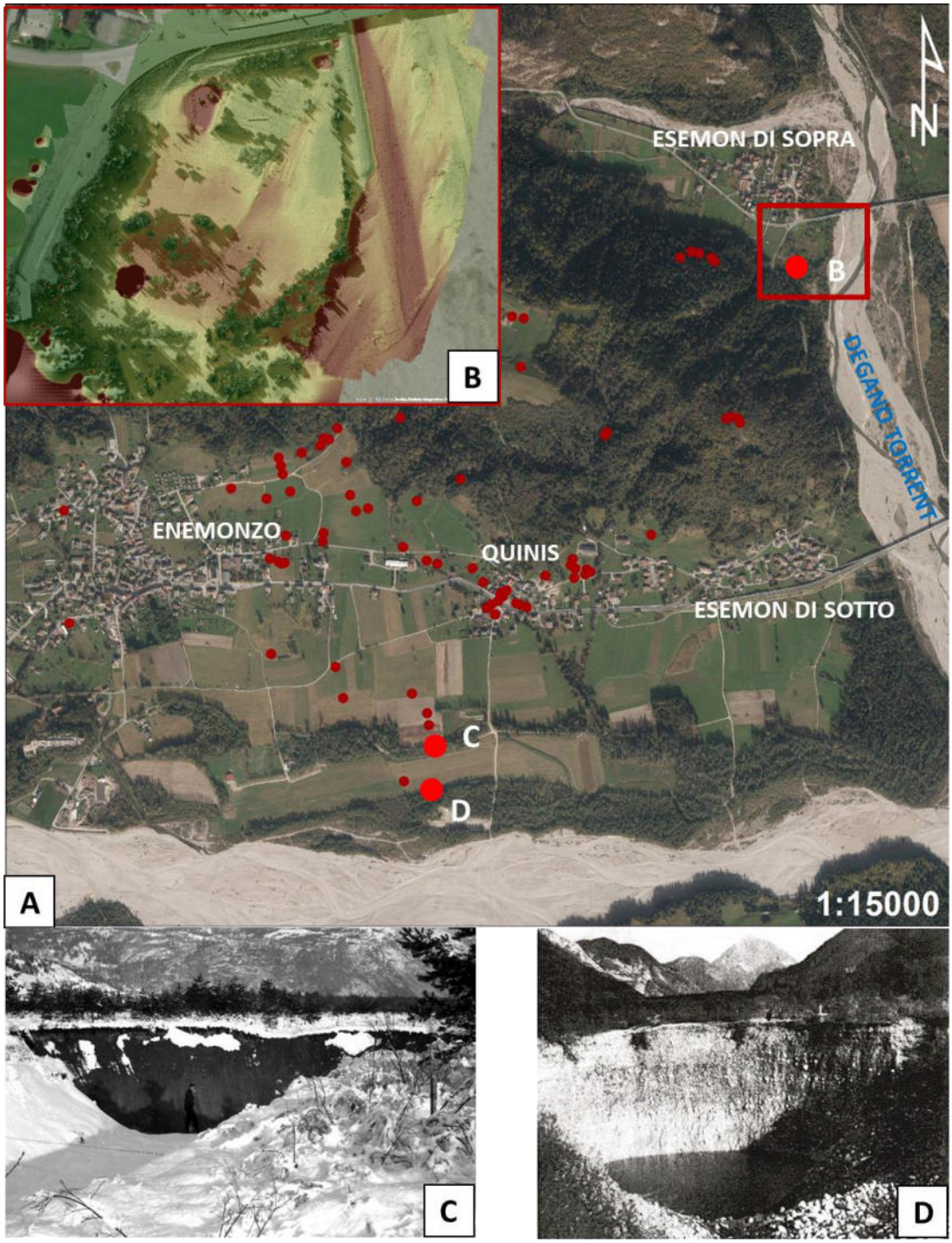

Figure 46 ***A)*** *The study area (red rectangle) and the surroundings. Sinkholes are marked with red dots;* ***B)*** *New collapse sinkhole in Esemon di Sopra village;* ***C)*** *and* ***D)*** *Sinkholes in Enemonzo municipality occurring in 1962 and in 1964 respectively*

A preliminary geomorphological survey on the sudden collapse in Esemon di Sopra village was carried out and a drone flight (DJI Phantom 4 RTK) was performed both outside and inside the sinkhole, allowing for its three-dimensional reconstruction (*Figure 47*).

Figure 47 *The collapse sinkhole of Esemon di Sopra*

Geophysical investigations, such as electric tomography (ERT) and seismic refraction (*Figure 48*), were conducted in the area surrounding the sinkhole to clarify the causes of its formation and determine the depth to the bedrock. The surveys followed an East-West oriented profile, positioned adjacent, but south of the occurred sinkhole. The location was chosen based on both logistical and technical considerations, in particularly the need to extend the profiles in length to increase the depth of investigation.

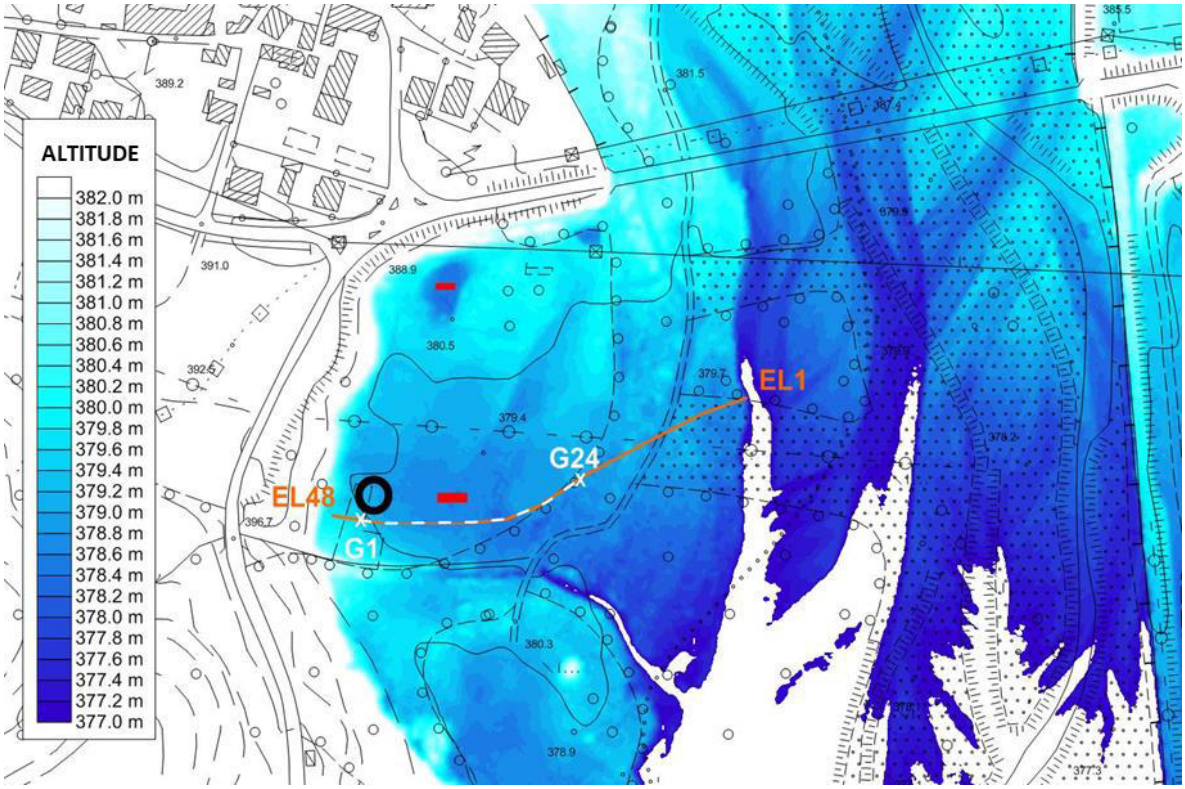

Figure 48 *Location of the surveys carried out. The orange line represents the ERT profile and the white dotted line represents the RF profile. The black circle indicates the approximate position of the sinkhole. The red segments represent two depressed areas*

Electrical resistivity tomography (ERT)

The ERT profile (188 m in length) was made using a Syscal Pro georesistivimeter connected with 48 metal electrodes spaced 4 meters with an electrode configuration Wenner-Schlumberger. This configuration was chosen as the best approach to detect both vertical and lateral variations. Special attention was given to minimizing contact resistance between the electrodes and the soil, particularly in the eastern part, where the first 15 electrodes were embedded in the dry riverbed of the Degano Torrent.

The acquired data demonstrated excellent quality with low standard deviation values always in between 0.5% and 1.3%, and often lower than 0.5%.

Contact resistance values were also sufficiently low and constant throughout the survey. It is interesting to note that the contact resistance was higher towards the Degano riverbed and gradually decrease to the west, indicating a decrease in surface grain size and a greater presence of water.

Both apparent and real resistivity data, obtained using Res2DINV and ERTLab software (*Figure 49* above and below, respectively), were analysed.

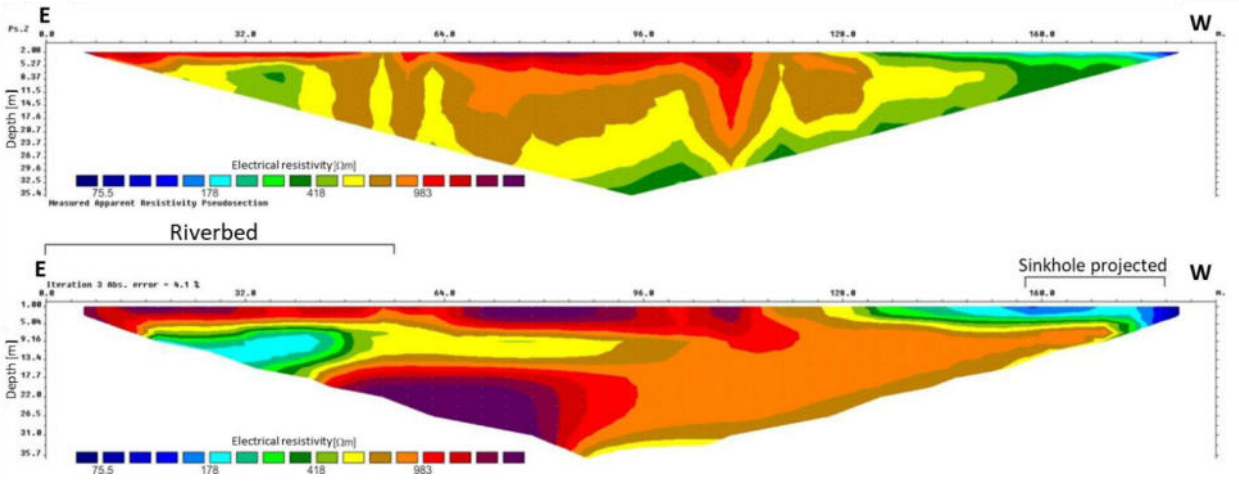

Figure 49 *ERT: apparent resistivity data (above) and real resistivity data (below). All the reference scales are the same*

Seismic refraction (RF)

The RF profile was realized along a portion of the ERT profile, with 24 vertical geophones (fn=14 Hz) 4m-spaced and with a Geode Geometrics seismic collector. A 5 kg sledgehammer shooting on a metal plate was used as a source of energy. For each energizing position (shot point) a vertical stack of 4 was made. A total of 28 shots were taken in 7 positions along the profile and at -10/+10 m from the first and last geophones respectively. The total length of the profile was of 92 m.

The data acquired were of good quality (*Figure 50*) and allowed a very accurate semi-automatic picking of the first arrivals. For the inversion, the software Plotrefa (OYO) was used to obtain a seismic velocity profile of the P waves (*Figure 51*).

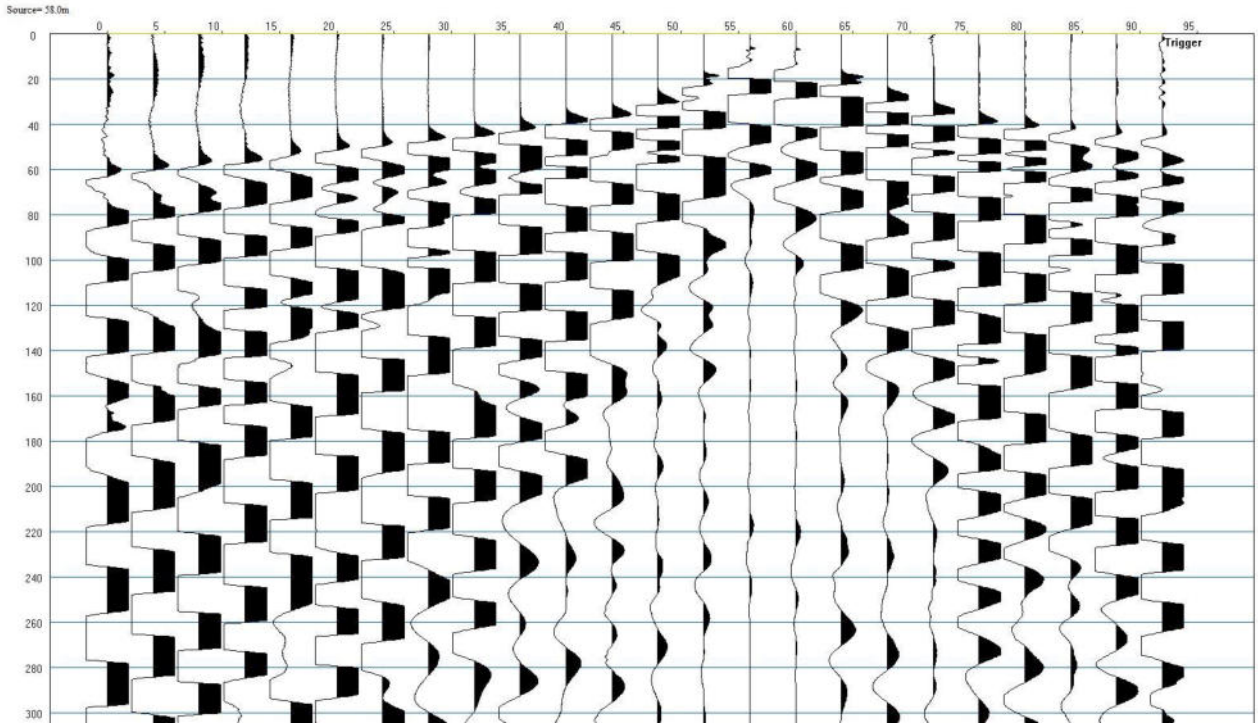

Figure 50 *RF. Example of obtained shot*

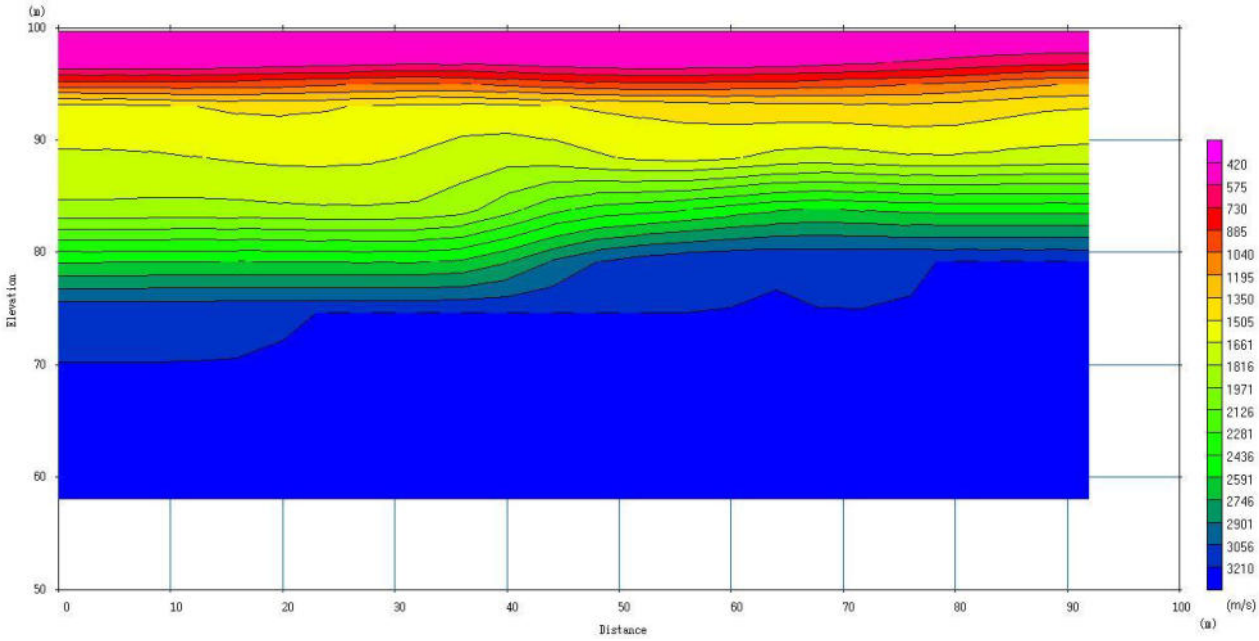

Figure 51 *RF: Final velocity profile of P wave*

RESULTS

The field survey and the drone flight have allowed a morphometric characterization and 3D reconstruction of the sinkhole, revealing its cylindrical-shaped with an approximately diameter of 18 m and a depth of 15 m. The vertical walls are characterized by an alternation of granular and cohesive layers (*Figure 52*), typical of alluvial deposits. The dry bottom is largely obliterated by the accumulation of debris. The model reconstruction, thanks to the flight carried out internally to the sinkhole, identified two continuation: WSW-ENE (segment 1 in purple) and SW-NE (segment 2 in blue) respectively (*Figure 53*).

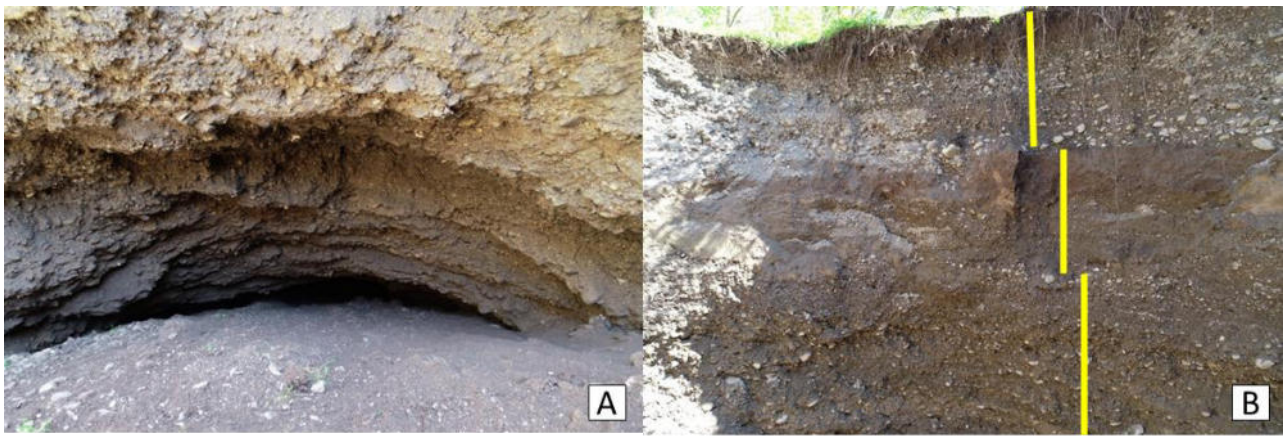

Figure 52 ***A)*** *Bottom of the sinkhole and* ***B)*** *Alternation of layer of granular and cohesive layers*

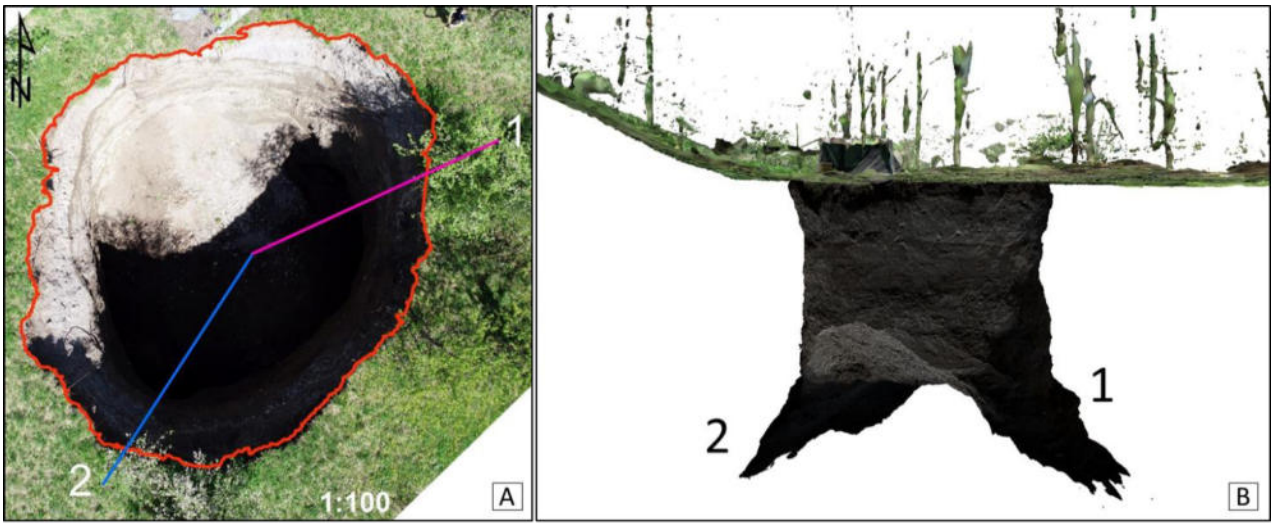

Figure 53 ***A)*** *Purple (1) and Blue (2) lines identify the directions in which the detected side continuations developed;* ***B)*** *3D representation of the sinkhole and its continuations*

As regards geophysical surveys, ERT and RF data have been analysed in an integrated way (*Figure 54*).

The ERT profile shows meaningful lateral variations. In the sinkhole area are present low resistive materials (values below 200 Ωm), while further east the values are above 500 Ωm. The approximate limit between the two zones is indicated by the black vertical dotted segment in *Figure 54*. This variation is probably linked both to finer materials in the sinkhole area and to the presence of water.

Along the whole profile, a clear vertical discontinuity is present between 3 and 5 m in depth. To the West, there is the passage towards materials with resistivity close to 1000 Ωm, while to the East, in the riverbed area, resistivity decreases to approximately 200 Ωm, probably linked to the presence of water (Degano River). These two levels are also present in the RF profile with a clear shift of velocity at a depth of about 4 m, between values of 400-500 m/s and more than 1000-1500 m/s.

However, at higher depths, the ERT and RF data are not in accordance. On the western side of the profile, the ERT shows a decrease in resistivity, while the RF data shows a defined increase in velocity with values in the order of 3000 m/s.

This difference is not related to measurement or data processing/inversion errors, but is probably due to different saturation conditions at different points below the investigated area.

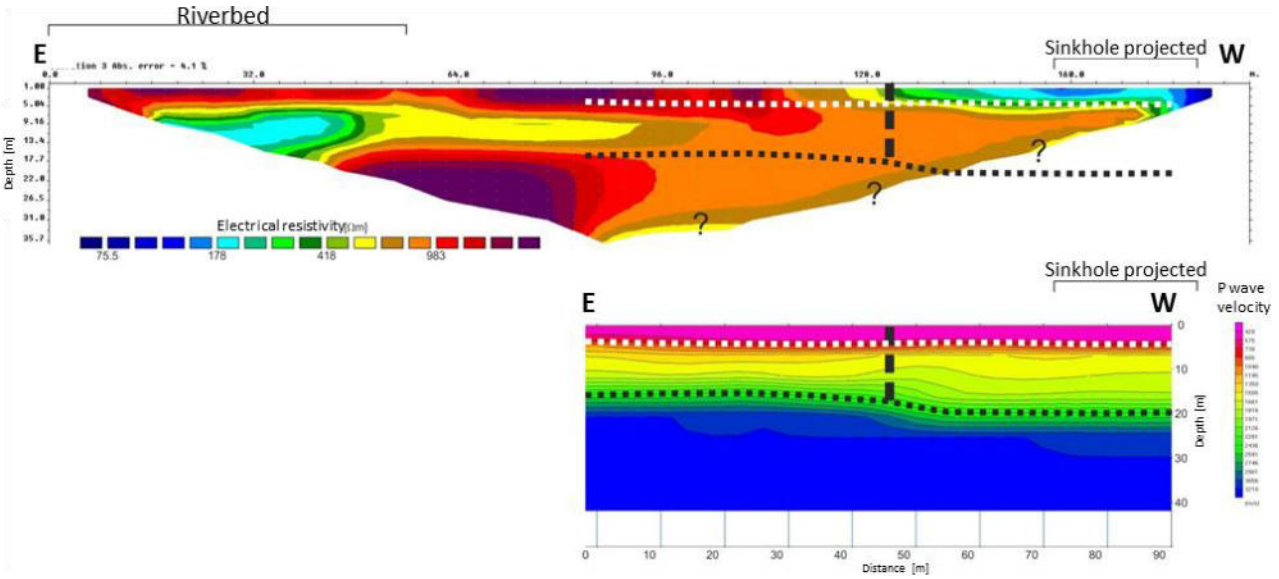

Figure 54 *Comparison between ERT profile (above) and RF profile (below). The white dotted line marks a clear variation in seismic velocity and it has also been reported on the ERT profile for comparison. The same applies to the black dotted line. The vertical dotted segment indicates a clear lateral discontinuity of resistivity, and it has been reported on the RF profile, where there is a deepening towards West of the deepest seismic discontinuity*

Based on the available data, and within the resolution limits of the methods employed, no cavities seem to be present in correspondence of the acquired profiles.

On the basis of the data exposed and the geological and geomorphological surveys carried out in the surrounding areas, there are numerous elements of interest that can be directly or indirectly correlated with the sinkhole and that deserve further study and investigation. One key objective is to identify the depth and characteristics of the bedrock, which outcrops along the road connecting Esemon di Sopra with Esemon di Sotto, approximately 200 meters SW of the sinkhole (*Figure 45*).

An interesting element indicating previous and potentially occurring movements is the deformation of a retaining stone wall located upstream of the same road, positioned about 100 m SW of the sinkhole (*Figure 55*A).

Another feature of interest is a depression *(Figure 55B)* located about 80 m north of the sinkhole, currently artificially filled with water (marked with a red sign "-" further North in *Figure 48*). The genesis of this depression is not fully understood at present, and, further investigation is required to determine whether it is of anthropogenic or natural origin.

Figure 55 ***A)*** *Deformed retaining stone wall;* ***B)*** *Depression artificially filled with water located North of the sinkhole (photo taken from NW)*

The analysis of the surrounding area is noteworthy (*Figure 48*). The area where the sinkhole developed exhibits a lower morphological profile compared to its surrounding (excluding the current Degano riverbed). This aspect warrants further analysis and investigation.

Finally, it is essential to highlight a potential criticality regarding the presence of a methane pipeline oriented in the EW direction, located less than 50 m north of the sinkhole.

CONCLUSION

For what concern the genesis of the phenomenon, a plausible hypothesis involves a correlation with the presence of a lateral inflow of water, which deepened following the lowering of the water table during the prolonged period of drought that characterized the end of 2021 and the first months of 2022.

Given the size of the sinkhole, its proximity to the village of Esemon di Sopra, and the predisposing characteristics for the occurrence of similar phenomena in the mountain valley areas where the evaporites deposits are present, it would deserve further study. The terebration of a borehole would allow a more in-depth analysis of the lithotypes interested by the phenomenon and the desirable interception and characterization of the evaporitic bedrock. It would also be appropriate to conduct a historical analysis of the aquifer levels, aiming to define a threshold value below which potential future phenomena might be expected.

CHAPTER 4.2

ANALYSIS OF IGM AERIAL FRAMES IN THE SAURIS MUNICIPALITY

When a sinkhole occurs, it would be important to know the triggering factors, and how it could evolve in order to avoid further losses in terms of damages or possible human deaths. The historical reconstruction of past events can be of particular interest in forecasting future developments.

Thanks to the aerial frames acquired from the Military Geographic Institute (IGM), it was possible to reconstruct the historical evolution of several sinkholes in the Sauris municipality (those shown in *Figure 11* and *Figure 12*). The eight frames available span from 1945 to 2000. In addition to the IGM aerial frames, the orthophotos for the years 2012, 2018, 2022 and 2023 (downloaded from Google Earth and Bing Maps) were also accessible (see *Figure 58*). This comprehensive set of images allows for a total temporal reconstruction of sinkholes spanning almost 80 years.

Frame	Year	Month	Elevation	Scale
78	**1945**	September	8100	60000
5046	**1954**	October	10000	55000
2960	**1957**	July	5200	29000
822	**1977**	July	4300	20000
256	**1980**	July	3500	15000
455	**1986**	September	5100	25000
9047	**1993**	July	6980	38000
7719	**2000**	September	5400	35000

Table 8 *Data about the year, month, elevation and scale of each acquired aerial frame from IGM*

Already from the first frame, despite its low resolution and high flight height, 4 sinkholes can be recognized (*Figure 56*), as an evidence that they occurred before 1945.

In *Figure 57* it is possible to observe that in 1957 the two main sinkholes (A and B) were still poorly delineated with a woodland cover oblitering the understanding of their depth and development. Subsequently, the 1977 frame reveals collapsing walls in sinkhole B suggesting a wider activation in the last 20 years.

Between 1977 and 1980, there is evidence of deepening in sinkhole B and a collapse in sinkhole A. From 1986 to 2000, there was a reforestation which partly prevented the definition of the perimeter of sinkhole B and the evaluation of its evolution. One of the elements to take into account is the road passing between the two sinkholes which, in particular since 1993, has been on the edge of both. As regards sinkholes C and D, they are also pre-1945 and until 2000 a slow but continuous sinking was observed.

In the 12 years following 2000, there was a gap in information. However, thanks to Google Earth and Bing Maps images, it was possible to observe the continuous evolution and deepening of the sinkholes A and B, as well as the inactivity of sinkholes C and D. In particular, it has been observed the presence of water in the sinkhole B in 2012 and the disappearance of the road between sinkholes A and B. In term of risk and for planning purposes this is an important information to take into account.

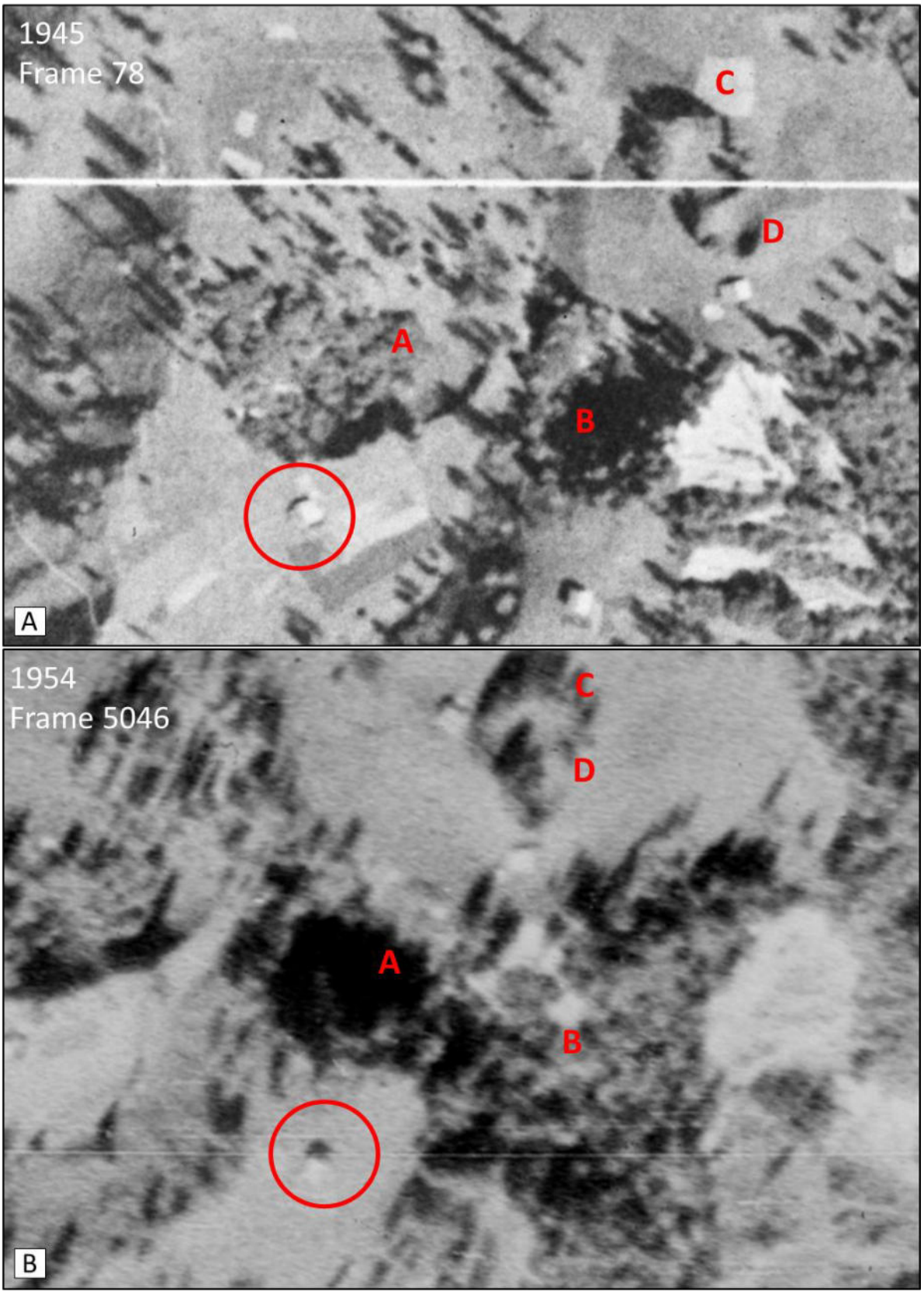

Figure 56 *IGM frames:* ***A)*** *Data frame 1945 and* ***B)*** *Data frame 1954. Red letters A, B, C and D indicate the same sinkholes of the Figure 12. The red circle identifies the house used as a reference point*

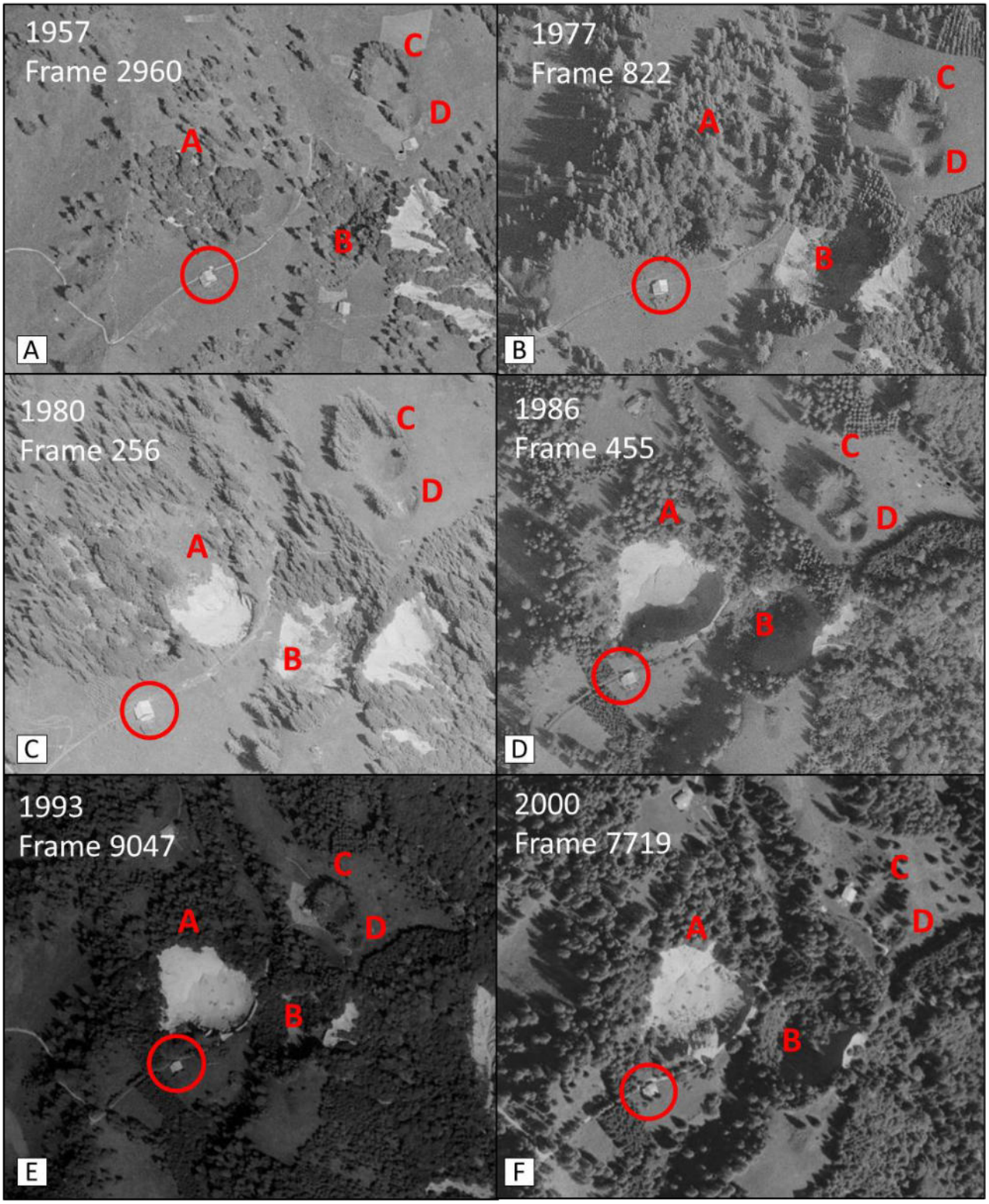

Figure 57 *IGM frames.* ***A)*** *data frame 1957;* ***B)*** *data frame 1977;* ***C)*** *data frame 1980;* ***D)*** *data frame 1986;* ***E)*** *data frame 1993;* ***F)*** *data frame 2000. Red letters A, B, C and D indicate the same sinkholes of the Figure 12. The red circle identifies the house used as a reference point*

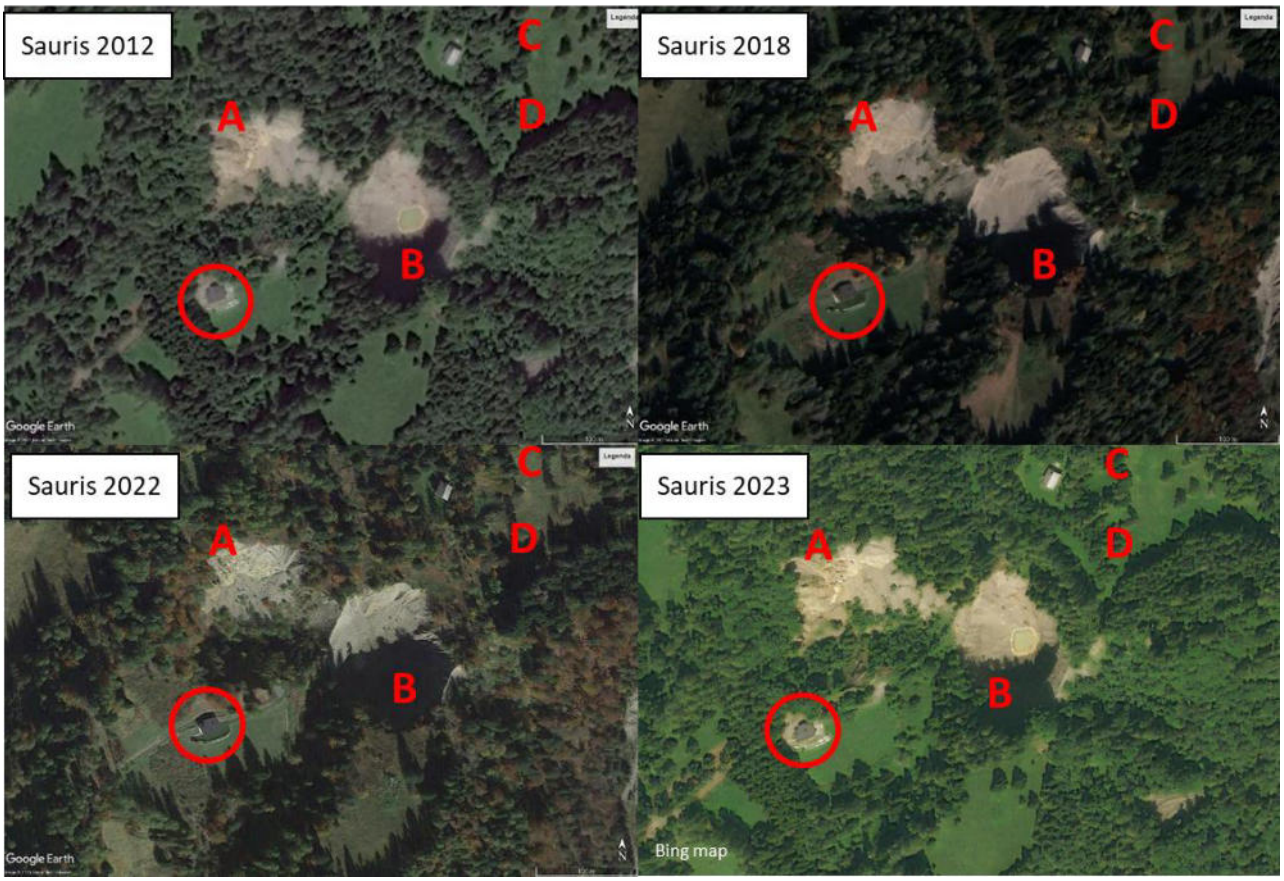

Figure 58 O*rtophotos taken by Google Earth for the years 2012, 2018 and 2022 and by Bing map for the 2023*

CHAPTER 4.3

TRENCH EXCAVATION IN ENEMONZO MUNICIPALITY

Trenching is a well-known direct investigation method widely used for depth characterization of sinkholes. This approach has been frequently used in Spain (Gutiérrez et al., 2017; Sevil et al., 2020), but in Italy, the trench hereafter presented is the first investigation done on these type of phenomenon.

The site for the realization of the trench was chosen taken into account an area in which researchers from the Department of Mathematics and Geosciences at the University of Trieste, over the years, have conducted numerous researches and investigations, acquiring an in-depth knowledge of the area. The area is located between Via delle Scuole and Via Nazionale, in the Enemonzo municipality and it is known not only for the presence of an active sinkhole but also for other sinkholes known since 1976. In fact, at the end of the 1976 a collapse sinkhole opened in a grassy area not far from some houses. The void was filled with aggregates and soil. About six months later, it suddenly reactivated and it was filled again with landfill. In 1985 a new sinkhole opened a few meters from the previous one. Reaching a depth of about 3.5 meters, and an estimated width of 7-8 meters. As a result of the event, two houses that were located very close to the site were demolished and the material from the demolition was partially used to filled the void. Finally, in 2012, near the area of the 1976 sinkhole, a new depression of about 4 meters in diameter and 2 meters deep formed. After an initial paroxysmal phase, the bottom of the depression is still slowly deepening.

On 4 April 2022, two tomographic arrays (ERT), orthogonal to each other (N-S and E-W) were realised to identify the best orientation for the excavation of the trench (*Figure 59*).

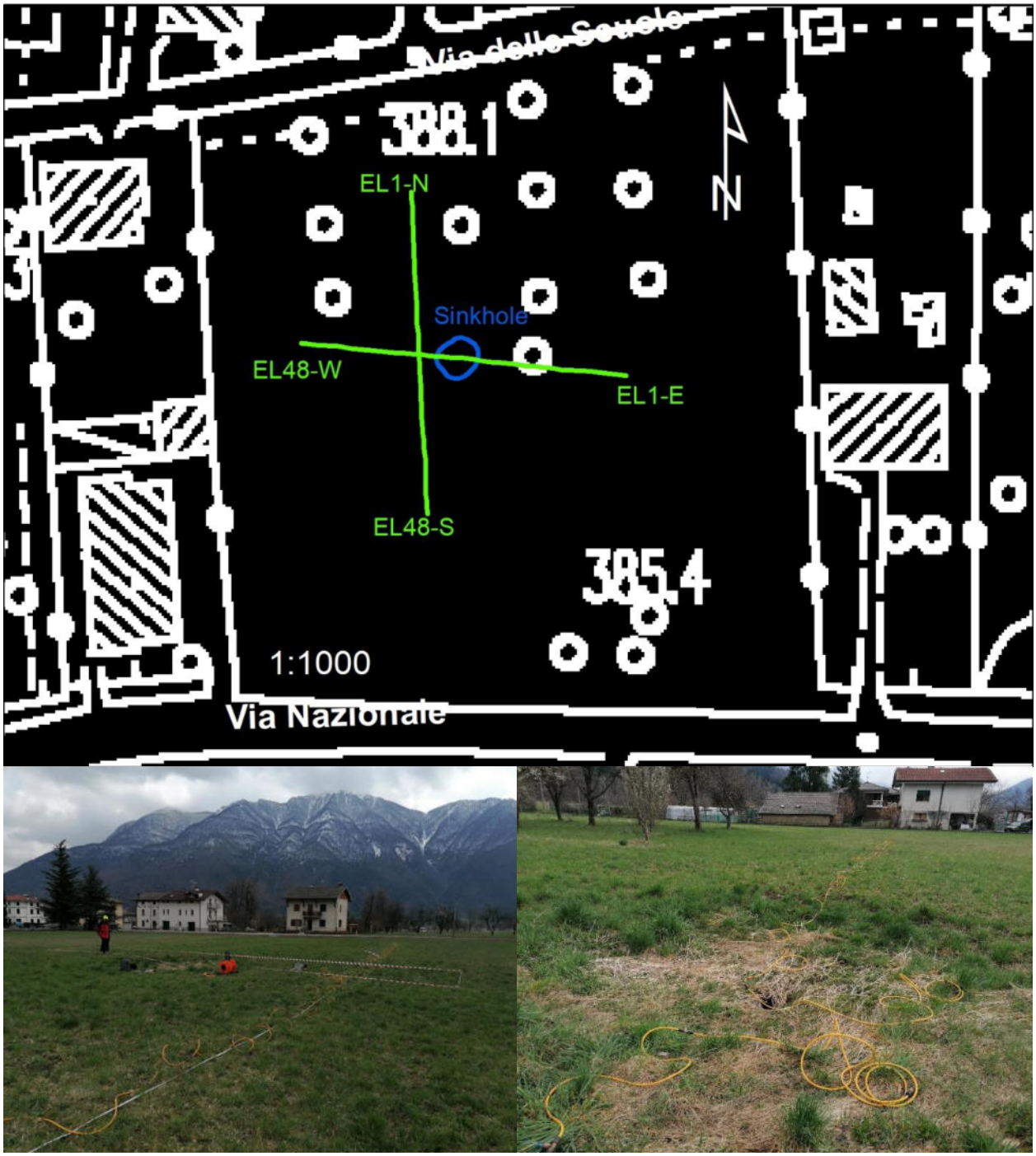

Figure 59 *Electrical tomography (ERT) along the N-S and E-W arrays*

The E-W array crossed the active sinkhole (shown in blue in *Figure 59*), identified by GPS. Analysing the inversion models obtained from the geophysical investigations (*Figure 60*), it is evident that West of the current sinkhole, there is the presence of a more resistivity material (red-orange area). It probably corresponds to the material used to fill the 1976 sinkhole. This investigation allowed to opt for an excavation in the E-W direction, aiming to intercept both the historic sinkhole (1976) and the current one visible on the surface.

The diameter of the historical sinkhole is approximately 20 meters with a depth of 5-6 meters. Above this latter, a less resistive portion was present, consisting of fine materials witnesses of a further probable sinking that over the years has affected the old sinkhole. Further east, there is another more resistive area (yellow-orange), corresponding to the current subsidence with a diameter of about 4-5 meters and a depth of 2-3 meters. This area is not located within the sinkhole of 1976, and does not correspond to lateral resettlements of the latter, as there is no presence of filling material below it. Consequently, the new sinkhole is independent from the previous event, probably resulting from another deep void or the conveying of materials into voids that remained between the filling material.

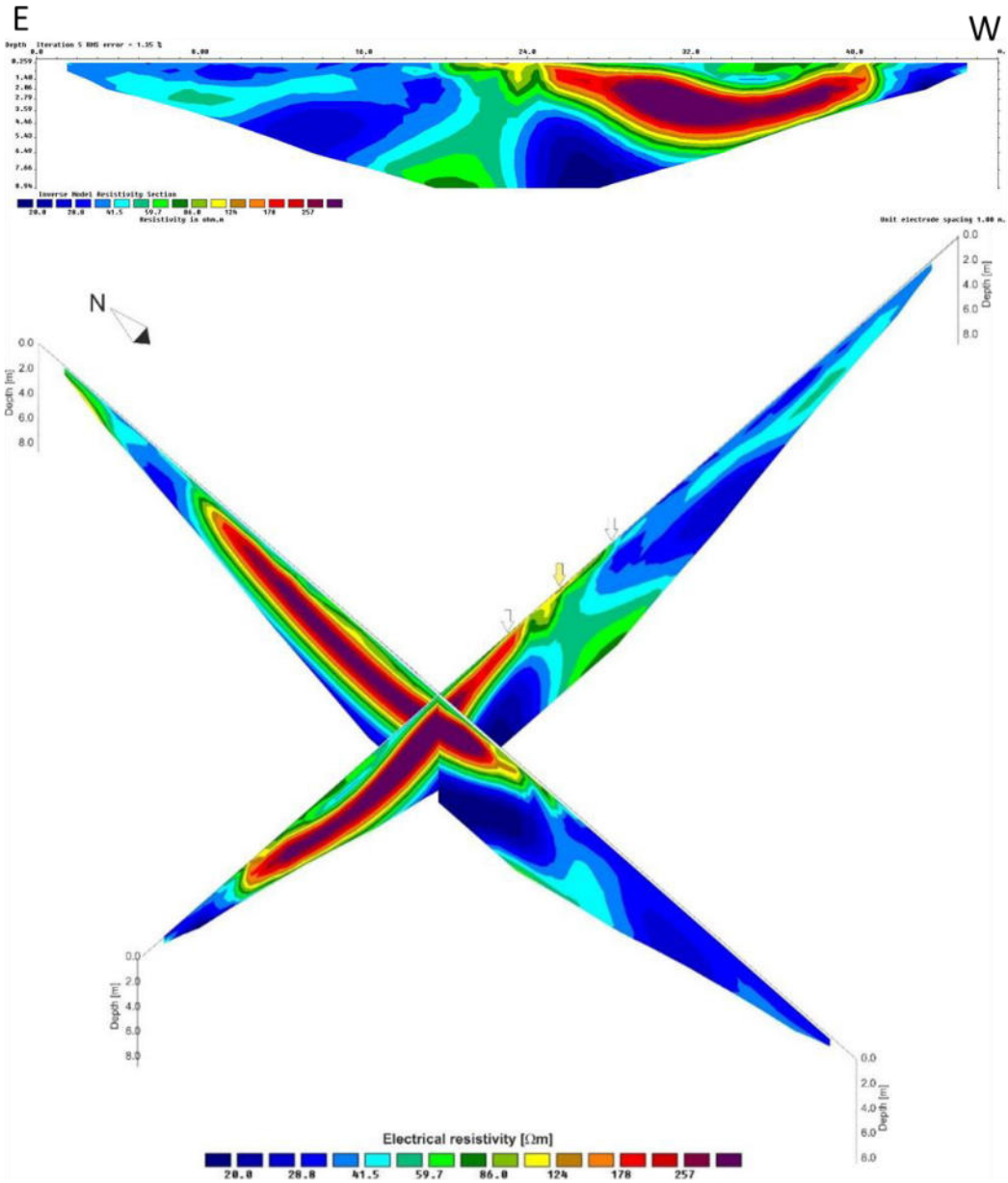

Figure 60 *Electrical tomographic profile*

After the preliminary studies, the excavation of the trench (5-7 April 2022) was performed. It was oriented E-W with a length of 20 m, a width of 3 m and a depth of 2.5 m (*Figure 61*), and digged throughout the active sinkhole.

During the excavation activities, as hypnotized from the geophysical investigation, part of the extracted material was attributable to the material used to fill the 1976 sinkhole (*Figure 62*).

Figure 61 *The phases of the trench excavation*

Figure 62 *Evidence of fill material*

The preparation of the trench involved the scraping and verticalization of the south wall of the trench, the installation of a yellow reference gridlines of 1x1 meter and gridlines numbering. After a preliminary analysis of the wall, deep excavations of additional parts in areas of particular interest were done.

Three different camera-equipped devices (a DJI Air 2S drone, a Nikon D5300 camera, and an iPhone 13 Pro) were used to collect photos of the entire area and the trench (*Figure 63*).

Figure 63 *Preparation of the trench and image acquisition by drone*

Different units of the Quaternary deposits were identified, described and later sampled for granulometric analysis (*Figure 64*). The units consist of a succession of clay-sands, silt-sands and gravel (fan-colluvial deposits). The parameters described in the field are summarized in *Table 9*: texture, colour (Munsell scale colour), reaction to HCL, percentage of clasts, maximum and average size of clasts and their composition.

Figure 64 *The sampling collection phase*

Table 9 *Description of the stratigraphic units*

UNITS	TEXTURE	MATRIX COLOUR	RX HCL	% CLASTS	D MAX (CM)	D MED (CM)	CLASTS COMPOSITION	NOTES
A (torrential fan debris flow)	Gravel with silty sand	10YR 5/2	3-4	65 %	5	0,5	Dolomites, siltstones, shales e marls	Coarse sub-horizontal stratification. Slightly to moderately altered clasts. The lower part of the unit is characterized by silty sand with rare sub-cm clasts (colour 2.5Y 5/3) with a massive structure.
B (colluvial deposits)	Clay with silt	2,5Y 4-3/2	1	--	--	--		Massive structure, rare mm clasts present. Locally (between sections 10 and 13) the lower part of the unit has a 2.5Y 4/3 colour.
C (torrential fan deposits)	Alternation of gravel with sand and slightly sandy silt levels	2,5Y 5/3	4	65 %	3	0,5	Dolomites, siltstones, shales e marls	The silty levels have a massive structure and are on average 10-20 cm thick.
D (torrential fan debris flow)	Gravel with sand and silt	2,5Y 4/3	3-4	70 %	10	1,5	Dolomites, siltstones, shales e marls	Poorly expressed sub-horizontal stratification; there are multi-metric lenses 10-15 cm thick of gravelly sand (colour 2.5Y 5/2) and sandy silt (colour 2.5Y 5/4) with a massive structure. The clasts are predominantly angular and subordinately sub-rounded. Upper limit of the unit wavy and irregular.
E (colluvial deposits)	Clayey silt	2,5Y 4/2	2-3	5 %	1	0,5		Massive structure; rare angular clasts present; frequent carbonaceous frustules. Wavy and irregular upper limit.
F (torrential fan debris flow)	Fine gravel in a slightly sandy silty matrix	2,5Y 5/2	3	70 %	3	0,5	Dolomites, siltstones, shales e marls	There are layers and lenses, including multi-metric ones, of silt (10-15 cm thick, colour 2.5Y 4/3). Upper limit poorly expressed and wavy.
G (colluvial deposits)	Gravelly silt	2,5Y 5/3	2-3	15 %	1	0,5		Massive structure; predominantly sub-angular clasts.
H (anthropogenic horizon)	Clayey silt, slightly gravelly	2,5Y 4/2	1	20 %	5	1		Present vegetal fragments, roots, fragments of bricks.

The comparison in AutoCAD between the hand-draw graph paper representation and the topographic reconstruction using a scaled and georeferenced drone survey revealed the primary units identified on the vertical wall of the trench. Eastward of the center of the active sinkhole, observed in the 11th section, a horizon failure of approximately 30 cm was identified. The limit of the active sinkhole is highlighted in red in *Figure 65*. About 1 meter below the topographic surface, it became vertical showing a 3D cylindrical shape. On the western side of the trench (*Figure 66*) there is evidence of the material used to fill the void from the collapse sinkhole of 1976. Although not entirely distinct, as one moves westward, another deepening of the filling material can be discerned, indicating the presence of the older sinkhole (in orange in *Figure 67*).

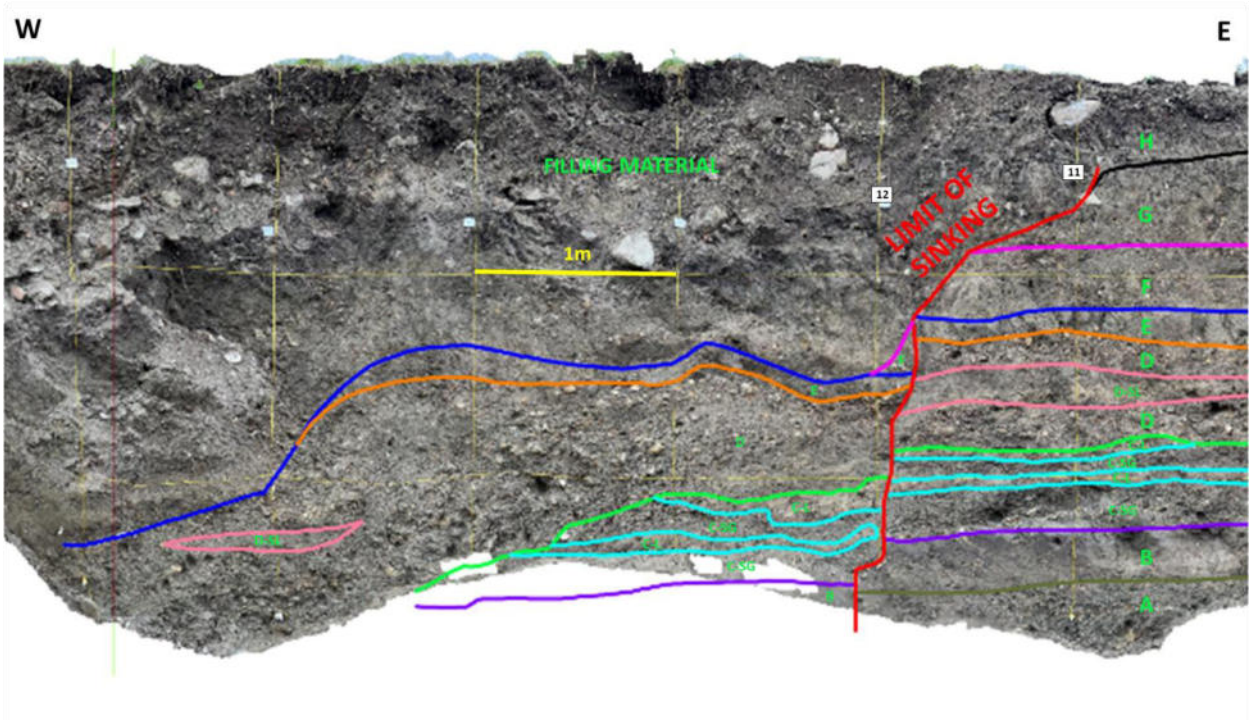

Figure 65 *Trench wall with detail on the limit of the sinking in red. Divisions of the stratigraphic limits are highlighted with different colors. In yellow it is visible the reference gridlines 1x1m*

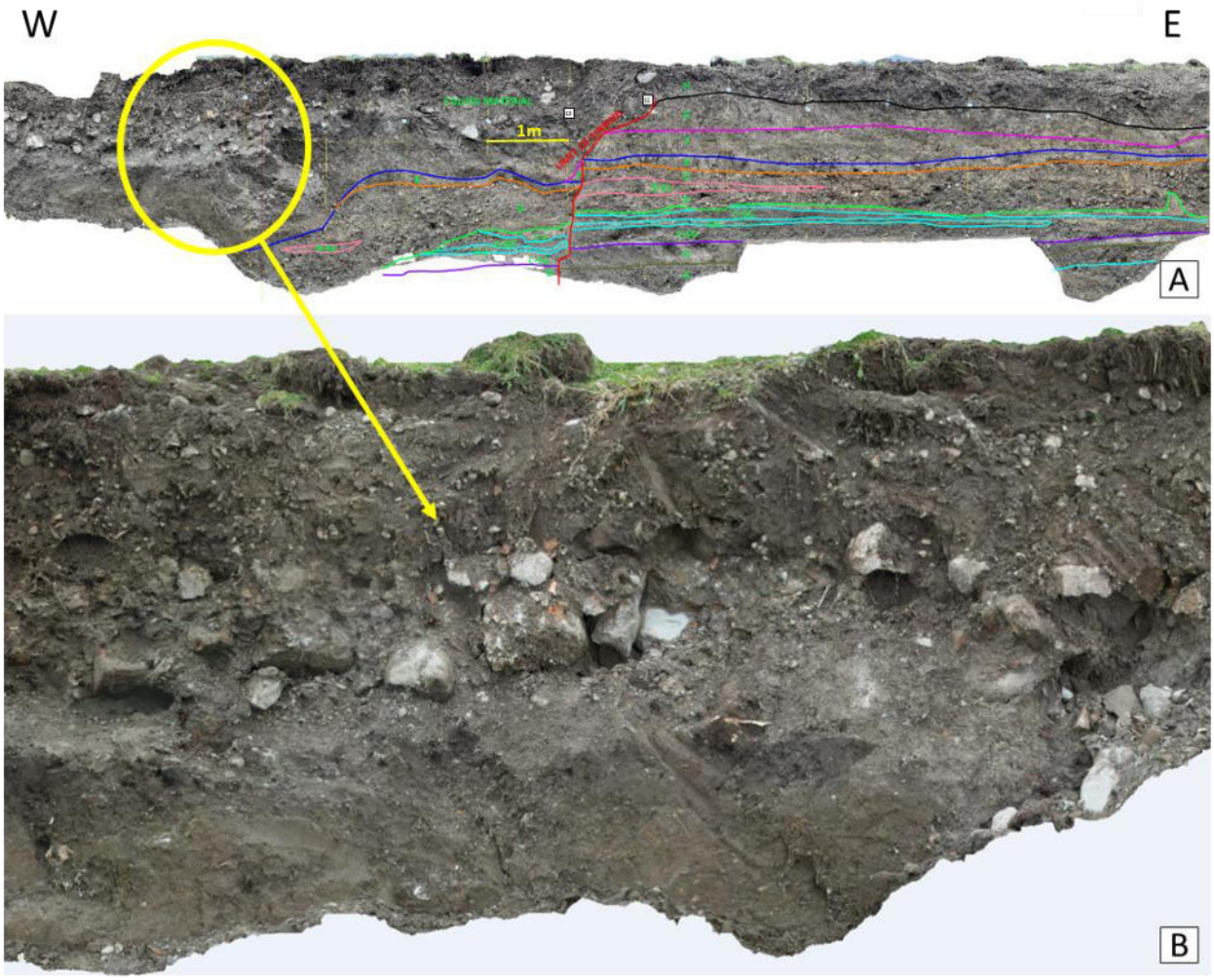

Figure 66 ***A)*** *Trench wall with subdivisions of the stratigraphic units with different colors. In red the limit of the sinkhole;* ***B)*** *Detail of the material used to fill the old sinkhole*

The results of the field surveys are presented in *Figure 67*. The integration between the geophysical survey and the structures identified by the trench has allowed to identify not only the presence of the current sinkhole, but also the one that occurred in 1976 (in orange in *Figure 67* is represented the 1976 sinkhole and in blue the active one). Thanks to the trench across the active sinkhole, it was also possible to clarify its 3D cylindrical shape, characteristic of a cover collapse. In the area, there are also absorption points that confirm, once again, the high degree of karstification in this area, highlighted already in the 80s during the terebration of some boreholes that identified the presence of voids at different depths.

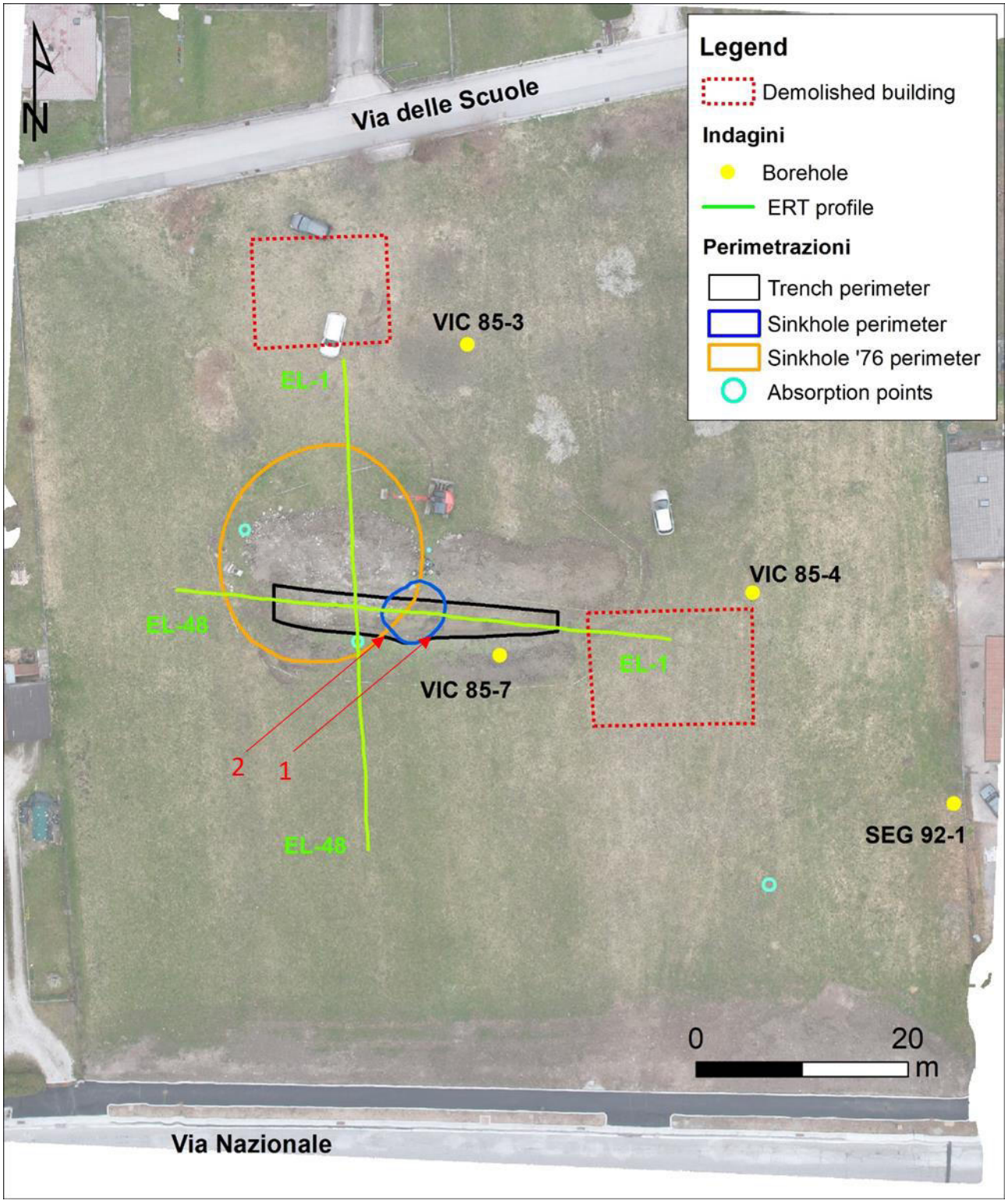

Figure 67 *Summary map with perimeters of both the new sinkhole (in blue) and the sinkhole opened in 1976 (in orange). The red arrows indicate: with no. 1 the Eastern limit of the active sinkhole and with no. 2 the intersection with the filling material of the historical sinkhole. The perimeters of the demolished buildings are outlined in dotted red. Yellow points identify the boreholes of the 80s*

REFERENCES

- Gutierrez F., Zarroca M., Linares R., Roqué C., Carbonel D., Guerrero J., McCalpin J.P., Comas X., Cooper A.H. (2018) Identifying the boundaries of sinkholes and subsidence areas via trenching and establishing setback distances. Engineering Geology 233 255–268. https://doi.org/10.1016/j.enggeo.2017.12.015
- Sevil J., Gutiérrez F., Zarroca M., Desir G., Carbonel D., Guerrero J., Linares R., Roqué C., Fabregat I. (2017) Sinkhole investigation in an urban area by trenching in combination with GPR, ERT and high-precision levelling. Mantled evaporite karst of Zaragoza city, NE Spain. Engineering Geology 231, 9-20. http://dx.doi.org/10.1016/j.enggeo.2017.10.009

CHAPTER 4.4

Paper published in Remote Sensing 2022, 14, 5187

https://doi.org/10.3390/rs14205187

Benchmarking Different SfM-MVS Photogrammetric and iOS LiDAR Acquisition Methods for the Digital Preservation of a Short-Lived Excavation: A Case Study from an Area of Sinkhole Related Subsidence

Amerigo Corradetti [1]*, Thomas Seers[2], Marco Mercuri[3], Chiara Calligaris[1], Alice Busetti[1] and Luca Zini[1]

[1] Mathematical and Geosciences Department, University of Trieste, Via Weiss 2, 34128 Trieste, Italy
[2] Petroleum Engineering Program, Texas A&M University at Qatar, Education City, Doha P.O. Box 23874, Qatar
[3]Dipartimento di Scienze Della Terra, Sapienza University of Rome, P.le Aldo Moro 5, 00185 Rome, Italy

remote sensing

MDPI

Article

Benchmarking Different SfM-MVS Photogrammetric and iOS LiDAR Acquisition Methods for the Digital Preservation of a Short-Lived Excavation: A Case Study from an Area of Sinkhole Related Subsidence

Amerigo Corradetti [1,*], Thomas Seers [2], Marco Mercuri [3], Chiara Calligaris [1], Alice Busetti [1] and Luca Zini [1]

[1] Dipartimento di Matematica e Geoscienze, University of Trieste, Via Weiss 2, 34128 Trieste, Italy
[2] Petroleum Engineering Program, Texas A&M University at Qatar, Education City, Doha P.O. Box 23874, Qatar
[3] Dipartimento di Scienze Della Terra, Sapienza University of Rome, P.le Aldo Moro 5, 00185 Rome, Italy
* Correspondence: amerigo.corradetti@units.it

Abstract: We are witnessing a digital revolution in geoscientific field data collection and data sharing, driven by the availability of low-cost sensory platforms capable of generating accurate surface reconstructions as well as the proliferation of apps and repositories which can leverage their data products. Whilst the wider proliferation of 3D close-range remote sensing applications is welcome, improved accessibility is often at the expense of model accuracy. To test the accuracy of consumer-grade close-range 3D model acquisition platforms commonly employed for geo-documentation, we have mapped a 20-m-wide trench using aerial and terrestrial photogrammetry, as well as iOS LiDAR. The latter was used to map the trench using both the 3D Scanner App and PIX4Dcatch applications. Comparative analysis suggests that only in optimal scenarios can geotagged field-based photographs alone result in models with acceptable scaling errors, though even in these cases, the orientation of the transformed model is not sufficiently accurate for most geoscientific applications requiring structural metric data. The apps tested for iOS LiDAR acquisition were able to produce accurately scaled models, though surface deformations caused by simultaneous localization and mapping (SLAM) errors are present. Finally, of the tested apps, PIX4Dcatch is the iOS LiDAR acquisition tool able to produce correctly oriented models.

Keywords: SfM-MVS photogrammetry; iOS LiDAR; digital transition; fieldwork; geo-documentation; virtual outcrop models; GCP alternatives

Citation: Corradetti, A.; Seers, T.; Mercuri, M.; Calligaris, C.; Busetti, A.; Zini, L. Benchmarking Different SfM-MVS Photogrammetric and iOS LiDAR Acquisition Methods for the Digital Preservation of a Short-Lived Excavation: A Case Study from an Area of Sinkhole Related Subsidence. *Remote Sens.* **2022**, *14*, 5187. https://doi.org/10.3390/rs14205187

Academic Editor: Jorge Delgado García

Received: 9 September 2022
Accepted: 12 October 2022
Published: 17 October 2022

1. Introduction

Digital photogrammetry and LiDAR-based geospatial field data acquisition using smartphones and tablets is revolutionizing the use of close-range 3D remote sensing within the geosciences [1–7]. Commensurately, the rapid uptake of low-cost, readily deployable multi-senor drones has extended the reach of such techniques, enabling nadir view photogrammetric surveys of horizontal outcrops, as well as occlusion free reconstructions of large vertical sections [8–10]. Despite the relative simplicity with which 3D surface reconstructions of geological exposures (i.e., virtual or digital outcrop models: [11–19]) can be acquired using such platforms, the reliability of the geospatial information extracted from their data products is typically unclear, particularly when survey grade measurements are unavailable to calibrate and benchmark the resultant outcrop models. The deployed sensor platform's accuracy and precision in terms of position and orientation is often a key consideration for many geoscientific applications of 3D surface reconstructions, with deviations in the resultant scale, geolocation and attitude of the generated models being deleterious to the quality of metric data extracted thereof. Recently, Uradziński

and Bakuła [20] have shown that under optimal conditions, dual-frequency receivers on smartphone devices allow geolocation with accuracies of a few tens of centimeters with post-processing carrier phase correction, providing accurate ground control points (GCPs) for georeferencing and scaling. Analogously, additional authors have demonstrated that 3D models can be satisfactorily oriented and scaled by utilizing the smartphone camera pose information (i.e., the camera's extrinsic parameters) to register photogrammetry-derived models (e.g., [21–23]). In similitude, Corradetti et al. [4] obtained oriented and scaled 3D models using inertial measurement unit (IMU) derived smartphone orientation data, with constraints on the device's (and thus image's) major axis using a handheld gimbal. Whilst relatively streamlined in comparison to conventional GCP geolocation using survey grade tools (i.e., differential GNSS or total station surveys), these methods still require a degree of setup in the field and significant post-processing. However, many casual users routinely acquire photographs for close-range photogrammetry, and more recently, scans through the iOS LiDAR devices do so without any predefined strategy for the georectification of the resultant 3D model, severely limiting their utility as a medium for quantitative geological analysis. Conversely, it is well established amongst geospatial specialists that the absence of a sound registration strategy can negatively impact upon results.

Three-dimensional models of outcrops represent valuable tools to document, analyze and interpret geology as they provide the basis to efficiently extract quantitative information from geological exposures inaccessible by manual fieldwork [11,13,24–29]. To date, geological surface reconstructions have enjoyed diverse applications within numerous geoscientific disciplines, including structural geology (e.g., [24,30]), sedimentology (e.g., [31,32]), stratigraphy (e.g., [33]), volcanology (e.g., [34]), geomorphology (e.g., [35,36]), and applications in slope stability analysis and landslide monitoring (e.g., [37–40]). Such models are also routinely employed within geo-heritage site documentation (e.g., [41,42]), as well as for the documentation of excavations (e.g., [30,43]). In recent years, geological surface reconstructions have also been leveraged as pedagogical tools to enhance contextual understanding and 3D thinking within the classroom [44–47], and to deliver virtual geological field trips to geoscience students, industry practitioners and the wider public (e.g., [48–51]). Applications of modern digital mapping have also been used to assist the inclusion of persons with disabilities in geoscience education and research (e.g., [52]). The demand for sharing such models has led to the development of dedicated online virtual outcrop model databases, such as e-Rock [53], Svalbox [54], and V3Geo [55]. Though the aforementioned developments can be viewed as positive for the geoscience community, the wider proliferation of digital outcrop modelling techniques requires awareness of the accuracy limits of these powerful tools, particularly when sharing quantitative data extracted from such media (e.g., [55]).

Using a case study of a trench that was recently excavated to probe historical subsidence in the proximity of an infilled sinkhole in the municipality of Enemonzo (Italy), we have investigated the utility of various acquisition strategies for the generation of correctly oriented and scaled 3D models. The geological interpretation of the study area has been presented elsewhere [56,57] and the reader is invited to consult the aforementioned work for further details. In summary, the area is characterized by the presence of several types of sinkholes [58,59] with the studied trench being located proximally to the west of a phenomenon that manifested at the surface during the 1970s ([56] and the references cited therein) and reactivated in the 1980s and 2010s. The presence of this sinkhole is related to a Triassic evaporitic bedrock mantled by variably consolidated and loose Quaternary deposits having variable thickness, which varies in the area, from north to south, from a few meters to more than 60 m [56,60]. Bedrock dissolution associated with groundwater flux is thought to have caused the collapse of the sinkholes [61,62] within the present study area.

A detailed description of the acquisition procedure and setup is presented within the method section below. In summary, we have used three camera-equipped devices: namely, a DJI Air 2S drone, a Nikon D5300 camera, and an iPhone 13 Pro, to generate a structure from motion-multiview stereo (SfM-MVS) photogrammetric reconstructions of

the trench. The model made from the DJI Air 2S dataset (hereafter named Air 2S) included a larger acquisition area, which coupled with its superior nominal accuracy, provided a benchmark against which the ground-based surveys could be compared. The Air 2S model was also compared against a LiDAR-derived Digital Terrain Model (DTM) available at 1 m resolution to check for its vertical accuracy in relation to the world frame. Moreover, additional field-based surveys were performed using the embedded LiDAR sensor of the iPhone 13 Pro, using the 3D Scanner App and PIX4Dcatch apps in order to evaluate their utility towards geospatial site documentation.

The comparative analysis here indicates that only in optimal scenarios (i.e., when the accuracy of the geospatial positioning is intrinsically high), geotagged field-based photographs alone can result in models with acceptable scaling errors, though even in these cases the orientation of the transformed models cannot be sufficiently accurate for many geoscientific applications. Moreover, misalignment of the reconstructed scene is exacerbated when the acquisition is performed in a collinear fashion. The apps tested for iOS LiDAR acquisition were able to produce accurately scaled models. However, their resultant scene reconstructions exhibited surface deformations caused by simultaneous localization and mapping (SLAM) errors, which in turn may prove detrimental to the accuracy of structural measurements extracted from the model surfaces. Finally, of the tested apps, PIX4Dcatch is the only iOS LiDAR acquisition tool able to produce correctly oriented models.

2. Methods

The studied trench is ~20 m long, having an approximate east-west strike direction. The southern wall of the trench was cut vertical and prepared for the study, whereby gridlines demarcating 1 m^2 subregions were installed, providing a reference frame for the comparative analysis. Proceeding with the preparation of this framework, field surveys using the aforementioned remote sensing platforms were performed on 6 April 2022. Weather conditions on the day of the surveys were overcast, providing uniform diffuse light, favoring the acquisition of the north-facing trench wall, minimizing the impact of shadowing upon the captured images and their resultant reconstructed scenes, thus limiting the impact of shifts in solar azimuth and zenith upon model quality.

The drone used for the acquisition is a DJI Air 2S (Table 1), which is equipped with an embedded GNSS positioning system (GPS, GLONASS, and Galileo constellations), compass, and an inertial measurement unit (IMU). According to the manufacturer, the hovering accuracy range of vertical and horizontal positioning with GNSS is ~0.5 m and ~1.5 m respectively. The DJI Air 2S is equipped with a 20-megapixel camera with a 1″ CMOS sensor, mounted on a three-axis gimbal. A total of 226 photos were taken in JPG format (5472 × 3648 pixels) and 72 dpi resolution, at distances between ~0.4 to 80 m from the scene in manual flight mode. Every photo's camera position (latitude, longitude, and altitude) and pose information (yaw, pitch, and roll angles) are automatically recorded. All photos taken with this platform have a ~0° roll angle, attributable to gimbal stabilization (e.g., [4]). This dataset includes aerial views of the trench, including the surrounding roads and buildings.

Table 1. In this table are summarized the parameters of the photographic devices used.

Device	Positioning System	Sensor	Image Resolution	Lens Parameters	Production Year
DJI Air 2S	GPS + GLONASS + Galileo	1″ CMOS	20 MP	f/2.8, 22 mm (35 mm equivalent)	2021
Nikon D5300	GPS	CMOS APS-C	24.2 MP	f/3.5–5.6 G VR	2014
iPhone 13 Pro	GPS + GLONASS + Galileo + QZSS + Beidou	dual pixel PDAF	12.2 MP	5.7 mm f/1.5, 26 mm (35 mm equivalent)	2021

The third set of photographs was taken using an iPhone 13 Pro (Table 1). This device is also equipped with a GNSS receiver (GPS, GLONASS, Galileo, QZSS, and Beidou constellations) with the final location provided by the Apple Core Location framework, which combines GNSS geolocation measurements with data provided by Bluetooth and Wi-Fi networks when available. The iPhone 13 Pro embeds an IMU and a magnetometer able to provide orientation data. However, only the azimuthal orientation of the camera direction is preserved in each photo in addition to their geographic coordinates and altitude. A total of 329 photographs at 12.2-megapixels resolution were acquired, with the majority captured at close range from inside the trench.

These three photographic datasets were processed independently in Agisoft Metashape Professional (version 1.8.1): a commercially available SfM-MVS photogrammetric reconstruction software platform. Geographic coordinates obtained from each platform were converted to UTM zone 33N-WGS84 (EPSG: 32633) within Metashape. Exported point clouds were subjected to comparative analysis within CloudCompare: an open-source software for point cloud processing and analysis [63]. The computation speed of this analysis was enhanced by leveraging a virtual machine installed on a Dell PowerEdge R7525 server rack placed at the Department of Mathematics and Geosciences at the University of Trieste (Italy) equipped with an AMD EPYC™ 7F72 (beanTech, Udine, Italy) chipset and NVIDIA GRID RTX8000P GPU architecture. Moreover, to further improve computation speed, all point clouds were decimated using random sampling to 12 M points within CloudCompare. This value was chosen arbitrarily and considered adequate to represent the reconstructed geometry. In CloudCompare, the comparative analysis was performed after point cloud manual alignment using a minimum of four non-collinear points. The results were visually inspected, and the alignment procedure repeated when deemed unsatisfactory.

In addition to its 12.2-megapixel digital camera, the iPhone 13 Pro is equipped with a built-in LiDAR scanner. This sensor utilizes the simultaneous emission of 576 rebounded laser pulses to acquire scene geometry, which under optimal conditions has a range of up to 5 m [5,7]. After introducing this sensor in the iPad Pro and iPhone 12 Pro in 2020, several apps have been developed to retrieve geospatial information in the form of point clouds and textured meshes [5,64]. In this work, we have tested the 3D Scanner App (v. 1.9.8) and PIX4Dcatch (v. 1.12.0) apps. During each acquisition, the iPhone was mounted on a DJI OSMO 3 gimbal to limit the deleterious impacts that abrupt movements imbue upon the iPhone's IMU measurements, and hence reduce possible errors resulting from the simultaneous localization and mapping (SLAM) required to generate the LiDAR models.

The 3D Scanner App is a free app for iOS LiDAR acquisition, which produces a textured mesh of the scanned scene as the output. Several settings related to the resolution of the acquisition can be set. In this work, we set the acquisition at (i) low confidence, (ii) 2.0 m range, (iii) no masking, and (iv) 8 mm resolution. The entire duration of the 3D Scanner App LiDAR survey required ~6 min. The scanning duration was long to accommodate coverage of the entire trench (including the trench floor). The textured model output by the 3D Scanner App was processed in less than two minutes using the acquisition device at the field site. Moreover, the output models are natively scaled, thus providing metric information directly in the field, with the size of model features being ascertained by selecting two points on the model surface within the 3D Scanner App. The textured meshes can be exported using the Wavefront *.obj format while colored point clouds of the scene can be exported via the *.xyz format. During the acquisition, the app also captures low-resolution (2.7 MP) images of the scene at a frequency of ~2 Hz. These images are primarily used for generating texture maps and to assign RGB attributes to the point cloud but can also constitute a backup dataset that can be used to generate a stand-alone SfM-MVS model.

The PIX4Dcatch app is part of a larger software suite that includes PIX4Dmapper, a popular SfM photogrammetric reconstruction software. The PIX4Dcatch app is free to use but requires a subscription to export data. In this work, the default acquisition settings with PIX4Dcatch were used, including an image overlap of 90%. With the device mounted on

the DJI OSMO 3, we acquired the north-facing wall of the trench. The PIX4Dcatch app does not process the data within the smartphone but requires the LiDAR project to be uploaded to the PIX4Dcloud for processing (an upload of 1.51 Gb was required for the test case in this study). This app, in addition to the textured mesh and point cloud, stores 2.7 MP images of the scene including their position (latitude, longitude, and altitude) and pose information (omega, phi, and kappa), that are directly readable even when imported into third party software (i.e., Metashape). Despite this flexibility, the LiDAR-generated depth maps can only be read if processed using PIX4Dcatch.

3. Processing Outline and Results

In total, 226 photos from the drone (56 nadir view and 170 oblique images of the trench wall) were processed in Metashape, using high accuracy alignment and high-quality densification settings. The resulting dense point cloud has ~111 million points and comprises the trench and its surrounding area (Figure 1a). Ostensibly, due to the robust GNSS positioning data provided by the drone, coupled with a wider acquisition area, the resulting model appears reasonably georeferenced with respect to its horizontal components (Figure 1a). By contrast, after comparison with a freely available 1 m resolution LiDAR-derived Digital Terrain Model (DTM) of the region Friuli Venezia Giulia (available at http://irdat.regione.fvg.it/CTRN/ricerca-cartografia/ (accessed on 15 July 2022)), a significant vertical translation was observed (Figure 1b). It should be noted that both datasets are framed in terms of their altitude above sea level (ASL). The cloud-cloud computed distance between the DTM and the Air 2S model is relatively uniform throughout the area, lying at about 8 m (Figure 1c), indicating minimal angular deviation between the two reconstructions. It is worth noting that accurate positioning of ground control points (GCPs) should be provided to obtain below centimeter accuracy estimates in both horizontal and vertical directions and to check the consistency of the model throughout the investigated area (e.g., [65]). Nevertheless, in spite of this vertical shift, for the scope of this work we consider this dataset without any vertical translation as the benchmark against which the other models will be compared. To enhance the reconstruction quality of the trench, we selected a smaller region and repeated the densification procedure in Metashape after disabling all aerial photographs, whilst keeping the pre-established alignment. This procedure resulted in a benchmark point cloud composed of ~124 million points (~0.47 point/mm^2 at the center of the scene), which was later decimated in CloudCompare, as described within the Methods section.

Metashape is able to read the EXIF metadata tagged onto photographs, which in the case of the Air 2S dataset includes the gimbal yaw, pitch and roll angles. Note that in this study, the roll angle is effectively fixed at 0°, owing to gimbal stabilization. The iPhone dataset only records the image's direction with respect to true north, which Metashape automatically identifies as the yaw angle. The Nikon D5300 does record GNSS geolocation data but does not record camera orientation parameters.

In Metashape, photo-alignment based on the extrinsic parameters only takes into account location information, though orientation parameters can be utilized in post-processing. In the case of the Air 2S dataset, the use of the orientation parameters results in an anticlockwise rotation of the model around the world frame's vertical axis of ~3.4 degrees. This value is close to the angular deviation between magnetic and true declination at the site (3.2°). Hence, this additional registration may prove useful in cases where the model needs to be aligned to the magnetic instead of geographic north (e.g., the collection of orientation data from a model matched to equivalent field measurements collected using a compass or compass-clinometer).

The iPhone alignment was produced using medium accuracy and high-quality densification settings. The resulting dense point cloud has ~123 million points (~0.64 point/mm^2 at the center of the scene). The use of the azimuthal orientation parameter associated with iPhone photographs for the model's alignment to magnetic north is troublesome. Camera azimuth with respect to the north cannot be used alone since the software assigns null

values to pitch and roll fields. Moreover, the north bearing may also not match that of a yaw angle, for example in the case of portrait photos. Whilst we have not robustly tested the use of the iPhone orientation parameters, it appears to match the orientation and scale to the Air 2S generated model when visually compared (Figure 2a), although a major vertical translation of ~5.5 m is observed (Figure 2b). This translation reduces to ~2.5 m ASL in real-world coordinates considering the vertical shift between the Air 2S model and the LiDAR-derived DTM. Closer inspection reveals that whilst the scaling between the two models is comparable, with a scaling factor of 0.995, a rotation of ~13° around the x-axis (which corresponds to the strike of the trench) is observed (Figure 2c).

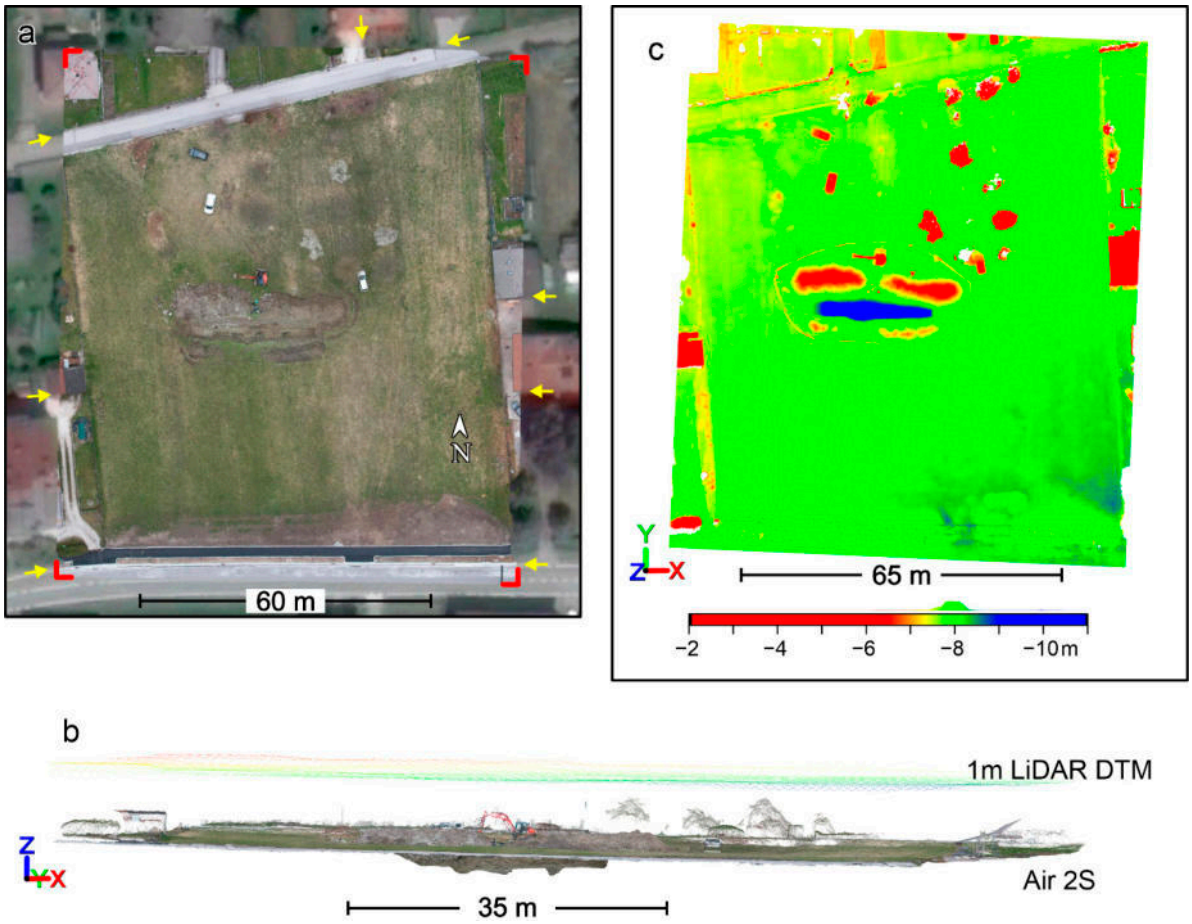

Figure 1. (**a**) Zenithal view of the kmz orthomosaic generated in Metashape from the Air 2S model. Note that no GCPs were used. Red corners highlight the limits of the orthomosaic overlay. Yellow arrows highlight matched features identified within the orthomosaic and Google Earth remotely sensed imagery. (**b**) Orthographic section view in CloudCompare of the Air 2S model with the LiDAR-derived Digital Terrain Model (DTM) at 1 m resolution of the region Friuli Venezia Giulia, and (**c**) zenithal view resultant cloud-cloud computed distance.

Both models acquired by directly using the iPhone's LiDAR sensor through the 3D Scanner App and PIX4Dcatch apps lack georeferencing but are registered within a local coordinate system. Consequently, a translation had to be applied to observe both LiDAR models together with the benchmark model (Figure 3). Notably, the PIX4Dcatch model was correctly oriented. To test whether the PIX4Dcatch model's orientation was coincidental with the benchmark model, we undertook a second survey at a different locality (not shown) and found that the model was correctly oriented. In contrast, the 3D Scanner App model was misoriented with the z-axis oriented almost at 90° to its expected value (Figure 3). The x-axis was approximately parallel to the world frame x axis but inverted.

To test if the erroneous registration related to an incorrect reading order of the registered x, y and z coordinates, the model was rotated 180° around the word frame z-axis and 90° around the x-axis. The resulting model still deviated ~30° around a z-axis rotation from the world frame. Finally, a scaling factor of 1.00123 and of 1.00646 had to be applied to the 3D Scanner App and PIX4Dcatch models, respectively, to match the photogrammetric benchmark model.

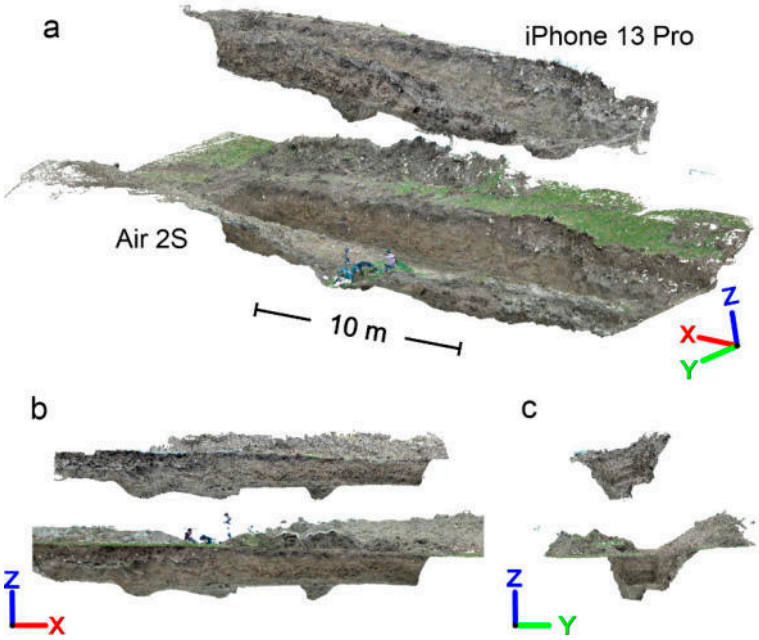

Figure 2. Visual comparison in CloudCompare of the Air 2S model with the iPhone model, using oblique (**a**) north (**b**) and east (**c**) oriented views.

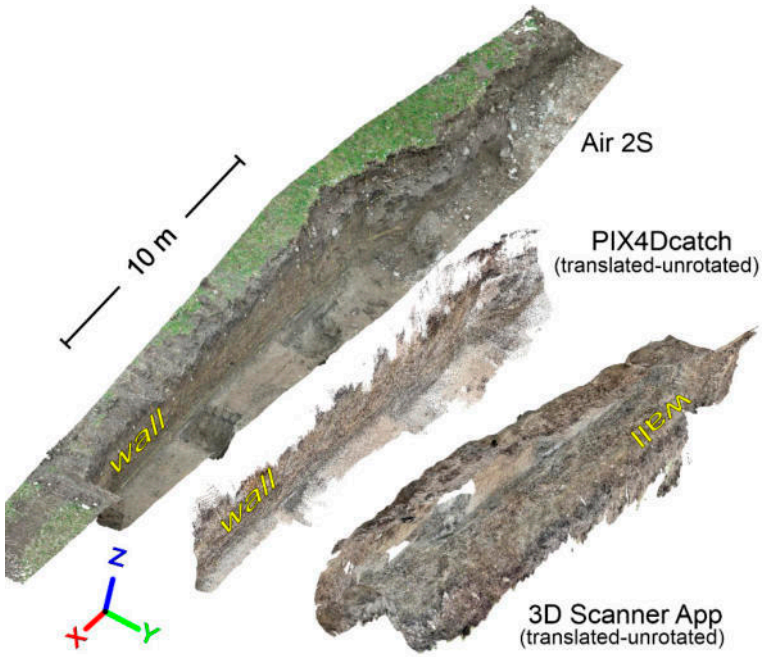

Figure 3. Visual comparison in CloudCompare of the Air 2S model with the PIX4Dcatch and 3D Scanner App models after translation next to the Air 2S model.

The photo-alignment of the Nikon DSLR generated model was also problematic. Despite using medium accuracy settings in Metashape (in source preselection mode), the

initial reconstruction failed after more than eight hours processing time using the available computing hardware (in the virtual machine described above). Thus, a second attempt to reconstruct the scene captured using the Nikon D5300 was attempted at low accuracy in source preselection mode, which was later reset to medium accuracy in estimated preselection mode for a secondary alignment. This resulted in a sparse point cloud of ~2.7 million points, which expanded to 334 million points (~0.18 point/mm^2 at the center of the scene) after dense reconstruction. The resulting model (hereafter termed Nikon model) is poorly scaled and oriented. The scaling factor with the reference model was ~10, meaning the Nikon model was about 10 times larger. The orientation of the model (not shown) was also arbitrary, with the z-axis aligned almost perpendicular to the world frame.

3.1. Comparative Analysis in CloudCompare

After registering all test point clouds with the benchmark in CloudCompare, we meshed the benchmark model and then performed a point cloud to mesh distance calculation for each test point cloud to investigate the occurrence of the surface deformations (Figure 4). As shown in the histogram of Figure 4b, ~82% of the points belonging to the iPhone photogrammetric point cloud are within ±1.5 cm of the benchmark model's surface (and ~68% within ±1 cm), with the majority of outliers being located on the floor of the trench. The Nikon point cloud only represented the north-facing wall of the trench, which in similitude to the iPhone point cloud, exhibited 85.6% of points lying within ±1.5 cm distance from the benchmark model (and ~72% of points within ±1 cm). For the Nikon model, some outliers were located at the eastern wall of the trench and on the western side of the north-facing wall. The iPhone LiDAR model captured using the 3D Scanner App covered the entirety of the trench. Data acquisition using the 3D Scanner App started from the area indicated by the green arrow in Figure 4e and followed an approximately anticlockwise transect, which tracked the sidewalls of the trench and the trench floor. After completing this circuit, the acquisition returned to the center of the scene terminating at the location indicated by the dark-red arrow in Figure 4e. About 77% of the points of the 3D Scanner App point cloud are located within ±6 cm from the benchmark model's surface. In this case, most of the outliers are located on the western sector of the north-facing wall. Notably, this area coincided with the start and end of the survey transect used for 3D Scanner App LiDAR acquisition. Finally, ~94% of the PIX4Dcatch point cloud lies within ±2.5 cm distance from the benchmark model with outliers mainly present in the western sector of the acquisition area.

3.2. Orthomosaics

In Metashape, the 3D models of the photographic datasets (Air 2S, Nikon and iPhone) were also used to produce three orthomosaics from their associated textured meshes (Figure 5). It should be noted that the Air 2S orthomosaic in Figure 5 was produced after removing all the nadir view images oriented at an acute angle to the trench wall from the aerial survey prior to texturing, which would introduce blurring into the resultant texture map. Resultant orthomosaics reached different pixel sizes of 0.99, 1, and 0.635 mm/pixel for the Air 2S, Nikon and iPhone, respectively. Interestingly, a former Air 2S orthomosaic produced prior to the removal of nadir view images (not shown) reached a pixel size of 2.96 mm/pixel. The orthomosaics in Figure 5 were exported using a fixed resolution of 3 mm/pixel for comparison. The orthomosaics generated using each 3D imaging modality are able to capture the scene of interest adequately, such that details like individual clasts within the trench wall are resolvable (see Figure 5).

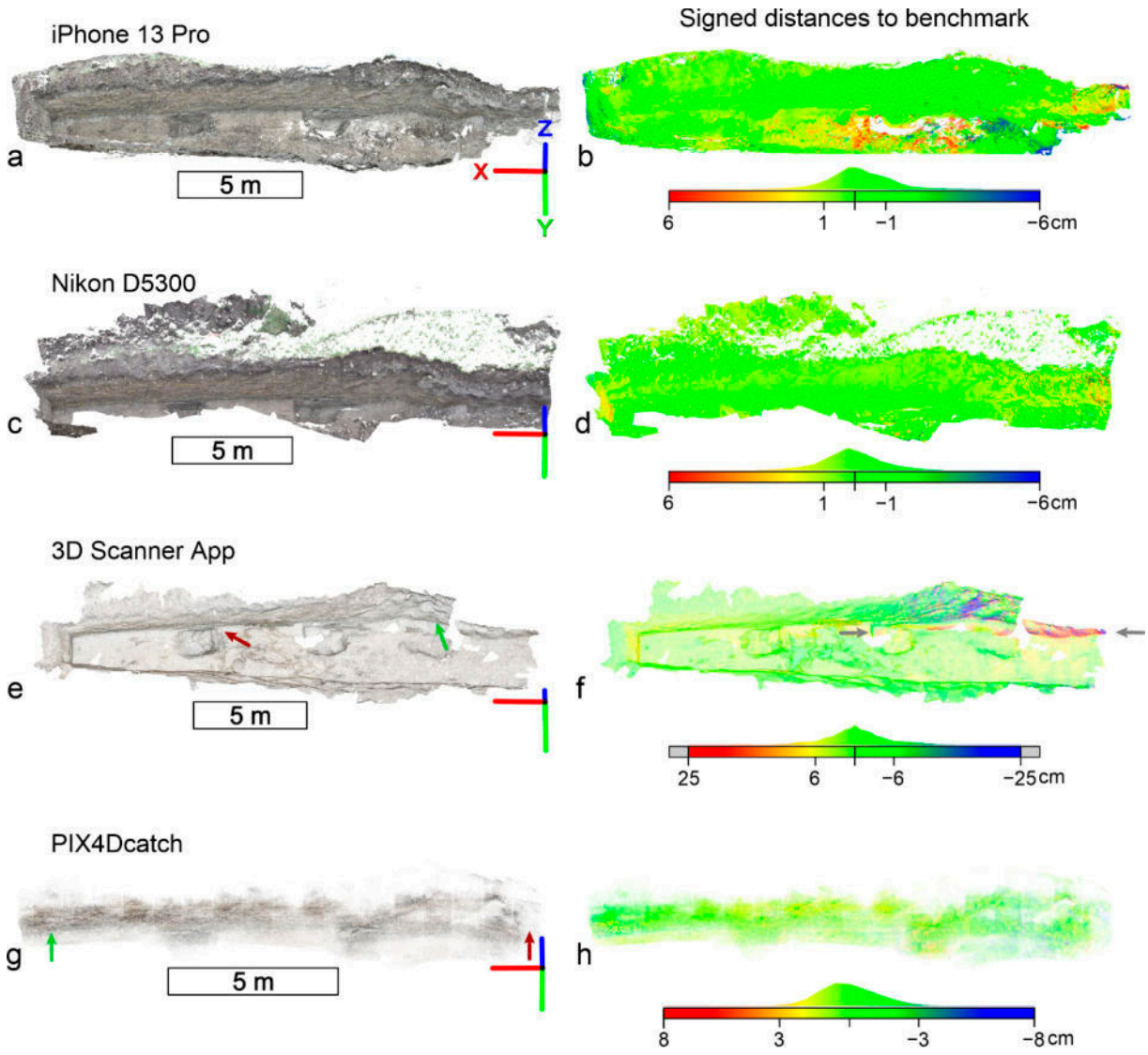

Figure 4. The iPhone (photogrammetric) RGB colored point cloud (**a**) and its distance to the benchmark model (**b**). The Nikon RGB colored point cloud (**c**) and its distance to the benchmark model (**d**). The 3D Scanner App colored point cloud (**e**) and its distance to the benchmark model (**f**). The PIX4Dcatch app RGB colored point cloud (**g**) and its distance to the benchmark model (**h**). Green and red arrows in e and g represent the first and last view of the acquisition. Gray arrows in f represent artifact points related to self-localization and mapping (SLAM) errors. The Red Green and Blue Cartesian system represent the East, North and Up directions, respectively.

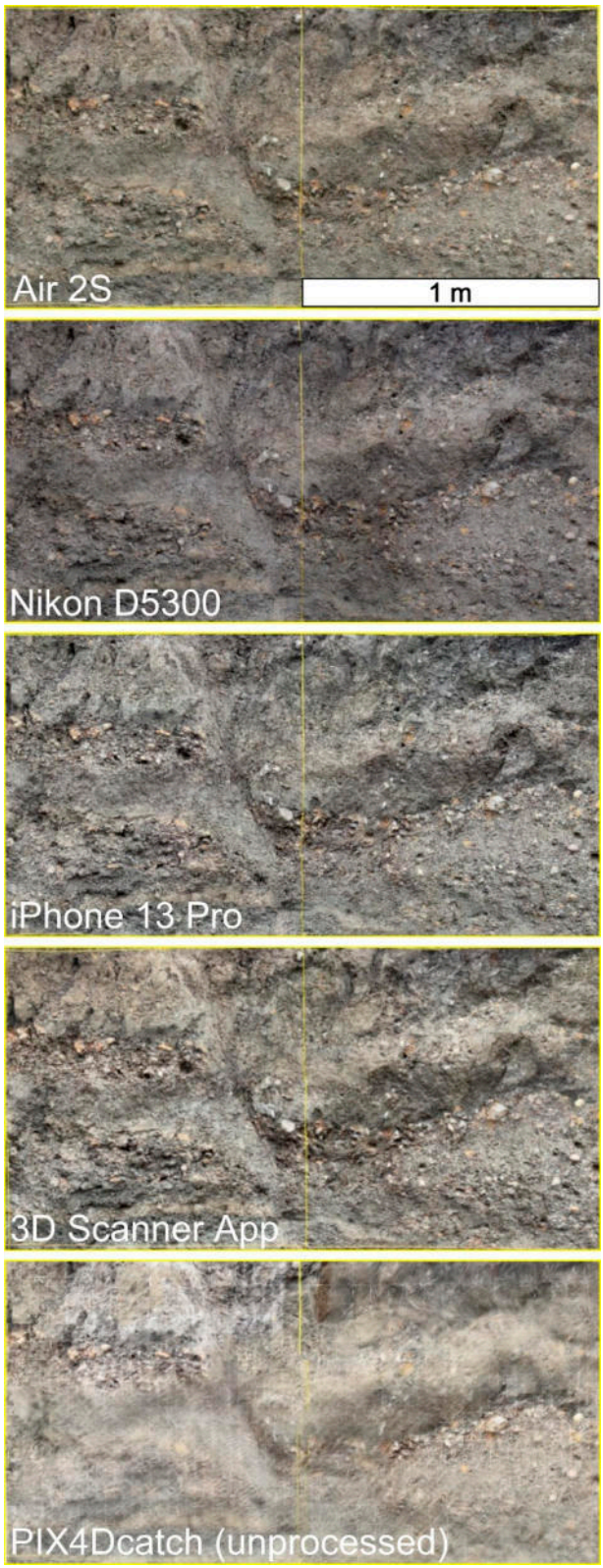

Figure 5. Detailed view of the reconstructed scene (2 × 1 m) using different 3D image capture systems and showing one sidewall of the studied sinkhole.

The two available textured meshes obtained from the 3D Scanner App and the PIX4Dcatch app were also used to generate two orthopanels using the LIME software suite [66] (Figure 5).

4. Discussion

Three SfM-MVS photogrammetry-based surveys using consumer-grade camera platforms and two iOS LiDAR-based apps were tested in this work to evaluate their ability to reproduce the geometry and optical signature of a typical geoscience and geoarchaeological field site (a trench transecting a sinkhole).

4.1. Scaling and Orientation Accuracy of SfM-MVS Models

The first of the three SfM-MVS photogrammetry-derived models (hereafter termed SfM models for parsimony) was generated using an aerial photographic survey using a DJI Air 2S drone (226 images), including photographs captured within the trench. The Air 2S dataset covered a much larger area (>1200 m^2) than the compared surveys. This acquisition strategy, coupled with the excellent GNSS, IMU and stabilization capability of this device resulted in the most accurately scaled and (horizontally) georeferenced of the SfM models, as evidenced by the aerial orthophoto derived from the model added as an overlay in Google Earth (Figure 1). Consequently, the Air 2S model was used as a benchmark with which to test the reconstruction quality of the remaining survey methods. It should be noted that the Air 2S model is vertically translated by ~8 m (Figure 1). The assumed fidelity of the Air 2S model is therefore an approximation, though its internal scaling and registration with respect to the horizontal axes of the world frame is likely reliable for the sake of comparison.

The use of photographs taken with the Nikon D5300, which are characterized by low accuracy (GPS) geotags and lack camera orientation metadata, resulted in the model having a scaling factor of about 10 and arbitrary orientation. Despite the larger quantity of photographs in the Nikon dataset (382 images) and the larger sensor resolution, the accuracy of the GPS sensor was above the size of the investigated area (>100 images had position error > 100 m). It was only after 150 images were taken that the signal error stabilized below 20 m. It is likely that low accuracy of the dataset's geolocation information in combination with the relatively high pixel count of the survey contributed to the failed alignment in Metashape encountered during the first attempted reconstruction.

The third SfM model was built from 329 photographs captured using an iPhone 13 Pro. The resultant 3D model was natively scaled, with a scale factor to the benchmark of ~0.995. This revealed that the multi-satellite GNSS receiver of the iPhone used by the Apple Core Location framework to retrieve the camera position provides reliable location data when large enough datasets are used. Nevertheless, recent single-point accuracy tests performed with the previous iPhone Pro model (the iPhone 12 Pro, [7]), have evidenced a location accuracy within a few meters that stabilized within seconds. Further to this, the Apple Core Location framework can provide more accurate positioning over standard consumer grade GNSS receivers while utilized within residential areas by combining data provided by the GNSS receiver, Wi-Fi networks, and nearby Bluetooth devices. The device is also equipped with the iBeacon micro-location system enabling indoor navigation when available. A possible way to discern whether the final precision is due to averaging of a large dataset or to the intrinsic location accuracy by the Apple Core Location framework is by testing the precision and the accuracy of each photo's position in comparison to the values estimated through the photo-alignment process in Metashape. During the photo-alignment workflow, each photo is re-positioned in a new location that better fits the overall geometry of the scene linking each image to the reconstructed scene and minimizing the reconstruction error (e.g., [67,68]). If the model is properly scaled, the difference between the estimated and measured camera locations provide a proxy for the precision of the Apple Core Location framework at the site. It can be seen in Figure 6a that the estimated precision of the iPhone 13 Pro positioning is generally <1 m in each axis. The highest error can be observed in the first three photographs, suggesting that after a minimal time, the location signal stabilizes (as also previously observed by Tavani et al. [7]). To estimate the accuracy of the camera positions (which differs from the precision being compared to a benchmark), we have aligned the iPhone model to the Air 2S model (considered in this

work as the benchmark model) such that the difference between the new estimated camera positions and the measured positions represent the accuracy of the device (Figure 6b). The alignment in Metashape was achieved by providing the coordinates of three non-collinear markers as obtained by the Air 2S model (in lieu of robust GCPs). It has to be noted that this is an ambitious assumption as even though it has been observed that the lat-long positioning of the benchmark model is approximately correct (see Figure 1), the actual altitude of the model suffers from a vertical translation of ~−8 m in the absence of a survey-grade registration. This comparison shows that there exists significant error in the vertical axis of the world frame (~5.9 m). Considering that the Air 2S model itself suffers a ~−8 m translation from the LiDAR-derived DTM (Figure 1b,c), the mean vertical error of the iPhone is ~2.1 m. The accuracy estimate in the east direction is within 1 m (average easting error is 0.6 m). The north direction accuracy estimate is mostly between 0 and 3 m (average northing error is 1.5 m) (Figure 6b). The total accuracy error is 6.14 m in total and mostly reflects the vertical shift. Regarding the anticlockwise rotation of about 13° around the x-axis, this is likely related to the photo-survey acquisition strategy. In fact, having performed the acquisition along the east-west direction (i.e., parallel to the strike of the trench), most of the photographs lie along the x-axis of the world frame. The high collinearity of this dataset is conducive to the introduction of rotational errors along this axis. The availability of camera pose information in the EXIF files (i.e., in similitude to the Air 2S dataset) would have provided the means to mitigate such errors.

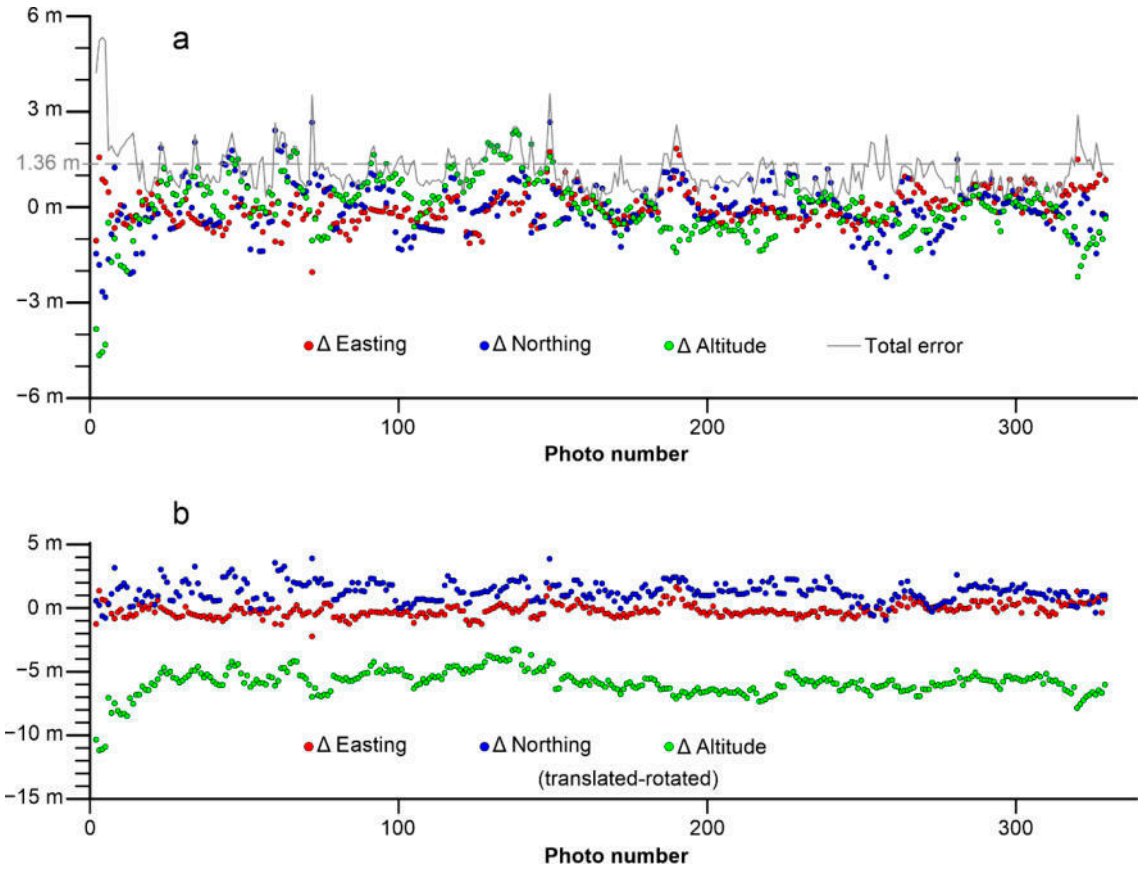

Figure 6. (**a**) iPhone 13 Pro geotag precision estimated via the difference between the iPhone 13 Pro's geotags, as indicated in the EXIF metadata and their estimated values in Metashape. (**b**) iPhone geotag accuracy error estimated after aligning the iPhone model to the Air 2S model (benchmark). Note that the benchmark model has a −8 m vertical translation from the real altitude ASL of the site.

4.2. Scaling and Orientation Accuracy of the iPhone LiDAR Reconstructions

The scaling of the point clouds derived from the LiDAR sensor of the iPhone 13 Pro closely matches that of the Air 2S model. The 3D Scanner App model had a scaling factor of 1.0012, while the PIX4Dcatch model had a scaling factor of 1.0065. Whilst the latter mentioned app is also able to return correctly oriented models, the 3D Scanner App generated model was arbitrarily oriented. Prior to its latest updates, the PIX4Dcatch app was also unable to produce correctly oriented models [7]. The capacity to build accurately scaled and oriented models directly in the field (assuming mobile network connectivity) offers a potential gamechanger for applications that require the rapid collection of attitude data at a given study site (e.g., fault and fracture analysis). It should also be noted that handheld GNSS Real-time kinematic (RTK) rovers have recently become available for selected iPhone and Android devices (e.g., the viDoc RTK rover). These highly accurate add-on receivers offer the potential to turn smartphones into survey grade GNSS tools, though at present, the cost of these devices rivals that of standalone RTK-GNSS platforms. We acknowledge that a relatively modest upgrade has been announced with the release of dual-frequency receivers in the iPhone 14 Pro. Nevertheless, the typically limited access to the Apple Core Location framework raw data may limit or impede the post-processing carrier phase fix (e.g., [20]).

4.3. Internal Accuracy of Reconstructions

All point clouds produced by the survey methods deployed in this study were compared to test for deformations in the reconstructed scene after point clouds manual alignment (similarity transform). After translating, rotating, and scaling each cloud to fit the Air 2S model, their distance to the benchmark model was computed (Figure 4). When using such a comparison it must be taken into consideration that the point-to-mesh distance will encounter some disparity due to the tessellation of the surface (mesh). Most of the points composing the iPhone model (~82%) are <1.5 cm from the benchmark model surface, with most of the outlier points at the floor of the trench. These deformations observable at the base of the model are probably caused by the obliquity between the photo view direction and the ground, which is typical of ground-based surveys targeting vertical edifices. In this work, the main objective was to reconstruct a single trench wall. In cases where the acquisition of the floor of the trench is required, it is recommended, even during ground-based surveys, to include photos that are normal to sub-normal to the base of the excavation. As for the iPhone model, the Nikon model has 85.6% of the values within a 1.5 cm distance from the benchmark model. Outlier points are more randomly distributed. The fact that both the iPhone and the Nikon models have a similar distribution of errors in relation to the distance from the benchmark model (e.g., Figure 4c,d) suggesting that, for these two models, reconstruction errors are largely dictated by the limitations of SfM estimation. Reconstruction errors related to the SfM techniques are strongly coupled to the resolution of the input image dataset, as well as additional factors, such as camera sensor noise and motion blur (e.g., [69]). The internal deformation error associated with the LiDAR acquisition is mostly within 6 cm (for 77% of the point population) and 2.5 cm (94%) for the 3D Scanner App and the PIX4Dcatch models, respectively. It should be noted that the size of these two models and their acquisition strategies were distinct (Figure 4). As a result of the strategy followed during the 3D Scanner App acquisition, the area between the green and red arrows in Figure 4e was scanned at least twice over a relatively long and convoluted path. This path exacerbated errors associated with simultaneous localization and mapping (SLAM) [70]. When the user moves the smartphone while scanning, its position and orientation (i.e., the pose information) must be continuously determined in order to append consecutive scanned portions of the scene. This is generally achieved by merging the pose information provided by visual and inertial sensors [70]. As a result, small errors in the phone's pose estimation can accumulate and propagate, giving rise to mispositioned points within the model. These deleterious effects are evident from the survey performed with the 3D Scanner App, where the last portions of the scan produced

a 'ghost' planar feature at a distance of about 25 cm from the features' true position. The acquisition carried out through the PIX4Dcatch app was much smoother, having acquired only the north-facing wall of the trench (not the floor nor any of the other walls). The acquisition proceeded from east to west as indicated by the green and red arrows in Figure 4g. It can be observed (Figure 4h) that for smaller and smoother acquisitions, such as the survey conducted with the PIX4Dcatch app, the majority of points (94%) are <2.5 cm distance to the benchmark model's surface. Qualitatively, it can be observed that most of the outlier points are located at the periphery of the acquisition. Again, this is likely the result of SLAM errors. In effect, SLAM errors are roughly comparable to the so-called 'doming effect', which may impact SfM-MVS photogrammetric reconstructions in terms of their deleterious impact upon model analysis (e.g., [22,71]).

4.4. Orthopanels

Any of the acquisition methods tested herein can be used to generate textured models of the scene, and to orthographically project the resulting model over a panel, thus generating an orthomosaic (or orthopanel) of the scene [30,31,72–74]. This procedure finds considerable applications in structural geology, stratigraphy, geoarchaeology and geomorphology, as well as other earth science disciplines, where orthomosaics are generated by orthogonally projecting the model towards a direction that minimizes geometry distortion of the targeted features observable in the model (e.g., geologic structures, bedding planes, clasts, etc. [75–77]). In the case of the three SfM models, the orthomosaic construction is a trivial additional step in the SfM-MVS reconstruction workflow, available within photogrammetric reconstruction software tools (e.g., Metashape [73]). All three SfM-derived orthomosaics faithfully reproduced the scene with variable resolutions (<3 mm pixels) that primarily relate to the average spatial resolution of the photo survey. A 2 $\times$ 1 m subregion of these orthomosaics is shown for comparison (Figure 5) after export at a fixed resolution of 3 mm pixels. In this section, a small (<40 cm throw) structure cutting through the Quaternary strata can be observed (Figure 5). At a glance, it can be confused with a small normal fault, but it corresponds to the eastern side wall of the active sinkhole. How this structure relates to the subsiding evolution of the area is beyond the scope of this work. The resolution of the orthomosaic produced from the textured model processed in the field by the 3D Scanner App is less sharp than the SfM models, although the sidewall and stratification are still discernable (Figure 5). The PIX4Dcatch app allows for the uploading of data to the PIX4Dcloud for remote processing, although in this work we have only used the textured model available in the saved folder of the app. The latter model is not sharp enough to recognize most of the features observed in the other models, as can be seen from the derived orthomosaic (Figure 5).

4.5. Final Remarks

In this work, we have tested readily available surface reconstruction methods, leveraging consumer-grade sensor platforms to produce 3D models of a typical field location encountered within geoscience and geoarchaeology applications. Our results have highlighted that only the SfM-MVS-derived Air 2S model and the iPhone LiDAR-derived PIX4Dcatch model satisfactorily recovered the orientation of the scene, with the Air 2S model also being georeferenced. Nevertheless, the Air 2S model has suffered a vertical translation of ~8 m with respect to the real-world ASL coordinates. The comparison of the Air 2S model with the LiDAR-derived DTM and aerial orthoimage of Google Earth together with the geometric consistency of the Air 2S model with the tested iPhone LiDAR's models (which should nominally excel in distance accuracy in lieu of SLAM errors) demonstrates that aerial photogrammetry deployed from consumer-grade drones reached levels of accuracy in an uncontrolled field setting sufficient for many geoscience field surveying applications where survey grade measurements are not mission critical (e.g., gauging approximate bed thicknesses, orientations, etc.). In general, there are several geoscience applications where the internal scales and geometrical consistency of the scene supersede

the need for accurate georeferencing, such as for models intended for the quantitative extraction of oriented data (e.g., [29,78]), the production of oriented orthopanels (e.g., [12,73]), and the qualitative observation, preservation, and sharing of models (e.g., [79,80]). For all those cases, our results suggest that modern drones, such as the DJI Air 2S, can be used to produce stand-alone surveys with orientation accuracies sufficient for the vast majority of user cases. Nevertheless, we suggest using such an approach with caution, since the GNSS signal can be subject to occlusions, particularly within mountainous or urban areas. Direct georeferencing alone is not sufficient to establish survey-grade registrations, even when RTK-drones with centimetric position accuracy are used (e.g., [81]). Therefore, direct georeferencing alone is not recommended for all applications where absolute orientation accuracy is required. For the cases where an approximate alignment to the real-world coordinates is sufficient, we suggest extending the coverage of the acquisition over a much larger area than the region of interest whilst avoiding the acquisition of collinear images. It is also recommended to always implement routine quality checking of 3D surface reconstructions produced within the field. Assuming no GCP's are available, it is possible to insert objects of known scale and orientation into the mapped scene to meet this objective (e.g., [4,9]).

A noteworthy aspect of this work is the recognition of the recent improvement obtained by the PIX4Dcatch app in aligning iOS LiDAR-derived models to the world frame. To confirm this observation, we performed an additional test over an object characterized by a simplistic geometry. The test consisted of five independent iOS LiDAR surveys of the base of an obelisk made of limestone blocks in the city of Trieste (Italy) through the PIX4Dcatch app. The survey strategy involved circumnavigating the obelisk around either half or the entirety of its perimeter, whilst continuously acquiring LiDAR data using the iPhone 13 Pro (Figure 7a). In similitude to the workflow presented within Section 2, we were able to provide an estimate of the positional accuracy of the GNSS during the LiDAR acquisition by generating an SfM-MVS photogrammetry model of the obelisk using all frames recorded by the app during five distinct acquisitions (Figure 7b). Note that, unlike the LiDAR-derived models themselves, each image used for texturing is georeferenced, which is recorded in its EXIF data. In comparison to what was observed from the case study presented in Section 2, the accuracy estimates in the east and north directions is ~1 m, while it is ~2 m in the vertical direction. Note that the positioning error is almost stable during each discreet acquisition (Figure 7b). This suggests that proceeding the acquisition of the first frame, subsequent image locations are established based upon inertial measurements. The five resultant LiDAR models, although shifted, are consistently aligned to the world frame. The observation was corroborated by deriving the obelisk orientation data from each of the generated LiDAR point clouds using the Compass plugin of CloudCompare [82] (Figure 7c). All measurements (from 10 to 20 for each model) are plotted as black great circles in Figure 7d. Orientation measurements of the obelisk were also made at the site using the Clino app for iOS on the iPhone 13 Pro and the FieldMove app for iOS on an iPad Pro (https://www.petex.com/products/move-suite/digital-field-mapping/ (accessed on 21 July 2022)). Particular attention was paid during this procedure to avoid magnetic interactions with the target object that might perturb measurement accuracy. In the field, orientation measurements were taken as planar and linear features (Figure 7d). Field measurements in Figure 7d are referred to with respect to geographic north (the magnetic declination at the site was +4). Incidentally, an average rotational error around the vertical axis of the world frame of <5 degrees is observed. Unfortunately, due to the limited magnetic declination at the site, and the proprietary nature of the PIX4Dcatch app's registration procedure, we cannot discern if the LiDAR models were intended to be aligned with geographic or magnetic north. If the LiDAR model is natively aligned to the magnetic north then the rotation error is potentially reduced to <1 degree. In any case, knowing this rotation, one can decide to rotate the models, or any derived structural data, accordingly, to maintain a degree of accepted accuracy where possible.

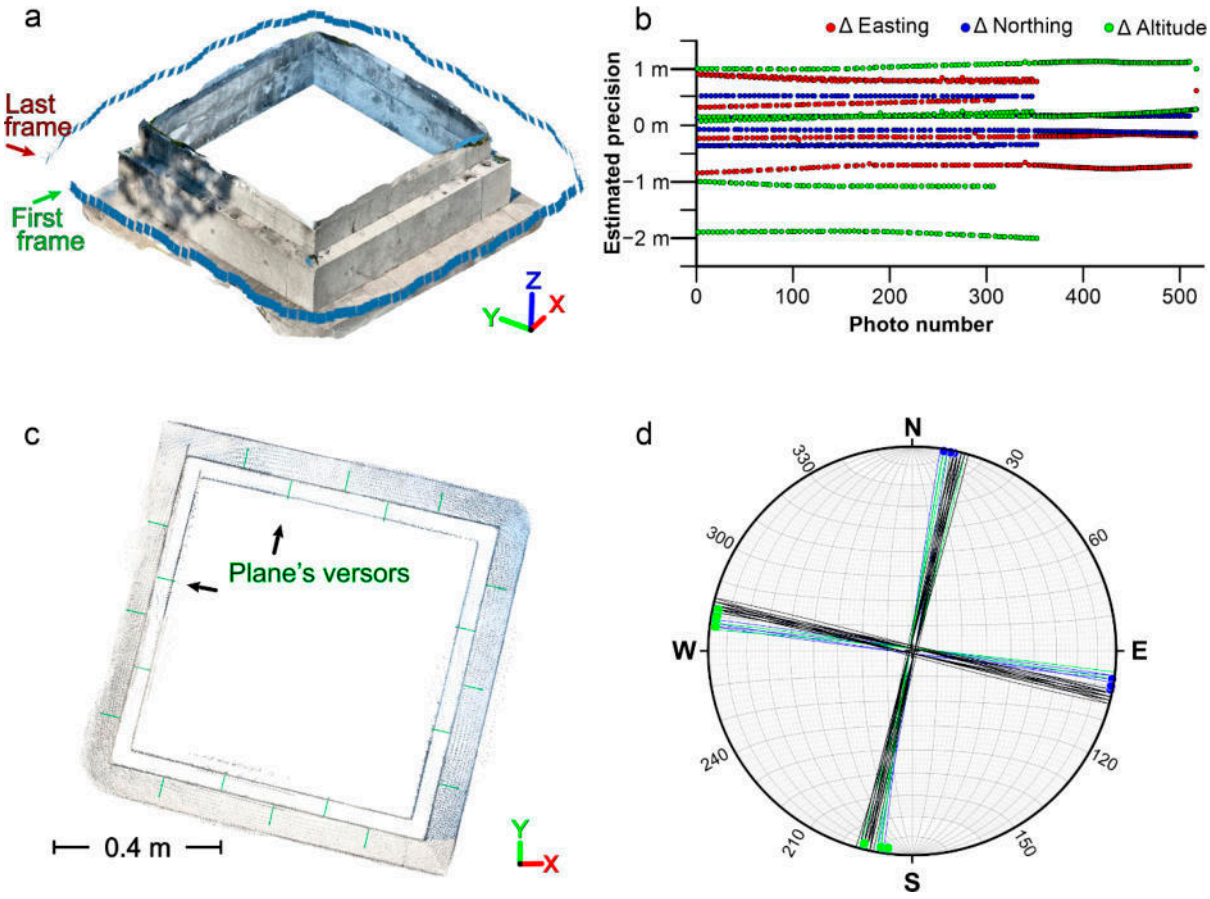

Figure 7. (**a**) SfM-MVS photogrammetric reconstruction of the base of the obelisk by means of oriented images captured by the PIX4Dcatch app. (**b**) Precision estimates of the image geotags collected by the PIX4Dcatch app. Each independent acquisition is identifiable by the different number of photos. (**c**) Orientation data of the orthogonal walls of the obelisk measured in CloudCompare from the LiDAR derived models. (**d**) Lower hemisphere, equal-area projection of measurements taken in CloudCompare (black great circles) and in the field using the Clino (green) and FieldMove (blue) apps. Green and blue great circles are the walls of the obelisks, whilst the markers are their trend axes.

Overall, the results obtained by this study highlight that commercial products, such as the DJI Air 2S and the iPhone 13 Pro, are able to prove useful as standalone field data acquisition platforms for diverse applications in the geosciences. Nevertheless, these instruments are subject to several sources of error (e.g., SLAM, geolocation, etc.) that can compromise entire studies. It is recommended that users remain cautious about the data quality models derived from such sensor platforms if no accuracy estimates exist, particularly for applications where the fidelity of the resultant metric data is critical.

5. Conclusions

Progressively more geoscientists are relying upon the claimed accuracy of commercial-grade tools for the 3D modeling of outcrops and landforms, commonly without site-specific validation. Nevertheless, this work has shown that even the most up-to-date consumer-grade tools (e.g., the DJI Air 2S and the iPhone 13 Pro) are subject to numerous errors, which are potentially deleterious to the intended application. Indeed, the magnitude of these errors may be sufficiently profound to nullify the results of entire studies or may lie within a range that is acceptable for many user cases. In order to provide baseline reliability, accuracy must always be checked and evaluated for a given study site and/or application.

Herein, we tested the geolocation capabilities and the native LiDAR sensor of the iPhone 13 Pro. The obtained results are to be considered positive, particularly with respect to the PIX4Dcatch app, which is able to provide well-scaled and oriented point clouds image geotags within their associated EXIF metadata.

Author Contributions: Conceptualization, A.C., T.S., M.M., A.B. and L.Z.; investigation, A.C. and A.B.; methodology, A.C., T.S., M.M. and C.C.; software and formal analysis, A.C. and M.M.; writing—original draft preparation, A.C., A.B., C.C., and L.Z.; writing—review and editing, T.S. and M.M.; funding acquisition, A.C. and L.Z. All authors have read and agreed to the published version of the manuscript.

Funding: This research was partially funded by the Geological Survey of the Friuli Venezia Giulia Region within the framework of the following project: Accordo attuativo di collaborazione per l'aggiornamento censimento e pericolosità dei sinkhole del territorio regionale (prot.no. 0035220 of 27 July 2020).

Data Availability Statement: All data in support of this publication, including Agisoft Metashape reports, are available upon request to the corresponding author. A 3D surface reconstruction of the trench is available at https://skfb.ly/ouI7o (accessed on 8 September 2022).

Acknowledgments: The authors would like to acknowledge Chiara Piano (functionary of the Geological Survey of FVG Region), as well as the functionaries of the Enemonzo Municipality Mauro De Prato and Alessandra Fiorese for their assistance, as well as the land owners who facilitated access to the main study site. AC acknowledges Microgrants 2021 resources, funded by the FVG Region (LR 2/2011 "Finanziamenti al Sistema Universitario regionale").

Conflicts of Interest: The authors declare no conflict of interest. The funders had no role in the design of the study; in the collection, analyses, or interpretation of data; in the writing of the manuscript; or in the decision to publish the results.

References

1. Pavlis, T.L.; Langford, R.; Hurtado, J.; Serpa, L. Computer-Based Data Acquisition and Visualization Systems in Field Geology: Results from 12 Years of Experimentation and Future Potential. *Geosphere* **2010**, *6*, 275–294. [CrossRef]
2. Micheletti, N.; Chandler, J.H.; Lane, S.N. Investigating the Geomorphological Potential of Freely Available and Accessible Structure-from-Motion Photogrammetry Using a Smartphone. *Earth Surf. Process. Landf.* **2015**, *40*, 473–486. [CrossRef]
3. Jaud, M.; Kervot, M.; Delacourt, C.; Bertin, S. Potential of Smartphone SfM Photogrammetry to Measure Coastal Morphodynamics. *Remote Sens.* **2019**, *11*, 2242. [CrossRef]
4. Corradetti, A.; Seers, T.D.; Billi, A.; Tavani, S. Virtual Outcrops in a Pocket: The Smartphone as a Fully Equipped Photogrammetric Data Acquisition Tool. *GSA Today* **2021**, *31*, 4–9. [CrossRef]
5. Luetzenburg, G.; Kroon, A.; Bjørk, A.A. Evaluation of the Apple IPhone 12 Pro LiDAR for an Application in Geosciences. *Sci. Rep.* **2021**, *11*, 22221. [CrossRef] [PubMed]
6. An, P.; Fang, K.; Zhang, Y.; Jiang, Y.; Yang, Y. Assessment of the Trueness and Precision of Smartphone Photogrammetry for Rock Joint Roughness Measurement. *Meas. J. Int. Meas. Confed.* **2022**, *188*, 110598. [CrossRef]
7. Tavani, S.; Billi, A.; Corradetti, A.; Mercuri, M.; Bosman, A.; Cuffaro, M.; Seers, T.D.; Carminati, E. Smartphone Assisted Fieldwork: Towards the Digital Transition of Geoscience Fieldwork Using LiDAR-Equipped IPhones. *Earth Sci. Rev.* **2022**, *227*, 103969. [CrossRef]
8. Devoto, S.; Macovaz, V.; Mantovani, M.; Soldati, M.; Furlani, S. Advantages of Using UAV Digital Photogrammetry in the Study of Slow-Moving Coastal Landslides. *Remote Sens.* **2020**, *12*, 3566. [CrossRef]
9. Panara, Y.; Menegoni, N.; Carboni, F.; Inama, R. 3D Digital Outcrop Model-Based Analysis of Fracture Network along the Seismogenic Mt. Vettore Fault System (Central Italy): The Importance of Inherited Fractures. *J. Struct. Geol.* **2022**, *161*, 104654. [CrossRef]
10. Prabhakaran, R.; Urai, J.L.; Bertotti, G.; Weismüller, C.; Smeulders, D.M.J. Large-Scale Natural Fracture Network Patterns: Insights from Automated Mapping in the Lilstock (Bristol Channel) Limestone Outcrops. *J. Struct. Geol.* **2021**, *150*, 104405. [CrossRef]
11. Xu, X.; Aiken, C.L.V.; Bhattacharya, J.P.; Corbeanu, R.M.; Nielsen, K.C.; McMechan, G.A.; Abdelsalam, M.G. Creating Virtual 3-D Outcrop. *Lead. Edge* **2000**, *19*, 197–202. [CrossRef]
12. Pringle, J.K.; Clark, J.D.; Westerman, A.R.; Stanbrook, D.A.; Gardiner, A.R.; Morgan, B.E.F. Virtual Outcrops: 3-D Reservoir Analogues. *J. Virtual Explor.* **2001**, *4*, 51–55. [CrossRef]
13. Bellian, J.A.; Kerans, C.; Jennette, D.C. Digital Outcrop Models: Applications of Terrestrial Scanning Lidar Technology in Stratigraphic Modeling. *J. Sediment. Res.* **2005**, *75*, 166–176. [CrossRef]
14. McCaffrey, K.J.W.; Jones, R.R.; Holdsworth, R.E.; Wilson, R.W.; Clegg, P.; Imber, J.; Holliman, N.; Trinks, I. Unlocking the Spatial Dimension: Digital Technologies and the Future of Geoscience Fieldwork. *J. Geol. Soc. London.* **2005**, *162*, 927–938. [CrossRef]

15. Buckley, S.J.; Enge, H.D.; Carlsson, C.; Howell, J.A. Terrestrial Laser Scanning for Use in Virtual Outcrop Geology. *Photogramm. Rec.* **2010**, *25*, 225–239. [CrossRef]
16. Jones, R.R.; Pringle, J.K.; McCaffrey, K.J.W.; Imber, J.; Wightman, R.H.; Guo, J.; Long, J.J. Extending Digital Outcrop Geology into the Subsurface. In *CSP010 Outcrops Revitalized: Tools, Techniques and Applications*; Martinsen, O.J., Pulham, A.J., Haughton, P., Sullivan, M.D., Eds.; SEPM (Society for Sedimentary Geology): Tulsa, OK, USA, 2011; pp. 31–50, ISBN 978-1-56576-306-7.
17. Howell, J.A.; Martinius, A.W.; Good, T.R. The Application of Outcrop Analogues in Geological Modelling: A Review, Present Status and Future Outlook. *Geol. Soc. Lond. Spec. Publ.* **2014**, *387*, 1–25. [CrossRef]
18. Inama, R.; Menegoni, N.; Perotti, C. Syndepositional Fractures and Architecture of the Lastoni Di Formin Carbonate Platform: Insights from Virtual Outcrop Models and Field Studies. *Mar. Pet. Geol.* **2020**, *121*, 104606. [CrossRef]
19. Bonali, F.L.; Corti, N.; Russo, E.; Marchese, F.; Fallati, L.; Mariotto, F.P.; Tibaldi, A. Commercial-UAV-Based Structure from Motion for Geological and Geohazard Studies. In *Building Knowledge for Geohazard Assessment and Management in the Caucasus and Other Orogenic Regions*; Springer: Berlin/Heidelberg, Germany, 2021; pp. 389–427.
20. Uradziński, M.; Bakuła, M. Assessment of Static Positioning Accuracy Using Low-Cost Smartphone GPS Devices for Geodetic Survey Points' Determination and Monitoring. *Appl. Sci.* **2020**, *10*, 5308. [CrossRef]
21. Tavani, S.; Corradetti, A.; Granado, P.; Snidero, M.; Seers, T.D.; Mazzoli, S. Smartphone: An Alternative to Ground Control Points for Orienting Virtual Outcrop Models and Assessing Their Quality. *Geosphere* **2019**, *15*, 2043–2052. [CrossRef]
22. Tavani, S.; Pignalosa, A.; Corradetti, A.; Mercuri, M.; Smeraglia, L.; Riccardi, U.; Seers, T.D.; Pavlis, T.L.; Billi, A. Photogrammetric 3D Model via Smartphone GNSS Sensor: Workflow, Error Estimate, and Best Practices. *Remote Sens.* **2020**, *12*, 3616. [CrossRef]
23. Tavani, S.; Granado, P.; Riccardi, U.; Seers, T.D.; Corradetti, A. Terrestrial SfM-MVS Photogrammetry from Smartphone Sensors. *Geomorphology* **2020**, *367*, 107318. [CrossRef]
24. Fernández, O.; Muñoz, J.A.; Arbués, P.; Falivene, O.; Marzo, M. Three-Dimensional Reconstruction of Geological Surfaces: An Example of Growth Strata and Turbidite Systems from the Ainsa Basin (Pyrenees, Spain). *Am. Assoc. Pet. Geol. Bull.* **2004**, *88*, 1049–1068. [CrossRef]
25. Bistacchi, A.; Griffith, W.A.; Smith, S.A.F.; Di Toro, G.; Jones, R.R.; Nielsen, S. Fault Roughness at Seismogenic Depths from LIDAR and Photogrammetric Analysis. *Pure Appl. Geophys.* **2011**, *168*, 2345–2363. [CrossRef]
26. Vasuki, Y.; Holden, E.-J.; Kovesi, P.; Micklethwaite, S. Semi-Automatic Mapping of Geological Structures Using UAV-Based Photogrammetric Data: An Image Analysis Approach. *Comput. Geosci.* **2014**, *69*, 22–32. [CrossRef]
27. Seers, T.D.; Hodgetts, D. Comparison of Digital Outcrop and Conventional Data Collection Approaches for the Characterization of Naturally Fractured Reservoir Analogues. *Geol. Soc. London Spec. Publ.* **2014**, *374*, 51–77. [CrossRef]
28. Pavlis, T.L.; Mason, K.A. The New World of 3D Geologic Mapping. *GSA Today* **2017**, *27*, 4–10. [CrossRef]
29. Seers, T.D.; Sheharyar, A.; Tavani, S.; Corradetti, A. Virtual Outcrop Geology Comes of Age: The Application of Consumer-Grade Virtual Reality Hardware and Software to Digital Outcrop Data Analysis. *Comput. Geosci.* **2022**, *159*, 105006. [CrossRef]
30. Bemis, S.P.; Micklethwaite, S.; Turner, D.; James, M.R.; Akciz, S.; Thiele, S.T.; Bangash, H.A. Ground-Based and UAV-Based Photogrammetry: A Multi-Scale, High-Resolution Mapping Tool for Structural Geology and Paleoseismology. *J. Struct. Geol.* **2014**, *69*, 163–178. [CrossRef]
31. Pringle, J.K.; Westerman, A.R.; Clark, J.D.; Drinkwater, N.J.; Gardiner, A.R. 3D High-Resolution Digital Models of Outcrop Analogue Study Sites to Constrain Reservoir Model Uncertainty: An Example from Alport Castles, Derbyshire, UK. *Pet. Geosci.* **2004**, *10*, 343–352. [CrossRef]
32. Westoby, M.J.; Dunning, S.A.; Woodward, J.; Hein, A.S.; Marrero, S.M.; Winter, K.; Sugden, D.E. Instruments and Methods: Sedimentological Characterization of Antarctic Moraines Using Uavs and Structure-from-Motion Photogrammetry. *J. Glaciol.* **2015**, *61*, 1088–1102. [CrossRef]
33. Nesbit, P.R.; Durkin, P.R.; Hugenholtz, C.H.; Hubbard, S.M.; Kucharczyk, M. 3-D Stratigraphic Mapping Using a Digital Outcrop Model Derived from UAV Images and Structure-from-Motion Photogrammetry. *Geosphere* **2018**, *14*, 2469–2486. [CrossRef]
34. Favalli, M.; Fornaciai, A.; Mazzarini, F.; Harris, A.; Neri, M.; Behncke, B.; Pareschi, M.T.; Tarquini, S.; Boschi, E. Evolution of an Active Lava Flow Field Using a Multitemporal LIDAR Acquisition. *J. Geophys. Res. Solid Earth* **2010**, *115*, B11. [CrossRef]
35. Brodu, N.; Lague, D. 3D Terrestrial Lidar Data Classification of Complex Natural Scenes Using a Multi-Scale Dimensionality Criterion: Applications in Geomorphology. *ISPRS J. Photogramm. Remote Sens.* **2012**, *68*, 121–134. [CrossRef]
36. Carrivick, J.L.; Smith, M.W. Fluvial and Aquatic Applications of Structure from Motion Photogrammetry and Unmanned Aerial Vehicle/Drone Technology. *WIREs Water* **2019**, *6*, 1–17. [CrossRef]
37. Turner, D.; Lucieer, A.; de Jong, S.M. Time Series Analysis of Landslide Dynamics Using an Unmanned Aerial Vehicle (UAV). *Remote Sens.* **2015**, *7*, 1736. [CrossRef]
38. Lucieer, A.; de Jong, S.M.; Turner, D. Mapping Landslide Displacements Using Structure from Motion (SfM) and Image Correlation of Multi-Temporal UAV Photography. *Prog. Phys. Geogr. Earth Environ.* **2014**, *38*, 97–116. [CrossRef]
39. Fang, K.; An, P.; Tang, H.; Tu, J.; Jia, S.; Miao, M.; Dong, A. Application of a Multi-Smartphone Measurement System in Slope Model Tests. *Eng. Geol.* **2021**, *295*, 106424. [CrossRef]
40. Fu, L.; Zhu, J.; Li, W.-L.; You, J.-G.; Hua, Z.-Y. Fast Estimation Method of Volumes of Landslide Deposit by the 3D Reconstruction of Smartphone Images. *Landslides* **2021**, *18*, 3269–3278. [CrossRef]
41. Santos, I.; Henriques, R.; Mariano, G.; Pereira, D.I. Methodologies to Represent and Promote the Geoheritage Using Unmanned Aerial Vehicles, Multimedia Technologies, and Augmented Reality. *Geoheritage* **2018**, *10*, 143–155. [CrossRef]

42. Burnham, B.; Bond, C.; Flaig, P.; van der Kolk, D.; Hodgetts, D. Outcrop Conservation: Promoting Accessibility, Inclusivity, and Reproducibility through Digital Preservation. *Sediment. Rec.* **2022**, *20*, 5–14. [CrossRef]
43. Reitman, N.G.; Bennett, S.E.K.; Gold, R.D.; Briggs, R.W.; DuRoss, C.B. High-Resolution Trench Photomosaics from Image-Based Modeling: Workflow and Error Analysis. *Bull. Seismol. Soc. Am.* **2015**, *105*, 2354–2366. [CrossRef]
44. Carrera, C.C.; Asensio, L.A.B. Augmented Reality as a Digital Teaching Environment to Develop Spatial Thinking. *Cartogr. Geogr. Inf. Sci.* **2017**, *44*, 259–270. [CrossRef]
45. Whitmeyer, S.J.; Atchinson, C.; Collins, T.D. Using Mobile Technologies to Enhance Accessibility and Inclusion in Field- Based Learning Enhance Accessibility and Inclusion. *GSA Today* **2020**, *30*, 4–10. [CrossRef]
46. Bond, C.E.; Cawood, A.J. A Role for Virtual Outcrop Models in Blended Learning–Improved 3D Thinking and Positive Perceptions of Learning. *Geosci. Commun.* **2021**, *4*, 233–244. [CrossRef]
47. Uzkeda, H.; Poblet, J.; Magán, M.; Bulnes, M.; Martín, S.; Fernández-Martínez, D. Virtual Outcrop Models: Digital Techniques and an Inventory of Structural Models from North-Northwest Iberia (Cantabrian Zone and Asturian Basin). *J. Struct. Geol.* **2022**, *157*, 104568. [CrossRef]
48. Eusden, J.D.; Duvall, M.; Bryant, M. Google Earth Mashup of the Geology in the Presidential Range, New Hampshire: Linking Real and Virtual Field Trips for an Introductory Geology Class. *Geol. Soc. Am. Spec. Pap.* **2012**, *492*, 355–366.
49. Cliffe, A.D. A Review of the Benefits and Drawbacks to Virtual Field Guides in Today's Geoscience Higher Education Environment. *Int. J. Educ. Technol. High. Educ.* **2017**, 14. [CrossRef]
50. Harknett, J.; Whitworth, M.; Rust, D.; Krokos, M.; Kearl, M.; Tibaldi, A.; Bonali, F.L.; Van Wyk de Vries, B.; Antoniou, V.; Nomikou, P.; et al. The Use of Immersive Virtual Reality for Teaching Fieldwork Skills in Complex Structural Terrains. *J. Struct. Geol.* **2022**, *163*, 104681. [CrossRef]
51. Pugsley, J.H.; Howell, J.A.; Hartley, A.; Buckley, S.J.; Brackenridge, R.; Schofield, N.; Maxwell, G.; Chmielewska, M.; Ringdal, K.; Naumann, N.; et al. Virtual Field Trips Utilizing Virtual Outcrop: Construction, Delivery and Implications for the Future. *Geosci. Commun.* **2022**, *5*, 227–249. [CrossRef]
52. Rutkofske, J.E.; Pavlis, T.L.; Ramirez, S. Applications of Modern Digital Mapping Systems to Assist Inclusion of Persons with Disabilities in Geoscience Education and Research. *J. Struct. Geol.* **2022**, *161*, 104655. [CrossRef]
53. Cawood, A.; Bond, C. ERock: An Open-Access Repository of Virtual Outcrops for Geoscience Education. *GSA Today* **2019**, *29*, 36–37. [CrossRef]
54. Senger, K.; Betlem, P.; Birchall, T.; Buckley, S.J.; Coakley, B.; Eide, C.H.; Flaig, P.P.; Forien, M.; Galland, O.; Gonzaga, L.; et al. Using Digital Outcrops to Make the High Arctic More Accessible through the Svalbox Database. *J. Geosci. Educ.* **2021**, *69*, 123–137. [CrossRef]
55. Buckley, S.J.; Howell, J.A.; Naumann, N.; Lewis, C.; Chmielewska, M.; Ringdal, K.; Vanbiervliet, J.; Tong, B.; Mulelid-Tynes, O.S.; Foster, D.; et al. V3Geo: A Cloud-Based Repository for Virtual 3D Models in Geoscience. *Geosci. Commun.* **2022**, *5*, 67–82. [CrossRef]
56. Zini, L.; Calligaris, C.; Forte, E.; Petronio, L.; Zavagno, E.; Boccali, C.; Cucchi, F. A Multidisciplinary Approach in Sinkhole Analysis: The Quinis Village Case Study (NE-Italy). *Eng. Geol.* **2015**, *197*, 132–144. [CrossRef]
57. Busetti, A.; Calligaris, C.; Forte, E.; Areggi, G.; Mocnik, A.; Zini, L. Non-Invasive Methodological Approach to Detect and Characterize High-Risk Sinkholes in Urban Cover Evaporite Karst: Integrated Reflection Seismics, PS-INSAR, Leveling, 3D-GPR and Ancillary Data. a Ne Italian Case Study. *Remote Sens.* **2020**, *12*, 3814. [CrossRef]
58. Gortani, M. Le Doline Alluvionali. *Nat. Mont.* **1965**, *3*, 120–128.
59. Calligaris, C.; Devoto, S.; Galve, J.P.; Zini, L.; Pérez-Peña, J.V. Integration of Multi-Criteria and Nearest Neighbour Analysis with Kernel Density Functions for Improving Sinkhole Susceptibility Models: The Case Study of Enemonzo (NE Italy). *Int. J. Speleol.* **2017**, *46*, 191–204. [CrossRef]
60. Calligaris, C.; Devoto, S.; Zini, L. Evaporite Sinkholes of the Friuli Venezia Giulia Region (NE Italy). *J. Maps* **2017**, *13*, 406–414. [CrossRef]
61. Gutiérrez, F.; Guerrero, J.; Lucha, P. A Genetic Classification of Sinkholes Illustrated from Evaporite Paleokarst Exposures in Spain. *Environ. Geol.* **2008**, *53*, 993–1006. [CrossRef]
62. Gutiérrez, F.; Parise, M.; De Waele, J.; Jourde, H. A Review on Natural and Human-Induced Geohazards and Impacts in Karst. *Earth-Sc. Rev.* **2014**, *138*, 61–88. [CrossRef]
63. Girardeau-Montaut, D. Cloud Compare—3D Point Cloud and Mesh Processing Software. Available online: https://www.danielgm.net/cc/ (accessed on 17 April 2022).
64. Chase, P.P.C.; Clarke, K.H.; Hawkes, A.J.; Jabari, S.; Jakus, J.S. Apple IPhone 13 Pro Lidar Accuracy Assessment for Engineering Applications. In Proceedings of the 2022: The Digital Reality of Tomorrow, Fredericton, NB, Canada, 23–25 August 2022; pp. 1–10.
65. Sanz-Ablanedo, E.; Chandler, J.H.; Rodríguez-Pérez, J.R.; Ordóñez, C. Accuracy of Unmanned Aerial Vehicle (UAV) and SfM Photogrammetry Survey as a Function of the Number and Location of Ground Control Points Used. *Remote Sens.* **2018**, *10*, 1606. [CrossRef]
66. Buckley, S.J.; Ringdal, K.; Naumann, N.; Dolva, B.; Kurz, T.H.; Howell, J.A.; Dewez, T.J.B. LIME: Software for 3-D Visualization, Interpretation, and Communication of Virtual Geoscience Models. *Geosphere* **2019**, *15*, 222–235. [CrossRef]
67. Verhoeven, G. Taking Computer Vision Aloft—Archaeological Three-Dimensional Reconstructions from Aerial Photographs with Photoscan. *Archaeol. Prospect.* **2011**, *18*, 67–73. [CrossRef]

68. Remondino, F. Heritage Recording and 3D Modeling with Photogrammetry and 3D Scanning. *Remote Sens.* **2011**, *3*, 1104. [CrossRef]
69. Ruggles, S.; Clark, J.; Franke, K.W.; Wolfe, D.; Reimschiissel, B.; Martin, R.A.; Okeson, T.J.; Hedengren, J.D. Comparison of Sfm Computer Vision Point Clouds of a Landslide Derived from Multiple Small Uav Platforms and Sensors to a Tls-Based Model. *J. Unmanned Veh. Syst.* **2016**, *4*, 246–265. [CrossRef]
70. Kelly, J.; Sukhatme, G.S. Visual-Inertial Sensor Fusion: Localization, Mapping and Sensor-to-Sensor Self-Calibration. *Int. J. Rob. Res.* **2011**, *30*, 56–79. [CrossRef]
71. James, M.R.; Robson, S. Mitigating Systematic Error in Topographic Models Derived from UAV and Ground-Based Image Networks. *Earth Surf. Process. Landf.* **2014**, *39*, 1413–1420. [CrossRef]
72. Niethammer, U.; James, M.R.; Rothmund, S.; Travelletti, J.; Joswig, M. UAV-Based Remote Sensing of the Super-Sauze Landslide: Evaluation and Results. *Eng. Geol.* **2012**, *128*, 2–11. [CrossRef]
73. Tavani, S.; Corradetti, A.; Billi, A. High Precision Analysis of an Embryonic Extensional Fault-Related Fold Using 3D Orthorectified Virtual Outcrops: The Viewpoint Importance in Structural Geology. *J. Struct. Geol.* **2016**, *86*, 200–210. [CrossRef]
74. Menegoni, N.; Inama, R.; Crozi, M.; Perotti, C. Early Deformation Structures Connected to the Progradation of a Carbonate Platform: The Case of the Nuvolau Cassian Platform (Dolomites—Italy). *Mar. Pet. Geol.* **2022**, *138*, 105574. [CrossRef]
75. Gattolin, G.; Preto, N.; Breda, A.; Franceschi, M.; Isotton, M.; Gianolla, P. Sequence Stratigraphy after the Demise of a High-Relief Carbonate Platform (Carnian of the Dolomites): Sea-Level and Climate Disentangled. *Palaeogeogr. Palaeoclimatol. Palaeoecol.* **2015**, *423*, 1–17. [CrossRef]
76. Corradetti, A.; Tavani, S.; Russo, M.; Arbués, P.C.; Granado, P. Quantitative Analysis of Folds by Means of Orthorectified Photogrammetric 3D Models: A Case Study from Mt. Catria, Northern Apennines, Italy. *Photogramm. Rec.* **2017**, *32*, 480–496. [CrossRef]
77. Cawood, A.J.; Corradetti, A.; Granado, P.; Tavani, S. Detailed Structural Analysis of Digital Outcrops: A Learning Example from the Kermanshah-Qulqula Radiolarite Basin, Zagros Belt, Iran. *J. Struct. Geol.* **2022**, *154*, 104489. [CrossRef]
78. Jablonska, D.; Pitts, A.; Di Celma, C.; Volatili, T.; Alsop, G.I.; Tondi, E. 3D Outcrop Modelling of Large Discordant Breccia Bodies in Basinal Carbonates of the Apulian Margin, Italy. *Mar. Pet. Geol.* **2021**, *123*, 104732. [CrossRef]
79. McCaffrey, K.J.W.; Feely, M.; Hennessy, R.; Thompson, J. Visualization of Folding in Marble Outcrops, Connemara, Western Ireland: An Application of Virtual Outcrop Technology. *Geosphere* **2008**, *4*, 588. [CrossRef]
80. Nesbit, P.R.; Boulding, A.D.; Hugenholtz, C.H.; Durkin, P.R.; Hubbard, S.M. Visualization and Sharing of 3D Digital Outcrop Models to Promote Open Science. *GSA Today* **2020**, *30*, 4–10. [CrossRef]
81. Nesbit, P.R.; Hubbard, S.M.; Hugenholtz, C.H. Direct Georeferencing UAV-SfM in High-Relief Topography: Accuracy Assessment and Alternative Ground Control Strategies along Steep Inaccessible Rock Slopes. *Remote Sens.* **2022**, *14*, 490. [CrossRef]
82. Thiele, S.T.; Grose, L.; Samsu, A.; Micklethwaite, S.; Vollgger, S.A.; Cruden, A.R. Rapid, Semi-Automatic Fracture and Contact Mapping for Point Clouds, Images and Geophysical Data. *Solid Earth* **2017**, *8*, 1241–1253. [CrossRef]

CHAPTER 4.5

METHODOLOGICAL APPROACH PROPOSAL FOR THE DEFINITION OF HAZARD IN EVAPORITIC ENVIRONMENT

As revealed by the analyses conducted at the beginning of Chapter 4, assign a setback value is a challenging task. Typically, it is site-specific and requires detailed investigations to create an accurate geological model of sinkholes, enabling the evaluation of their possible evolution. Given the data availability in different geomorphological and geological contexts, considering the state of activity, type of sinkhole (classification), lithology and geomorphology, a methodological approach was developed. The latter specifies the criteria used to attribute hazard levels to each individual perimeter contained in the geodatabase (*Figure 68*).

The protocol was designed only for sinkholes in evaporitic environments. The decision to separate carbonates from evaporites is driven by the differences in solution processes between the two types of rock and the presence of voids in the subsoil. Within carbonates, the size and development of sub-horizontal caves play crucial role in hazard definition. As a result, defining these hazards must be done site-specifically and cannot be automated.

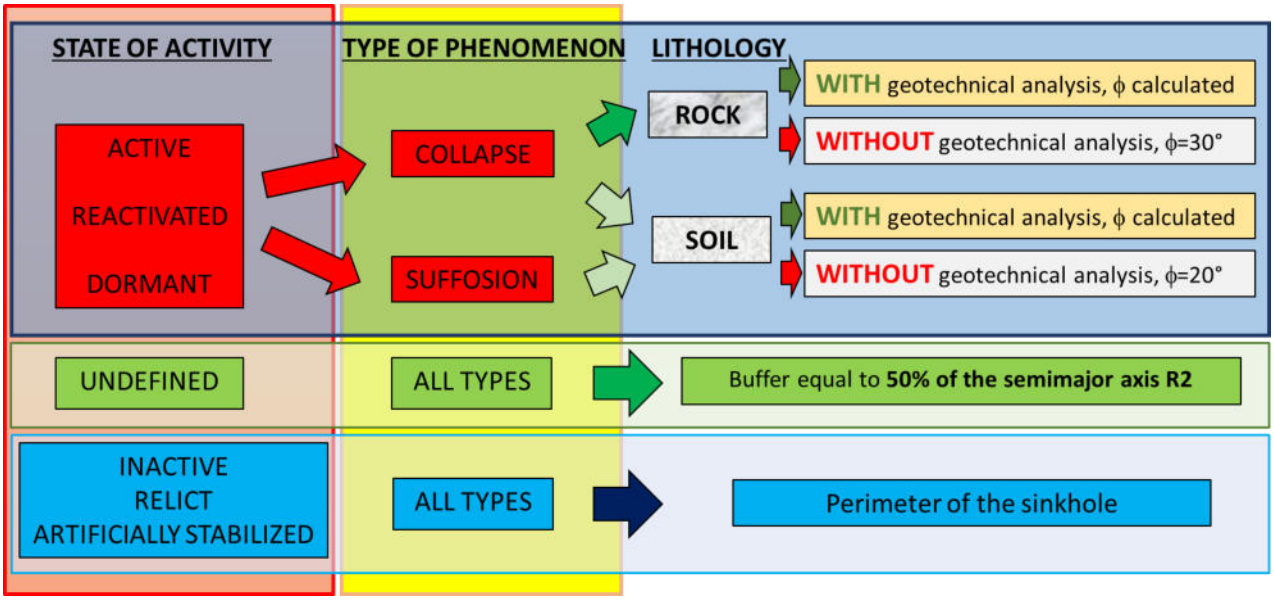

Figure 68 *Schematic flow chart aimed at clarifying the methodological approach studied to assign to each sinkhole its own hazard*

The state of activity, type of sinkhole (classification) and lithology are considered the most important parameters in criteria identification.

The state of activity is categorized based on definitions derived from WP/WLI (1993a, 1993b), Cruden D.M. and Couture R., (2011), Canuti P. and Esu F. (1995), ARPA Piemonte (2009) and modified according the following list:

- ***Active***: the sinkhole is currently evolving;
- ***Reactivated:*** the sinkhole is currently active after a dormant phase;
- ***Dormant (quiescent):*** The phases of activity seem to have ceased, but a possible reactivation cannot be ruled out;
- ***Inactive:*** Geomorphologically, it is an evolved form, considered stable, with no historical memory of movement and no evidence of activity;
- ***Relict:*** The sinkhole originated in geomorphological or climatic conditions considerably different from the current ones, and reactivation is considered impossible due to those or other causes;
- ***Artificially stabilized:*** Possible reactivation is excluded due to the mitigation measures;
- ***Undefined:*** This definition is assigned when there is no information regarding the state of activity.

Based on the activity, the entire population in the database was divided into three main categories:

1) ACTIVE, REACTIVATED and DORMANT;

2) UNDEFINED;

3) INACTIVE, RELICT and ARTIFICIALLY STABILIZED.

Subsequently, each macrocategory was treated according to the type of sinkhole, the type of material involved, and its potential evolution over time.

MACROCATEGORY 1

State of activity: ACTIVE, REACTIVATED and DORMANT

Sinkholes belonging to macrocategory 1 have been divided into two subcategories: collapses and suffosions.

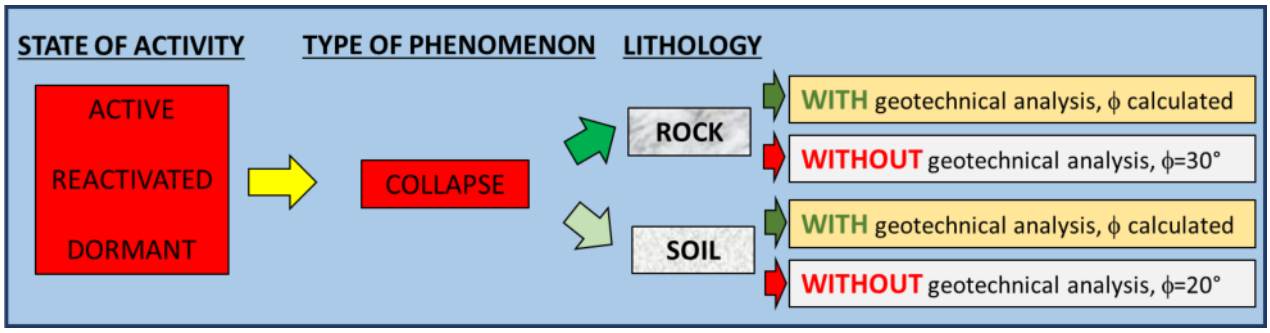

Figure 69 *Methodological approach for buffer calculation for the active, reactivated and dormant collapse sinkhole in rock and soil material*

For the collapse sinkholes, the methodology focuses on creating a buffer zone, defined starting from the minor semi-axis (R_{1top}) which describes the upper outline of the sinkhole. R_{1top} was chosen because it typically represents the steepest slope. The buffer zone is calculated as the difference between a theoretical equilibrium semi-axis (R_{eq}), trigonometrically evaluated based on the depth of the feature, and the semi-axis of the perimeter (R_{1top}).

The formula applied for buffer calculation is:

$$BUFFER = (P * \tan(90 - ANGLE)) - R1top + R1bot$$

Where P is the depth, ANGLE is the stable angle defined below, R_{1top} is the minor semi-axis of the perimeter of the sinkhole and R_{1bot} is the minor semi-axis of the bottom of the sinkhole.

For the cover collapses, the theoretical equilibrium angle (ANGLE) has been set equal to 20°, for the bedrock and caprock collapses, the angle was chosen equal to be 30°. These values were derived from the analyses of the data present in the regional geodatabase. To obtain them, the slope was considered. Specifically, for each sinkhole, the slope angle was evaluated considering only the slopes of the feature. From the surface perimeter, the bottom one has been subtracted, obtaining a donut for which the slope was computed (*Figure 70*).

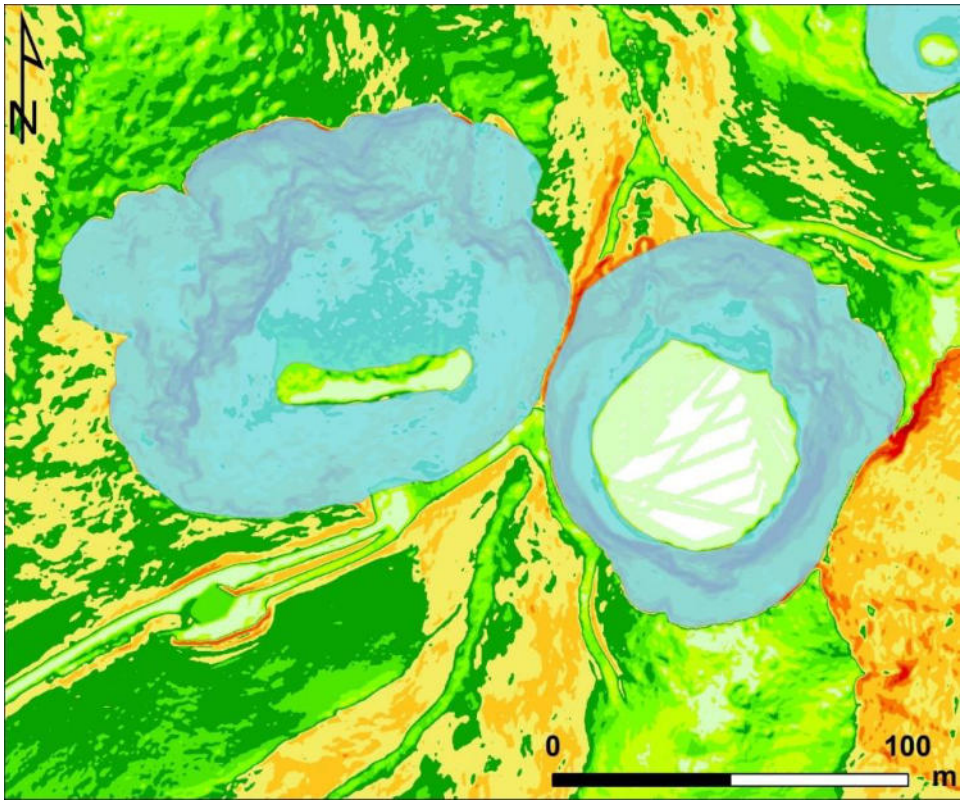

Figure 70 *Slope map with the donuts elaborated*

The Zonal statistic tool was applied to the donuts, enabling the calculation of minimum, maximum and mean slope values (*Table 10*). The values in Table 10 are categorized based on the different state of activity and type of sinkholes, representing average values. Among the three options (Min, Mean and Max), the mean value associated to inactive, relict and artificially stabilized sinkholes was selected. This choice was made considering it to be the most representative of a stable feature.

STATE OF ACTIVITY		EVAPORITES		
		COLLAPSE		SUFFOSION
		ROCK	COVER	SOIL
ACTIVE, REACTIVATED and DORMANT	MIN	5.77	5.85	7.05
	MAX	51.74	37.18	33.32
	MEAN	31.75	23.22	21.3
INACTIVE, RELICT and ARTIFICIALLY STABILIZED	MIN	4.06	3.99	6.28
	MAX	50.41	41.65	31.47
	MEAN	28.28	21.95	18.85
UNDEFINED	MIN	5.7	5.42	7.3
	MAX	56.55	36.48	33.27
	MEAN	37.85	22.19	21.4

Table 10 *Average values (min, max, mean) of the slope of the sinkholes considering different state of activity and the type of sinkholes and material involved. The value used as stable angle is highlighted in orange*

If the difference between the theoretical equilibrium semi-axis (R_{eq}) and the minor semi-axis (R_{1top}) is a positive number (case A in *Figure 71*), an area is generated around the identified sinkhole, and its value is set equal to this difference (buffer area). If the aforementioned difference is a negative number (case B in *Figure 71*), the buffer area is not created because the shape is considered stable.

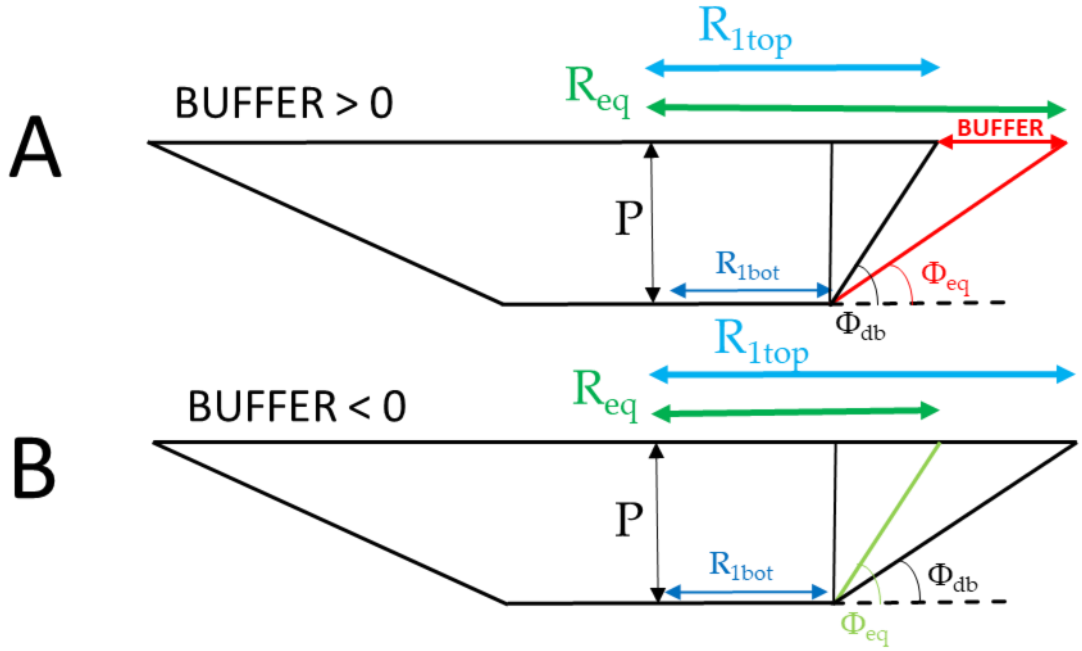

Figure 71 *Methodology used to create the buffer:* ***A)*** *When the equilibrium semi-axis is longer than the minor semi-axis;* ***B)*** *When the equilibrium semi-axis is shorter than the minor semi-axis*

The methodology for suffosion sinkholes is the same as that used for collapse sinkholes in soil material, utilizing an angle of stability of 20°.

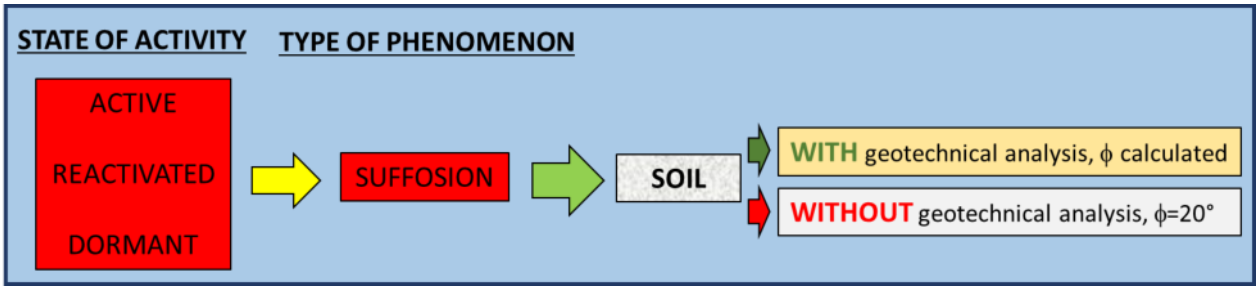

Figure 72 *Calculation of the buffer for the suffosion sinkhole*

MACROCATEGORY 2

State of activity: UNDEFINED

For sinkholes with an "undefined" state of activity, the methodology involves creating a buffer with an extension of 50% of the semi-major axis (R_{2top}). This value was estimated on a heuristic analysis of the data in the geodatabase.

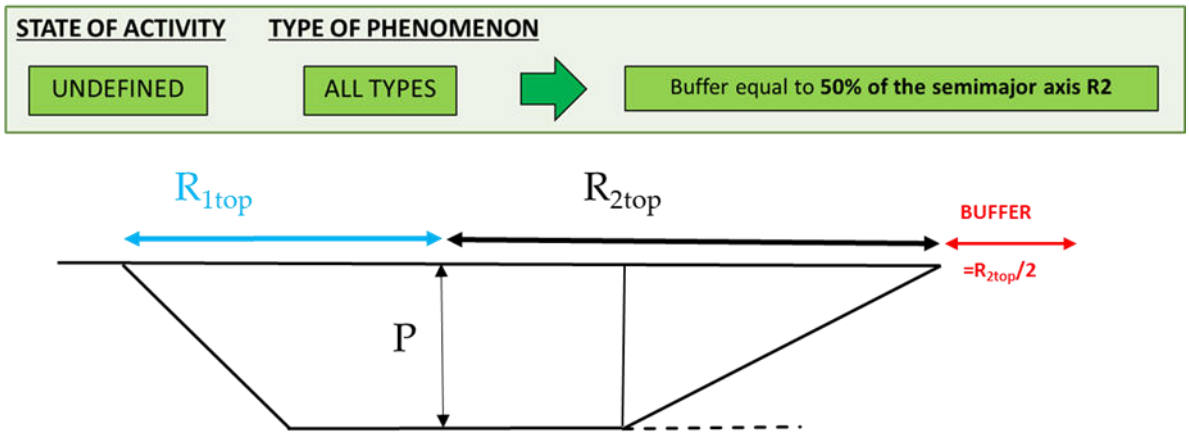

Figure 73 *Calculation of the buffer for all types of sinkhole with an "undefined" state of activity*

MACROCATEGORY 3

State of activity: INACTIVE, RELICT, ARTIFICIALLY STABILIZED

For sinkholes categorized as inactive, relict and artificially stabilized, recognized as stable forms, the proposed methodology entails maintaining the existing perimeter without creating a buffer.

HAZARD ASSESSMENT

In analogy with the P.A.I. (Piano di Assetto Idrogeologico) classification it was decided to adopt the following hazard scale identified by the acronyms P1, P2, P3 and P4 (*Figure 74*). P1 defines a low/moderate risk for which marginal social and economic damages are possible; P2 defines a medium risk for which minor damages to buildings and infrastructure are possible, without compromising the safety of individuals, the habitability of buildings, and the conduct of socio-economic activities; P3 defines a high risk for which potential issues include threats to personal safety, functional damage to buildings and infrastructure leading to their inoperability, interruption of socio-economic activities, and damage to cultural heritage; P4 defines a very high risk for which potential outcomes involve the loss of human lives and severe injuries, significant damage to buildings and infrastructure, harm to cultural heritage, and the destruction of socio-economic activities.

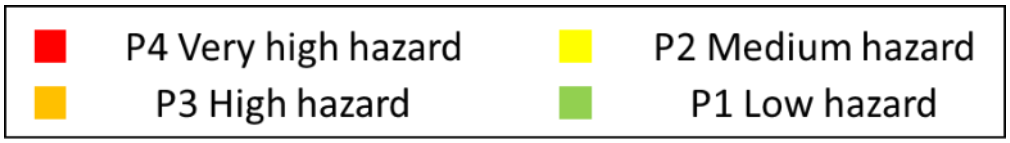

Figure 74 *Hazard level used for the sinkhole assessment*

Following the proposed methodology, various hazard values were assigned to identified sinkholes and their calculated buffers.

For sinkholes with a state of activity defined as ACTIVE, REACTIVATED and DORMANT, both sinkholes and buffer areas are associated with a P4 hazard.

Sinkholes with a state of activity defined as UNDEFINED, are linked to a P4 hazard, while their buffer are assigned a P3 hazard.

Lastly, for sinkholes with a state of activity defined as INACTIVE, RELICT and ARTIFICIALLY STABILIZED, the sinkhole areas are associated with a P3 hazard.

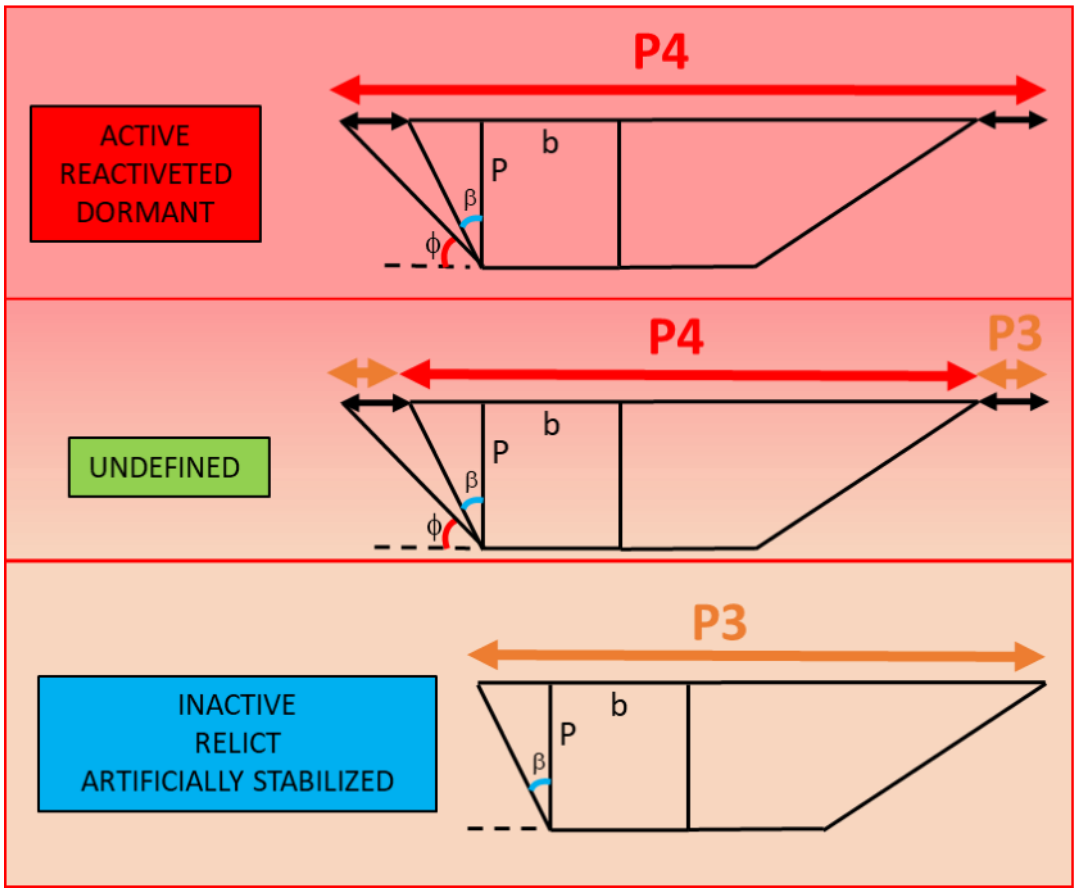

Figure 75 *Perimeter and buffer hazard value*

UNIVERSITÀ DEGLI STUDI DI TRIESTE

CHAPTER 4.6

TOOL ELABORATION AND APPLICATION

Building upon the methodology outlined in the previous paragraph, the Model Builder tool available in the ArcGIS environment was employed to establish geoprocessing workflows for hazard definition. The obtained sinkhole tool, designed specifically for phenomena occurring in an evaporitic environment, is easily integrable into the ArcToolbox, and comprises three modules:

A. Calculation of the minor and major semi-axes of the sinkhole perimeter and the bottom;

B. Creation of a buffer area and attribution of the hazard level to both the sinkhole area and the buffer;

C. Creation of a sinkhole hazard map.

Starting with the calculation of the main geomorphometric parameters, the tool allows to select only sinkholes linked to the evaporitic environment and, according to their state of activity and classification, it creates or not a buffer area with an associate hazard.

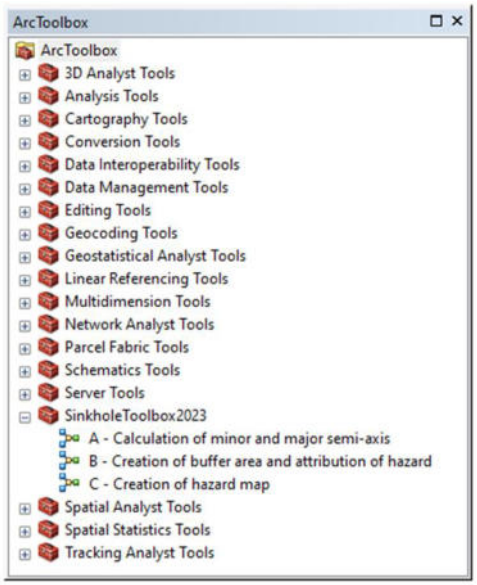

Figure 76 *ArcToolbox in ArcGIS environment with the new sinkhole toolbox*

DATA PREPARATION

Each sinkhole is depicted as a polygon, and to enhance the visual representation, a smoothing tool (Bezier Interpolation) has been applied to the perimeter. This process rounds the shapes and eliminates any sharp edges. *Table 11* provides a summary of the fields created and utilized for defining the hazard of the perimeter and calculating the potential buffer area.

Field	Field description
STATCODE	State of activity
CLASSCODE	Type of sinkhole
ANGLE	Theoretical equilibrium angle
DEPTH	Depth of the sinkhole

Table 11 *New fields used for the tool application*

State of activity - STATCODE

Using this parameter, the hazard level for both the sinkhole area and the any potential associated buffer area was determined. The table below details the codes employed in the model to define the state of activity and the corresponding hazard level attributed to the sinkhole area and buffer area. The model stores the hazard values for the sinkhole area and the buffer area in the new fields named HAZARD and HAZARDBUF.

STATCODE	State of activity	HAZARD	HAZARBUF
AC	Active	P4	P4
RA	Reactivated	P4	P4
QU	Dormant	P4	P4
UN	Undefined	P4	P3
IN	Inactive	P3	/
RE	Relict	P3	/
AS	Artificially stabilized	P3	/

Table 12 *State activity code and area and buffer hazard value*

Classification (type of sinkhole) - CLASSCODE

The table below lists the codes employed by the tool to categorized each individual sinkhole.

CLASSCODE	Classification
CO	Collapse
SU	Suffosion
UN	Undefined

Table 13 *Classcode*

Angle of stability - ANGLE

For rock collapses, the slope angle (relative to a defined stable shape) has been conservatively set to 30°, while for soil collapses and suffosion, the angle has been set fixed at 20°.

Depth of the sinkhole - P

Concerning depth, data acquired in the field was initially used. However, recognizing the subjectivity and often undetectable nature of this data, a decision was made to calculate depth (P) based on the available DTM with a resolution of 0.5 m.

The depth (P) is computed as the difference between the mean elevation (E_{mean}) and the lowest elevation of the sinkhole (E_{bot}). The mean elevation (E_{mean}) is the arithmetic mean of the highest elevation (E_{max}) and the lowest elevation (E_{min}), both statistically calculated along the perimeter line of the top of the feature. The lowest elevation of the sinkhole (E_{bot}) instead, is statistically calculated on the 3D polygon feature using the Zonal Statistics tool (*Figure 77*). The choice to use average depth (P) was driven by the varied physiographic units in the Friuli Venezia Giulia region. The northern part of the region is characterized by the presence of the major ranges with the Alps, while moving southward the landscape become gentler with the PreAlps and the wide plain areas. Separate units include the Classical karst area and the Cansiglio-Cavallo plateau. Sinkholes, widespread throughout all these different contexts, developing both on slopes and in flat areas, defining distinct geometries. Therefore, the average depth (P) aims to be representative of all sinkholes, regardless of the geomorphological context in which they occur.

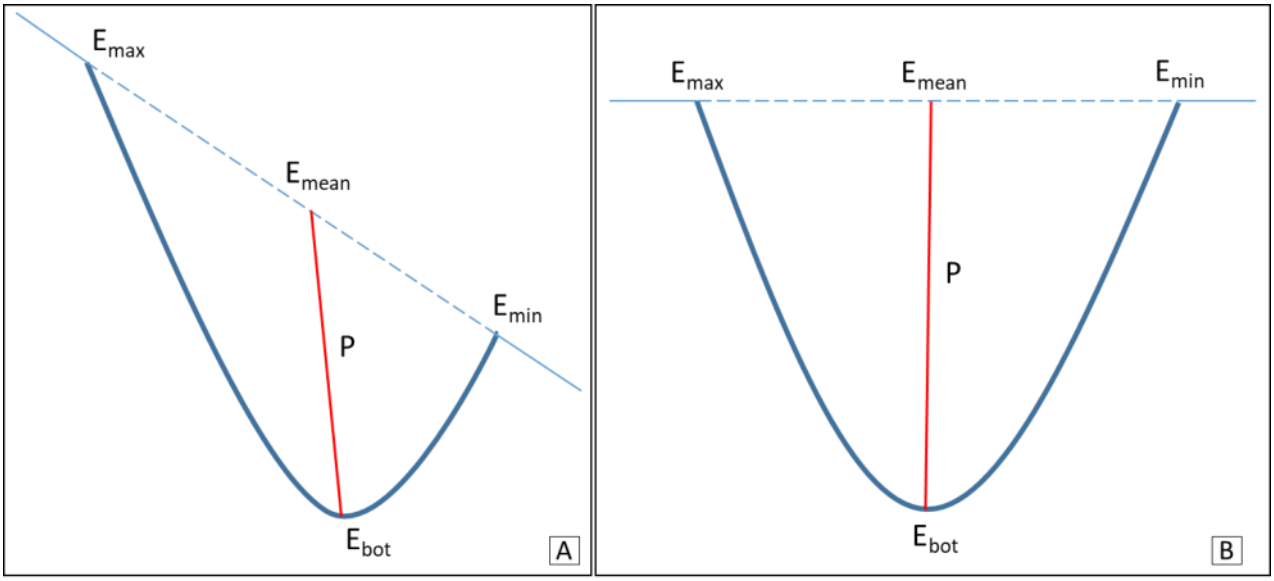

Figure 77 *Sketch of the evaluated depth in sinkhole developed in:* ***A)*** *slope area;* ***B)*** *Plain area*

Once the fields to be utilized were defined, the 3 sub-models (A-B-C) were applied to all the sinkholes in the evaporitic environment present in the regional geodatabase.

A. Calculation of minor (R_{1top}) and major (R_{2top}) semi-axis of the sinkhole perimeter and of minor (R_{1bot}) and major (R_{2bot}) semi-axis of the bottom

The minor and major semi-axes were determined starting from the digitized perimeters. For each sinkhole, the minimum width rectangle was calculated using the minimum bounding geometry tool available in ArcGIS. This rectangle circumscribes the perimeter of the identified shape. The same procedure was applied to sinkhole bottoms (*Figure 788*). The geometrical parameters calculated were later added to the DB:

- R_{1top}: Minor semi-axis of the sinkhole perimeter;
- R_{2top}: Major semi-axis of the sinkhole perimeter;
- $Orien_{Top}$: orientation of the major semi-axis of the sinkhole (degree with respect to the North);
- R_{1bot}: Minor semi-axis of the bottom of the sinkhole;
- R_{2bot}: Major semi-axis of the bottom of the sinkhole;
- $Orien_{Bot}$: orientation of the major semi-axis of the bottom of the sinkhole (degree with respect to the North).

The next figures illustrate an example of the tool's application in 7 different sinkholes in Sauris municipality, including two active bedrock collapses (A and B), two inactive bedrock collapses (C and D), two undefined bedrock collapses (F and G) and one dormant cover collapse (E).

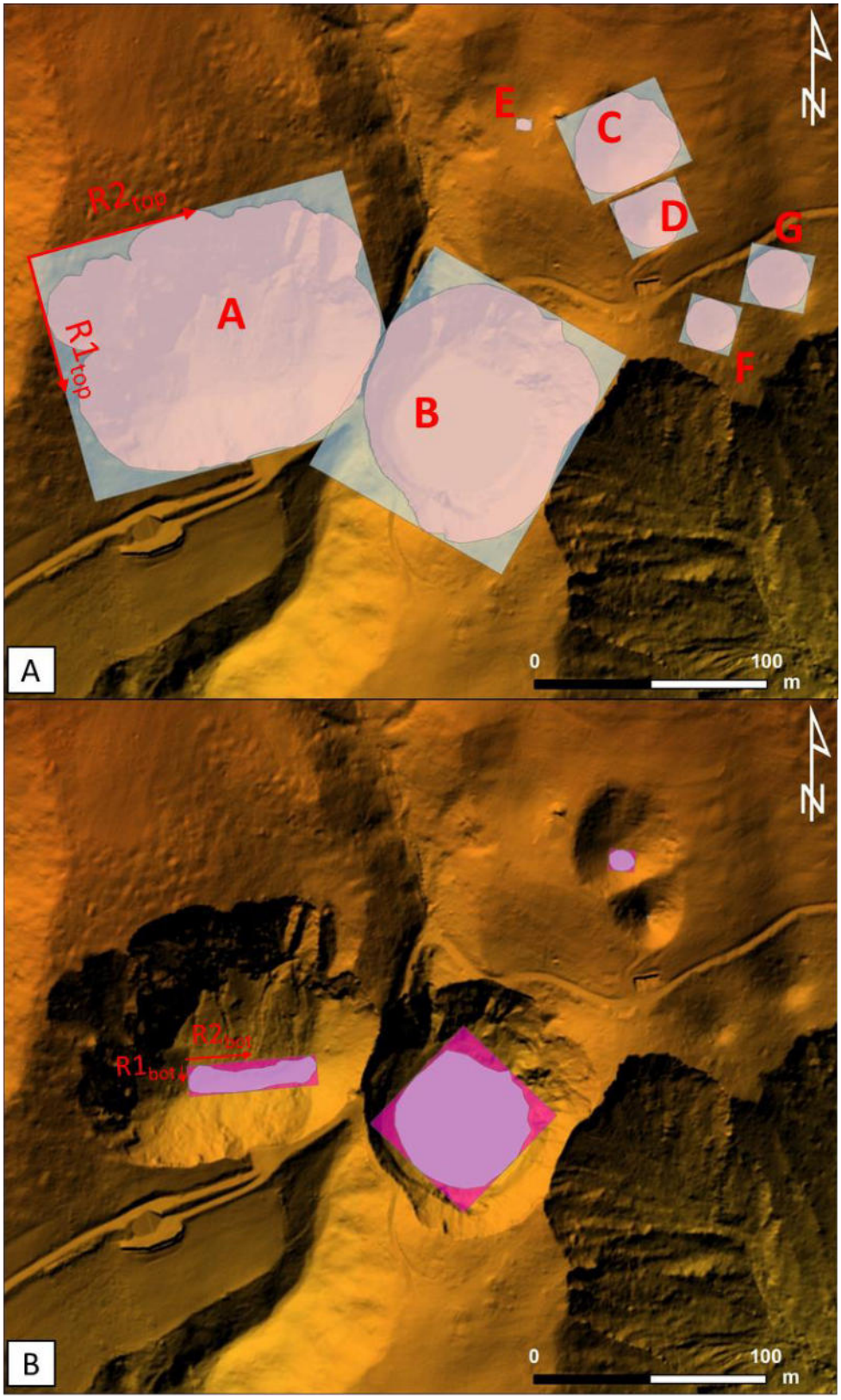

Figure 78 *Example of application of sub-model A in Sauris municipality:* ***A)*** *Minimum bounding geometry applied to the sinkhole perimeter and calculation of* $R1_{top}$ *and* $R2_{top}$*;* ***B)*** *Minimum bounding geometry applied to the perimeter of the sinkhole bottom and calculation of* $R1_{bot}$ *and* $R2_{bot}$

Sub-model_A.py - C:\Users\Alice\Desktop\TESI\Sub-model_A.py (2.7.18.4)

File Edit Format Run Options Window Help

```
# Process: Minimum Bounding Geometry
arcpy.MinimumBoundingGeometry_management(PerimeterSinkhole, Sinkhole_MBG, "RECTANGLE_BY_WIDTH", "NONE", "", "MBG_FIELDS")

# Process: Join Field
arcpy.JoinField_management(PerimeterSinkhole, "ID_SH", Sinkhole_MBG, "ID_SH", "MBG_Width;MBG_Length;MBG_Orientation")

# Process: Add Field
arcpy.AddField_management(PerimeterSinkhole, "R1top", "DOUBLE", "", "", "", "", "NULLABLE", "NON_REQUIRED", "")

# Process: Add Field (2)
arcpy.AddField_management(PerimeterSinkhole, "R2top", "DOUBLE", "", "", "", "", "NULLABLE", "NON_REQUIRED", "")

# Process: Add Field (5)
arcpy.AddField_management(PerimeterSinkhole, "OrienTop", "DOUBLE", "", "", "", "", "NULLABLE", "NON_REQUIRED", "")


message = "R1top - minor axis"
arcpy.AddMessage(message)
# Process: Calculate Field
arcpy.CalculateField_management(PerimeterSinkhole, "R1top", "[MBG_Width] /2", "VB", "")

message = "R2top - major axis"
arcpy.AddMessage(message)
# Process: Calculate Field (2)
arcpy.CalculateField_management(PerimeterSinkhole, "R2top", "[MBG_Length] /2", "VB", "")

message = "OrienTop - orientation of the major axis in degrees relative to North"
arcpy.AddMessage(message)
# Process: Calculate Field (5)
arcpy.CalculateField_management(PerimeterSinkhole, "OrienTop", "[MBG_Orientation]", "VB", "")
```

Figure 79 *Sub-model A (example of calculation of major and minor semi-axes of the sinkhole)*

B. Definition of the setback distance (buffer)

Sub-model B applied the method outlined in the previous paragraph (*Figure 68*). Following its application, the fields BUFFER, HAZARD and HAZBUF were incorporated into the DB. The model assigns the hazard to the sinkhole perimeter as function of the state of activity and the type of sinkhole. For example, it selects the AC, RA and QU STATCODE and assigns a hazard level of P4 to each sinkhole). After calculating the buffer, the model then assigns the corresponding hazard level to each of them.

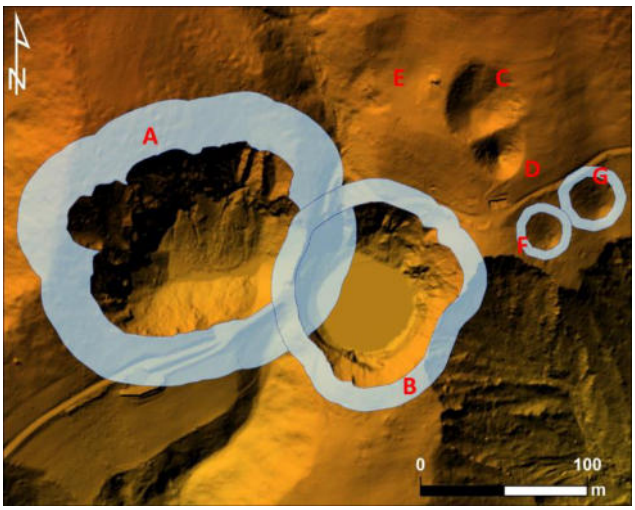

Figure 80 *Example of application of sub-model B (buffer calculation) in Sauris Municipality*

The application of sub-model B in the example *(Figure 80)*, highlighted the creation of a buffer for sinkholes with an active and undefined state of activity (A, B, F and G), while no buffer was generated for the inactive sinkholes (C and D). In particular, the dormant cover collapse (E) has a steepness lower than the stable angle and therefore no buffer has been created.

Sub-model_B.py - C:\Users\Alice\Desktop\TESI\Sub-model_B.py (2.7.18.4)

File Edit Format Run Options Window Help

```
arcpy.AddMessage(message)
# Process: Select Layer By STAT IN( 'AC' , 'RA' , 'QU' )
arcpy.SelectLayerByAttribute_management(Sinkhole, "NEW_SELECTION", "STATCODE IN( 'AC' , 'RA' , 'QU' )")
# Process: Calculate Field (4)
arcpy.CalculateField_management(Sinkhole, "HAZARD", "\"P4\"", "PYTHON_9.3", "")
# Process: Calculate Field (7)
arcpy.CalculateField_management(Sinkhole, "HAZBUF", "\"P4\"", "PYTHON_9.3", "")


message = "- P4 hazard to the sinkhole with undefined state of activity and P3 to their buffer"
arcpy.AddMessage(message)
# Process: Select Layer By STAT IN( 'UN' )
arcpy.SelectLayerByAttribute_management(Sinkhole, "NEW_SELECTION", "STATCODE IN( 'UN')")
# Process: Calculate Field (5)
arcpy.CalculateField_management(Sinkhole, "HAZARD", "\"P4\"", "PYTHON_9.3", "")
# Process: Calculate Field (8)
arcpy.CalculateField_management(Sinkhole, "HAZBUF", "\"P3\"", "PYTHON_9.3", "")


message = "- P3 hazard to the sinkhole with inactive, relict and artificially stabilized state of activity"
arcpy.AddMessage(message)
arcpy.SelectLayerByAttribute_management(Sinkhole, "NEW_SELECTION", "STATCODE IN( 'IN' , 'RE' , 'AS' )")
# Process: Calculate Field (6)
arcpy.CalculateField_management(Sinkhole, "HAZARD", "\"P3\"", "PYTHON_9.3", "")



# Process: Add Field
arcpy.AddField_management(Sinkhole, "BUFFER", "DOUBLE", "", "", "", "", "NULLABLE", "NON_REQUIRED", "")


message = "- calculation of the buffer for the active, reactivated and dormant sinkhole classified as collapse"
arcpy.AddMessage(message)
# Process: Select Layer By STAT IN( 'AC' , 'RA' ,'QU' ) AND CLASS = 'CO'
arcpy.SelectLayerByAttribute_management(Sinkhole, "NEW_SELECTION", "STATCODE IN( 'AC' , 'RA' ,'QU') AND CLASSCODE = 'CO'")
# Process: Calculate Field
arcpy.CalculateField_management(Sinkhole, "BUFFER", "( !P!*math.tan(math.radians(90- !ANGLE!) ))-!R1top! + !R1bot!", "PYTHON_9.3", "")

message = "- calculation of the buffer for the active, reactivated and dormant sinkhole classified as suffosion"
arcpy.AddMessage(message)
# Process: Select Layer By STAT IN( 'AC' , 'RA' ,'QU', ) AND CLASS = 'SU'
arcpy.SelectLayerByAttribute_management(Sinkhole, "NEW_SELECTION", "STATCODE IN( 'AC' , 'RA' ,'QU') AND CLASSCODE = 'SU'")
# Process: Calculate Field
arcpy.CalculateField_management(Sinkhole, "BUFFER", "( !P!*math.tan(math.radians(90- !ANGLE!) ))-!R1top! + !R1bot!", "PYTHON_9.3", "")

message = "- calculation of the buffer for the undefined sinkhole 1/2 major semi-axis)"
arcpy.AddMessage(message)
# Process: Select Layer By STAT = 'UN'
arcpy.SelectLayerByAttribute_management(Sinkhole, "NEW_SELECTION", "STATCODE = 'UN'")
# Process: Calculate Field (2)
arcpy.CalculateField_management(Sinkhole, "BUFFER", "!R2top!/2", "PYTHON_9.3", "")

message = "- no buffer for the inactive, relict and artificially stabilized sinkhole"
arcpy.AddMessage(message)
# Process: Select Layer By (STAT IN( 'IN' , 'RE' , 'AS' )
arcpy.SelectLayerByAttribute_management(Sinkhole, "NEW_SELECTION", "STATCODE IN('IN', 'RE', 'AS')")
# Process: Calculate Field (3)
arcpy.CalculateField_management(Sinkhole, "BUFFER", "0", "PYTHON_9.3", "")
```

Figure 81 *Sub-model B (Buffer calculation considering different state of activity and type of sinkhole)*

C. Creation of a sinkhole hazard map

The final sub-model considered both the sinkhole area and any buffer area based on the assigned hazard class. On highly hazardous areas "merge" and "dissolve" tools were applied. The same happens for the very high hazard areas on which the tools "merge" and "dissolve" were applied. These areas were superimposed on the less hazard areas. In the case of overlap, the higher risk value is assigned.

Sub-model_C.py - C:\Users\Alice\Desktop\TESI\Sub-model_C.py (2.7.18.4)

File Edit Format Run Options Window Help

```
# Local variables:
arcpy.env.workspace = desc.path
Sinkhole_SelectP3 = "Sinkhole_SelectP3"
Sinkhole_Buffer_SelectP3 = "Sinkhole_Buffer_SelectP3"
P3_Merge = "P3_Merge"
P3_Merge_Dissolve = "P3_Merge_Dissolve"
Sinkhole_Buffer_SelectP4 = "Sinkhole_Buffer_SelectP4"
Sinkhole_SelectP4 = "Sinkhole_SelectP4"
P4_Merge = "P4_Merge"
P4_Merge_Dissolve = "P4_Merge_Dissolve"

message = "- selection, merge and dissolve of the sinkhole and the buffer with P3 hazard"
arcpy.AddMessage(message)
# Process: Select
arcpy.Select_analysis(Layer_of_perimeter_of_sinkhole, Sinkhole_SelectP3, "HAZARD = 'P3'")
# Process: Select (2)
arcpy.Select_analysis(Layer_of_perimeter_of_sinkhole, Sinkhole_Buffer_SelectP3, "HAZBUF = 'P3'")
# Process: MergeP3
arcpy.Merge_management("Sinkhole_SelectP3;Sinkhole_Buffer_SelectP3", P3_Merge)
# Process: Add Field
arcpy.AddField_management(P3_Merge, "HAZTOT", "TEXT", "", "", "10", "", "NULLABLE", "NON_REQUIRED", "")
# Process: Calculate Field
arcpy.CalculateField_management(P3_Merge, "HAZTOT", "\"P3\"", "VB", "")
# Process: DissolveP3
arcpy.Dissolve_management(P3_Merge, P3_Merge_Dissolve, "HAZTOT", "", "SINGLE_PART", "DISSOLVE_LINES")


message = "- selection, merge and dissolve of the sinkhole and the buffer with P4 hazard"
arcpy.AddMessage(message)
# Process: Select (4)
arcpy.Select_analysis(Layer_of_perimeter_of_sinkhole, Sinkhole_Buffer_SelectP4, "HAZBUF = 'P4'")
# Process: Select (3)
arcpy.Select_analysis(Layer_of_perimeter_of_sinkhole, Sinkhole_SelectP4, "HAZARD = 'P4'")
# Process: MergeP4
arcpy.Merge_management("Sinkhole_Buffer_SelectP4;Sinkhole_SelectP4", P4_Merge)
# Process: Add Field (2)
arcpy.AddField_management(P4_Merge, "HAZTOT", "TEXT", "", "", "10", "", "NULLABLE", "NON_REQUIRED", "")
# Process: Calculate Field (2)
arcpy.CalculateField_management(P4_Merge, "HAZTOT", "\"P4\"", "VB", "")
# Process: DissolveP4
arcpy.Dissolve_management(P4_Merge, P4_Merge_Dissolve, "HAZTOT", "", "SINGLE_PART", "DISSOLVE_LINES")

message = "- combination of sinkhole and buffer with P3 and P4 hazard and creation of hazard map"
arcpy.AddMessage(message)
# Process: Update
arcpy.Update_analysis(P3_Merge_Dissolve, P4_Merge_Dissolve, Output_layer_map_of_Hazard, "BORDERS", "")
```

Figure 82 *Sub-model C (Hazard map)*

Figure 83 displays the final map of areas with different hazards based on the previously defined criteria. The tool automatically assigns a P4 hazard value to the active sinkholes and their buffer (A and B), a P4 hazard value to the area of the undefined sinkholes and a P3 value to their buffer (F and G). Additionally, it assigns a P3 value for the inactive sinkholes (C and D) and a P4 to the dormant cover collapse (E).

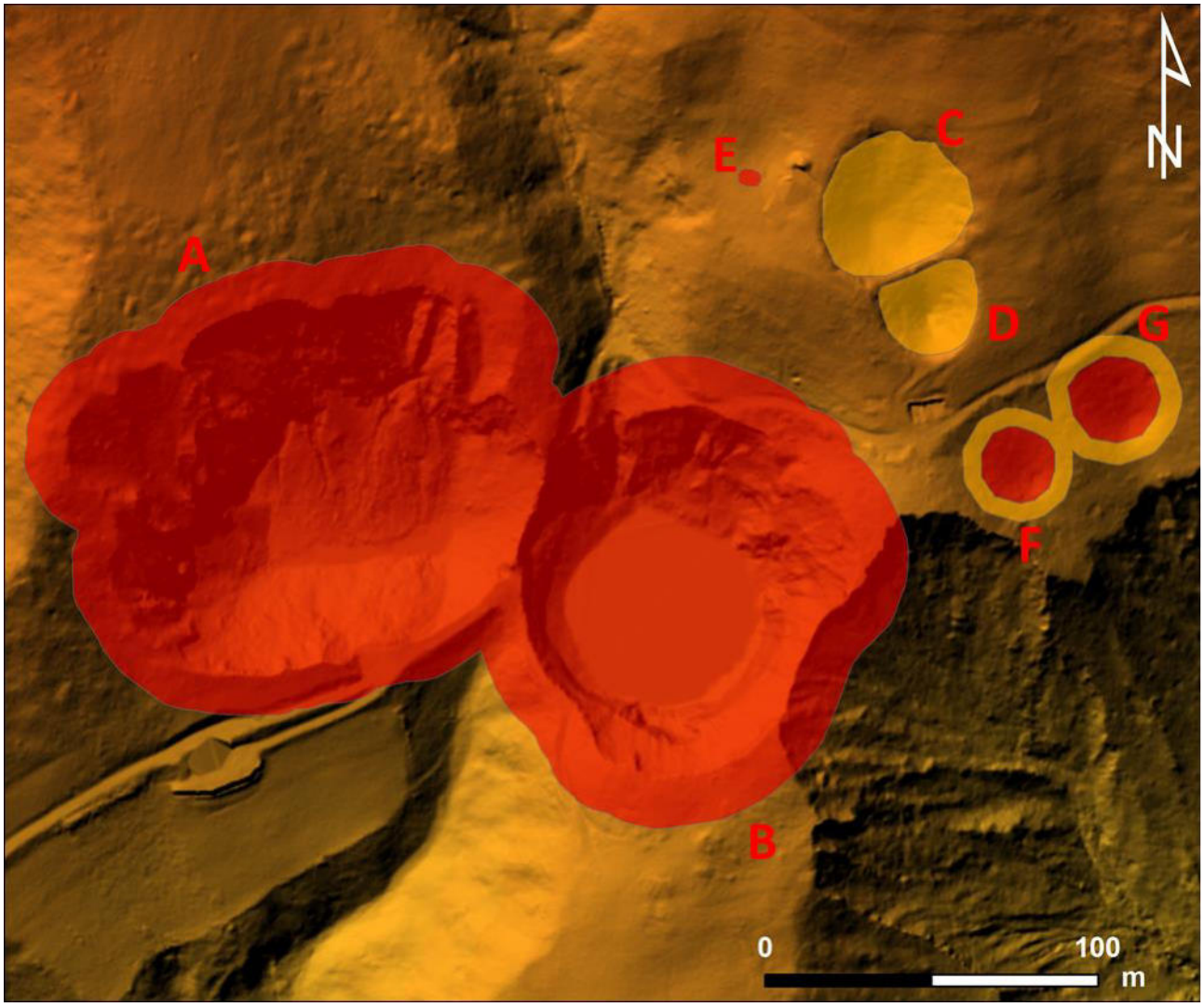

Figure 83 *Example of application of sub-model C (hazard map) in Sauris municipality*

UNIVERSITÀ DEGLI STUDI DI TRIESTE

CHAPTER 5
CONCLUSION

From a land use planning and guideline proposal point of view, the work carried out within the three-years of PhD was devoted to the identification, characterization and in-depth study of sinkholes. The aim was to define the setback distances and create an informatics protocol capable of automatically assigning a hazard value to each sinkhole. In Italy, these phenomena are widespread in many regions, but only in recent years the interest in national sinkhole problems greatly increased due to serious consequences and damages in urban areas. In 2014, ISPRA started a national project to inventory sinkholes. The Friuli Venezia Giulia, being one of the most sinkhole prone regions in Italy with phenomena occurring in different physiographic and geological contexts, was chosen as test area for the PhD research.

The research work involved a thorough review of the structure of the existing regional geodatabase of sinkholes and its subsequent update. The DB was enriched with new information related to previously catalogued sinkholes and the addition of new ones.

The initial regional census focused only the evaporitic environment due to the rapid occurrence of sinkholes and the higher associated hazard. However, significant updates were made to include mapping and characterization of sinkhole events in other lithological contexts. Regarding carbonates, the most hazardous events are related to the collapse of the ceiling of a cave. For this reason, a detail investigation began with the analysis of the FVG Regional Speleological Inventory (CSR). Desk activities, involving the analysis of plans, sections and descriptions, was conducted on the 8004 caves to select the entrances linked to a collapse sinkhole. Countless field surveys were carried out to better understand the critical issues of the regional territory linked to these events, considering the lithologies and the geomorphological and hydrogeological contexts. These field surveys led to the identification of 159 new sinkholes and the update of the classification and, where possible, the 2D and 3D shapes and the state of activity of another 184 sinkholes (previously classified as "undefined").

To be useful, the regional sinkhole geodatabase must be continually updated with not only new phenomena but also new information and insights into what has already been recorded. This may include the updates of new information after the drafting of new geological and topographical maps or the updates with the implementation of new classifications or with new data deriving from more detailed investigations.

Several in-depth studies were conducted in different test sites to define the best methodology for characterizing these phenomena. Field surveys in Quinis and Baus villages allowed for the comparison of different non-invasive methodologies. Interferometric data analysis, compared with geometric levelling acquired in Quinis

village, allowed to identify areas with higher downward displacement. Geophysical investigations (Electrical Resistivity Tomography, 3D GPR, Seismic Refraction) instead, allowed for the 3D characterization of the sinkhole and analysis of its evolution. The possibility to compare data acquired in the same area at different periods allowed the study of the development over time of the phenomena, determining possible continuous sinking. Going more in detail, a trench across an active sinkhole was excavated for the first time in Italy in the Enemonzo municipality. While the visible shape on the surface is typical of a suffosion sinkhole, the analysis of the trench clarified the 3D cylindrical shape characteristic of a collapse sinkhole. Therefore, the trench proved essential to define the type of sinkhole (classification) and to characterize the nearby area.

Due to its geological and hydrogeological characteristic, Quinis village has been subjected of further detailed investigation. An on-site experiment was conducted to evaluate the dissolution rate of evaporites. After one year, the results highlighted a dissolution rate eight times higher than the values available in literature data (0.68 – 1.14 mm/y, Klimchouk et al., 1996 and 0.4 – 1.0 mm/y, Cucchi et al., 1998).

Data collections, detailed mapping and characterization of sinkholes are mandatory precondition for the development of a methodological approach to define their hazard. The method, applied to sinkholes developed in an evaporitic environment, is based on a simple trigonometric formula, allowing the calculation of a buffer around each feature to outline a safeguard area. However, what is done for evaporites, is not applicable to carbonates. Most sinkholes in a carbonate context are linked to the collapse of the ceiling of a sub-horizontal cave. This requires more site-specific analysis and the application of an automatic approach is not recommended.

The developed approach has been transformed into an ArcGIS tool using geodatabase data to define the hazard of the contained sinkholes.

ACKNOWLEDGMENTS

I would like to start by thanking my supervisor for her immense patience, indispensable advice, shared knowledge, and crucial support. As someone once said "two blondes like us could either walk arm in arm or tear each other apart", luckily we got along.

A special thanks to Dott. Geol. Chiara Piano for her valuable insights and for always being available and present during this research work.

I thank Prof. Luca Zini, who welcomed me into the research group and, in all these years, involved me in various projects that enriched my professional knowledge. Thanks to Dott. Fernetti for his contribution and help in my work.

Special thanks to Prof. Emanuele Forte, extraordinary from both a personal and professional point of view. Thank you for the many geophysical data acquired to support my research.

I would like to warmly thank my parents and grandparents who supported and motivated me during my years of study.

Thanks to the super Gerry, friend and fellow student for more than 10 years.

Last but not least, I would like to thank my two special friends, Sharon and Benedetta, for supporting and putting up with me especially in the last year. Thanks for the dinners, the aperitifs, the trips and all the possible distractions from working.